

Numerical Simulations of Earthquake Scenarios
in the Lower Rhine Embayment Area

Numerische Simulation von Erdbebenszenarien
im Raum der Niederrheinischen Bucht

Michael Ewald

Dissertation

zur Erlangung des akademischen Grades
Doktor der Naturwissenschaften

der Fakultät für Geowissenschaften
Ludwig-Maximilians-Universität München

Oktober 2005

Darauf nahm Loki die Gestalt eines Lachses an und entsprang in den Wasserfall Franang. Da fingen ihn die Asen und banden ihn mit den Gedärmen seines Sohnes Nari. Sein anderer Sohn Narfi aber wurde in einen Wolf verwandelt. Skadi nahm eine Giftschlange und hing sie auf über Lokis Antlitz. Der Schlange entträufelte Gift. Sigyn, Lokis Weib, setzte sich neben ihn und hielt eine Schale unter die Gifftropfen. Wenn aber die Schale voll war, trug sie das Gift hinweg: unterdessen träufelte das Gift in Lokis Angesicht, wobei er sich so stark wand, daß die ganze Erde zitterte. Das wird nun Erdbeben genannt.

(Oegirs Trinkgelag, Die Edda (Codex Regius), 1851 durch Karl Simrock übersetzt.)

Zusammenfassung

Der englischsprachigen Dissertation ist eine Zusammenfassung in deutscher Sprache vorangestellt, um ausschließlich deutschsprachigen Lesern einen Überblick über diese Arbeit zu geben. Der Inhalt dieses Abschnitts entspricht einer ausführlicheren Fassung von Kapitel 1 in deutscher Sprache. Analog gliedert sich der Abschnitt in eine Einleitung, in der die Arbeit motiviert wird und eine anschließende Inhaltsangabe der einzelnen Kapitel.

Motivation

Ein großer Teil der tektonischen Verformungen der Erdkruste entlädt sich in Form von Erdbeben, gewöhnlich durch instabiles Rutschen benachbarter tektonischer Einheiten entlang bereits existenter Schwächezonen, sogenannter Störungszonen. Die tatsächliche Bruchfläche variiert zwischen einigen Quadratmetern für die schwächsten noch nachweisbaren Erdbeben bis hin zu tausenden von Quadratkilometern für große Beben. Innerhalb kontinentaler Kruste verteilen sich die Tiefenlagen der Bebenherde von flachen Ereignissen bis hin zu einer Maximaltiefe von 10 bis 30 Kilometer Tiefe abhängig von der jeweiligen Region und ihrer tektonischen Beschaffenheit. Dieser Tiefenbereich wird als "seismogenic layer" oder erdbebenträchtige Schicht bezeichnet. Der Bereich ist nach unten hin begrenzt durch den Übergang zu plastischen Verformungen.

Erdbeben, deren Bruchfläche den genannten Tiefenbereich in seiner Gesamtheit umfassen werden gemeinhin als große Beben eingestuft. Das Auftreten von Verformungen an der Oberfläche ist eine Folge solcher Ereignisse. Die Entfernungen, die die seismische Bruchfront dabei zurücklegt beträgt mindestens 10 km und dementsprechend werden Magnituden von 6 und mehr beobachtet. Die Grabenstrukturen im nordwestlichen Teil Europas, nämlich die aktiven Verwerfungszonen der niederrheinischen Bucht und des Ruhrtalesgrabensystems sind in der Lage Erdbeben der beschriebenen Größe hervorzubringen (Camelbeeck and Meghraoui (1998); Camelbeeck et al. (2001)). Aufgrund hoher Besiedlungsdichte und der Ballung von Industriestandorten im angesprochenen Raum ist das Schadenspotential eines solchen Ereignisses gewaltig. Hinzu kommt eine Gefährdung besonders exponierter Gebäude und Industrieanlagen bereits durch Erdbeben geringer Magnitude im Falle räumlicher Nähe zu den jeweiligen Epizentren. Rezente Ereignisse, wie die Beben von 2002 bei Alsdorf (Magnitude 4.9) und 1992 bei Roermond (Magnitude 5.9) haben das Potential von Schadenbeben im Raum der niederrheinischen Bucht verdeutlicht. Der wirtschaftliche Schaden des letztgenannten Erdbebens wird auf über 100 Millionen Euro geschätzt (Berz (1994)).

Es ist wichtig, klarzustellen, daß das Schadenspotential eines Erdbebens der genannten Größe deutlich höher einzuschätzen ist, wenn das Hypozentrum nur eine geringfügig andere Lage gehabt hätte, dies betrifft insbesondere die Tiefe des Bebenherds. Darüber hinaus wäre die Anzahl von verletzten Personen höher ausgefallen, wäre das Ereignis nicht während der Nachtstunden eingetreten.

Das Wissen um die große potentielle Gefährdung der Region in Hinblick auf Erdbeben steht in Gegensatz zu deren öffentlicher Wahrnehmung. Dieses Mißverhältnis gründet sich auf die niedrigen Deformationsraten von Bruchzonen im nordwestlichen Europa und die damit einhergehenden langen Zeiträume zwischen dem Wiederauftreten großer Beben. Für die Bruchzonen der niederrheinischen Bucht werden diese Intervalle mit mehreren Jahrhunderten angegeben (Ahorner (1992); Camelbeeck et al. (2000)). Eine weitere Folge solch langer Zeiträume ist ein Mangel an Beobachtungsdaten größerer Beben im genannten Gebiet. Große Ungenauigkeiten in der Abschätzung des seismischen Gefährdungspotentials für Regionen rezent niedriger Seismizität sind die Folge. Eine realistische Einschätzung der seismischen Gefährdung einer derart intensiv genutzten Region ist indes unumgänglich zur Erstellung von Auflagen für künftige Bauvorhaben. Dies gilt insbesondere für Einrichtungen mit erhöhten Sicherheitsmaßstäben, wie zum Beispiel Kernkraftwerke (Corradini (2003)).

Die Herausforderung einer realistischen Abschätzung der seismischen Gefährdung in Gebieten geringer Seismizität kann nur mit Hilfe des vereinten Einsatzes verschiedener geowissenschaftlicher Disziplinen bewältigt werden. So kann unter Berücksichtigung paläoseismischer Untersuchungen der Störungszonen in der niederheinischen Bucht der Beobachtungszeitraum auf geologische Zeitspannen ausgedehnt werden (Atakan et al. (2000); Sintubin et al. (2001)). Die Interpretation historischer Gebäudeschäden aus der römischen Zeit in Köln und Umgebung kann ebenfalls zur Erweiterung des zeitlichen Rahmens der Beobachtung von Erdbeben und deren Folgeerscheinungen beitragen. Kleinräumige Schwankungen in der Verteilung geschätzter Maximalwerte der Bodenbewegung können durch Techniken der Mikrozonierung erfasst werden. In der Folge werden hochauflösende Kartierungen des örtlichen Schwingungsverhaltens erstellt. Verschiedene Techniken, darunter solche, die auf der Nutzung künstlicher Schwingungsquellen beruhen, können zur Erstellung von verbesserten Geschwindigkeitsmodellen der Region eingesetzt werden (Fäh et al. (2003); Scherbaum et al. (2003); Ohrnberger et al. (2004)).

Numerische Simulationen erlauben die flächenhafte Abschätzung der Bodenbewegung in Folge regionaler Erdbebenszenarien (Olsen (2001); Komatitsch et al. (2004); Pitarka et al. (1996)). Die Durchführung solcher Simulationen für entsprechend entworfene Schlimmstfall-Szenarien können darüber hinaus Maximalwerte der Bodenbewegung liefern. Die Ergebnisse können in der Folge in probabilistischen Gefährdungsabschätzungen berücksichtigt werden. Numerische Simulationen bieten darüber hinaus die Möglichkeit, differentielle Effekte in Abhängigkeit geringfügiger Veränderungen eines oder mehrerer Parameter des Szenarios zu erkennen. So kann zum Beispiel die Frage beantwortet werden, welche Auswirkungen das Erdbeben von 1992 bei Roermond gehabt hätte, wäre es in 5 Kilometer geringerer Tiefe aufgetreten.

Ein dreidimensionaler Finite Differenzen Ansatz kommt in dieser Arbeit zum Einsatz, um die Bodenbewegung in Folge größerer historischer und rezenter Erdbeben in der niederrheinischen Bucht zu untersuchen. Besondere Beachtung findet die Ab-

hängigkeit der Ergebnisse von der Wahl der Simulationsparameter hinsichtlich des Modells und der technischen Umsetzung, wie etwa der Diskretisierung. Im Folgenden werden die Inhalte der einzelnen Kapitel und die wichtigsten Ergebnisse der Arbeit erläutert.

Struktur der Arbeit

Kapitel 2 In diesem Kapitel werden die der Wellenausbreitung in elastischen und viskoelastischen Materialien zugrunde liegenden physikalischen Grundlagen beschrieben. Ausgehend von der Elastizitätstheorie werden die elementaren Größen als Tensoren eingeführt und deren Zusammenhänge im Falle anisotroper Wellenausbreitung hergeleitet. Da sich diese Arbeit auf isotrope Wellenausbreitung beschränkt, steht dieser Spezialfall im Mittelpunkt der Diskussion. Ausbreitungsgeschwindigkeiten der verschiedenen Wellentypen sowie viskoelastische Dämpfung und damit einhergehende Dispersion werden behandelt. Im Rahmen dieser Arbeit kann es nicht Ziel sein, die Zusammenhänge detailliert zu diskutieren sondern es wird lediglich die zum Verständnis der folgenden Kapitel notwendige Basis vermittelt.

Kapitel 3 Die Modellierung von Wellenausbreitung in beliebig komplexen heterogenen Strukturen kann mit Hilfe numerischer Methoden modelliert, das heißt näherungsweise beschrieben werden. Der Finite Differenzen Ansatz, der in dieser Arbeit Anwendung findet wird in diesem Kapitel detailliert vorgestellt. Besonderes Augenmerk wird auf die Darstellung der in dieser Arbeit relevanten Themen gelegt: Ausgedehnte Quellen und Modellierung anelastischen Verhaltens. Eine aktuelle Entwicklung der Methode, die von einer alternativen Aufstellung der Finite Differenzen Operatoren Gebrauch macht - das sogenannte rotated staggered grid - wird vorgestellt.

Kapitel 4 In diesem Kapitel wird das Untersuchungsgebiet der Arbeit, die nieder-rheinische Bucht, beschrieben. Drei zusammenspielende Faktoren lassen diese Region im Nordwesten des europäischen Kontinents zu einem Gebiet erhöhter seismischer Gefährdung werden. Zum einen ist es die geographische Lage in unmittelbarer Nähe tektonisch aktiver Grabensysteme, die das Potential größerer Erdbeben in sich tragen, zweitens liegt in besagter Region eine Beckenstruktur vor, in der sich im Laufe von Jahrmillionen Sedimentschichten mit einer Mächtigkeit von bis zu zwei Kilometern abgelagert haben. Diese geologischen Strukturen können von Erdbeben hervorgerufene Bodenbewegungen erheblich verstärken. Zum dritten folgt aus der dichten Besiedlung und intensiven wirtschaftliche Nutzung der Region eine erhöhte Vulnerabilität der Gegend. Die genannten Aspekte werden in dem Abschnitt diskutiert.

Kapitel 5 Drei historische und rezente Erdbebenszenarien im Raum der niederrheinischen Bucht werden mit den beschriebenen Finite Differenzen Methoden modelliert. Zu jedem Szenario werden die Ergebnisse von zwei Simulationen mit unterschiedlichem Setup verglichen. Setup I entspricht dem möglichst einfachen Ansatz, unter der Annahme vollständig elastischen Verhaltens und einer Punktquelle, während in Setup II

Komplexitäten in Form von Viskoelastizität, also Dämpfung, und einer ausgedehnten Quelle enthalten sind. Darüber hinaus wurden die betreffenden Simulationen mit erhöhtem Rechenaufwand durchgeführt, was eine deutlich feinere Diskretisierung zuläßt. Die verwendeten Geschwindigkeitsmodelle sind ebenfalls deutlich verschieden und im Falle von Setup II realistischer. Ergebnisse aus beiden Simulationen werden verglichen, wobei das Hauptgewicht auf flächendeckend auswertbaren Parametern, wie Maxima der Bodenbewegung, seismische Intensität oder Schwingungsdauer, liegt. Diese Auswahl der untersuchten Parameter trägt dem begrenzten Beobachtungsumfang, insbesondere für die historischen Erdbeben, Rechnung. Während der Einfluß des Sedimentbeckens auf die Maximalamplituden bereits in den vereinfachten Simulationen deutlich zum Ausdruck kommt, werden eine Reihe von Details unter Verwendung des realistischeren Setups realistischer modelliert. Als Beispiel ist die Schwingungsdauer zu nennen, deren Verteilung unter Verwendung von Setup II ein deutlich konsistenteres und besser interpretierbares Bild ergibt. Für eine Station ist ein Datenabgleich mit Beobachtungen möglich, auch hier zeigt sich eine deutliche Verbesserung in der Reproduktion realer Seismogramme mit verbesserter Modellierung.

Kapitel 6 Am 22. Juli 2002 ereignete sich nahe der Ortschaft Alsdorf im Raum der niederrheinischen Bucht ein Erdbeben der Lokalmagnitude 4.9. Dank eines unmittelbar vorher fertiggestellten seismischen Netzwerks liegen für dieses Ereignis detaillierte Aufzeichnungen vor. Die Modellierung dieses Erdbebens und der Vergleich mit dem genannten Datensatz steht im Mittelpunkt dieses Abschnittes. Dazu wird die Komplexität der Simulation hinsichtlich Material und Quelle schrittweise erhöht. Das Material variiert zwischen elastischer und viskoelastischer Beschreibung, während die Quelle als punktförmig beziehungsweise ausgedehnt beschrieben wird. Die Resultate der Simulationen für die vier sich hieraus ergebenden Kombinationen werden untereinander und mit den Beobachtungsdaten verglichen. Eine Parametrisierung der Seismogramme in Eckdaten, wie zum Beispiel Maximalamplitude, Enveloppe und Frequenzgehalt wird vorgeschlagen um einen quantitativen Vergleich synthetischer und beobachteter Seismogramme zu ermöglichen. Die Verwendung einer Deltafunktion für die Quellenregung erlaubt die systematische Analyse der Ergebnisse in verschiedenen Frequenzbereichen. Bereits bei Betrachtung der Maximalamplituden zeigt sich eine wesentlich verbesserte Übereinstimmung mit Beobachtungen bei erhöhter Komplexität des Modells. Nur eine unter Verwendung von einer ausgedehnten Quelle in Verbindung mit einem anelastischem Sedimentmodell durchgeführte Simulation ermöglicht die Reproduktion beobachteter Maximalamplituden für alle Stationen. Die frequenzabhängige Analyse der Ergebnisse offenbart bei der verwendeten Quellbeschreibung eine überproportionale Verschiebung der Wellenenergie in den niederfrequenten Bereich. Dies läßt den Schluß zu, daß die gewählte Parametrisierung eines kreisförmigen, homogenen Bruches eine zu starke Idealisierung des tatsächlichen Bruchvorgangs darstellt. Mögliche Verbesserungen werden vorgeschlagen. Abgesehen von dieser Einschränkung zeigt die detaillierte Analyse der Spektren und Enveloppen, daß unter Verwendung erhöhter Modellkomplexität Seismogramme erhalten werden, die den Beobachtungen in allen Eckdaten entsprechen.

Kapitel 7 Die Komplexität der Wellenfelder in Gegenwart stark streuender Strukturen, wie der eines Sedimentbeckens, erschwert eine Abschätzung der Variabilität von Simulationsergebnissen in Abhängigkeit veränderter Eingabewerte. Da solche Eingabewerte, wie zum Beispiel Quellparameter oder Informationen über die Geologie des Untergrunds in der Realität immer fehlerbehaftete Größen sind ist das Wissen um solche Variabilitäten notwendig um eine Abschätzung hinsichtlich der Fehlerfortpflanzung vornehmen zu können. In diesem Kapitel wird eine Methode beschrieben, die Variabilität der Simulationsergebnisse zu quantifizieren. Da die beschriebene Methode äußerst rechenaufwendig ist, wird nur das Schema mit einer begrenzten Anzahl zu variierender Eingabewerte, darunter die Tiefe des Sedimentbeckens und der Quellmechanismus, aufgezeigt. Maximalamplituden und daraus resultierende seismische Intensität werden als flächendeckend bestimmbare Parameter gewählt, um Heterogenitäten der Variabilität darstellen zu können. Darüber hinaus werden für besonders auffällige Lokationen Seismogramme verglichen, um starke Abweichungen in ihrer Entstehung zu erklären. Es zeigt sich, daß eine um 10 Prozent variierende Sedimenttiefe lokale Unterschiede von bis zu 50 Prozent in der Maximalamplitude nach sich ziehen kann. Das Muster von Abschwächung und Verstärkung ist hierbei räumlich äußerst komplex. Der Vergleich der Wellenformen läßt verschiedene Mechanismen, die zu diesem räumlich stark variierenden Verhalten führen erkennen. Auf die übrigen untersuchten Parameter trifft das in ähnlicher Weise zu. Starke Wechselwirkungen zwischen den einzelnen Modellparametern erschweren eine Abschätzung der Ergebnisse, wenn in einem zukünftigen Schritt mehrere Parameter gleichzeitig variiert werden.

Kapitel 8 Die bei der numerischen Simulation seismischer Wellenausbreitung anfallenden sehr großen Datenmengen stellen hinsichtlich Speicherung und Verarbeitung hohe Anforderung an Hard- und Software. In diesem Abschnitt wird ein webbasierter Ansatz zur Erstellung einer interaktiven Datenbank für synthetische Daten von Erdbebenszenarien vorgestellt. Die Anwendung basiert auf einem PHP Code, der von Kim Olsen entwickelt und im Rahmen einer Diplomarbeit (Rieger (2005)) in seinem Funktionsumfang erweitert wurde. Während die einzelnen Schnittstellen in dieser Diplomarbeit ausführlich beschrieben wurden, werden hier die zugrunde liegende Datenstruktur und die für den Anwender notwendigen Verarbeitungsschritte zum Einbinden neuer Erdbebenszenarien erläutert.

Kapitel 9 Im letzten Kapitel werden die Ergebnisse der vorangegangenen in komprimierter Form vorgestellt und Schlußfolgerungen sowie Ausblicke präsentiert.

Appendix A Sämtliche im Rahmen dieser Arbeit vorgestellten Simulationen wurden mit einer Fortran Implementierung der Finite Differenzen Modellierung von seismischer Wellenausbreitung durchgeführt. Das zugrunde liegende Programm YAC wird dieser Arbeit hinzugefügt. Dieser Abschnitt gibt Auskunft über die einzelnen Programmblöcke, die Programmstruktur und die vorhandenen Ein- und Ausgabeschnittstellen. Die einzelnen Subroutinen des Codes werden in einer Art beschrieben, die es dem Benutzer erlaubt, das Programm eigenen Anforderungen anzupassen.

Appendix B Obwohl nicht direkt in Zusammenhang mit den vorgestellten Simulationen stehend, wird eine rudimentäre Implementierung des “Rotated Staggered Grid” Ansatzes zur Simulation von Wellenausbreitung mit dieser Arbeit zur Verfügung gestellt. Der Code wird analog zu Appendix A hinsichtlich Struktur und Schnittstellen vorgestellt. Die einzelnen Subroutinen sind erklärt um die Anpassung an tatsächliche Problemstellungen zu ermöglichen.

Appendix C Inhaltsangabe der mitgelieferten CD-ROM.

Summary

The choice of the Lower Rhine Embayment as study area for strong ground motion modeling may be puzzling at first glance. This region in the northwest of the European continent is characterized by active tectonics on a complex system of fault-zones with relatively low deformation rates. Consequently, the area has shown low to moderate seismicity in the time frame covered by observational seismology. However, historical and geological evidence proves that the fault systems of the Lower Rhine Embayment have the potential of producing large earthquakes with magnitudes 6 and above accompanied by surface rupture. The presence of large sediment deposits in this region leads to local amplification of ground motion with large lateral variations. Dense population and an agglomeration of industry results in an elevated seismic risk.

Assessment of seismic hazard in regions characterized by low recent seismicity is afflicted with large uncertainties. This is mainly due to the dearth of observational data on strong ground motions associated with large earthquakes. Numerical simulations of earthquake scenarios can account for estimates on peak ground motion and waveforms and therefore help closing this gap.

Naturally the first step consists in accurate reproduction of the few observed events. An additional crucial quantity is the range of variations of the simulation results within the uncertainty margins associated with input parameters. Knowledge about this behavior enlarges the significance of numerical simulation results.

Four historical and recent earthquake scenarios are modeled using a finite difference approach. Results are analyzed with special emphasis given to their intrinsic variability with model complexity and simulation settings. The choice of investigated parameters is adopted to the differing scope of observational data available for the individual events. In general encouraging similarity between synthetic and observed ground motions is found, even when a simplified model is used. However, detailed investigation carried out for the most recent earthquake scenario - the magnitude 4.9 July 22 2002 Alsdorf event - strongly suggests the significance of an appropriate source description and the modeling of anelastic behavior on simulation results.

Finally a web-based application for storage and visualization of synthetic ground motion data is presented.

Contents

1	Introduction	1
1.1	Motivation	1
1.2	Structure of the thesis	2
2	Physics of Wave Propagation	5
2.1	Displacement and Strain	5
2.2	Stress	6
2.3	Anisotropic Case	6
2.4	Elastic Constants	8
2.5	Seismic Velocities	9
2.6	Viscoelastic Attenuation	9
3	Numerical Implementation	13
3.1	Numerical Simulation of Seismic Waves	13
3.2	Finite Differences	14
3.3	Viscoelasticity	17
3.3.1	Motivation	17
3.3.2	Technique	17
3.3.3	Standard Linear Solid	17
3.3.4	Determination of Relaxation Times	19
3.3.5	Numerical Stability	21
3.3.6	Note on Parallelization	21
3.4	Finite-Source Implementation	23
3.4.1	Motivation	23
3.4.2	Technique	23
3.4.3	Verification	26
3.5	Nonuniform Grid	31
3.5.1	Motivation	31
3.5.2	Technique	31
3.5.3	Verification	35

3.5.4	Performance	38
3.5.5	Note on Parallelization	39
3.6	Rotated Grid	40
3.6.1	Motivation	40
3.6.2	Technique	40
3.6.3	Sample Applications	44
3.6.4	Discussion	46
3.7	Absorbing Boundaries	53
3.7.1	Motivation	53
3.7.2	Perfectly Matched Layers (PML)	53
3.8	Parallelization	55
3.8.1	Motivation	55
3.8.2	Techniques	55
3.8.3	2D MPI Implementation	56
4	The Lower Rhine Embayment	61
4.1	Framework	61
4.2	Stratigraphy	64
4.3	Recent Tectonics	70
4.3.1	Regional Stress Regime	70
4.3.2	Local Stress Regime	72
4.4	Seismicity	74
4.4.1	Paleoseismicity	74
4.4.2	Historical Earthquakes	75
4.5	Urbanization and Seismic Hazard	75
5	Earthquake Simulations in the LRE	79
5.1	Motivation	79
5.2	Different Setups	80
5.2.1	Computational Parameters	80
5.2.2	Parameterization of Media and Source	83
5.3	Scenarios	88
5.3.1	Düren	88
5.3.2	Euskirchen	88
5.3.3	Roermond	88
5.3.4	Summary of Source Parameters	90
5.4	Results	90
5.4.1	Snapshots	90
5.4.2	Seismic Intensity	94

5.4.3	Shaking Duration	101
5.4.4	Seismograms	107
5.4.5	Cumulative Intensity	118
5.5	Discussion	121
6	Finite Source and Viscoelasticity	123
6.1	Motivation	123
6.2	Setup	124
6.3	Model	125
6.4	Scenario	125
6.5	Observations	126
6.6	Results	131
6.6.1	General Problems of Quantification	131
6.6.2	Profiles	133
6.6.3	Peak Ground Velocity	138
6.6.4	Seismogram Comparison	145
6.6.5	Envelopes	158
6.6.6	Spectra	165
6.6.7	Spectrograms	174
6.7	Discussion	176
7	Variability of Simulation Results	179
7.1	Motivation	179
7.2	Setup	180
7.3	Model	181
7.4	Scenario	182
7.5	Error axes	182
7.5.1	Basin Depth	184
7.5.2	Source Depth	186
7.5.3	Source Mechanism	187
7.6	Results	188
7.6.1	Reference Solution	188
7.6.2	Basin Depth	188
7.6.3	Source Depth	196
7.6.4	Source Mechanism	202
7.7	Combination of Variabilities	208
7.8	Discussion	208

8	The WWW Scenario Database	213
8.1	Motivation	213
8.2	Technique	214
8.3	Creation of a New Scenario Earthquake Entry	216
8.3.1	Database Structure	216
8.3.2	Necessary Files	218
8.3.3	Maps	218
8.3.4	Configuration files	219
8.3.5	Seismic data	222
8.3.6	Upload Procedure	225
8.4	Possible Applications	226
8.4.1	Research	228
8.4.2	Educational Purposes	228
8.4.3	Data Sharing	228
8.4.4	Benchmarking	228
8.5	Discussion	229
9	Conclusions	233
9.1	Summary	233
9.2	Outlook	235
	Bibliography	237
A	YAC - Code Description	265
A.1	Overview	265
A.2	Code Files	268
A.2.1	Parameter Files	268
A.2.2	Subroutines	269
A.3	Input Files	271
A.3.1	Receiver Location	274
A.3.2	Velocity Model Definition	274
A.4	Output Files	274
A.5	Tested Environments	276
A.6	Matlab Tool for Relaxation Times	276
B	Rotated Staggered Grid - Code Description	277
B.1	Overview	277
B.2	Code Files	277
B.2.1	Parameter Files	277
B.2.2	Subroutines	280
B.3	Input files	281
B.4	Output Files	282

CONTENTS

xiii

C Supplementary CD-ROM

283

Chapter 1

Introduction

In this chapter the basic ideas of this work are outlined. First the study is motivated, then a brief description of the individual chapters and their content is given.

1.1 Motivation

A large part of tectonic deformation is relaxed during earthquakes, commonly produced by the unstable slippage of two crustal blocks along a preexisting zone of weakness, a so called fault zone. Active rupture area can vary from a few m^2 for the weakest detectable earthquakes to several thousands of km^2 for large earthquakes. In continental zones the depth range of earthquake origins, the so called seismogenic layer spreads from shallow depth to a maximum of 10 to 30 km depending on the individual region and its tectonic setting. The bottom limit of this seismogenic zone is associated with a mechanical limit below which deformations are released in plastic flow.

Earthquakes affecting the whole vertical dimension of the seismogenic layer are commonly considered large earthquakes. A natural consequence of large earthquakes is therefore the occurrence of coseismic surface deformation. Typically a rupture propagation distance or fault dimension in the order of at least 10 km is observed for such a scenario, corresponding to a magnitude of 6.0. The graben structures of northwestern Europe, namely the active rift systems in the Lower Rhine Embayment and the Roer Valley Graben have the potential of producing earthquakes of the described size (Camelbeek and Meghraoui (1998); Camelbeek et al. (2001)). Due to the dense population and the agglomeration of industry in that area the occurrence of such an earthquake could potentially result in tremendous damage. Additionally, vulnerable structures of industry and dwellings can be already at risk from smaller earthquakes if the epicenters are located close to the considered places. The recent magnitude 4.9 earthquake in 2002 near Alsdorf and magnitude 5.9 near the town of Roermond in 1992, the latter resulting in losses extending 100 million Euro in the epicentral area (Berz (1994)), have proven the potentially damaging character of seismicity in the region of the Lower Rhine Embayment. It must be emphasized that the potential damage of an earthquake of the size of the Roermond event is a lot higher with only slightly changing hypocenter location, especially if shallower hypocenter depth is considered and the number of casualties would also be higher if it had not taken place during the

night.

Knowledge of this large potential of damage due to seismic sources is in contrast with a low level of public awareness. The reason for this discrepancy is found in the low deformation rates within northwestern Europe's graben structures and the consequently long recurrence intervals for large earthquakes which are in the order of hundreds of years (Ahorner (1992); Camelbeeck et al. (2000)). These long recurrence periods also result in a sparseness of observational data for major earthquakes in the region. The consequence being large uncertainties in seismic hazard assessment of regions which have shown low to moderate seismicity within the period of instrumental recordings and historical descriptions. A realistic estimation of the seismic hazard of such an intensively used area is inevitable for future building codes, especially when highly sensitive structures such as nuclear power plants are concerned (Corradini (2003)).

The challenge of achieving realistic estimates of earthquake ground motion in areas of low present day seismicity can be faced only through an integrated approach involving various disciplines of hazard assessment. Taking advantage of paleoseismic investigations along the fault systems within the Lower Rhine Embayment the temporal range of observations can be extended to geological time scales (Atakan et al. (2000); Sintubin et al. (2001)). Interpretations on historical damage observed at Roman buildings in Cologne and other Roman settlements can extend the catalogues of historical strong ground motion observations to longer time scales. Small-scale heterogeneities in estimated peak ground motion can be evaluated by microzonation techniques resulting in a high resolution mapping of local site response. Various techniques, including the exploitation of ambient ground motions can be applied in order to construct an improved velocity model for the basin structures within the Lower Rhine Embayment (Fäh et al. (2003); Scherbaum et al. (2003); Ohrnberger et al. (2004)).

Numerical simulations have the capability of providing area-wide estimates on ground motion caused by scenario earthquakes within the region of interest (Olsen (2001); Komatitsch et al. (2004); Pitarka et al. (1996)). Carrying out such simulations for an appropriately designed worst-case scenario can also answer the important question for upper limits on ground motion. The results can be incorporated in probabilistic hazard analysis. Numerical simulations are also a tool in revealing differential effects due to a slight change in one or a few scenario parameters. For example answering the question what actually would have happened if the 1992 Roermond earthquake had taken place at 5 km shallower depth.

In this study a three-dimensional finite difference approach is used in order to quantify ground motions caused by major historical and recent earthquake scenarios within the Lower Rhine Embayment. Special emphasis is given to the sensitivity of results on simulation parameters both on the side of the model representation as well as the computational aspects of the simulations, such as grid discretization. In the following paragraph the individual chapters of this work are briefly outlined.

1.2 Structure of the thesis

Chapter 2 A brief introduction to the physics of wave propagation is given in order to make the following discussion on numerical approaches and their technical im-

plementation understandable without previous knowledge. Both the elastic and viscoelastic case is covered in this chapter. The description starts with the general case of anisotropic media and focuses on the isotropic case this work is restricted to.

Chapter 3 Wave propagation in complex heterogeneous media can be modeled using numerical methods. In this chapter the finite difference approach, which is used in this work is described in detail. Special emphasis is given to several aspects of wave propagation simulation which are of importance in this study, such as viscoelastic attenuation and finite source effects. Computational aspects such as absorbing boundaries, variable grid spacing and parallelization are also discussed. A recent approach taking advantage of a modified design of the computational grid, the so called rotated staggered grid is presented.

Chapter 4 The study area of this work, the Cologne Basin or Lower Rhine Embayment is introduced. Various aspects are covered, such as: geographic, geologic and tectonic setting, seismic activity, urbanization and seismic hazard. Seismicity in this region is discussed in scientific and economic context.

Chapter 5 First of several chapters presenting applications of ground motion modeling in the study area. Simulation results for three historical and recent earthquakes in the Lower Rhine Embayment are presented. Results from simulations with a simplified approach using point source approximation and the assumption of pure elastic behavior are compared with ones achieved by more sophisticated modeling. Besides an improved resolution of the computational grid, complexity is introduced into the model in terms of attenuation and finite source effects. The effects of both the improved model representation and the increased complexity are discussed.

Chapter 6 In 2002 a magnitude 4.9 earthquake occurred in the Lower Rhine Embayment near the town of Alsdorf. Due to a recently installed network of strong motion seismometer within the basin detailed data is available for this event. Focusing on this dataset a detailed discussion on the significance of the effects of finite source and viscoelastic attenuation in ground motion modeling is presented. Possibilities in quantifying similarities between synthetic and observed seismograms are identified.

Chapter 7 Complex wavefields resulting from highly heterogeneous media with complex geometries make it difficult to estimate the range of variability of simulation results due to slightly varying input parameters. As any kind of input data is afflicted with some uncertainty knowledge of this variability is crucial for an estimation of the error margins of simulation results. In this chapter a kind of brute force approach towards achieving such estimates is suggested. Due to limitations of computational capabilities this is restricted to a pilot study.

Chapter 8 Huge amounts of data are produced by numerical simulations of seismic wave propagation. Taking advantage of webbased technologies an approach incorporating an interactive webbased earthquake scenario database is presented. An PHP

implementation of such an interface by Kim Olsen was taken as basis and extended in its capabilities. Whereas a description of the interfaces and its usage is provided in Rieger (2005) this chapter focuses on data preprocessing necessary for potential users of the database and outlines possible areas of application.

Chapter 9 The last chapter briefly summarizes the most important results from the previous chapters. Some concluding remarks are made and future perspectives on the topic are presented.

Appendix A The simulations in this work are carried out using a Fortran implementation of finite difference wave propagation called YAC. The source code of this program is provided as part of this thesis. In this appendix the program structure is outlined and the design of input and output interfaces are specified. All subroutines of the program are briefly described in order to allow adopting the code to specific problems by potential users.

Appendix B The recently invented approach of a rotated staggered grid for finite difference simulation of wave propagation was implemented and tested. Although it is not directly linked to the requirements of this study there are several areas of application that could potentially aim from this approach. The source code is provided as part of this thesis.

Appendix C A supplementary CD-ROM is provided along with this thesis. Its content is outlined in this appendix.

Chapter 2

Physics of Elastic and Viscoelastic Wave Propagation

In order to make the following chapters understandable without previous knowledge in this chapter a concise introduction to the physical basis of wave propagation in elastic and viscoelastic media is given.

2.1 Displacement and Strain

Displacement u is the deviation of a point from its reference position, that means the position it had in absence of external forces or elastic waves propagating through the medium. Since the deviation can be in all directions, u is a vectorial quantity and depends on the Cartesian components x, y and z of the initial position \vec{r} . Considering an infinitesimal small length l between two points within an elastic medium, we can describe the change of this length caused by deformation of the medium using the following equation:

$$l'^2 = l^2 + 2\epsilon_{ij}\delta x_i\delta x_j \quad (2.1)$$

The quantity ϵ_{ij} is the strain tensor and reads for small displacements:

$$\epsilon_{ij} = \frac{1}{2}(u_{i,j} + u_{j,i}) \quad (2.2)$$

The components of the strain tensor with $i = j$ denote compression along axis i , components with $i \neq j$ denote shear distortion of the i -axis in j -direction and vice versa. Considering a small area δV that has the volume $\delta V'$ after deformation, the change of volume depends directly on the strain tensor components. The new volume reads

$$\delta V' = \delta V(1 + \epsilon_{11} + \epsilon_{22} + \epsilon_{33}) \quad (2.3)$$

It should be noted that the strain tensor includes only 6 independent components, since

$$\epsilon_{ij} = \epsilon_{ji} \quad (2.4)$$

2.2 Stress

The stress tensor is commonly described in terms of forces acting on a unit volume V . Writing scalar quantities as the divergence of vectors, an acting force can be described completely as the divergence of a tensor, yielding

$$F_i = \sigma_{ij,j} \quad (2.5)$$

σ_{ij} is called stress tensor. In analogy with the strain tensor it consists of longitudinal components ($i = j$) and shear components ($i \neq j$). The stress tensor also has 6 independent components.

2.3 Anisotropic Case

From the previous section it is understood that in the most general case stresses and strains are tensorial quantities. These are related in the general anisotropic form of Hooke's law:

$$\sigma_{ij} = c_{ijkl}\epsilon_{kl} \quad (2.6)$$

where summation convention is applied on repeated subscripts k and l . The elastic stiffness tensor c_{ijkl} is a four-dimensional tensor quantity consisting of 81 elements. However the number of independent elements is significantly smaller. Symmetry of stress and strain implies

$$c_{ijkl} = c_{jikl} = c_{ijlk} = c_{jilk} \quad (2.7)$$

which reduces the number of independent elements to 36. Additionally, it can be concluded from the existence of unique strain energy potentials that

$$c_{ijkl} = c_{klij} \quad (2.8)$$

diminishing the number of independent elements to 21. This refers to the absolute maximum number of elastic constants necessary to describe the behavior of an arbitrary medium. Further restrictions can be imposed by intrinsic symmetries of the medium. Whereas triclinic systems with the lowest symmetry require all 21 constants

for their description, higher material symmetries result in a smaller number of independent constants. For example 9 constants are necessary to describe an orthorhombic material and for a cubic system the number of independent constants is as low as 3. Maximum symmetry is present in the case of isotropic media, which are completely characterized by two independent constants. Identical symmetry considerations hold on for the compliance tensor s_{ijkl} which relates strains as a linear combination of stresses in the alternative expression of Hooke's law:

$$\varepsilon_{ij} = s_{ijkl}\sigma_{kl} \quad (2.9)$$

The compliance tensor is the tensor inverse of the stiffness tensor and it can be written:

$$c_{ijkl}s_{klmn} = I_{ijmn} = \frac{1}{2}(\delta_{im}\delta_{jn} + \delta_{in}\delta_{jm}) \quad (2.10)$$

An abbreviated notation for stresses, strains and the tensors relating each other has become common. In this notation stresses and strains are written as six-element vectors:

$$T = \begin{bmatrix} \sigma_1 = \sigma_{11} \\ \sigma_2 = \sigma_{22} \\ \sigma_3 = \sigma_{33} \\ \sigma_4 = \sigma_{12} \\ \sigma_5 = \sigma_{13} \\ \sigma_6 = \sigma_{23} \end{bmatrix} \quad E = \begin{bmatrix} \epsilon_1 = \epsilon_{11} \\ \epsilon_2 = \epsilon_{22} \\ \epsilon_3 = \epsilon_{33} \\ \epsilon_4 = 2\epsilon_{12} \\ \epsilon_5 = 2\epsilon_{13} \\ \epsilon_6 = 2\epsilon_{23} \end{bmatrix}$$

The number of subscripts for the relating stiffness and compliance tensors is then reduced to two. Indices are replaced pairwise by one index following the convention:

$ij(kl)$	$I(J)$
11	1
22	2
33	3
12, 21	4
13, 31	5
23, 32	6

As mentioned above in the isotropic case the number of independent elements is reduced to two and the matrix can be written as:

$$\begin{bmatrix} c_{11} & c_{12} & c_{12} & 0 & 0 & 0 \\ c_{12} & c_{11} & c_{12} & 0 & 0 & 0 \\ c_{12} & c_{12} & c_{11} & 0 & 0 & 0 \\ 0 & 0 & 0 & c_{44} & 0 & 0 \\ 0 & 0 & 0 & 0 & c_{44} & 0 \\ 0 & 0 & 0 & 0 & 0 & c_{44} \end{bmatrix}$$

2.4 Elastic Constants

Hooke's law relates stress and strain and has in an isotropic, linear elastic medium the form:

$$\sigma_{ij} = \lambda \delta_{ij} \epsilon_{\alpha\alpha} + 2\mu \epsilon_{kl}. \quad (2.11)$$

This may be rewritten as

$$\epsilon_{ij} = \frac{1}{E} ((1 + \nu) \sigma_{ij} - \nu \delta_{ij} \sigma_{\alpha\alpha}) \quad (2.12)$$

where

ϵ_{ij} := elements of strain tensor

σ_{ij} := elements of stress tensor

$\epsilon_{\alpha\alpha}$:= volumetric strain

$\sigma_{\alpha\alpha}$:= mean stress

δ_{ij} := 0 if $i \neq j$, 1 if $i = j$.

In order to determine the stress strain relations in an isotropic, linear elastic medium only two constants are necessary. In equation 2.11 the constants are λ and μ , whereas in equation 2.12 E and ν describe the materials behavior. These pairs of constants can be derived from each other, and there are numerous conventions on the choice of these constants related to individual problems. Some of the most common ones are listed below.

- Young's modulus

$$\sigma_{zz} = E \epsilon_{zz}; \quad \sigma_{xx} = \sigma_{yy} = \sigma_{xy} = \sigma_{xz} = \sigma_{yz} = 0 \quad (2.13)$$

- Shear modulus

$$\sigma_{ij} = 2\mu \epsilon_{ij}; \quad i \neq j \quad (2.14)$$

- Bulk modulus

$$\sigma_0 = \frac{1}{3} \sigma_{\alpha\alpha} = K \epsilon_{\alpha\alpha} \quad (2.15)$$

- Poisson's Ratio

$$\nu = \frac{\epsilon_{xx}}{\epsilon_{zz}} \quad (2.16)$$

From energy conservation follows that the following relations hold for all isotropic materials:

$$\lambda + \frac{2\mu}{3} \geq 0; \quad \mu \geq 0 \quad (2.17)$$

as well as

$$-1 < \nu \leq 1/2; \quad E \geq 0 \quad (2.18)$$

2.5 Seismic Velocities

Phase velocities in isotropic media are given by:

$$v_p^2 = \frac{\lambda + 2\mu}{\rho} \equiv \frac{c_{11}}{\rho} \quad (2.19)$$

and

$$v_s^2 = \frac{\mu}{\rho} \equiv \frac{c_{44}}{\rho} \quad (2.20)$$

From above considerations it can be understood that the propagation of elastic waves can be described completely by:

$$\rho \ddot{u}_i = c_{ijkl} u_{j,k,l} + f_i \quad (2.21)$$

Where the implicitly space dependent elements of the equation are:

u : displacement,

ρ : density of the medium,

c_{ijkl} : stiffness tensor of the medium,

f_i : source term.

2.6 Viscoelastic Attenuation

Seismic waves propagating through earth media are attenuated due to numerous reasons. Whereas all of them have the common result of reduced amplitudes and distorted waveforms of the propagating waves, the mechanisms causing this are different. The most important distinction has to be made between geometrical spreading, attenuation caused by elastic scattering at small-scale heterogeneities which both leave the integrated energy contained in the wavefield unaffected and irreversible conversion of kinematic energy into internal heat. The latter is commonly known as absorption or viscoelastic attenuation and is briefly introduced in the following. For a sinusoidal excitation the energy loss associated with viscoelastic attenuation per unit volume is

$$\Delta E = \frac{\overline{E}}{Q} \quad (2.22)$$

where \overline{E} is the mean energy contained in the media and Q denotes the quality factor. From laboratory experiments Q is considered to be independent of deformation amplitude (e.g. Winkler and Nur (1982); Murphy (1983)) in the range of seismic deformations. Consequently, linear equations can be used in order to describe viscoelastic behavior. However, Stacey et al. (1975) discuss approaches including nonlinear absorption. For one dimensional viscoelastic media the stress strain relation yields

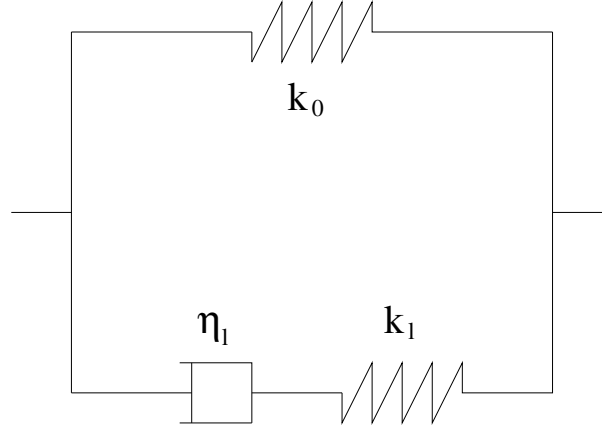


Figure 2.1: Standard Linear Solid.

$$\sigma(t) = \dot{\Psi}(t) * \epsilon(t) = \Psi(t) * \dot{\epsilon}(t) \quad (2.23)$$

with

$\sigma(t)$ describing stress as a function of time, $\epsilon(t)$ the temporal evolution of strain and $\Psi(t)$ the relaxation function which is zero for negative times. This relation imposes that the stresses in the media depend not only on the actual strains, but also on strains which had been applied previously. Viscoelastic media evolve a 'memory' of previous conditions.

In practice the relaxation function of viscoelastic media is described using rheologic analogies like a Kelvin-Voigt body or a Maxwell body. In this work the Standard Linear Solid (SLS) is used as rheologic analogy. Figure 2.6 shows a sketch of the Standard Linear Solid. The relaxation function for a single SLS is given by

$$\Psi(t) = M_R \left\{ 1 + \left(\frac{\tau_\epsilon}{\tau_\sigma} - 1 \right) e^{-t/\tau_\sigma} \right\} H(t) \quad (2.24)$$

where M_R describes the relaxation modulus, τ_ϵ is the retardation time for strain at the relaxation mechanism at constant stress and τ_σ the relaxation time for stresses acting on the relaxation mechanism. These three quantities describe the behavior of the standard linear solid entirely. Using viscous and elastic moduli of the individual mechanical parts of the SLS these times and the relaxation modulus are related as:

$$\tau_{\sigma l} = \frac{\eta_l}{k_l}, \quad (2.25)$$

$$\tau_{\epsilon l} = \frac{\eta_l}{k_0} + \frac{\eta_l}{k_l} \quad (2.26)$$

and

$$M_R = k_0 \quad (2.27)$$

Zener (1948). From the view of enhancing elastic wave propagation to viscoelastic description of the process it becomes clear that the additional quantities are the relaxation and retardation times, as the spring representing the elastic behavior is already defined by the media. Viscoelastic media alter passing seismic waves in two ways: dispersion and reduction of amplitudes. The effects are intrinsically coupled throughout the Kramers-Krönig relation. Consequently, amplitude decrease implies dispersion and vice versa.

Chapter 3

Numerical Implementation

In this chapter the finite difference concept and technical realization is presented. Special emphasis is given to state of the art features of finite difference wave propagation codes, such as finite sources and viscoelastic attenuation on the modeling side as well as computational aspects such as absorbing boundaries and new grid types.

3.1 Numerical Simulation of Seismic Waves

Modeling wave propagation and media response has become an important tool in understanding the physics of seismic waves. Whereas solutions for simple geometries can be achieved in analytical form, for more complex models the employment of numerical calculations is inevitable. With the increasing recent computational resources, realistic simulation of waveforms in the presence of highly heterogenous structures and source models have become available. Numerical methods most prominently applied to wave propagation problems are: Finite differences (e.g. Graves (1993); Frankel (1993); Olsen et al. (1995); Pitarka et al. (1998); Satoh et al. (2001)), finite elements (e.g. Bao et al. (1998); Bielak and Ghattas (1999); Garatani et al. (2000); Aagaard et al. (2001, 2004)) and spectral / pseudo-spectral methods, partly combined with a finite element scheme (Komatitsch and Vilotte (1998); Komatitsch and Tromp (1999); Komatitsch et al. (2004)). It is generally agreed that all these methods have their advantages and limitations compared to the others and that there is no optimal method for all possible application areas. In the presence of strong material contrasts, like it is the case for sedimentary basins within bedrock environment, the Finite Difference approach is still widely used.

Despite the limitations of this approach, mainly its extensive consumption of computational resources in terms of both core memory and CPU time, a number of advantages make the method attractive to researchers: First of all, the general simplicity of the methods ease the implementation of finite differences. Physical concepts such as viscoelasticity or finite sources can be applied relatively straight forward. Furthermore, finite difference operators are locally defined, which makes the method suitable for parallelization, the nowadays paradigm for the use of high performance computational facilities. This chapter gives an overview of the finite difference method used in this work with special emphasize to the implementation of viscoelasticity and finite sources

in the course of this project. An interesting and relatively new approach using alternatively oriented differential operators is presented shortly along with a number of possible applications which could benefit from the usage of this method.

3.2 Finite Differences

The following equations describe the basis for calculating wave propagation in three-dimensional, perfectly elastic isotropic media.

The equations describing the conservation of momentum:

$$\rho \delta_{tt} u_x = \delta_x \sigma_{xx} + \delta_y \sigma_{xy} + \delta_z \sigma_{xz} + f_x \quad (3.1)$$

$$\rho \delta_{tt} u_y = \delta_x \sigma_{xy} + \delta_y \sigma_{yy} + \delta_z \sigma_{yz} + f_y \quad (3.2)$$

$$\rho \delta_{tt} u_z = \delta_x \sigma_{xz} + \delta_y \sigma_{yz} + \delta_z \sigma_{zz} + f_z \quad (3.3)$$

and the stress-strain relations:

$$\sigma_{xx} = (\lambda + 2\mu) \delta_x u_x + \lambda (\delta_y u_y + \delta_z u_z) \quad (3.4)$$

$$\sigma_{yy} = (\lambda + 2\mu) \delta_y u_y + \lambda (\delta_x u_x + \delta_z u_z) \quad (3.5)$$

$$\sigma_{zz} = (\lambda + 2\mu) \delta_z u_z + \lambda (\delta_x u_x + \delta_y u_y) \quad (3.6)$$

$$\sigma_{xy} = \mu (\delta_y u_x + \delta_x u_y) \quad (3.7)$$

$$\sigma_{xz} = \mu (\delta_z u_x + \delta_x u_z) \quad (3.8)$$

$$\sigma_{yz} = \mu (\delta_z u_y + \delta_y u_z) \quad (3.9)$$

Herein the u_x, u_y, u_z are the vector components of the particle displacement and the stress tensor is given by the elements $\tau_{xx} \cdots \tau_{xz}$. The quantities f_x, f_y, f_z are equivalent body forces.

Differentiating the equations above with respect to time and substitution of velocity components v_x, v_y and v_z for the time derivatives $\delta_t u_x, \delta_t u_y$ and $\delta_t u_z$.

$$\delta_t v_x = \frac{1}{\rho} (\delta_x \sigma_{xx} + \delta_y \sigma_{xy} + \delta_z \sigma_{xz} + f_x) \quad (3.10)$$

$$\delta_t v_y = \frac{1}{\rho} (\delta_x \sigma_{xy} + \delta_y \sigma_{yy} + \delta_z \sigma_{yz} + f_y) \quad (3.11)$$

$$\delta_t v_z = \frac{1}{\rho} (\delta_x \sigma_{xz} + \delta_y \sigma_{yz} + \delta_z \sigma_{zz} + f_z) \quad (3.12)$$

$$\delta_t \sigma_{xx} = (\lambda + 2\mu) \delta_x v_x + \lambda (\delta_y v_y + \delta_z v_z) \quad (3.13)$$

$$\delta_t \sigma_{yy} = (\lambda + 2\mu) \delta_y v_y + \lambda (\delta_x v_x + \delta_z v_z) \quad (3.14)$$

$$\delta_t \sigma_{zz} = (\lambda + 2\mu) \delta_z v_z + \lambda (\delta_x v_x + \delta_y v_y) \quad (3.15)$$

$$\delta_t \sigma_{xy} = \mu (\delta_y v_x + \delta_x v_y) \quad (3.16)$$

$$\delta_t \sigma_{xz} = \mu (\delta_x v_z + \delta_z v_x) \quad (3.17)$$

$$\delta_t \sigma_{yz} = \mu (\delta_y v_z + \delta_z v_y) \quad (3.18)$$

This system of equations can be implemented in finite difference codes as described by various authors (e.g. Levander (1988); Igel et al. (1995); Graves (1996)). As it is necessary for the understanding of the discussion on particular issues dealing with the concept of finite differences, this well known procedure should here be briefly described in its major steps. Necessary spatial interpolations are carried out based on an approximation of the Taylor series:

$$f(x \pm \Delta x) = f(x) \pm f'(x) + \frac{\Delta x^2}{2!} f''(x) \pm \frac{\Delta x^3}{3!} f''' + \dots \quad (3.19)$$

from which the following differential quotients

$$\frac{\delta f}{\delta x} \approx \frac{f(x) - (f(x - \Delta x))}{\Delta x} \quad (3.20)$$

and

$$\frac{\delta f}{\delta x} \approx \frac{f(x + \Delta x) - (f(x))}{\Delta x} \quad (3.21)$$

for forward and backward differencing are retrieved. Another truncated Taylor series delivers the extrapolation in time necessary to calculate future values:

$$f(t + \Delta t) = f(t) + \Delta t f'(t) + \frac{\Delta t^2}{2!} f''(t) + \frac{\Delta t^3}{3!} f'''(t) + \dots \quad (3.22)$$

$$f(t + \Delta t) \approx f(t) + \frac{\delta f(t)}{\delta t} \Delta t. \quad (3.23)$$

For the time dependent propagation of a wave field it is necessary to discretize the medium on a spatial grid. The elastic constants as well as the variable values of stress and velocity are therefore only defined on particular grid points. The elastic equations as written above suggest the use of a so called staggered grid, in which the variables of the wave field and the media parameters are not defined on the same location in the grid. Figure 3.1 shows the distribution of variables and parameters on a staggered grid mesh.

Obviously the neighboring elements are only half a grid spacing away from each other. Because the numerical error of the derivatives is constrained by the distance to the neighbor elements errors on the staggered grid mesh are reduced compared to a centered grid. The difference operators are all centered automatically in both space and time. Therefore the system is not only spatially staggered but also temporally and it is possible to update velocities independently from stresses. In section 3.8 it will be discussed how this characteristic becomes important for efficient parallelization of the code.

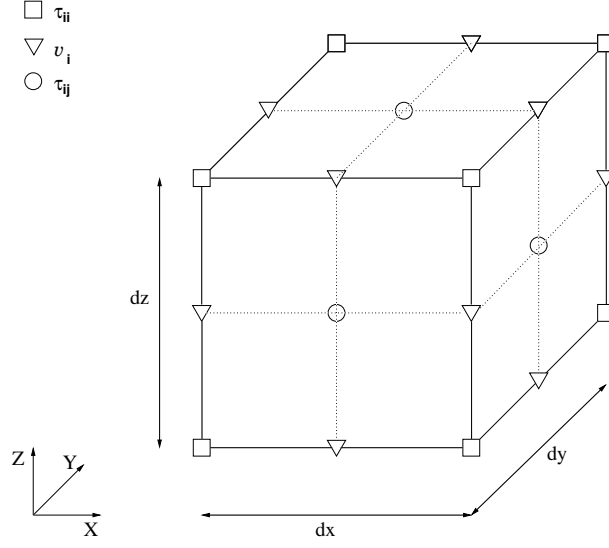


Figure 3.1: Sketch of the Staggered-Grid mesh. The location of individual wavefield variables and model parameters is shown.

As media parameters are distributed on different locations within one grid cell, whereas the media definition typically associates one set of parameters with one grid cell, it becomes necessary to interpolate values onto the locations where the actual calculation is taking place. This intuitive interpolation approach leads to effective model parameters as suggested by Graves (1996).

$$b_x = \frac{1}{2}(b_{i,j,k} + b_{i+1,j,k}) \quad (3.24)$$

$$b_y = \frac{1}{2}(b_{i,j,k} + b_{i,j+1,k}) \quad (3.25)$$

$$b_z = \frac{1}{2}(b_{i,j,k} + b_{i,j,k+1}) \quad (3.26)$$

Where b denotes inverse density or buoyancy. For the shear moduli similar relations are found.

$$\mu_{xy} = \frac{1}{4} \left(\frac{1}{\mu_{i,j,k}} + \frac{1}{\mu_{i+1,j,k}} + \frac{1}{\mu_{i,j+1,k}} + \frac{1}{\mu_{i+1,j+1,k}} \right)^{-1} \quad (3.27)$$

$$\mu_{xz} = \frac{1}{4} \left(\frac{1}{\mu_{i,j,k}} + \frac{1}{\mu_{i+1,j,k}} + \frac{1}{\mu_{i,j,k+1}} + \frac{1}{\mu_{i+1,j,k+1}} \right)^{-1} \quad (3.28)$$

$$\mu_{yz} = \frac{1}{4} \left(\frac{1}{\mu_{i,j,k}} + \frac{1}{\mu_{i,j+1,k}} + \frac{1}{\mu_{i,j,k+1}} + \frac{1}{\mu_{i,j+1,k+1}} \right)^{-1} \quad (3.29)$$

Recent work by Moczo et al. (2002) deriving these effective model parameters with a more analytical approach has shown results which are very similar to the ones achieved by the above given approach.

3.3 Viscoelasticity

3.3.1 Motivation

Earth media attenuate and disperse propagating mechanical waves. In presence of sedimentary basins this attenuation effect becomes very important as the net effect of such a basin on ground motion consists in amplification due to the low velocity character of the basin, focusing effects due to the basins geometry and a de-amplification due to increased attenuation in the relatively weak sedimental rocks. The significance of absorption effects from sedimentary basins and valley is known from the work of numerous authors (e.g. Gibbs et al. (1994); Hoshiya et al. (2001)). Incorporating viscoelasticity in the simulations should account for the damping effect on amplitudes as well as altered waveforms by dispersion. Viscoelastic attenuation in seismic wave propagation is studied by various authors (e.g. Day and Minster (1984); Carcione et al. (1988); Dong and McMechan (1995); Xu and McMechan (1995, 1998))

3.3.2 Technique

Whereas for an ideal plane wave with fixed wavelength attenuation can be modeled by incorporating a simple locally varying damping factor as supposed by Graves (1996), the more complex wavefield resulting from basin simulations should be modeled with a more physical approach. The use of Standard Linear Solids (SLS) is a possibility to model attenuation effects on both amplitude and waveforms. The latter due to the fact that SLSs are capable of producing relatively constant quality factors over a certain frequency range and therefore introduce dispersion into the wavefield. The approach used in this work follows the work of Robertsson (Robertsson et al. (1994), Blanch et al. (1995)).

3.3.3 Standard Linear Solid

Modeling viscoelastic materials with using mechanical analogs such as springs and dash-pots is an extension to the perfectly elastic model consisting only of springs with a spring constant corresponding to the elastic properties of the medium. The Standard Linear Solid is a simple viscoelastic model constructed of a spring in parallel to a spring and a dashpot in series (Pipkin (1986)). The layout of a standard linear solid is shown in figure 3.2. Typically, the attenuation of waves propagating through a material is characterized by the quality factor Q . Q is the length of the wave path through the material expressed as number of wavelengths after which the amplitude is reduced by a factor $e^{-\pi}$. From this loose definition it can be understood that estimations of the quality factor from seismic observations are difficult (White (1992)).

To fulfill the requirements of this study the implementation of the standard linear solid given by Robertsson et al. (1994) for the 2D case is enhanced to three dimensions. The following set of equations is derived. Formulae concerning the velocity update stay the same:

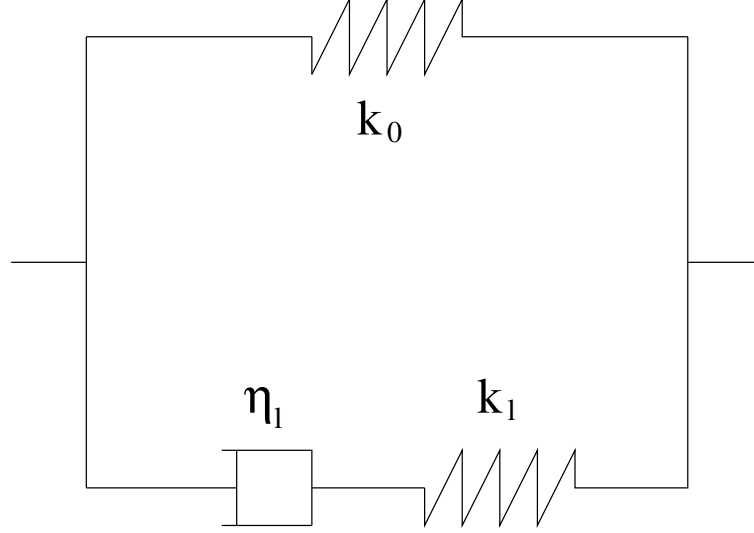


Figure 3.2: Sketch showing the mechanical analogies of the Standard Linear Solid (SLS).

$$\delta_t v_x = \frac{1}{\rho} (\delta_x \sigma_{xx} + \delta_y \sigma_{xy} + \delta_z \sigma_{xz} + f_x) \quad (3.30)$$

$$\delta_t v_y = \frac{1}{\rho} (\delta_x \sigma_{xy} + \delta_y \sigma_{yy} + \delta_z \sigma_{yz} + f_y) \quad (3.31)$$

$$\delta_t v_z = \frac{1}{\rho} (\delta_x \sigma_{xz} + \delta_y \sigma_{yz} + \delta_z \sigma_{zz} + f_z) \quad (3.32)$$

whereas the formulae for the stresses become:

$$\delta_t \sigma_{xx} = \pi \frac{\tau_\varepsilon^p}{\tau_\sigma} (\delta_x v_x + \delta_y v_y + \delta_z v_z) - 2\mu \frac{\tau_\varepsilon^s}{\tau_\sigma} (\delta_y v_y + \delta_z v_z) + r_{xx} \quad (3.33)$$

$$\delta_t \sigma_{yy} = \pi \frac{\tau_\varepsilon^p}{\tau_\sigma} (\delta_x v_x + \delta_y v_y + \delta_z v_z) - 2\mu \frac{\tau_\varepsilon^s}{\tau_\sigma} (\delta_x v_x + \delta_z v_z) + r_{yy} \quad (3.34)$$

$$\delta_t \sigma_{zz} = \pi \frac{\tau_\varepsilon^p}{\tau_\sigma} (\delta_x v_x + \delta_y v_y + \delta_z v_z) - 2\mu \frac{\tau_\varepsilon^s}{\tau_\sigma} (\delta_x v_x + \delta_y v_y) + r_{zz} \quad (3.35)$$

$$\delta_t \sigma_{xy} = \mu \frac{\tau_\varepsilon^s}{\tau_\sigma} (\delta_y v_x + \delta_x v_y) + r_{xy} \quad (3.36)$$

$$\delta_t \sigma_{xz} = \mu \frac{\tau_\varepsilon^s}{\tau_\sigma} (\delta_x v_z + \delta_z v_x) + r_{xz} \quad (3.37)$$

$$\delta_t \sigma_{yz} = \mu \frac{\tau_\varepsilon^s}{\tau_\sigma} (\delta_y v_z + \delta_z v_y) + r_{yz} \quad (3.38)$$

The quantities $r_{xx}.. r_{yz}$ are the so called memory variables. These variables are used to store a portion of wave energy which is detracted from the elastic stress update as visible in the above equations. The memory variables evolve with time according to the relations:

$$\delta_t r_{xx} = -\frac{1}{\tau_\sigma} (r_{xx} + \pi \left(\frac{\tau_\varepsilon^p}{\tau_\sigma} - 1 \right) (\delta_x v_x + \delta_y v_y + \delta_z v_z)) - \quad (3.39)$$

$$-2\mu \left(\frac{\tau_\varepsilon^s}{\tau_\sigma} - 1 \right) (\delta_y v_y + \delta_z v_z)$$

$$\delta_t r_{yy} = -\frac{1}{\tau_\sigma} (r_{yy} + \pi \left(\frac{\tau_\varepsilon^p}{\tau_\sigma} - 1 \right) (\delta_x v_x + \delta_y v_y + \delta_z v_z)) - \quad (3.40)$$

$$-2\mu \left(\frac{\tau_\varepsilon^s}{\tau_\sigma} - 1 \right) (\delta_x v_x + \delta_z v_z)$$

$$\delta_t r_{zz} = -\frac{1}{\tau_\sigma} (r_{zz} + \pi \left(\frac{\tau_\varepsilon^p}{\tau_\sigma} - 1 \right) (\delta_x v_x + \delta_y v_y + \delta_z v_z)) - \quad (3.41)$$

$$-2\mu \left(\frac{\tau_\varepsilon^s}{\tau_\sigma} - 1 \right) (\delta_x v_x + \delta_y v_y)$$

$$\delta_t r_{xy} = -\frac{1}{\tau_\sigma} (r_{xy} + \mu \left(\frac{\tau_\varepsilon^s}{\tau_\sigma} - 1 \right) (\delta_y v_x + \delta_x v_y)) \quad (3.42)$$

$$\delta_t r_{xz} = -\frac{1}{\tau_\sigma} (r_{xz} + \mu \left(\frac{\tau_\varepsilon^s}{\tau_\sigma} - 1 \right) (\delta_z v_x + \delta_x v_z)) \quad (3.43)$$

$$\delta_t r_{yz} = -\frac{1}{\tau_\sigma} (r_{yz} + \mu \left(\frac{\tau_\varepsilon^s}{\tau_\sigma} - 1 \right) (\delta_y v_z + \delta_z v_y)) \quad (3.44)$$

The stresses are updated with new values from the memory variables as expressed in equations 3.39 to 3.44 in a leap-frog scheme.

3.3.4 Determination of Relaxation Times

Using the complex stress modulus M_c which is defined as the Fourier transform of the stress relaxation function (Pipkin (1986)) as starting point, the quality factor Q may be written as

$$Q(\omega) = \frac{Re(M_c(\omega))}{Im(M_c(\omega))} \quad (3.45)$$

From this equation 3.45 it can be understood that Q equals the number of wavelengths a pulse must propagate before its amplitude is reduced by a factor of $e^{-\pi}$ (White (1992)). The quality factor is therefore frequency dependent. For a single SLS it can be written in the following form:

$$Q(\omega) = \frac{\frac{1+\omega^2\tau_\varepsilon\tau_\sigma}{1+\omega^2\tau_\sigma^2}}{\frac{\omega(\tau_\varepsilon-\tau_\sigma)}{1+\omega^2\tau_\sigma^2}} \quad (3.46)$$

An arbitrary viscoelastic medium can be described with two independent SLS for P and S-waves respectively. Their relaxation functions become:

$$M_P(t) = (\lambda + 2\mu) \left(-\frac{\tau_\varepsilon^p}{\tau_\sigma} e^{-t/\tau_\sigma} \right) \theta(t), \text{ and}$$

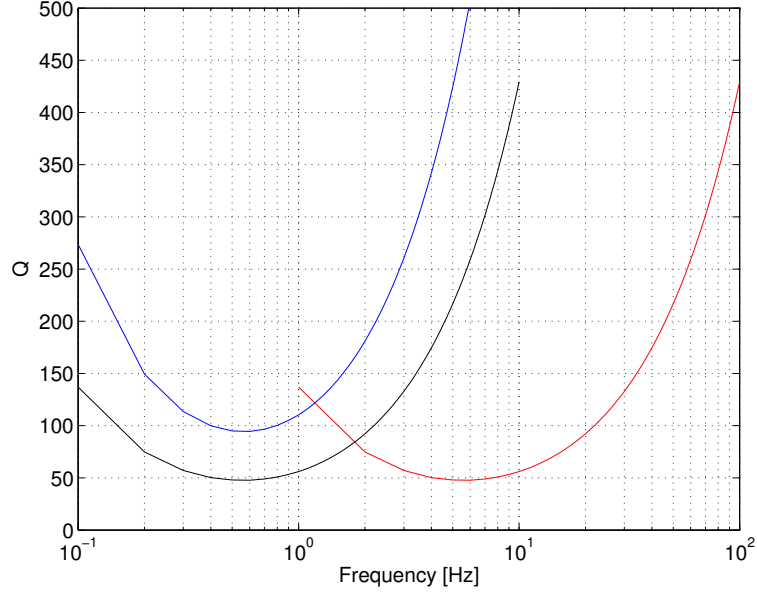


Figure 3.3: Dependency of the effective quality factor q on relaxation times. See text for details.

$$M_S(t) = \mu \left(-\frac{\tau_\epsilon^S}{\tau_\sigma} e^{-t/\tau_\sigma} \right) \theta(t),$$

where τ_ϵ^P and τ_ϵ^S are the strain relaxation times for P and S-waves respectively, τ_σ is the stress relaxation time and $\theta(t)$ denotes the Heaviside function. The inverse of Q for a single SLS can be written as

$$Q^{-1} = \frac{\omega \tau_\sigma \tau}{1 + \omega^2 \tau_\sigma^2 (1 + \tau)} \quad (3.47)$$

with

$\tau = \frac{\tau_\epsilon^S}{\tau_\epsilon^P} - 1$. The parameter τ describes the ratio between the relaxation times of stress and strain. From equation 3.47 it can be understood that τ_σ determines the frequency dependent behavior of the SLS whereas τ determines the value of Q . This is illustrated in figure 3.3. The black line indicates the frequency behavior of a chosen SLS setup, varying τ when τ_σ remains constant results in the blue line. Inversely, variation of τ_σ with τ being unaffected results in the red line. The different effect of both parameters can be recognized. From the frequency behavior within the limits 1 to 5 Hz, corresponding to the significant frequency range in the earthquake scenario simulations shown in this work it can be understood that a single SLS is assumed to be capable of modeling a nearly constant quality factor properly.

In order to find optimally adjusted relaxation times for this frequency range the following approach is made. From the above discussion it became clear that at a fixed frequency ω for any value of τ_ϵ an appropriate τ_σ can be found in order to model the desired quality factor Q . This relation is illustrated in figure 3.4.

In the next step a slight variation of the target quality factor is allowed. Figure 3.5 denotes the broader range of appropriate relaxation time pairs. Varying ω within the

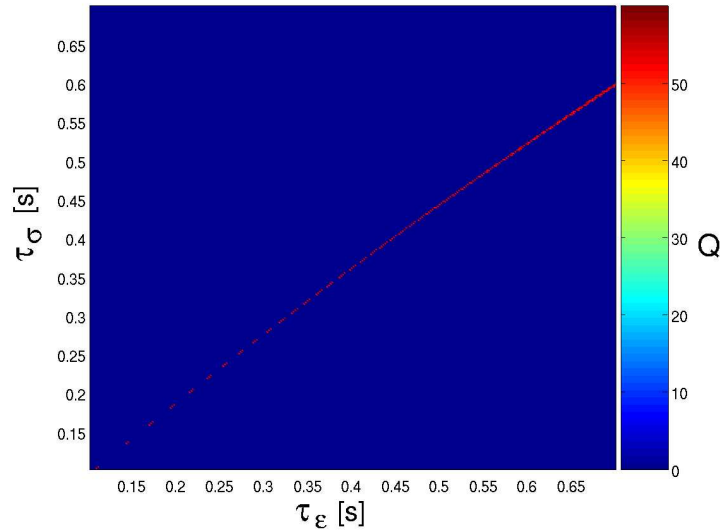


Figure 3.4: Relaxation time pairs for stress and strain appropriate to model a fixed quality factor at fixed frequency.

range of target frequencies for the simulations and stacking results as shown in example b) yields figure 3.6. From this the best fitting couple of relaxation times for stress and strain can be determined. The so found values are assumed to result in quality factors close to the desired one within the whole frequency range that is covered by the simulations. With respect to the limited accuracy of attenuation estimates in the input data this approach is considered to be adequate for earthquake scenario simulations in the presence of viscoelastic attenuation. A Matlab code for the estimation of appropriate relaxation times is provided with this work (see Appendix A).

3.3.5 Numerical Stability

Viscoelastic media have the intrinsic property of dispersion. As this behavior is modeled by the standard linear solid approach the stability criterion of the numerical simulation scheme must be slightly modified. Analog to elastic schemes the stability criterion is found through the Courant number $c\Delta t/\Delta x$ (Dablain (1986); Levander (1988)). This number has to be adjusted to the highest phase velocity within the dispersive wavefield, which is found at zero period. Dispersion relation yields: $c_{max} = \sqrt{\tau_\epsilon \bar{M}_R / \tau_\sigma \rho}$ (Robertsson et al. (1994)).

3.3.6 Note on Parallelization

As the above discussed stability condition yields a range of results for a highly heterogeneous medium it is necessary to spread the information over all computation nodes. The MPI command `MPI_BROADCAST` and `MPI_GATHER` provide this functionality (Message Passing Interface Forum (1996)).

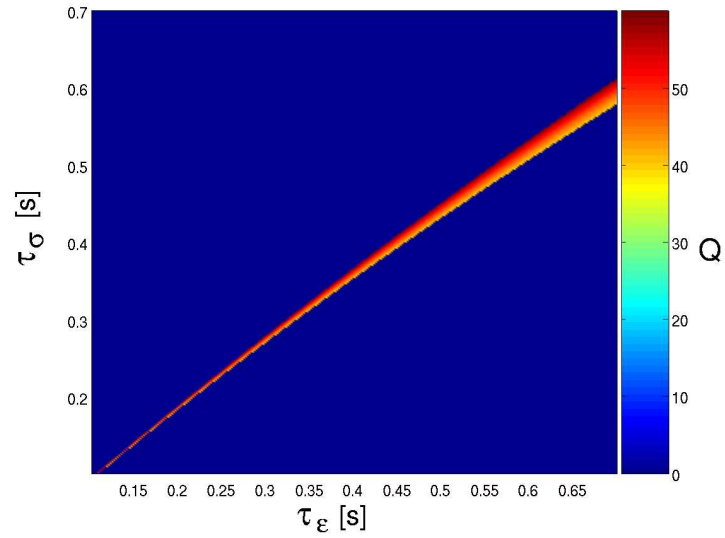


Figure 3.5: Allowing an error margin on the modeled quality factor leads to a broader range of possible relaxation time pairs.

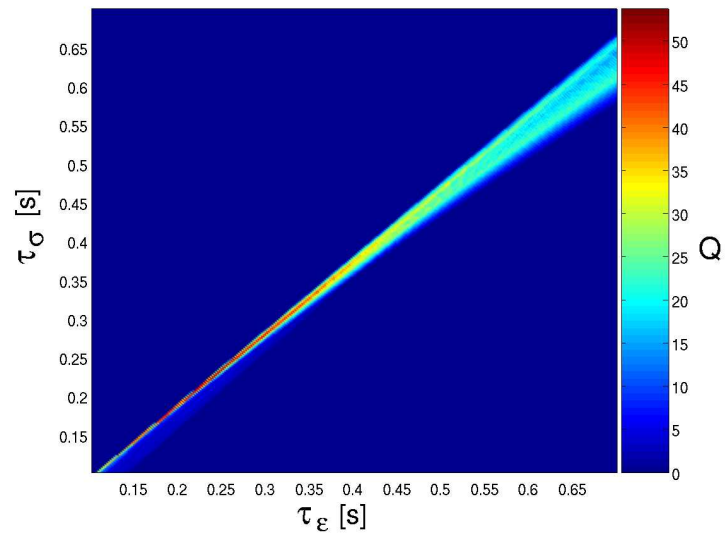


Figure 3.6: Resulting quality factors are averaged over the target frequency range to find the best fitting combination of relaxation times.

3.4 Finite-Source Implementation

One of the main aspects in this work concerns the use of finite sources. In this section the concept of implementing these into the finite difference code is described and the accuracy of the resulting seismograms is verified.

3.4.1 Motivation

Finite sources produce seismograms significantly different from the ones obtained using a point source approximation. Substantial work has been done on description of finite sources and wavefields emanating from such (e.g. Madariaga (1976); Miyatake (1980a,b); Boatwright (1980)). Dynamic rupture (e.g. Herrero and Bernard (1994); Olsen (2001); Peyrat et al. (2001)) accounts for an improved understanding of the physical processes at earthquake source. On the other hand kinematic fault descriptions (e.g. Dreger and Kaverina (2000); Kaverina and Dreger (2002); Ide (2002)) account for the reproduction of realistic seismograms without paying attention to the physics of the rupture itself. The significance of finite source effects on the emanating wave field is related to the analyzed frequency content, the size of the earthquake and the distance range of the receivers involved. Whereas for long period simulation of wave propagation on a global scale the effects of a finite source play a role only for large earthquakes (Tsuboi et al. (2004)), for shorter distances and period the effect must be taken into account also for smaller sources. The general effect of lower amplitude and enlarged period of individual phases is also studied by Brietzke (2003).

3.4.2 Technique

In finite differences an arbitrary finite source can be represented by a distribution of point sources. Therefore the moment tensor point source implementation is described first. Following the work of Pitarka (1999) the moment tensor source is implemented by the stress approach. The equivalent body forces calculated from the moment rate tensor are added to the stress components at every time step. With the grid layout described above a source at the grid node i, j, k is described by the following equations:

$$\tau_{xx\ i,j,k}^n = \tau_{xx\ i,j,k}^n - dt \frac{\dot{M}_{xx}(t)}{V} \quad (3.48)$$

$$\tau_{yy\ i,j,k}^n = \tau_{yy\ i,j,k}^n - dt \frac{\dot{M}_{yy}(t)}{V} \quad (3.49)$$

$$\tau_{zz\ i,j,k}^n = \tau_{zz\ i,j,k}^n - dt \frac{\dot{M}_{zz}(t)}{V} \quad (3.50)$$

$$\tau_{xy\ i+\frac{1}{2},j+\frac{1}{2},k}^n = \tau_{xy\ i+\frac{1}{2},j+\frac{1}{2},k}^n - dt \frac{\dot{M}_{xy}(t)}{V} \quad (3.51)$$

$$\tau_{yz\ i,j+\frac{1}{2},k+\frac{1}{2}}^n = \tau_{yz\ i,j+\frac{1}{2},k+\frac{1}{2}}^n - dt \frac{\dot{M}_{yz}(t)}{V} \quad (3.52)$$

$$\tau_{zx\ i+\frac{1}{2},j,k+\frac{1}{2}}^n = \tau_{zx\ i+\frac{1}{2},j,k+\frac{1}{2}}^n - dt \frac{\dot{M}_{zx}(t)}{V}. \quad (3.53)$$

The quantity V is equal to the volume of a grid cell:

$$V = dx * dy * dz. \quad (3.54)$$

According to Aki and Richards (1980) the moment tensor components can be obtained by following formulas from the orientation of strike, dip and rake.

$$m_{xx} = -\sin \delta \cos \lambda \sin 2\theta_s + \sin 2\delta \sin \lambda \sin^2 \theta_s \quad (3.55)$$

$$m_{yy} = \sin \delta \cos \lambda \sin 2\theta_s - \sin 2\delta \sin \lambda \cos^2 \theta_s \quad (3.56)$$

$$m_{zz} = \sin 2\delta \sin \lambda \quad (3.57)$$

$$m_{xy} = \sin \delta \cos \lambda \cos 2\theta_s + \frac{1}{2} \sin 2\delta \sin \lambda \sin \theta_s \quad (3.58)$$

$$m_{xz} = -\cos \delta \cos \lambda \cos \theta_s + \cos 2\delta \sin \lambda \sin \theta_s \quad (3.59)$$

$$m_{zy} = -\cos \delta \cos \lambda \sin \theta_s - \cos 2\delta \sin \lambda \cos \theta_s \quad (3.60)$$

To model the temporal history of the event the moment rate tensor $\dot{M}(t)$ is derived as

$$\dot{M}(t) = \sqrt{2}M_0\hat{M}\dot{m}(t) \quad (3.61)$$

where \hat{M} is the normalized moment tensor, M_0 denotes the seismic moment of the event and $\dot{m}(t)$ is a normalized source time function satisfying the relation:

$$\int_{t_0}^{t_f} \dot{m}(t)dt = 1. \quad (3.62)$$

(Dahlen and Tromp (1998)).

With the equations given above a moment tensor point source approximation is obtained. Simulations carried out using this approach reproduce realistic amplitudes and long period waveforms for simple models. However, to achieve more realistic results especially in the higher frequency part a finite source is obligatory. Results from this study (see chapter 6) prove the importance of coupling effects from finite sources and complex geometries. A simple approach is made in order to advance from point sources to finite ones. According to the strike and dip angles of the source a fault plane is defined within the model space. Onto this plane point sources with the same moment tensor are distributed on a circular area around the hypocenter. An equivalent portion of the overall moment of the earthquake scenario is associated with each of these point sources.

The effects of finite source representations on the emanating wavefield have been studied by various authors throughout the last decades (e.g. Madariaga (1976); Miyatake (1980a,b)). A good introduction to various kinematic source models and their implementation can be found in Mai (2005). Individual point sources on the source plane are activated with the same source time function, delayed by the time necessary for the uniform rupture to propagate from the hypocenter to the rim of the circular source. Figure 3.7 illustrates the geometry of such a finite source representation. The color-coded fault plane in subfigure a) shows the equivalent fractions of the overall seismic moment associated with each point. In this example the active part of the fault plane includes 383 point sources, whereas in subfigure b) delay times for the individual points are shown. The model is the same as it is used for the verification presented in the next chapter.

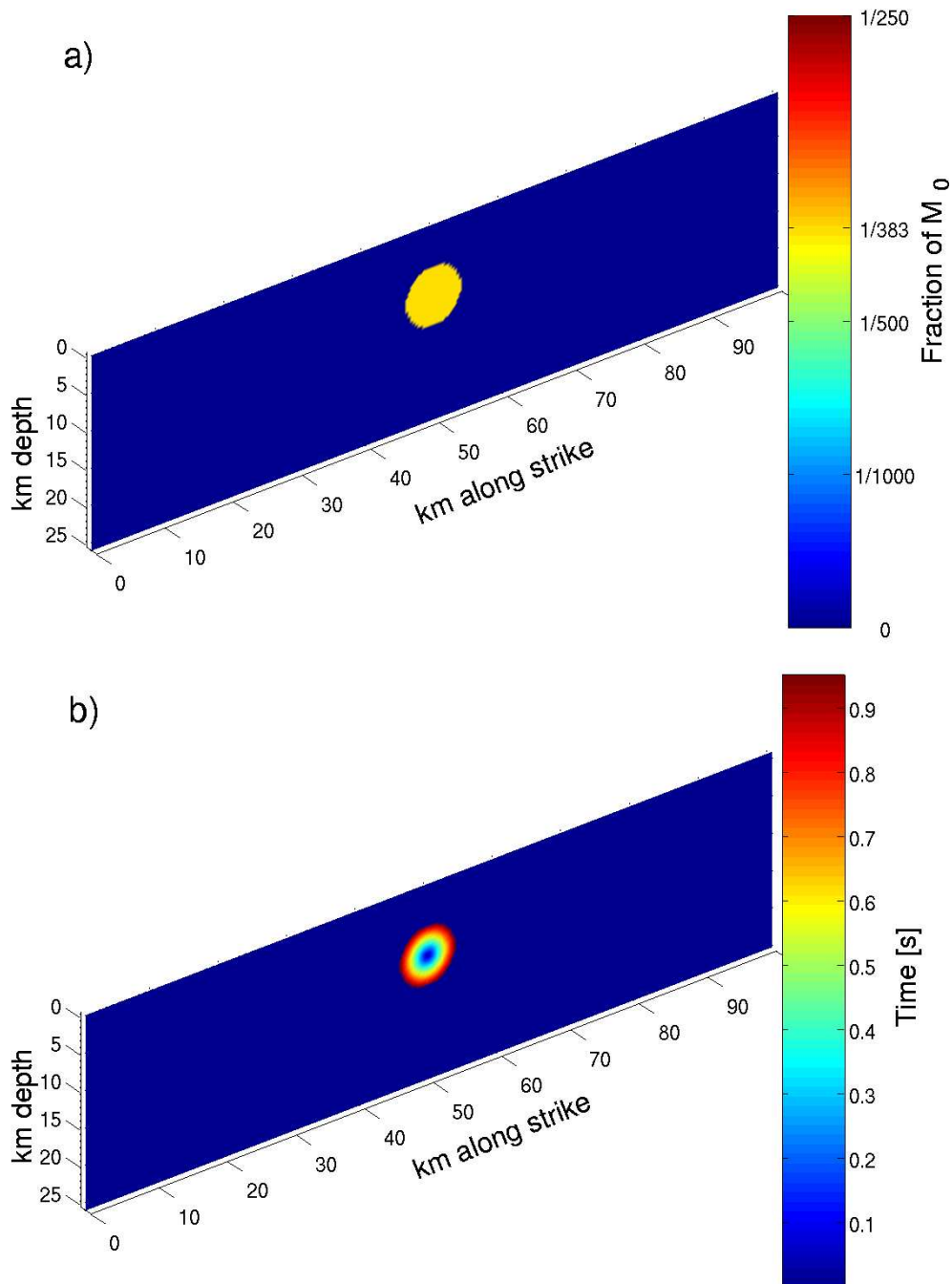


Figure 3.7: Representation of finite sources used for the verification of the method. a) Source plane with color-coded fraction of seismic moment applied to the individual point sources distributed across the circular fault. b) Color-coded rupture time for the individual point sources.

Table 3.1: Parameters for verification setup.

Parameter	Value
Grid points horizontal	282
Grid points vertical	72
Horizontal discretization	356 m
Vertical discretization	367 m
P-wave velocity	8000 m/s
S-wave velocity	4619 m/s
Rupture propagation speed	90 % of S-wave velocity

3.4.3 Verification

The simulation of a finite source using the above discussed algorithm appears straight forward as long as the defined source plane coincides with a grid plane. However, for realistic simulations arbitrarily oriented faults must be taken into account. The fault plane is defined herein by the two angles of strike and dip, which determine together with the rake angle the source mechanism for individual moment tensor point sources distributed onto that plane. For arbitrarily oriented faults this moment tensor is applied to the next grid point available. The key question arising is whether the described algorithm is capable of producing realistic seismograms without distinct signature of the staircase nature of the fault plane. In order to verify the following procedure is performed:

First, one simulation is carried out using a strike angle of zero degrees. This choice ensures that the associated fault plane is aligned with one plane of the computational grid. Results achieved with this model serve as reference solution for comparison with the ones achieved using an arbitrary oriented source plane.

The second simulation is carried out with a strike angle of 27 degrees resulting in a source plane which is not coinciding with a grid plane. It also does not coincide with an aligned plane of grid points in another direction as it would be the case for 45 degrees. Therefore the chosen strike direction can be considered a valid test for the general accuracy of the method. In figure 3.8 the resulting two fault planes are illustrated. Table 3.1 summarizes the computational and model parameters for the verification simulations.

Some effort must be done in order to achieve appropriate seismograms for a comparison. As the simulations provide data in three orthogonal components aligned with the grid axes (X , Y and Z) the results at the surface can be compared directly only for the vertical (Z) component. The horizontal components, which are generally considered more important, must be transformed with the strike angle. That means for the second simulation the horizontal components:

$$X' = \sin(\text{strike}) * X + \cos(\text{strike}) * Y, \text{ and}$$

$$Y' = -\cos(\text{strike}) * X + \sin(\text{Strike}) * Y$$

are derived. The resulting wavefield is shown in figure 3.9. For the fault with 27 degree turned fault orientation with respect to the reference fault an analogous wavefield can

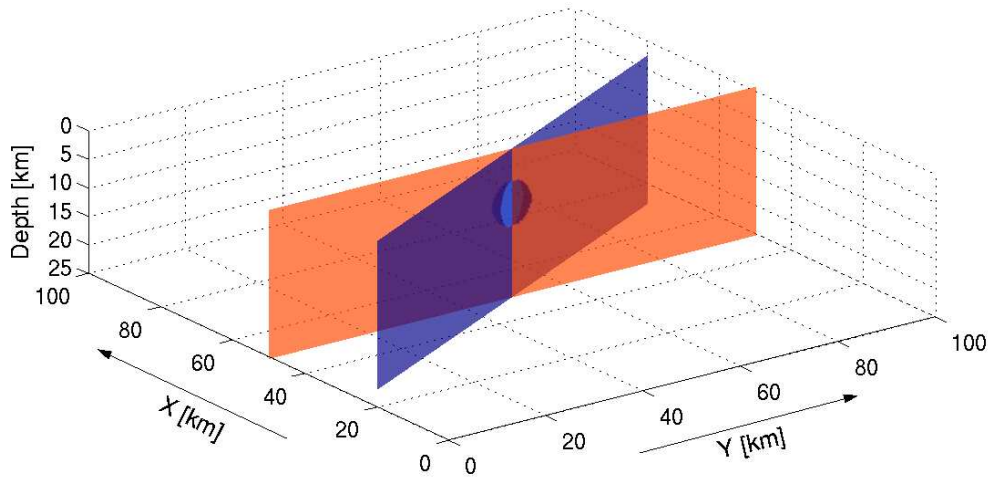


Figure 3.8: Three-dimensional view of the fault planes used for the finite source verification. The active area of each plane is demarcated in solid color.

be observed. Additionally, the pattern appears to have been turned by the correct angle. For a closer inspection of the accuracy of the finite fault simulation results in the presence of arbitrarily oriented faults, seismograms are compared. The receiver setup used for these comparisons is plotted in the snapshots of the wavefield (figure 3.9). Figure 3.10 displays the exact distribution. Four equidistant receiver rings are placed around the center of the fault planes at distances 7, 12, 17 and 22 kilometers. The individual rings consist of 360 receivers each in an angular distance of one degree. In this graph the different fault orientations are illustrated in red for the zero strike angle and for the 27 degrees rotated fault.

Dashed lines denote the projection of the source planes throughout the surrounding receiver rings. After deriving the appropriate horizontal component seismograms according to the formulae given above, recordings on associated receivers can be compared. As there is one receiver for each degree of the circumsphere simply the reference seismogram at receiver 1 (strike angle = 0°) is compared with the recording at receiver 333 from the simulation with rotated fault (strike angle = 27°). Results for receiver rings at 6, 12 and 24 km are shown in figures 3.11, 3.12 and 3.13 respectively. No difference is observable. However, receivers close to the nodal planes can possibly reveal large relative errors. That is inevitable, as the exact location of the nodal plane cannot be matched better than the grid allows. Nevertheless, as there is nearly no energy transferred in these directions the errors do not appear in seismograms as well as snapshots or any derived quantity of interest.

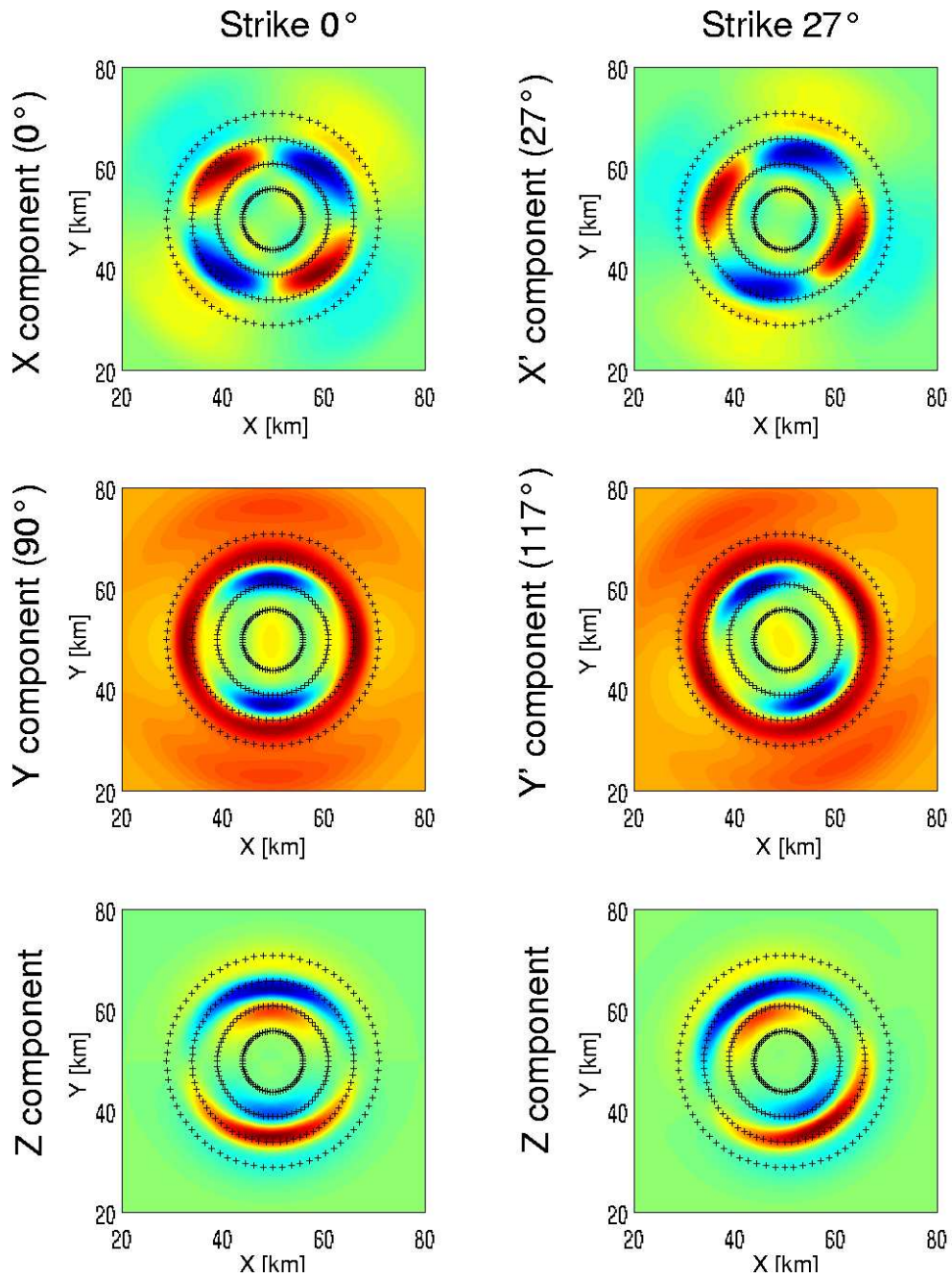


Figure 3.9: Snapshots of surface wave field from finite source verification. For the rotated fault (right column) the derived equivalent components of horizontal ground motions are shown to make a visual comparison feasible (see text).

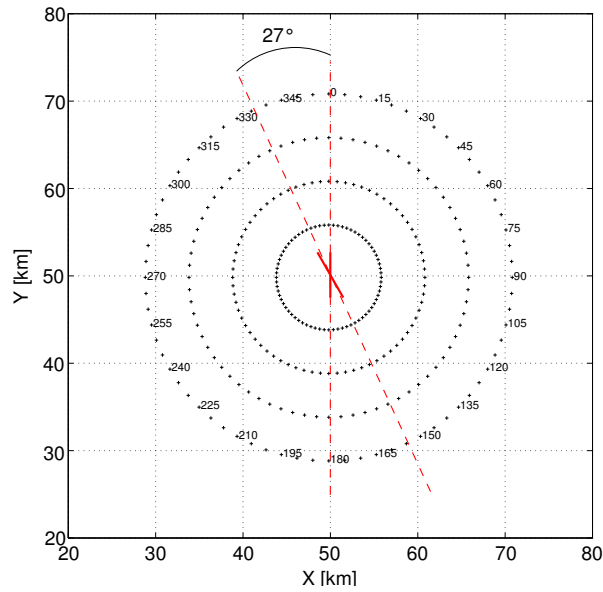


Figure 3.10: Receiver distribution for the verification of the finite source implementation. Orientations of the reference and rotated fault are plotted in red.

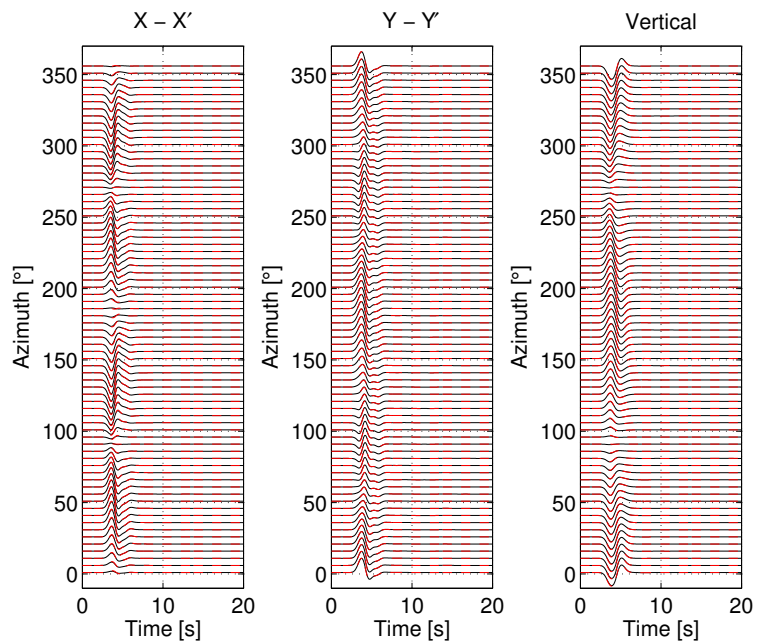


Figure 3.11: Seismograms from finite source verification at the innermost receiver ring (distance = 7 km). Black traces: Fault plane aligned with grid (reference case), red dashed traces: Fault plane rotated by 27 degrees with respect to the computational grid.

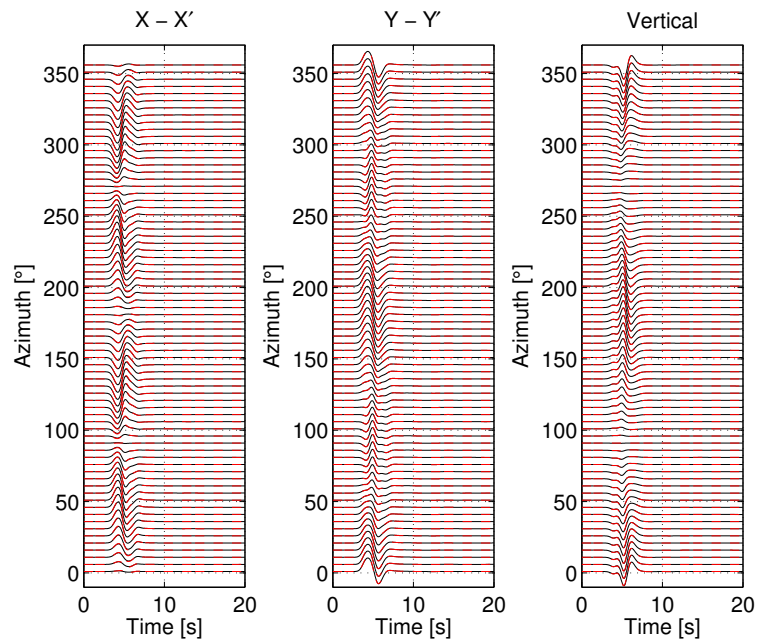


Figure 3.12: Seismograms from finite source verification at 2nd receiver ring (distance = 12 km). See figure 3.11 for details.

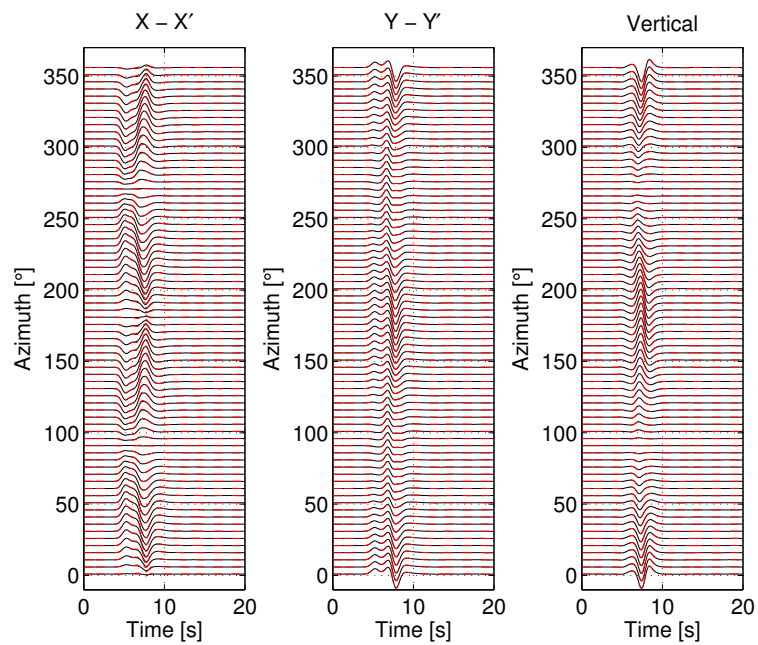


Figure 3.13: Seismograms from finite source verification at 4th receiver ring (distance = 22 km). See figure 3.11 for details.

3.5 Nonuniform Grid

3.5.1 Motivation

Modeling seismic wave propagation leads to massive requirements in both CPU time and core memory. The main factors determining these requirements are a combination of sampling rate in grid points per wavelength in order to meet accuracy requirements, frequency and model velocities. As a result the slowest part of the model space determines the grid interval for the whole model. For a basin model this part, the actual basin, is typically shallow compared to the background model with a vertical dimension controlled by the depth of the hypocenter. This leads to an oversampling of large parts of the model and consequently to a waste of memory and computational operations. One possible approach of coping with this problem is adjusting the grid size throughout the model in a way ensuring that the stability conditions determined by the velocity structure are locally fulfilled. This approach has been implemented in various ways including smooth variations on the grid spacing (e.g. Jastram and Behle (1992); Jastram and Tessmer (1994); Pitarka (1999); Wang et al. (2001)), discontinuous grid spacing (e.g. Aoi and Fujiwara (1997); Hayashi et al. (2001)), or discontinuous grid spacing in combination with varying time steps (Falk et al. (1998); Tessmer (2000); Kang and Baag (2004)). A vertically smoothly varying grid spacing is used in this study. The techniques and results presented in this section can be applied straightforward to the other two dimensions.

3.5.2 Technique

The implementation of a nonuniform spacing in the staggered grid finite difference scheme follows the work described by Pitarka (1999). The equations describing the velocity evolution for elasto-dynamic wave propagation as described above are the following.

$$v_x^{t+1/2}{}_{i,j,k} = v_x^{t-1/2}{}_{i,j,k} + \Delta t b_x (D_x \tau_{xx} + D_y \tau_{xy} + D_z \tau_{xz})_{i,j,k}^t \quad (3.63)$$

$$v_y^{t+1/2}{}_{i+1/2,j+1/2,k} = v_y^{t-1/2}{}_{i+1/2,j+1/2,k} + \Delta t b_y (D_x \tau_{xy} + D_y \tau_{yy} + D_z \tau_{yz})_{i+1/2,j+1/2,k}^t \quad (3.64)$$

$$v_z^{t+1/2}{}_{i+1/2,j,k+1/2} = v_z^{t-1/2}{}_{i+1/2,j,k+1/2} + \Delta t b_z (D_x \tau_{xz} + D_y \tau_{yz} + D_z \tau_{zz})_{i+1/2,j,k+1/2}^t \quad (3.65)$$

Where b_x , b_y and b_z denote the effective buoyancies at associated positions within an elementary grid cell. Similarly the equations dealing with stresses yield the relations below.

$$\begin{aligned} \tau_{xx}^{t+1}{}_{i+1/2,j,k} &= \tau_{xx}^t{}_{i+1/2,j,k} + \\ +\Delta t [(\lambda + 2\mu)D_x v_x + \lambda(D_y v_y + D_z v_z)]_{i+1/2,j,k}^{t+1/2} \end{aligned} \quad (3.66)$$

$$\begin{aligned} \tau_{yy}^{t+1}{}_{i+1/2,j,k} &= \tau_{yy}^t{}_{i+1/2,j,k} + \\ +\Delta t [(\lambda + 2\mu)D_y v_y + \lambda(D_x v_x + D_z v_z)]_{i+1/2,j,k}^{t+1/2} \end{aligned} \quad (3.67)$$

$$\begin{aligned} \tau_{zz}^{t+1}{}_{i+1/2,j,k} &= \tau_{zz}^t{}_{i+1/2,j,k} + \\ +\Delta t [(\lambda + 2\mu)D_z v_z + \lambda(D_x v_x + D_y v_y)]_{i+1/2,j,k}^{t+1/2} \end{aligned} \quad (3.68)$$

$$\begin{aligned} \tau_{xy}^{t+1}{}_{i,j+1/2,k} &= \tau_{xy}^t{}_{i,j+1/2,k} + \\ +\Delta t [\mu_{xy}(D_y v_x + D_x v_y)]_{i,j+1/2,k}^{t+1/2} \end{aligned} \quad (3.69)$$

$$\tau_{xz}^{t+1}{}_{i,j,k+1/2} = \tau_{xz}^t{}_{i,j,k+1/2} + \Delta t [\mu_{xz}(D_z v_x + D_x v_z)]_{i,j,k+1/2}^{t+1/2} \quad (3.70)$$

$$\begin{aligned} \tau_{yz}^{t+1}{}_{i+1/2,j+1/2,k+1/2} &= \tau_{yz}^t{}_{i+1/2,j+1/2,k+1/2} + \\ +\Delta t [\mu_{yz}(D_y v_z + D_z v_y)]_{i+1/2,j+1/2,k+1/2}^{t+1/2} \end{aligned} \quad (3.71)$$

Analogously to the buoyancies in previous equations, μ holds the effective quantities at the respective grid position. The operator D in the above equations describes the differential operation involving nonuniform stencils as shown in figure 3.14 can be written in the following way.

$$\begin{aligned} D_x g(x, y, z) &= c_1 g(x + \Delta_1, y, z) + c_2 g(x - \Delta_2, y, z) + \\ &+ c_3 g(x + \Delta_3, y, z) + c_4 g(x - \Delta_4, y, z) \end{aligned} \quad (3.72)$$

$$\begin{aligned} D_y g(x, y, z) &= c_1 g(x, y + \Delta_1, z) + c_2 g(x, y - \Delta_2, z) + \\ &+ c_3 g(x, y + \Delta_3, z) + c_4 g(x, y - \Delta_4, z) \end{aligned} \quad (3.73)$$

$$\begin{aligned} D_z g(x, y, z) &= c_1 g(x, y, z + \Delta_1) + c_2 g(x, y, z - \Delta_2) + \\ &+ c_3 g(x, y, z + \Delta_3) + c_4 g(x, y, z - \Delta_4) \end{aligned} \quad (3.74)$$

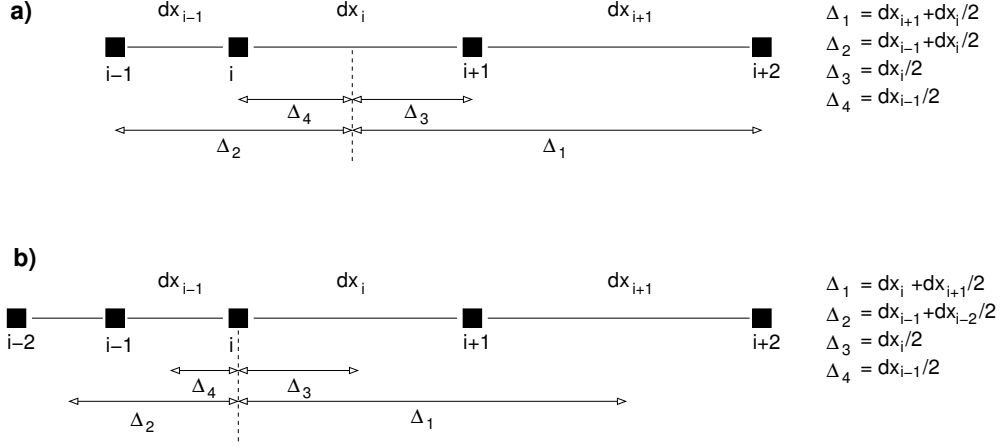


Figure 3.14: One dimensional representation of a non-uniform finite difference grid stencil as it is used in this work.

Where g_i denotes an arbitrary field variable the operators are acting on.

The weight factors $c_1 \dots c_4$ have to be calculated. From figure 3.14 it can be understood how the locally varying spatial increment Δ_i can be derived from the local grid spacing dx . With $g(x, y, z) = g_{x,y} \exp(ikx)$ describing the spatial derivative with respect to x it can be written:

$$ik = c_1 \exp(+ik\Delta_1) + c_2 \exp(-ik\Delta_2) + c_3 \exp(+ik\Delta_3) + c_4 \exp(-ik\Delta_4) \quad (3.75)$$

Taylor expansion of these terms yields the following approximation.

$$\exp(+ik\Delta_i) \approx \left(1 + ik\Delta_i - \frac{k^2\Delta_i^2}{2} - \frac{ik^3\Delta_i^3}{6} \right) \quad (3.76)$$

Substituting this approximation in the above formulae yields:

$$ik = (c_1 + c_2 + c_3 + c_4) \quad (3.77)$$

$$+k(c_1\Delta_1 - c_2\Delta_2 - c_3\Delta_3 - c_4\Delta_4) \quad (3.78)$$

$$+ \frac{k^2}{2}(-c_1^2\Delta_1 - c_2^2\Delta_2 - c_3^2\Delta_3 - c_4^2\Delta_4) \quad (3.79)$$

$$+ \frac{ik^3}{6}(-c_1^3\Delta_1 + c_2^3\Delta_2 - c_3^3\Delta_3 + c_4^3\Delta_4) \quad (3.80)$$

From this equation a system of four linear equations is achieved:

$$\begin{pmatrix} 1 & 1 & 1 & 1 \\ \Delta_1 & -\Delta_2 & \Delta_3 & -\Delta_4 \\ -\Delta_1^2 & -\Delta_2^2 & -\Delta_3^2 & -\Delta_4^2 \\ -\Delta_1^3 & \Delta_2^3 & -\Delta_3^3 & \Delta_4^3 \end{pmatrix} \begin{pmatrix} c_1 \\ c_2 \\ c_3 \\ c_4 \end{pmatrix} = \begin{pmatrix} 0 \\ 1 \\ 0 \\ 0 \end{pmatrix} \quad (3.81)$$

This system can be solved numerically for all components of c , from which the differential operators D can be derived. As the grid is invariant with respect to time in this approach these calculations have to be done only once in an initialization routine. The values for D are stored as a virtual representation of the grid layout. An example for a grid representation with varying grid spacing in vertical direction is shown in figure 3.15. This grid is also used in the verification shown in the next paragraph.

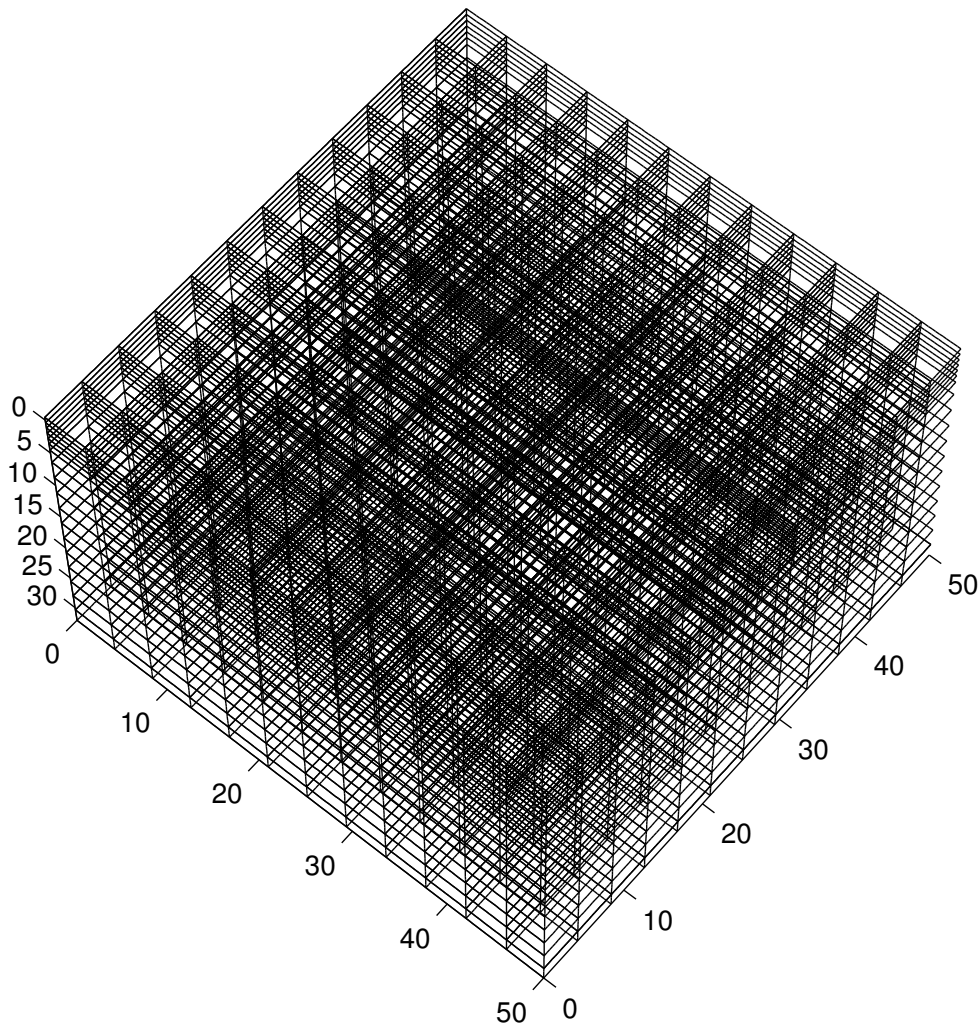


Figure 3.15: Example for a finite difference grid with nonuniform spacing in vertical direction.

3.5.3 Verification

The simulation setup for the verification presented in this section is designed in order to serve two purposes. On the one hand, the accuracy of the finite difference formulation using a non-uniform grid is verified. At the same time a realistic estimate on possible savings in terms of memory requirements and computation time using this approach is made. In terms of accuracy of the method two aspects have to be considered. The first is the accurate modeling of wave propagation in model domains with the coarser grid spacing. Secondly, absolute amplitudes have to be independent of the grid spacing at the source point. Application of the moment tensor source representation described in the previous section accounts for that.

As the approach of the non-uniform grid is motivated by the modeling of shallow basin structures a simple but relevant model is chosen for the verification. The velocity structure consists of a triangular shaped valley with low velocities within a high velocity background model. Media parameters are averaged across the domain interface. In order to get a realistic estimate on possible savings the vertical dimension of the low velocity structure is chosen similar to the one of existing sedimentary basins. The overall model dimension which is determined by the source depth of the earthquake scenario can also be considered typical for intra-plate earthquakes. Crosssections of the resulting velocity model in both uniform and nonuniform grid representation are shown in figure 3.17. In table 3.2 the model parameters are listed in detail.

Table 3.2: Verification of nonuniform grid implementation - parameters.

	Uniform Grid	Nonuniform Grid
Grid points horizontal	144	144
Grid points vertical	122	72
Horizontal discretization	350 m	350 m
Vertical discretization	200 m	200 - 600 m
Temporal discretization	0.01125 s	0.01125 s
P-wave velocity	1800 - 8000 m/s	1800 - 8000 m/s
S-wave velocity	1035 - 4600 m/s	1035 - 4600 m/s
Source depth	17800 m	17800 m
Source type	strike slip	strike slip
Density	2200 - 3000 kg/m^3	2200 - 3000 kg/m^3
Memory	680 MB	410 MB
Computation time	122 min	82 min
Time steps	1778	1778

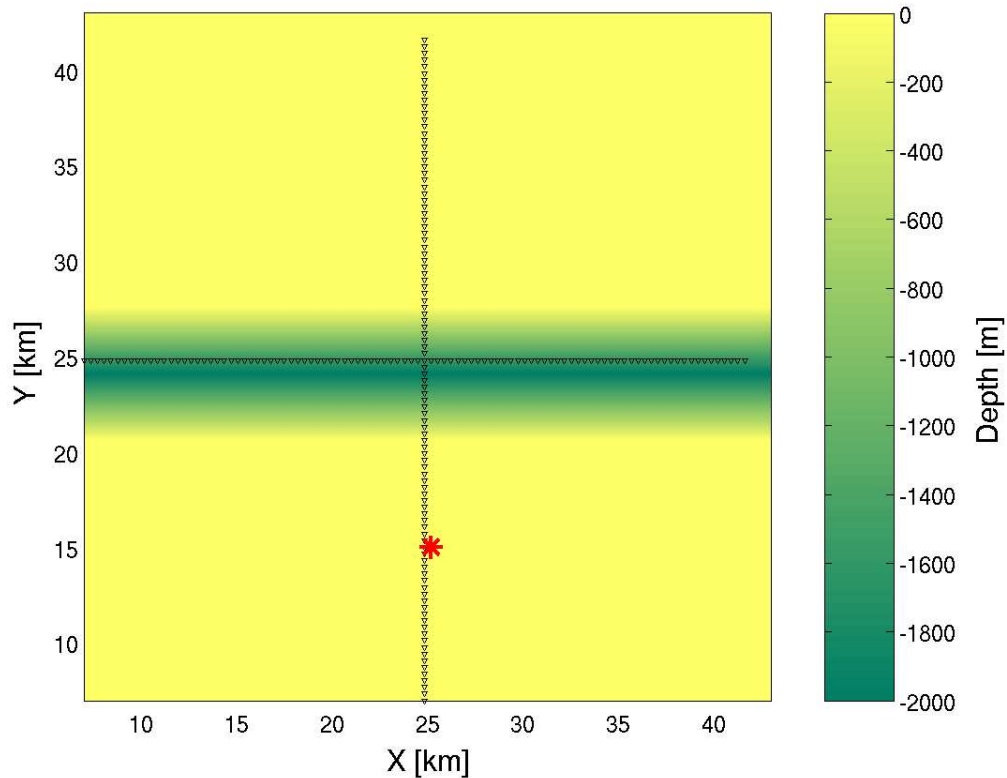


Figure 3.16: Receiver setup for the verification of the nonuniform grid approach. Depth of the triangular shaped low velocity structure is demarked in colors.

To perform a comparison between simulations carried out using homogenous and varying grid spacing this velocity model is discretized onto two grids: a homogenous grid with a horizontal spacing of 350 m and a vertical resolution of 200 m, and a grid with vertically varying spacing ranging from 200 m at the top to 600 m at the bottom of the model. The variation in spacing are made in a way that ensures the same sampling of the sedimentary structure by both grids, whereas the faster bottom part of the model is discretized coarser with the nonuniform grid. The sides of both models are attached with a 10 point wide region of perfectly matching layers in order to suppress artificial reflections. Seismograms for both grids are recorded on a cross shaped receiver array as shown in figure 3.16. In figure 3.17 the different discretization of the model are illustrated. Colors indicate the different velocities within the triangular low velocity structure and the surrounding bedrock. Grid lines are depicted in light gray. The different discretization of the lower half of the model using a uniform and nonuniform grid layout becomes clear. The hypocenter of the source is demarked as a yellow star. It is noteworthy that the seismogram comparison is carried out without any normalization of amplitudes. Due to the correct implementation of the moment tensor point source as described in section 3.4 the actual grid spacing at the source location does not affect the amplitudes of the resulting ground motion.

Figures 3.18 and 3.19 shows the comparison of three component seismograms achieved using a uniform (black traces) and a nonuniform grid (dashed red traces). For both receiver profiles the seismograms appear identical. It can be concluded that the coarser

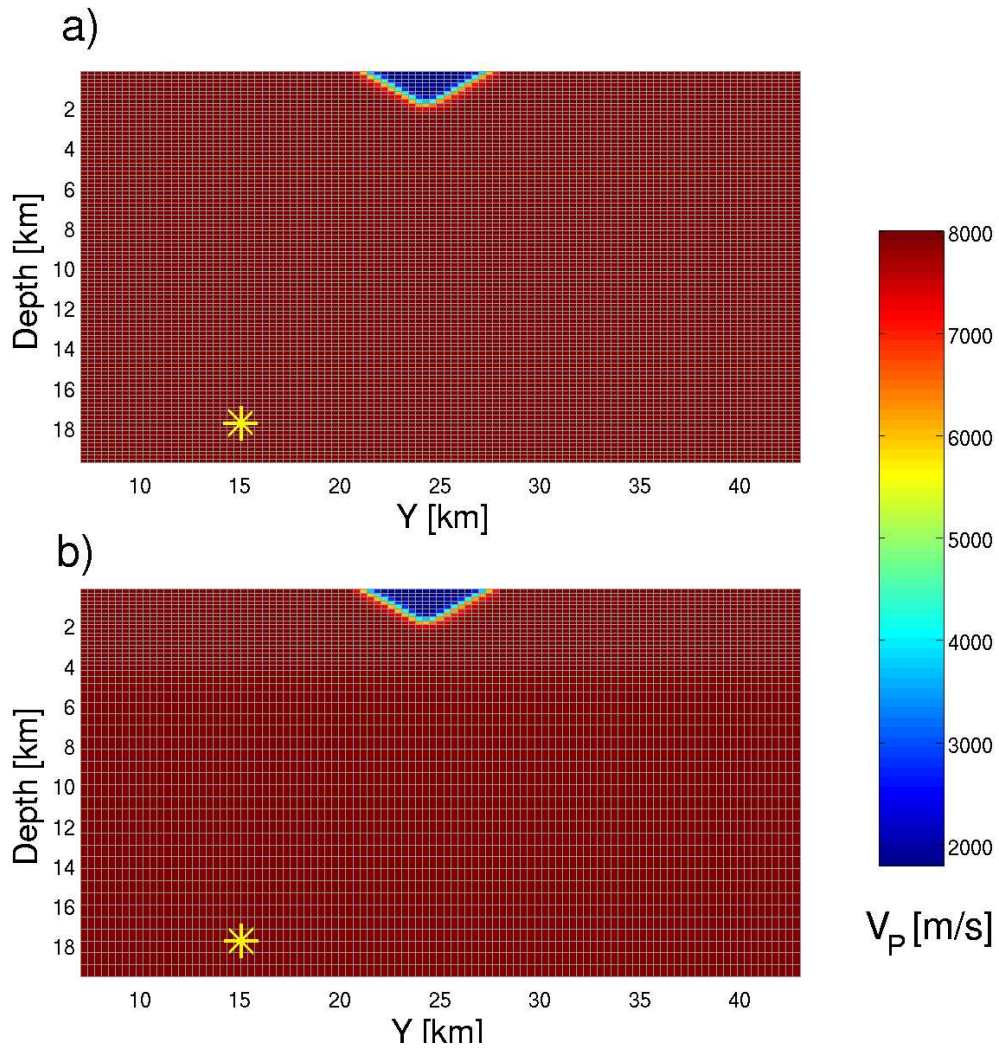


Figure 3.17: Crosssections of the model representations using a homogeneous grid spacing (a) and a vertically varying spacing (b). Actual grid lines are plotted in light gray. The different discretization of the homogeneous part of the model is obvious. Hypocenter location is demarked by the yellow cross.

grid discretization in the domains with high velocities does not affect the overall accuracy of the synthetic seismograms, if the wave is sampled locally with a sufficient number of points per wavelength at every grid position.

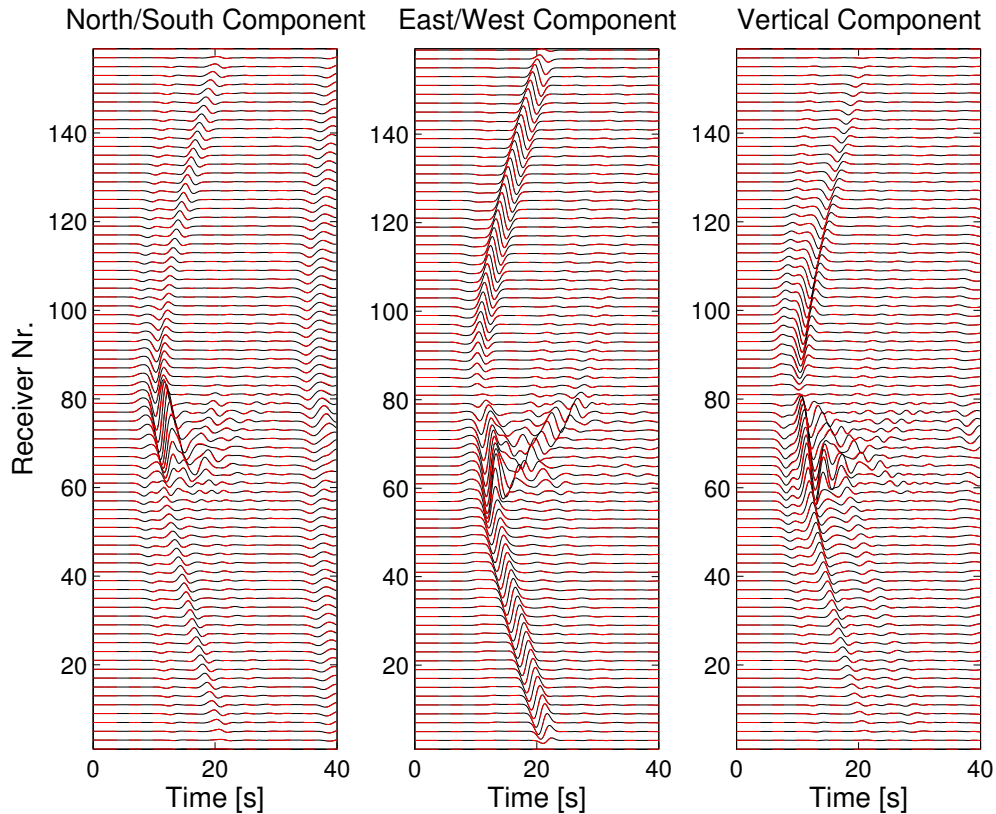


Figure 3.18: Comparison of three component seismograms recorded along receiver profile 1 (see 3.16). Black traces demark synthetics achieved with a uniform grid, red dashed traces are modeled using a nonuniform grid.

3.5.4 Performance

For the relatively small setup used for the above discussed verification of the nonuniform grid approach the potential savings achievable by this approach already becomes clear. Requirements in terms of core memory are reduced by about 40 percent and the consumption of computation time is reduced by about 35 percent. It is obvious that potential savings in terms of memory and computation time by this approach depend strongly on the specific model. The larger the contrasts in media parameters are and the smaller the spatial extent of low velocity heterogeneities is, the more efficient is consequently a possible reduction in grid discretization and memory. Usage of a varying grid spacing in one or more directions is motivated by possible savings in terms of memory and computation time. The latter is simply due to the fact that the less grid points a model contains the less operations have to be performed. This point is mentioned here to avoid misunderstanding - there is no additional gain due to longer time steps.

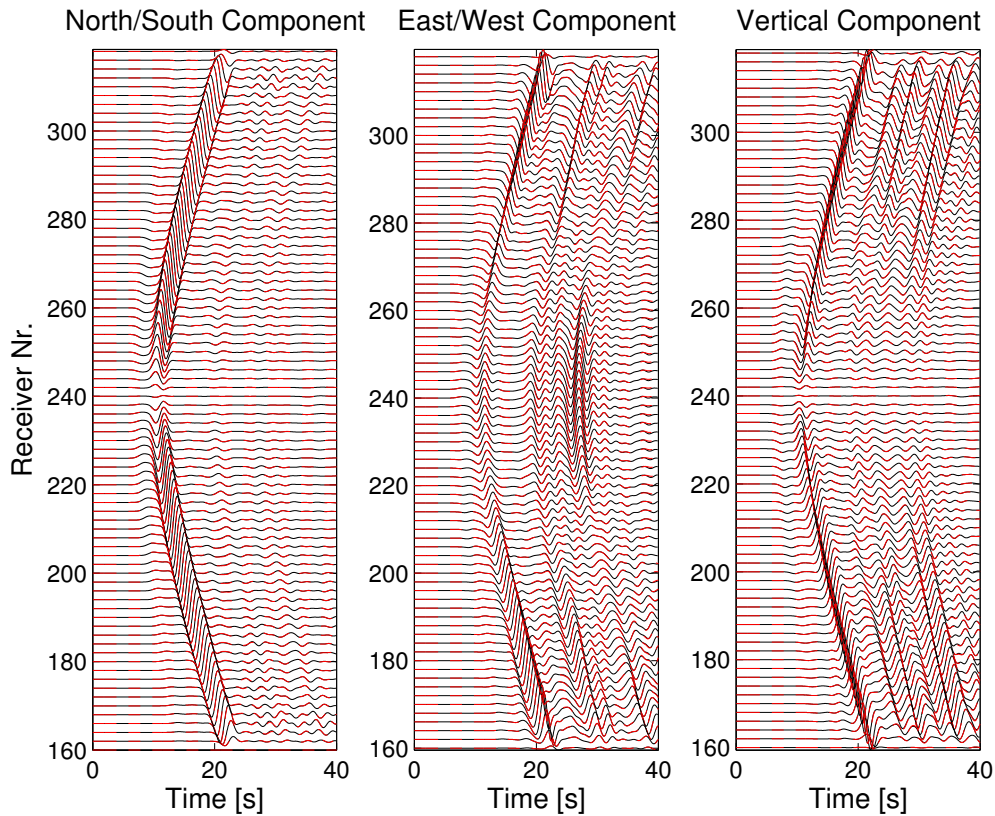


Figure 3.19: Comparison of three component seismograms recorded along receiver profile 2 (see 3.16). Black traces demark synthetics achieved with a uniform grid, red dashed traces are modeled using a nonuniform grid.

3.5.5 Note on Parallelization

Like in section 3.3 a note on the issue of parallelization should be made here. In most codes the time step necessary to achieve stability is calculated at run time of the program by the stability criterion. One consequence of varying spacing in combination with complex velocity structures is a more complex distribution of valid values for a stable dt . In a model with uniform spacing the time step is determined typically by the velocity at the bottom of the model because the highest velocities are located there and the uniform grid spacing. As the bottom velocities are normally the same for all processors all machines automatically have the same time step. For a varying grid spacing the relationship is possibly more complicated. To stay on the safe side it is necessary to use the above mentioned features `MPI_BROADCAST` and `MPI_GATHER` to spread the correct (smallest) time step over all nodes.

3.6 Rotated Grid

In this section a finite difference type is presented working with alternatively oriented differential operators. The implementation of this method is based on the work by Saenger (2000).

3.6.1 Motivation

Modeling elastic and viscoelastic wave propagation using a staggered grid approach can cause instability problems when strong contrasts in the medium are present. This is due to the fact that in a standard staggered grid medium parameters are distributed in different locations within one cell. Similar problems arise for the description of finite sources on arbitrary shaped faults. Whereas the implementation of a planar finite source produces accurate results for arbitrary orientation of the source plane this is not the case for curved faults. Recent studies on this subject circumvent the problem using a hybrid approach (Olsen (2001)). However hybrid methods have their own difficulties. Another possible solution to this problem is the usage of an alternatively oriented computational grid in which media parameters are automatically defined in appropriate positions within the grid cell, the so called rotated staggered grid (Saenger et al. (2000)).

3.6.2 Technique

In this section the basic principle of the rotated staggered grid is outlined by means of a two-dimensional medium. Extending the method to three dimensions is straightforward and the resulting equations are given. The standard finite difference discretization as described by Virieux (1984) results in the distribution of model parameters on a unit grid cell as shown in figure 3.20 a. It can be recognized that whereas all model parameters are defined in appropriate positions for the calculation of the derivatives, density and rigidity modulus μ are defined twice in different positions within the cell. That makes the interpolation of these quantities inevitable. An alternative approach deliberately uses model parameters defined at positions nearby (e.g. Kneib and Kerner (1993)) as illustrated by figure 3.20 b. In this scheme densities from the bottom and left hand side of the cell have been moved to the center and so has the rigidity modulus from the bottom left corner. As a consequence calculations of wavefield parameters affected by these quantities for example shear stress invoke a multiplication of values defined in different locations in this case strain and rigidity. Similar considerations are valid for the update of acceleration where a density defined at different position is invoked. These replacements can result in stability problems in presence of strong contrasts, although the overall Neumann stability criterion is fulfilled.

The rotated staggered grid approach solves such problems using an alternative configuration of the grid. All components of the stiffness tensor (i.e. in the isotropic case λ and μ) are placed in the center of the elementary cell. From figure 3.20 c it can be understood that the resulting positions of the modeling positions are sufficient to perform the calculations needed to update the wavefield parameters. Parameters that have

to be multiplied are located at the same place and derivatives in between the differentiated quantities. As densities are defined in locations different from the position of the stiffness tensor this quantity has to be either interpolated or defined on a different grid. Figure 3.20 c also illustrates the rhombic structure of this new grid. As this conflicts with the common discretization schemes which are based on rectangles it is convenient to rotate not the grid itself but the direction of derivatives as shown in figure 3.20 d. The spatial derivatives are now defined along the rotated axes \tilde{x} and \tilde{z} , which are rotated by 45 degrees against the standard directions x and z . In the following section the differential operators for these rotated derivatives are presented and several examples of application are given.

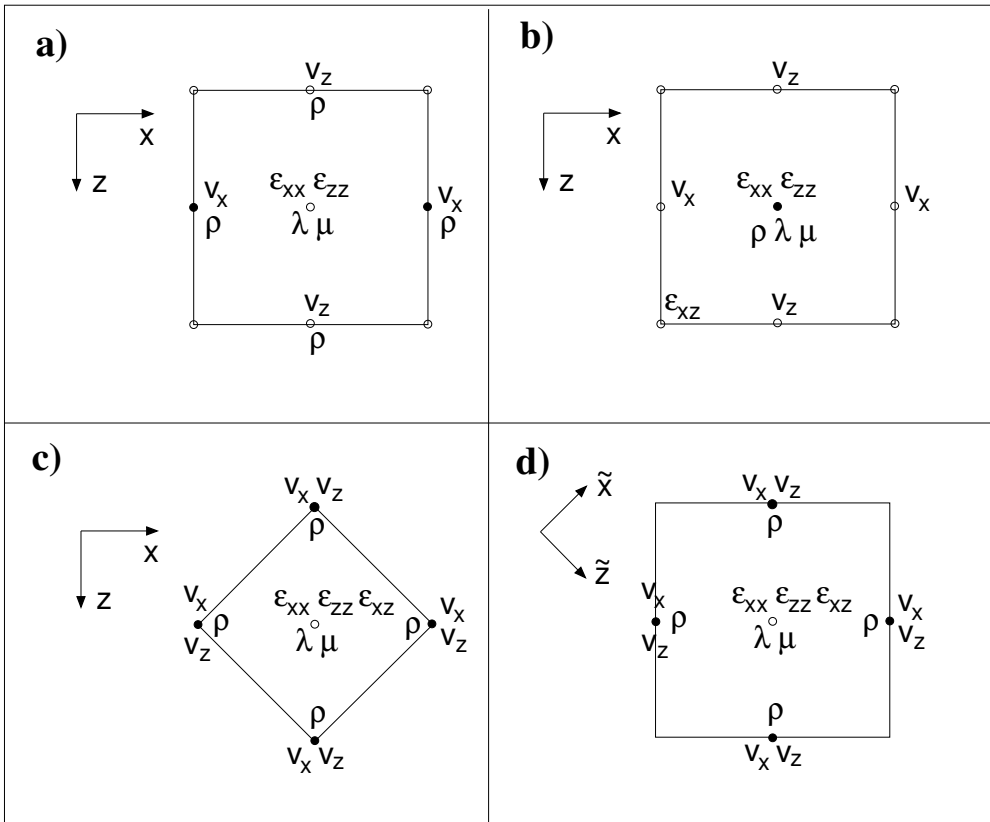


Figure 3.20: Evolution of the standard staggered grid scheme (a) to the alternatively oriented differential operators of the rotated staggered grid scheme (d). See text for details.

3.6.2.1 2D Formulation of the Rotated Staggered Grid

In a two-dimensional grid with grid spacing Δx and Δz the new spatial derivative directions are defined as:

$$\tilde{z} = \frac{\Delta x}{\Delta r}x + \frac{\Delta z}{\Delta r}z \tag{3.82}$$

$$x = \frac{\Delta x}{\Delta r}x - \frac{\Delta z}{\Delta r}z \quad (3.83)$$

$$\Delta r = \sqrt{\Delta x^2 + \Delta z^2} \quad (3.84)$$

As the grid itself remains oriented along the standard orthogonal axes the derivatives along these axes must be expressed by a linear combination of spatial derivatives along the new orientations:

$$\frac{\delta}{\delta x} = \frac{\Delta r}{2\Delta x} \left(\frac{\delta}{\delta z} + \frac{\delta}{\delta x} \right) \quad (3.85)$$

$$\frac{\delta}{\delta z} = \frac{\Delta r}{2\Delta z} \left(\frac{\delta}{\delta z} - \frac{\delta}{\delta x} \right) \quad (3.86)$$

For numerical simulations the differential operators D_x and D_z are necessary to achieve the derivatives $\frac{\delta}{\delta x}$ and $\frac{\delta}{\delta z}$. For a second order operator they are defined as:

$$D_x u(z, x, t) = \frac{1}{\Delta x} \left[u\left(z, x + \frac{\Delta x}{2}, t\right) - u\left(z, x - \frac{\Delta x}{2}, t\right) \right] \quad (3.87)$$

$$D_z u(z, x, t) = \frac{1}{\Delta z} \left[u\left(z + \frac{\Delta z}{2}, x, t\right) - u\left(z - \frac{\Delta z}{2}, x, t\right) \right] \quad (3.88)$$

Similar operators can be defined for the differentiation along the new directions \tilde{x} and \tilde{z} :

$$D_x u(z, x, t) = \frac{1}{\Delta r} \left[u\left(z - \frac{\Delta z}{2}, x + \frac{\Delta x}{2}, t\right) - u\left(z + \frac{\Delta z}{2}, x - \frac{\Delta x}{2}, t\right) \right] \quad (3.89)$$

$$D_z u(z, x, t) = \frac{1}{\Delta r} \left[u\left(z + \frac{\Delta z}{2}, x + \frac{\Delta x}{2}, t\right) - u\left(z - \frac{\Delta z}{2}, x - \frac{\Delta x}{2}, t\right) \right] \quad (3.90)$$

The finite difference approximation of these operators yields:

$$\frac{\delta}{\delta z} u(z, x, t) \approx \frac{\Delta r}{2\Delta z} (D_z u(z, x, t) - D_x u(z, x, t)) \quad (3.91)$$

$$\frac{\delta}{\delta x} u(z, x, t) \approx \frac{\Delta r}{2\Delta x} (D_z u(z, x, t) + D_x u(z, x, t)) \quad (3.92)$$

3.6.2.2 3D Formulation of the Rotated Staggered Grid

Analogous to the section above the three-dimensional operator scheme can be derived. The directions for the derivatives are:

$$d_1 = \frac{\Delta x}{\Delta l}x + \frac{\Delta z}{\Delta l}z + \frac{\Delta y}{\Delta l}y \quad (3.93)$$

$$d_2 = \frac{\Delta x}{\Delta l}x - \frac{\Delta z}{\Delta l}z + \frac{\Delta y}{\Delta l}y \quad (3.94)$$

$$d_3 = \frac{\Delta x}{\Delta l}x + \frac{\Delta z}{\Delta l}z - \frac{\Delta y}{\Delta l}y \quad (3.95)$$

$$d_4 = \frac{\Delta x}{\Delta l}x - \frac{\Delta z}{\Delta l}z - \frac{\Delta y}{\Delta l}y \quad (3.96)$$

$$\Delta l = \sqrt{\Delta x^2 + \Delta z^2 + \Delta y^2} \quad (3.97)$$

And the finite difference operators are:

$$\frac{\delta}{\delta x}u(z, x, y, t) \approx \frac{\Delta l}{4\Delta x}(D_{d_1} + D_{d_2} + D_{d_3} + D_{d_4})u(z, x, y, t) \quad (3.98)$$

$$\frac{\delta}{\delta y}u(z, x, y, t) \approx \frac{\Delta l}{4\Delta y}(D_{d_1} + D_{d_2} - D_{d_3} - D_{d_4})u(z, x, y, t) \quad (3.99)$$

$$\frac{\delta}{\delta z}u(z, x, y, t) \approx \frac{\Delta l}{4\Delta z}(D_{d_1} - D_{d_2} + D_{d_3} - D_{d_4})u(z, x, y, t) \quad (3.100)$$

These equations impose the necessity to use a linear combination of four derivatives in order to achieve one derivative along the standard orthogonal axes. This suggests a higher computational effort associated with the rotated grid approach. However, as the same four derivatives are involved in different combinations in the calculation of the three derivatives along the standard axes the additional effort is not that high. In actual fact the number of computations is exactly 4/3 of that of the standard staggered grid, corresponding to the number of space diagonals divided by the number of orthogonal axes.

Table 3.3: Simulation parameters for the simulation of porous media using the rotated staggered grid.

	Air-filled cracks	Oil-filled cracks
Grid points (vertical, horizontal)	500	500
Spatial discretization	0.1 mm	0.1 mm
Temporal discretization	$1.125 \cdot 10^{-8}$ s	$1.125 \cdot 10^{-8}$ s
Time steps	1200	1200
Bedrock		
P-wave velocity	4000 m/s	4000 m/s
S-wave velocity	2200 m/s	2200 m/s
Density	2500 kg/m ³	2500 kg/m ³
Cracks		
P-wave velocity	330 m/s	1050 m/s
S-wave velocity	0 m/s	0 m/s
Density	0.0001 kg/m ³	750 kg/m ³

3.6.3 Sample Applications

The rotated staggered grid technique has been applied successfully to numerous problems which are bent to cause problems with the standard finite difference approach (e.g. Saenger and Shapiro (2000); Saenger et al. (2005); Krüger et al. (2005)). In the following a few examples are shown.

3.6.3.1 Porous Media

As mentioned above one of the advantages of the new grid is the increased stability in presence of strong material contrasts. In this first example wave propagation on a small scale throughout a porous medium is demonstrated. The simulations are carried out using a two-dimensional P-SV implementation of the rotated staggered grid approach. Figures 3.21 and 3.22 show the divergence of the resulting wavefield, corresponding to the P-waves. The medium is artificially riddled with porous space of random shape and position. In the left column these porosities are filled with air whereas in the right column the same space is filled with an oil like fluid. The example should point out that the new method is capable of producing stable results in presence of interfaces both between solid and fluid as well as solid and gas. Computational and model parameters for these simulations are listed in table 3.3.

3.6.3.2 Topography

From the example above it can be understood that the simulation of complex topographies can be performed with the rotated staggered grid approach using a free air approach. That means cells above a surface are simple associated with the medium parameters of air. The applicability of this approach is shown by means of a realistic topography taken from an elevation model of a small area close to the LA basin which

Table 3.4: Parameters for the simulations of a complex topography using the rotated staggered grid.

Parameter	Value
Grid points horizontal	300 × 300
Grid points vertical	61
Horizontal discretization	50 m
Vertical discretization	50 m
Time steps	1000
Temporal discretization	0.0067 s
P-wave velocity	3000 m/s
S-wave velocity	1800 m/s
Density	2200 kg/m ³

has shown to cause trouble in previous finite difference simulations. Figures 3.23 and 3.24 show the wave field at the surface for times 0.6 to 1.8 seconds and 2.4 to 3.2 seconds respectively. Although strong scattering including maybe artificial effects can be observed the simulation remains stable. Accuracy analysis of these simulations is beyond the scope of this work. Computational and model parameters for this simulation are listed in table 3.4.

3.6.3.3 Kinematic rupture on a curved fault

Besides the application to strong medium contrasts the new staggered grid method can be successfully applied to the formulation of dynamic and kinematic rupture processes on finite faults with curved geometries. The significance of complex fault geometries on rupture simulations has been suggested in recent work (Aochi et al. (2000); Aochi and Fukuyama (2002); Aochi and Madariaga (2003); Cruz-Atienza and Virieux (2004)). In this simplified example a kinematic rupture is propagated along a fault with curved geometry. Figures 3.25 and 3.26 illustrate the wave field at the surface. The left columns show snapshots produced under the assumption that the propagation speed of the rupture is below the shear wave velocity. Snapshots in the right columns are related to a rupture speed higher than the shear wave velocity. Significant scattering of energy can be observed from changes in the faults strike direction. Computational and model parameters for these simulations are listed in table 3.5.

Table 3.5: Parameters for the simulation of a kinematic rupture on a non-planar fault using the rotated staggered grid approach.

Parameter	Value
Grid points horizontal	201×201
Grid points vertical	61
Horizontal discretization	50 m
Vertical discretization	50 m
Time steps	1500
Temporal discretization	0.0067 s
P-wave velocity	3000 m/s
S-wave velocity	1800 m/s
Rupture speed	1620 / 1980 m/s
Density	2100 kg/m ³

3.6.4 Discussion

The rotated staggered grid approach for finite difference wave propagation appears to be capable of solving numerous problems which are predestined to cause problems when a standard staggered grid is used. However, there are several drawbacks to the new approach: It turns out that a spatial interpolation of synthetic wavefields is necessary when point sources are used. Examination of the dispersion relations of the rotated grid layout proves that not only the direction of maximum errors are changed, but also their values. In Saenger et al. (2000) it becomes not entirely clear, but it can be shown that in the three dimensional case computational effort has to be increased by a factor of 9 to achieve the same accuracy as it is the case with the standard grid layout. This relation corresponds to the effective length of the operators which is increased by a factor of $\sqrt{3}$. Whereas the number of operations necessary for the spatial derivatives stays the same in the two-dimensional case, in the three-dimensional case it is increased by a factor of 4/3. This corresponds to the number of space diagonals divided by the number of orthogonal axes. Together with the necessity of denser spacing due to a higher level of grid dispersion the overall computational effort is raised by a factor of 12.

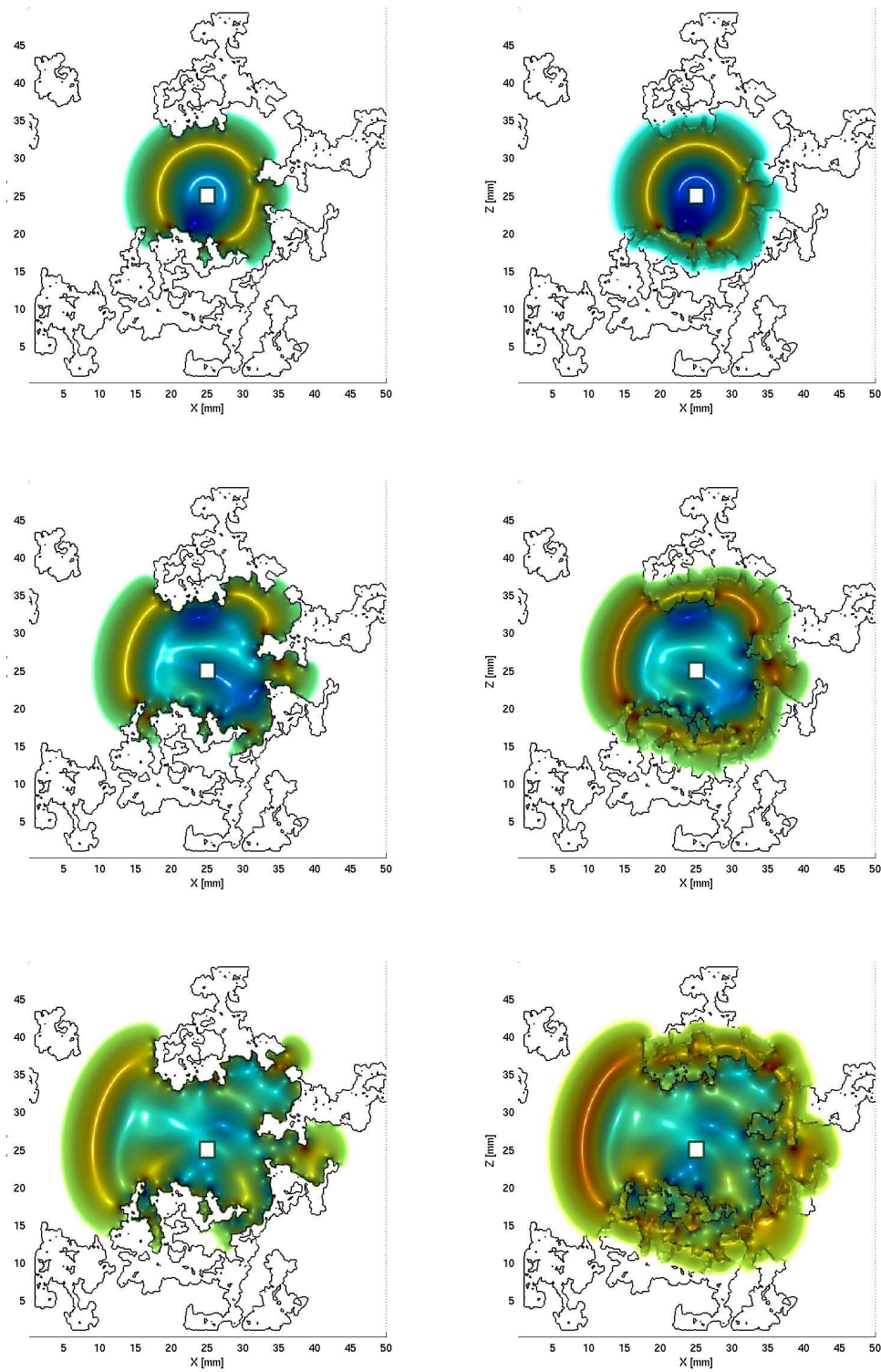


Figure 3.21: Wave propagation in porous media simulated by the rotated staggered grid approach. Snapshots of resulting P-wave field at 4, 5 and 6 micro seconds. Cavities in the left column are filled with air and with oil in the right column.

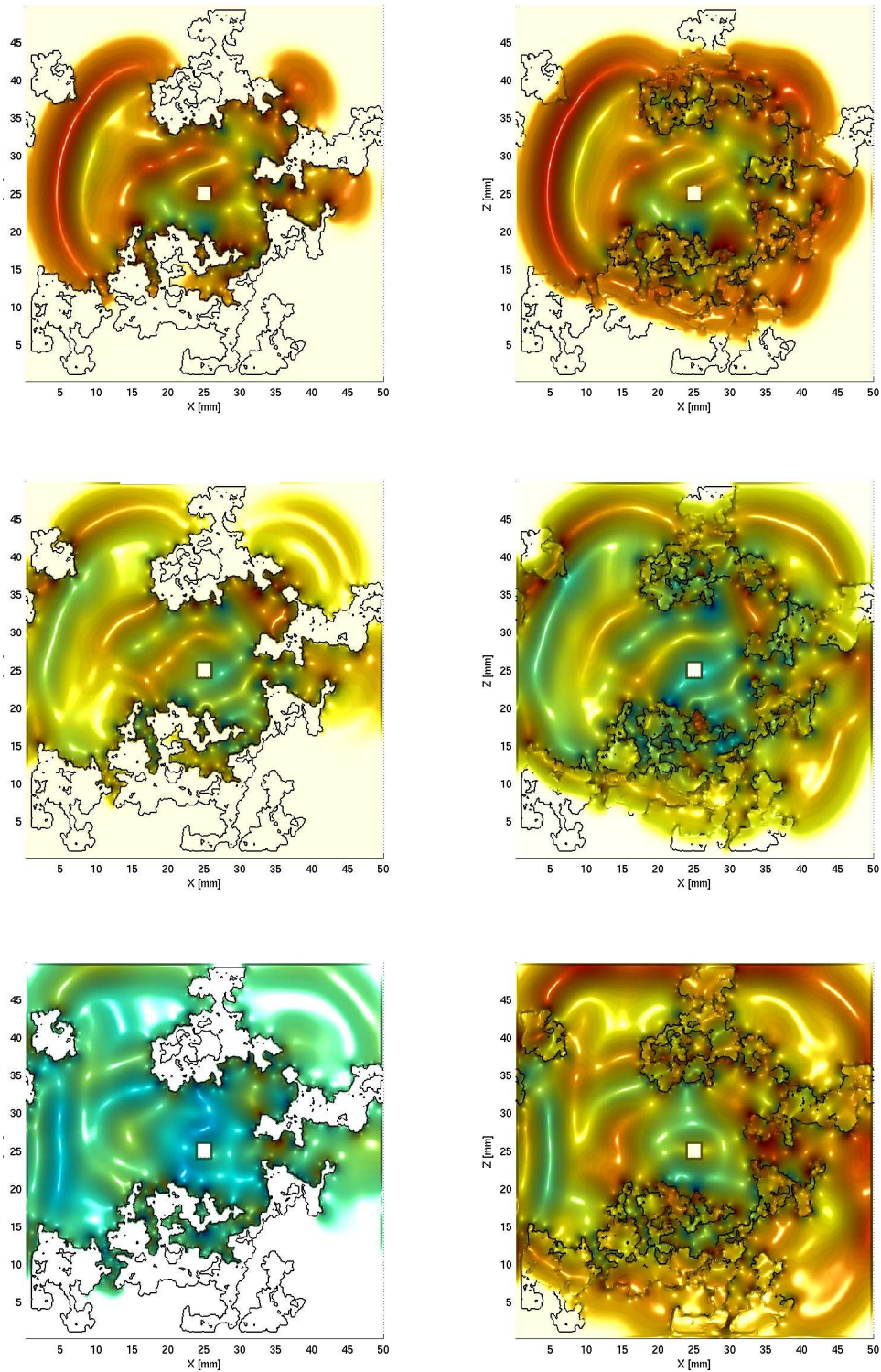


Figure 3.22: Wave propagation in porous media simulated by the rotated staggered grid approach. Snapshots of resulting P-wave field at 7, 8 and 9 micro seconds. Cavities in the left column are filled with air and with oil in the right column.

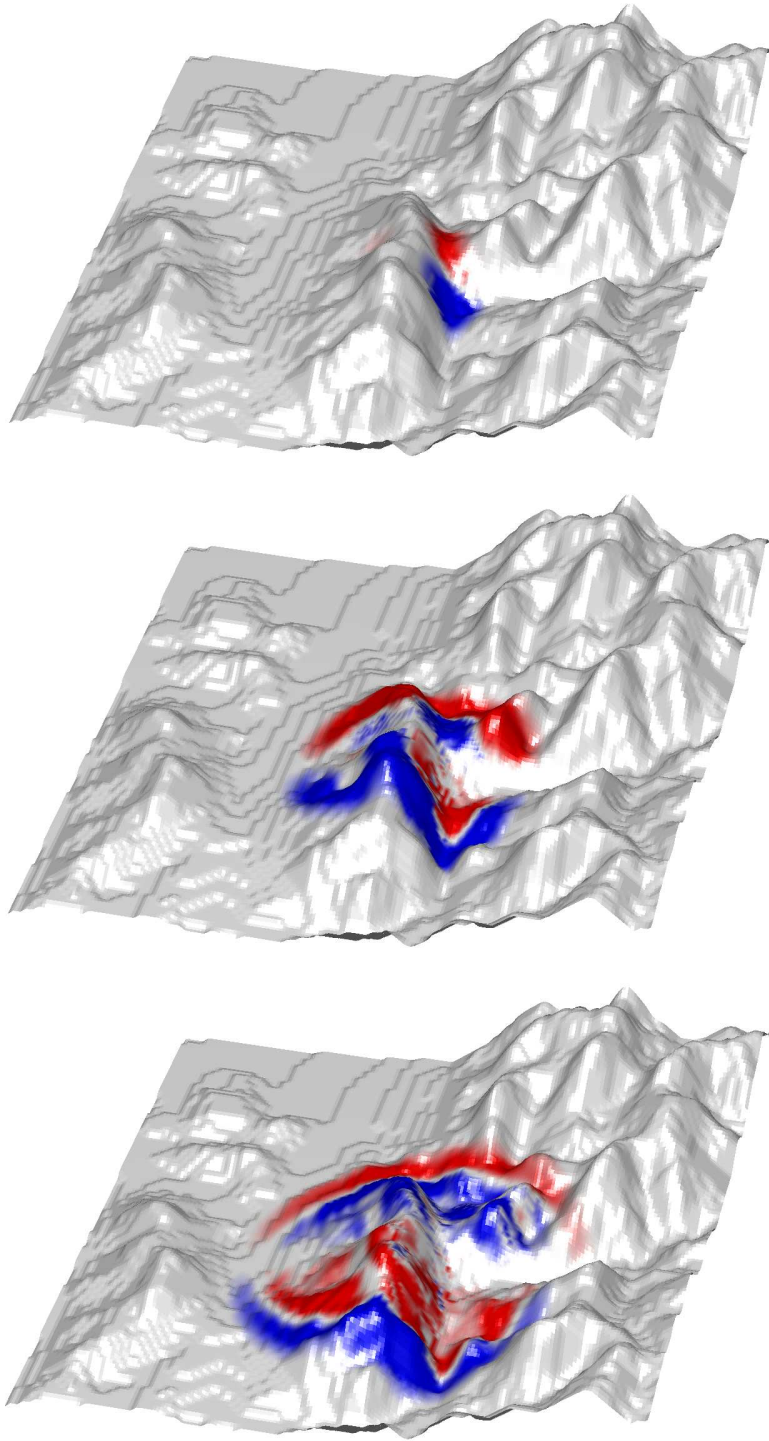


Figure 3.23: Wave propagation in presence of topography modeled with the rotated staggered grid approach. Snapshots of North-South horizontal component at 0.6, 1.2 and 1.8 seconds.

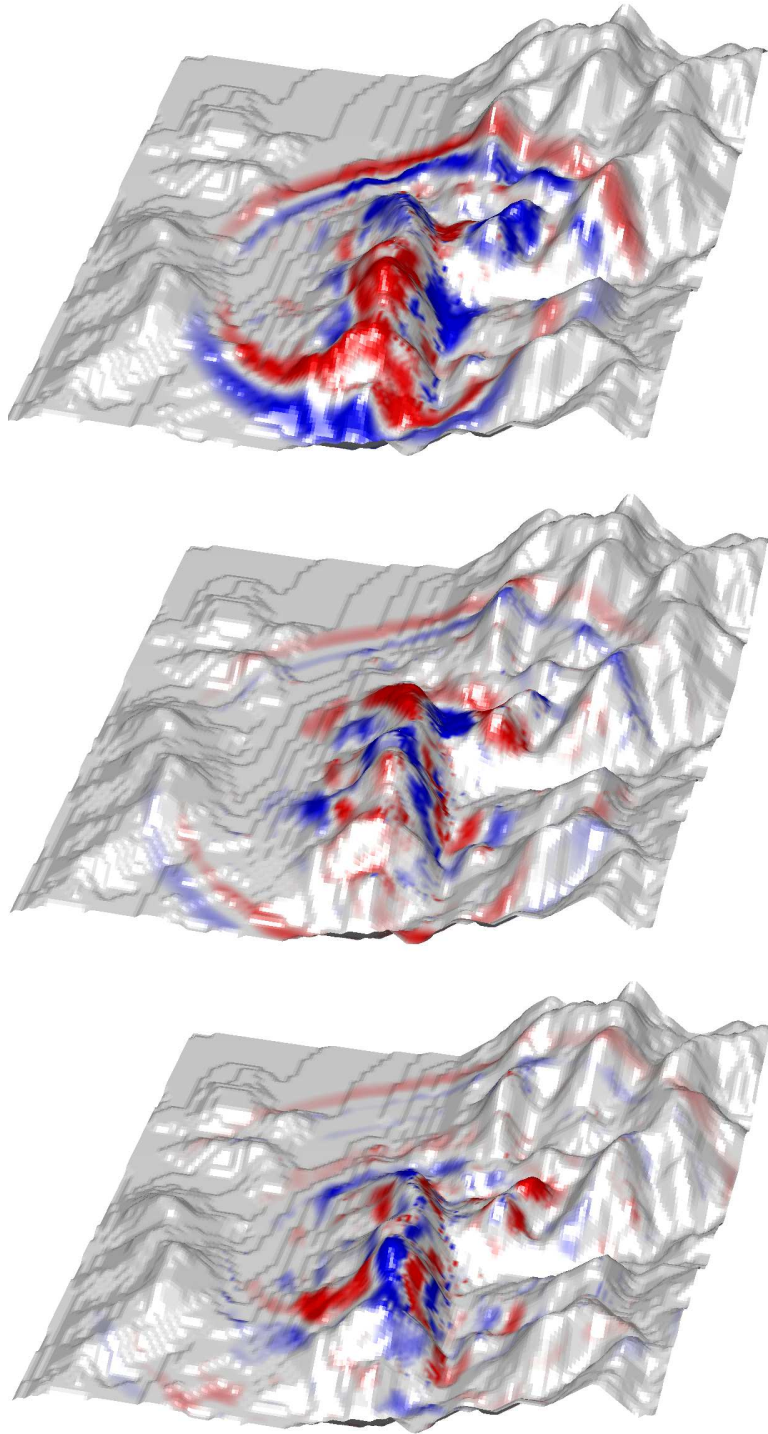


Figure 3.24: Wave propagation in presence of topography modeled with the rotated staggered grid approach. Snapshots of North-South horizontal component at 2.4, 3.0 and 3.6 seconds.

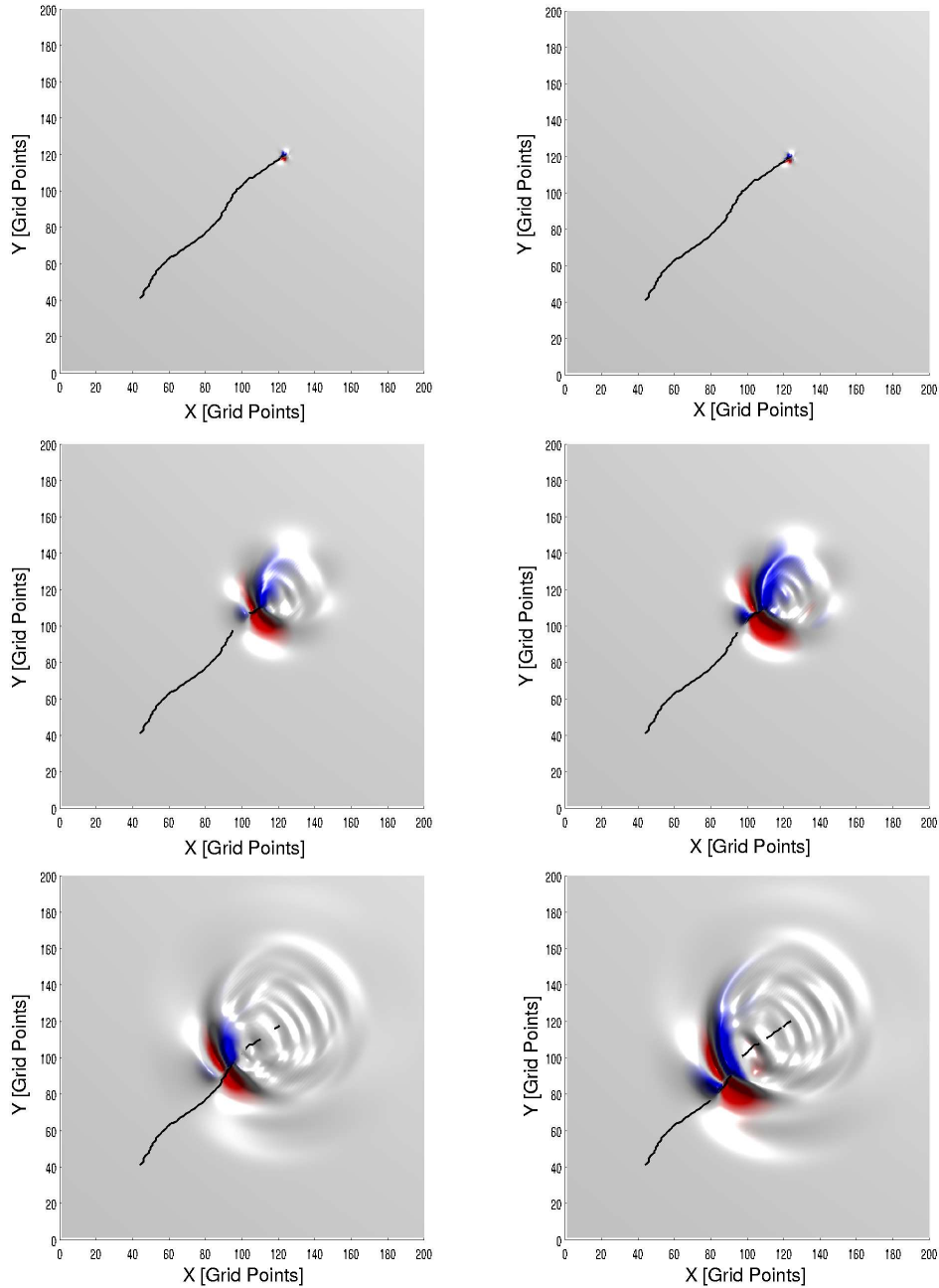


Figure 3.25: Wavefield emanating from kinematic rupture on curved fault. Snapshots of North-South horizontal component. Left column: assumed rupture speed below shear wave velocity, right column: assumed rupture speed above shear wave velocity.

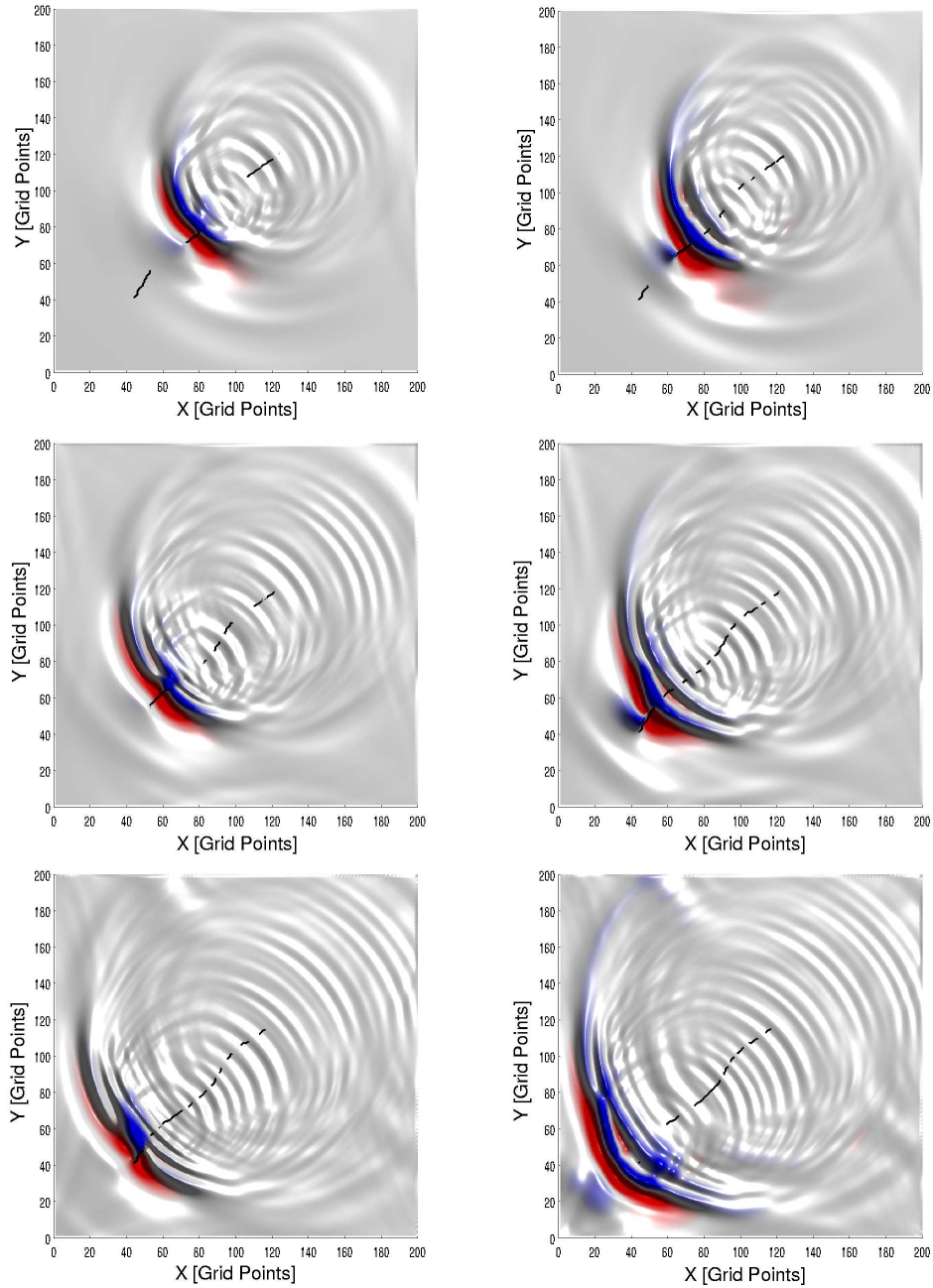


Figure 3.26: Wavefield emanating from kinematic rupture on curved fault. Snapshots of North-South horizontal component. Left column: assumed rupture speed below shear wave velocity, right column: assumed rupture speed above shear wave velocity.

3.7 Absorbing Boundaries

3.7.1 Motivation

Simulation of waves propagating through physically unbounded media by grid methods such as finite differences entails special treatment for the boundaries of the computational model which is inevitably limited in extent. There are two possible solutions to this problem: absorbing boundary conditions and absorbing boundary layers.

Absorbing boundary conditions attempt to simulate the outgoing nature of waves intrinsically by local conditions at the boundaries. The method was introduced for acoustic waves by Clayton and Engquist (1977) and has shown to work well particularly for waves impinging normally to the borders. However, for the elastic case the method is afflicted with problems. The exact boundary condition is not longer a scalar as it is the case for acoustic waves but becomes a matrix differential equation including integrals as well. Approximating these becomes complex especially for higher order finite difference schemes and the stability conditions of the problem are hard to predict. Simone and Hestholm (1998) have found highly visible reflections as well as conditional instabilities in some settings.

Attaching absorbing layers of finite width to the physical model domain in which waves become artificially attenuated and trapped is a possibility to circumvent these problems. There are several models suggested each afflicted with its own limitations (Reynolds (1978); Cerjan et al. (1985)). Whereas the definition of scalar attenuation factors within the absorbing layers is unconditionally stable and easy in its implementation the method requires a large width of the absorbing layers. Additionally, as the absorption factor is depending on the wave length artificial, reflections of long period waves are inevitable.

An elegant approach suggested by Sochacki et al. (1987) consists of employing layers of physically attenuative material to the domain boundaries following the viscoelastic algorithm presented in section 3.3. The problem arising from this approach is the inevitable impedance contrast between elastic and viscoelastic material which is recognized by incident waves. In order to avoid artificial reflections from that contrast thick layers with smooth gradients and relatively low attenuation have to be employed. As for scalar attenuation this results in large memory consumption due to solving the boundary problem.

In recent years a new approach involving so called Perfectly Matched Layers (PML) has been introduced in wave propagation algorithms. The method is adopted in this work and outlined in the following.

3.7.2 Perfectly Matched Layers (PML)

The PML approach was originally formulated for the Maxwell's equation (Berenger (1994)). Meanwhile the method has become widely used for the simulation of electromagnetic waves facing similar problems due to the conflict of unbounded physical and limited computational domains (e.g. Berenger (1996); Turkel and Yefet (1998); Harari et al. (2000); Singer and Turkel (2004)). The method was adopted to the modeling of seismic wave propagation in acoustic cases (Liu and Tao (1997)) and elastic

cases (e.g. Hastings et al. (1996); Collino and Tsogka (2001); Zeng and Liu (2001); Marcinkovich and Olsen (2002)). The basic principle of PML consists in splitting the elastic wave field into components perpendicular and parallel with respect to the boundary. A damping term is then applied to the perpendicular component inside a PML region which is added to the physical domain of the model. Equations inside the PML domain and inside the model interior domain are coupled in a way that the interface between these domains becomes non-reflective and wave amplitudes decrease exponentially within the PML domain.

A detailed description of the formulae for isotropic media as well as the finite difference implementation can be found in Marcinkovich and Olsen (2002)). The anisotropic case is covered in Collino and Tsogka (2001). Performance of the approach is discussed in a various studies (e.g. Marcinkovich and Olsen (2002); Brietzke (2003)) and there is agreement that a width of 20 grid points is sufficient in order to erase artificial reflections when PML boundaries are used.

3.8 Parallelization

3.8.1 Motivation

From the discussion in previous sections it is understood that numerical simulations of wave propagation provide new insights by modeling the complete three dimensional wavefield in presence of strong heterogeneities. However, this has to be paid with extremely high computational requirements both in terms of core memory and CPU time. Memory requirements are due to the description of complex models, whereas a large number of floating point operations has to be done while propagating the wavefield in space and time.

For a typical scenario simulation as carried out in this work, the memory usage is on the order of hundreds of Gigabytes, whereas the number of floating point operations reaches the PetaFlop range (10^{15} floating point operations). That imposes, that for example an of the shelf PC would need about 60 days to solve the computations given the fact that the model would fit into its memory. Despite rapid improvements in memory size and floating point performance of modern computers a problem of that size cannot be expected to fit into a single machine for the next years. However, from this example it also becomes clear that a sufficient number of PCs could save the problem if it is distributed among them. The issue of parallelizing large problems in order to solve them on many processors simultaneously is vastly used in modern High Performance Computing. All computers currently ranked among the 500 fastest machines world wide are to some extent working in parallel, about 60 percent are pure clusters, 24 percent massive parallel processor machines and 16 percent are constellations, that means clusters of symmetric multiprocessors (SMP). Especially the fraction of clusters based on standard PC processors has increased throughout recent years.

Finite difference codes, especially on regular grids are naturally adopted for parallel execution. Not only that the differential operators are defined locally, which reduces the amount of communication between nodes, furthermore the layout of a regular grid matches the architecture of parallel machines which often have two-dimensional or three-dimensional rectangular topologies.

3.8.2 Techniques

Various techniques are employed to distribute a problem over numerous processors or computation nodes. A few approaches are briefly discussed in the following paragraphs, before a detailed description on the implementation used in this work is presented.

3.8.2.1 Shared Memory / OpenMP

OpenMP is a specification for a set of compiler directives, library routines, and environment variables that can be used to specify shared memory parallelism in Fortran and C/C++ programs. The MP in OpenMP stands for Multi Processing. Shared-memory parallel programming directives have never been standardized in the industry. An earlier standardization effort, ANSI X3H5 was never formally adopted. Since then, vendors have provided different sets of directives, very similar in syntax and semantics.

OpenMP consolidates these directive sets into a single syntax and semantics, and finally delivers the promise of single source portability for shared-memory parallelism. OpenMP also addresses the inability of previous shared-memory directive sets to deal with coarse grain parallelism.

3.8.2.2 Shared Memory / Numa

NUMA stands for Non-Uniform Memory Access. Non-Uniform Memory Access means that it will take longer to access some regions of memory than others. This is due to the fact that some regions of memory are on physically different busses from other regions. The NUMA architecture was designed to surpass the scalability limits of the SMP architecture. With SMP, which stands for Symmetric Multi-Processing, all memory access are posted to the same shared memory bus. This works fine for a relatively small number of CPUs, but the problem with the shared bus appears when you have dozens, even hundreds, of CPUs competing for access to the shared memory bus. NUMA alleviates these bottlenecks by limiting the number of CPUs on any one memory bus, and connecting the various nodes by means of a high speed interconnect.

3.8.2.3 Message Passing

MPI stands for Message Passing Interface (Message Passing Interface Forum (1996)). The goal of MPI is to develop a widely used standard for writing message passing programs. As such the interface attempts to establish a practical, portable, efficient, and flexible standard for message passing. The main advantage of establishing a message passing standard consists in portability. In a distributed memory communication environment in which the higher level routines are build upon lower level message passing routines the benefits of standardization are particularly apparent. Furthermore, the definition of a message passing standard provides vendors with a clearly defined base set of routines that they can implement efficiently, or in some cases provide hardware support for, thereby enhancing scalability. There are various implementations of the MPI standard available, for example MPICH (Cropp and Lusk (1996a,b)).

3.8.3 2D MPI Implementation

The code used in this study is designed for the simulation of wave propagation in presence of sedimentary basins where the horizontal extent of the model overwhelms the vertical one. Consequently, parallelization is carried out in the two horizontal directions, whereas the vertical direction is considered small relative to the overall horizontal dimensions of the model and parallelization in this direction is not considered useful. A two-dimensional layout including communication in both horizontal directions x and y is chosen to provide adequate performance and flexibility on a large range of problem sizes and computational equipment. In order to minimize the amount of data communicated between nodes the individual parts of the model solved by one node should be close to quadratic. The reason can be understood from figure 3.27. The width of margins which have to communicate is determined by the operator length and therefore remains constant. Thus, the amount of data that has to be transferred can be

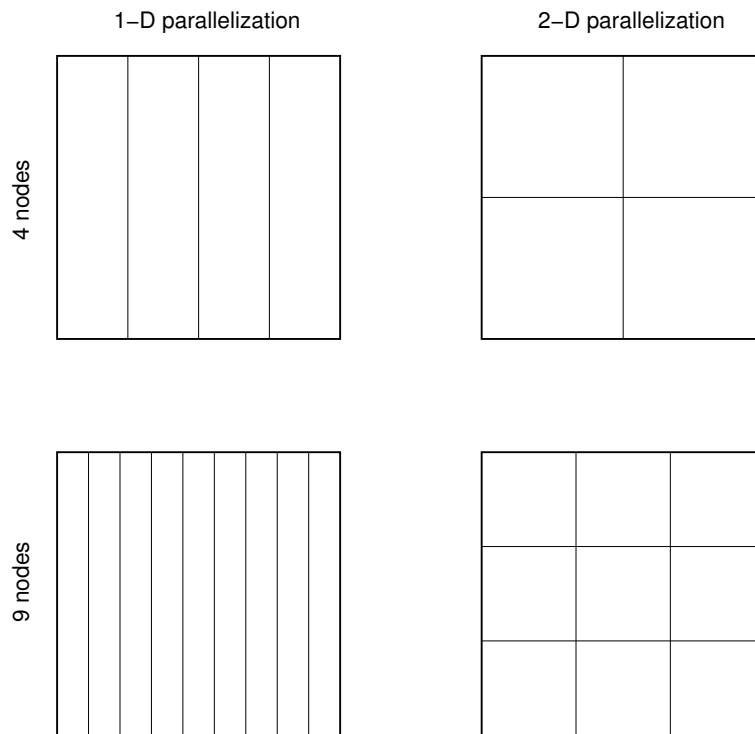


Figure 3.27: Examples for 4 and 9 nodes demonstrating the reduced amount of necessary communication when parallelization is applied in two directions.

estimated simply by the length of border lines between nodes. In figure 3.27 a solution with parallelization in only one direction (left column) is compared with one acting in both horizontal directions (right column). The difference is obvious. In the 4 node case the border length is reduced from 3 to 2 times the model dimension when communication is done in two dimensions, whereas for 9 nodes the length is decreased from 8 times the model space to only 4 times the model dimension. This example makes clear that a higher-dimensional parallelization becomes important when larger numbers of nodes are involved.

The parallelization layout is illustrated in figure 3.28 for arbitrary numbers of nodes in both directions, which are termed n_x and n_y , respectively. The area of the model shared by two nodes is depicted light blue, whereas the corners which are shared by four nodes are colored dark blue.

The updating scheme is illustrated in figure 3.29 considering the situation on a corner shared by four nodes. Grid points are demarked as black circles filled with a color reflecting their status. Green color depicts valid values at this location, whereas red colors demark grid points that have to be updated. The initial status after the finite difference time evolution is shown in subfigure a). Also depicted are the paths for communication in X direction (in this graph horizontal) as black arrows. The situation after this communication is completed is shown in subfigure b). Paths for the communication in y direction (vertical) are shown in subfigure c). From subfigure d) it can be recognized that the whole area has been updated successfully after the second communication is completed.

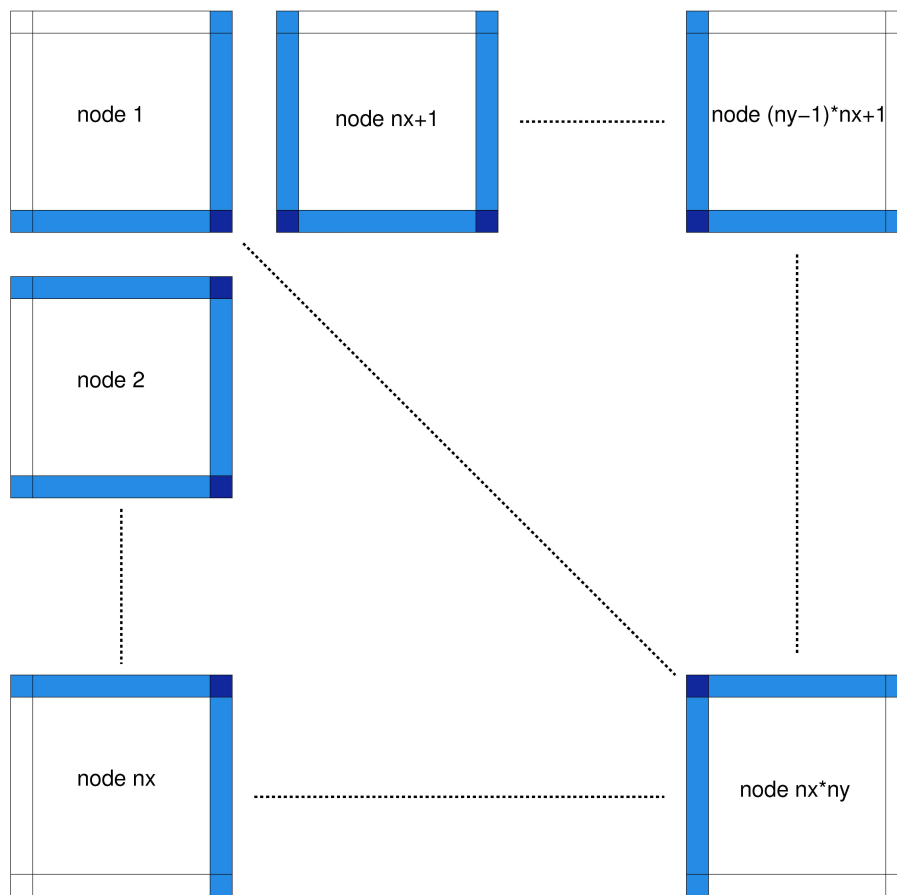


Figure 3.28: Layout of two-dimensional parallelization, margins shared by 2 nodes are demarked light blue, corners shared by 4 nodes are demarked dark blue.

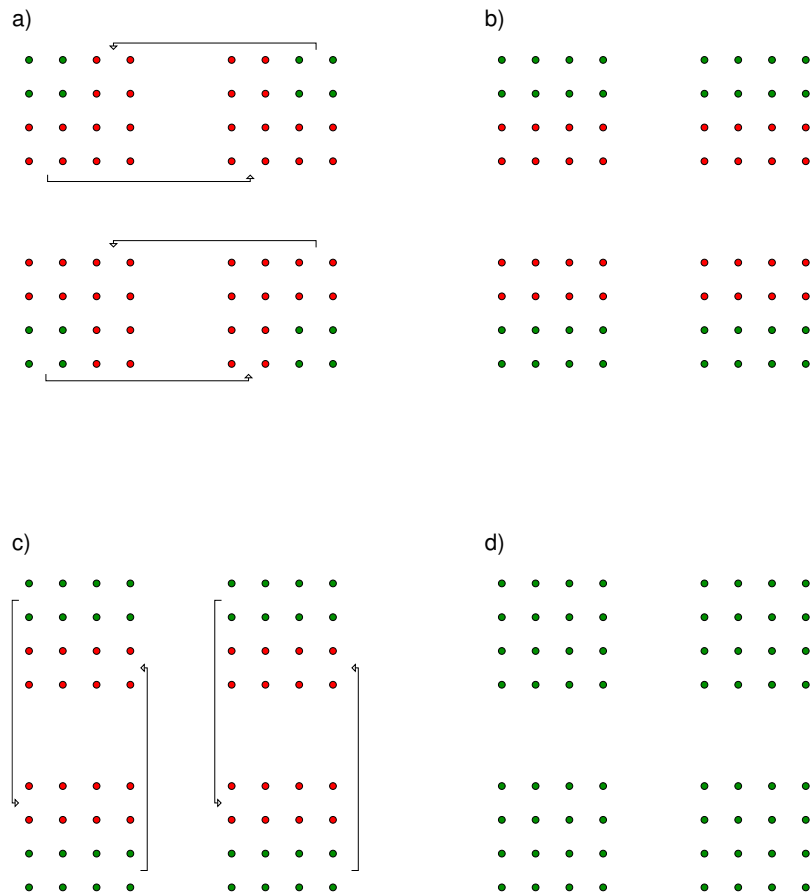


Figure 3.29: Message passing communication scheme at domain corners, where grid points are shared by 4 nodes.

It is noteworthy that in this context the term `update` is used rather than the often used denotation `exchange`. The term `exchange` in the context of communication between nodes is prone to be misunderstood. Communication of data between nodes does not have the character of an exchange. The most important aspect is that repeated communication does not restore the initial status. Communication between nodes updates non-valid values on grid points in the neighboring nodes with values from matching points within the sending node. The old values are simply erased and a repeated communication has no effect.

Chapter 4

The Lower Rhine Embayment

In this chapter an overview of the geologic and tectonic setting of the study area, the Lower Rhine Embayment (LRE) is given. As this is discussed already in Ewald (2001) considerations presented in this chapter are focused on recent literature.

4.1 Framework

The presently still active European Cenozoic Rift System (abbreviated ECRS or ECRIS) developed during the Late Eocene. It extends over 1100 km from the western Mediterranean in the south to its northern ends in the Dutch North Sea. Its southern elements are the Valencia Through, the graben systems of the Gulf of Lion and the Valence, Limagne and Bresse grabens, the latter three striking northwards. The Burgundy transfer zone links these graben structures to the northern elements of the ECRS: The Upper Rhine Graben beginning in the northern alpine foreland and bifurcating at the Rhenish triple junction into the northwest striking Roer Valley Graben as part of the Lower Rhine Embayment and the northeast trending Hessian Grabens, such as the Leine Graben and the Eger Graben, the latter transecting the Bohemian Massif. Figure 4.1 illustrates the European Cenozoic Rift System and the location of the Lower Rhine Embayment within its context.

It is broadly accepted that reactivation of Variscan Permo-Carboniferous shear systems played an important role in the development of the ECRS (Schumacher (2002); Dezes et al. (2004); Cloetingh et al. (2005)). Seismic lines shown in figures 4.5 and 4.6 illustrate how the evolution of the graben has been controlled by main border faults dissecting Mesozoic sediments. Despite the fact that the evolution of the ECRS was accompanied by the development of major volcanic centers in Iberia, on the Massif Central and the Bohemian Massif it is considered as passive rifting.

The present stress regime which built up during the Pliocene is directed northwestwards for large parts of central Europe (Gölke and Coblenz (1996); Müller et al. (1997)). These stress directions have their expression in sinistral shear in the Upper Rhine Graben, active extension in the Lower Rhine Embayment and for the Roer Valley Graben in particular, and accelerated subsidence of the North Sea Basin (Sissingh (2003); Dezes et al. (2004); Cloetingh et al. (2005)).

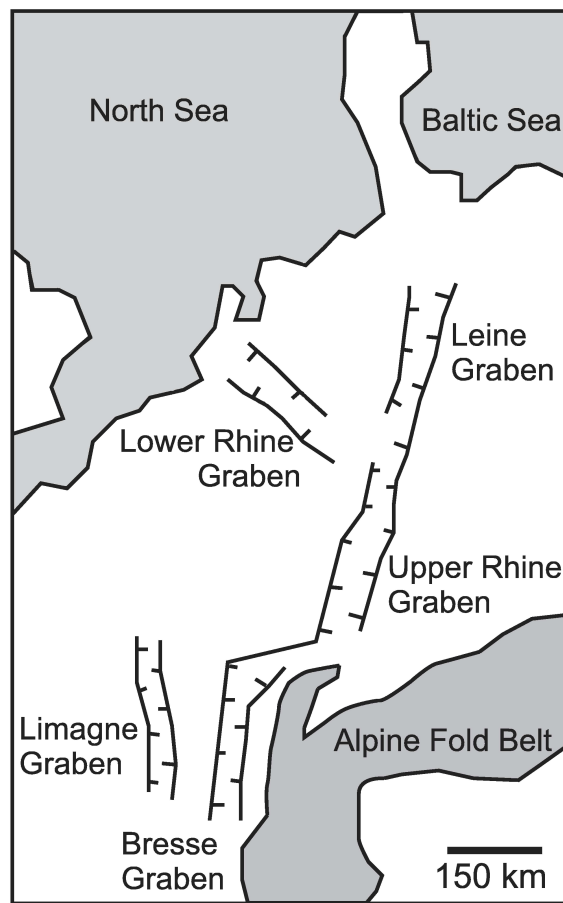


Figure 4.1: Tectonic elements of the European Cenozoic Rift System (modified after van Balen et al. (2005)).

As southernmost part of the North Sea Dutch-German rift structure the Lower Rhine Embayment forms an asymmetric graben system with the rough shape of a triangle opening to the north-west. On the south-eastern side its start is defined with the Rhenish Triple Junction, whereas the north-western extensions evolve into the North Sea Rift System. Its extensions are about 50 km in width and 100 to 200 km in length depending on the definition. It consists of numerous tectonic blocks, which have shown varying amounts of subsidence throughout the evolution of the rift system, separated by numerous faults showing normal faulting under the present stress field. The most active part of the basin is the Roer Valley Rift system located at western margin of the Lower Rhine Embayment. With dimensions of 20 km in width and 120 km in length itself consists of three structural units, the Campine block, the Roer Valley Graben, the Peel block and the associated faults: The Peel boundary fault, the Rijen fault zone, the Veldhoven fault zone and the Feldbiss fault zone.

Towards the East the structural elements of the remaining part of the basin are: The Erft block, the Köln block and the Venlo Block with the associated fault zones of Erft-sprung, Venlo fault zone and Tegelen fault zone (Ziegler (1994); Michon et al. (2003)). As mentioned above, the in general northwest striking Lower Rhine Embayment began its subsidence in Late Eocene. The development of the basin was accompanied by rotational divergence of its flanks. Paleomagnetic measurements (Schreiber and Rotsch (1998)) indicate a clockwise rotation of the eastern Rhenish Massif. Subsidence of the Lower Rhine Embayment continued throughout the Oligocene and accelerated in Pliocene due to the development of the present north-west south-east oriented field of regional compressional stress. At present extension in the Lower Rhine Embayment is active (Zijerveld et al. (1992)), whereas the Roer Valley Graben reveals subsidence under the influence of sinistral transtension (Geluk et al. (1994)).

According to Sissingh (2003) upper crustal extension by faulting is as high as 600 m, whereas the actual crustal configuration demands a stretching of 1-2 km. Dezes et al. (2004) suggests extension by upper crustal faulting to vary from 4 to 5 km in the south-eastern parts of the Roer Valley Graben to zero at the graben's termination near the Dutch North Sea coast. The larger values may also account for pre-tertiary rifting (Ziegler (1994)).

4.2 Stratigraphy

Major factors determining the amount and nature of sedimentary deposits in the Lower Rhine Embayment are relative paleo-heights of individual tectonic blocks and their subsidence history. In figure 4.2 the main tectonic features of the area are illustrated, whereas figure 4.3 presents the subsidence of the individual blocks throughout the Tertiary. The area of the Lower Rhine Embayment was situated above sea level during the early Tertiary. Periodic flooding by the North Sea resulted in cyclic deposition of calcareous and clastic sediments. Beginning with the reactivation of Variscan faults at the Eocene-Oligocene transition the Lower Rhine Embayment as a whole developed into a low-lying region with elevations close to global sea level. However, in response to crustal movements it subsided differentially in space and time. Largest amounts of subsidence and consequently sedimentation can be found in the Roer Valley Graben.

Throughout Oligocene-Pliocene another representation of marine-nonmarine cycle in sedimentation can be found in the basin ranging from Rupelian Marine Series over several Continental-Marine Series to Late Pliocene Continental Series. This suggests regression of the sea, related to both tectonic uplift of the basin region and a global lowering of the sea level. Most prominent expression of this uplift is the Peel High, a raise in basin topography between the Venlo and Roer valley subgrabens. Nevertheless, throughout Late Tertiary sedimentation was still overwhelming erosion in the Lower Rhine Embayment. Continuously shifting coast lines and repeated transgressions of the north sea combined with the interim deposition of continental sediments culminated into the complex stratigraphy of this region including important brown coal mining districts. Figure 4.4 gives an impression of the directions of sediment transport and deposition areas in the Lower Rhine Embayment at the Late Oligocene and Early Miocene. Maximum thicknesses of the Cenozoic fill amount to 2000 m in the Roer Valley Graben and 1200 m in the south eastern basin.

Due to the economical importance of the deposits, the sedimentary structure of the Lower Rhine Embayment is subject to intensive studies for the last decades. Recently, modern techniques have been applied to the region, such as deposition modeling (Cloetingh et al. (2005)) and calculation of litho-facies logs using digitized well log data (Klett et al. (2002)). Detailed investigations of the seismic velocity structure have been carried out, using single station as well as array techniques and taking into account both earthquake sources and ambient noise recordings (e.g. Hinzen et al. (2004); Ohrnberger et al. (2004); Parolai et al. (2005, 2002); Scherbaum et al. (2003); von Seht and Wohlenberg (1999); Fäh et al. (2003)). These investigations have lead to numerous velocity models based on power law depth dependence for sediment velocities as proposed by Budny (1984).

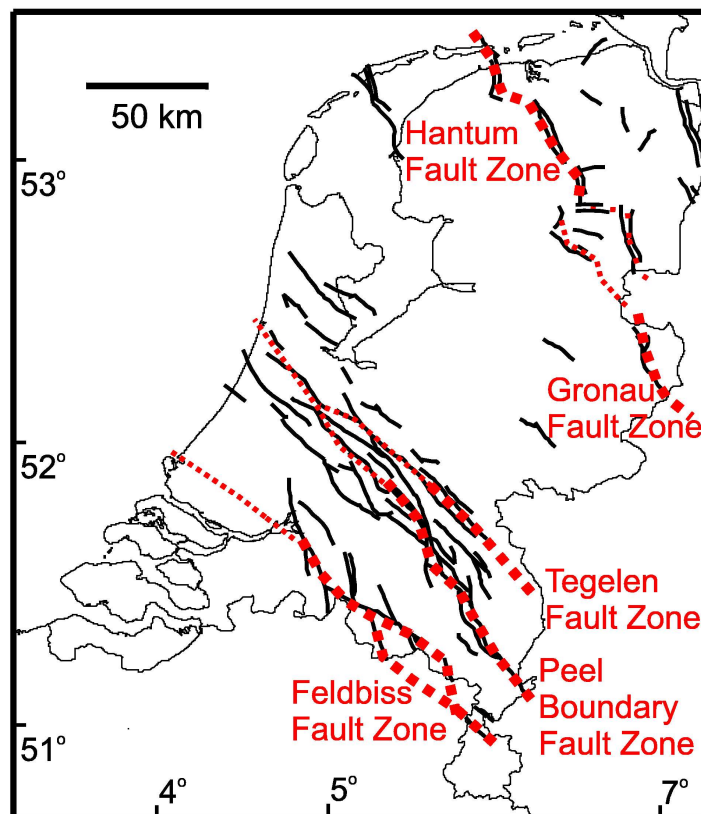


Figure 4.2: Structural framework of the Lower Rhine Embayment (van Balen et al. (2005)).

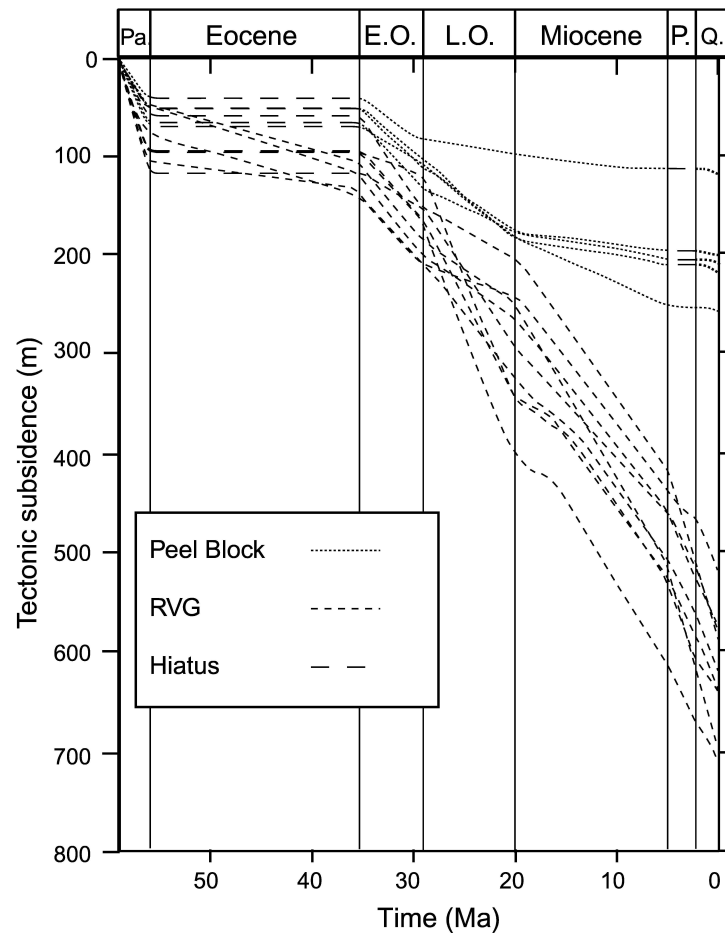


Figure 4.3: Cenozoic subsidence history of individual tectonic blocks within the Lower Rhine Embayment (Michon et al. (2003)).

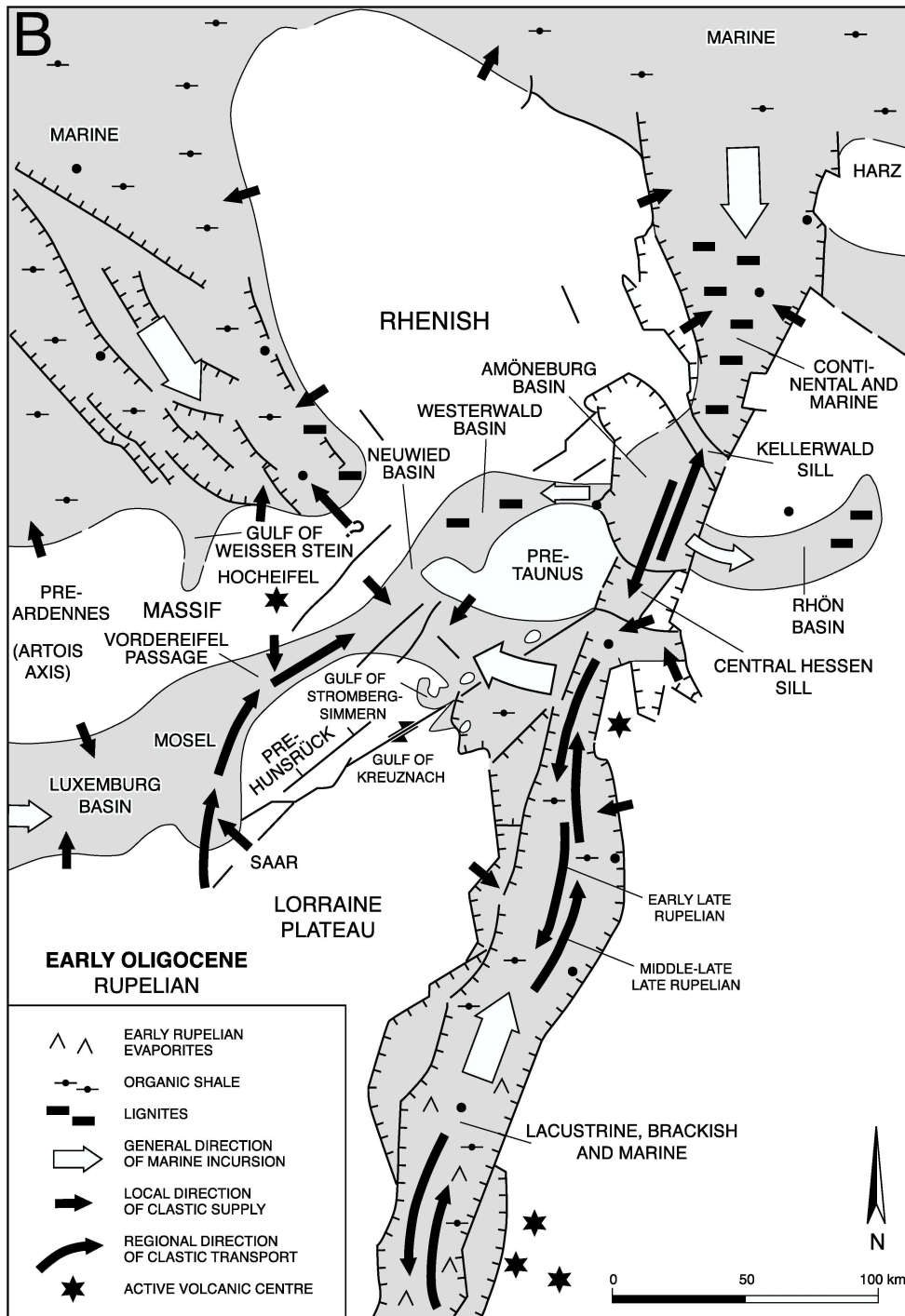


Figure 4.4: Directions of clastic and marine sediment transport in the Lower Rhine Embayment during early Miocene (Sissingh (2003)).

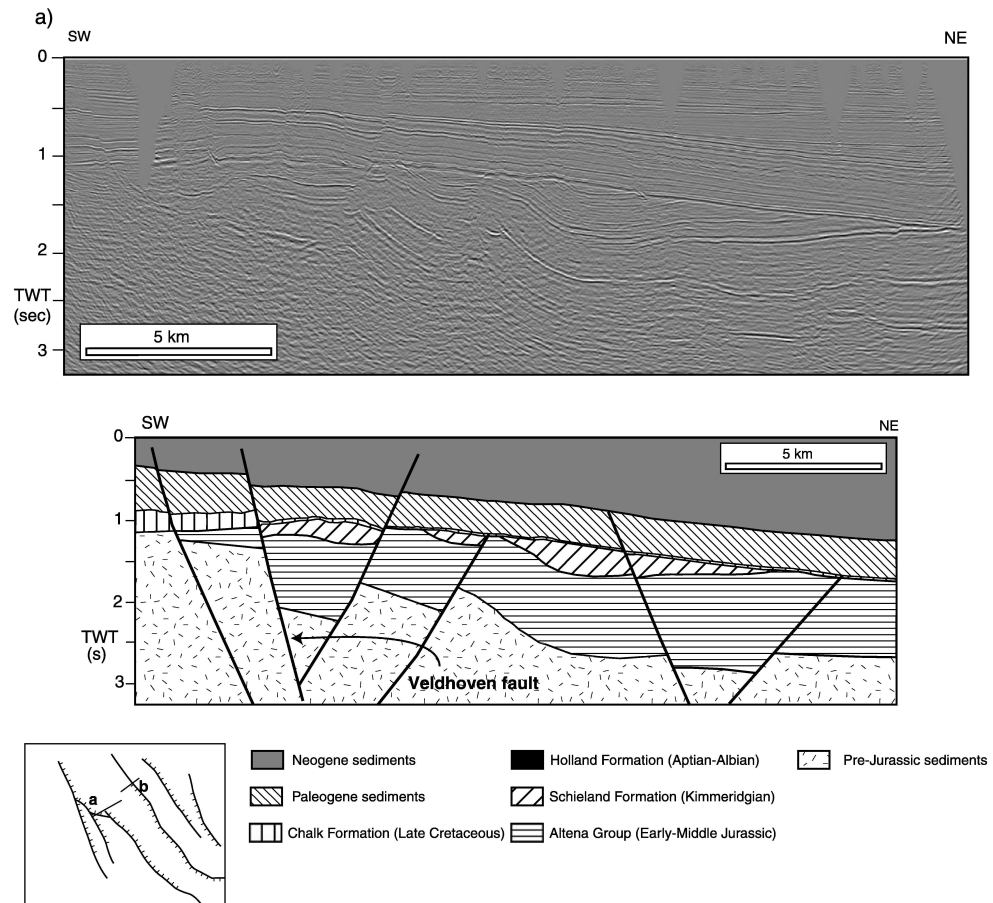


Figure 4.5: Seismic line and profile of structural interpretation across the Veldhoven fault (marked a in subfigure). The Mesozoic age of main tectonic fault systems is clearly expressed in the stratigraphy (Michon et al. (2003)).

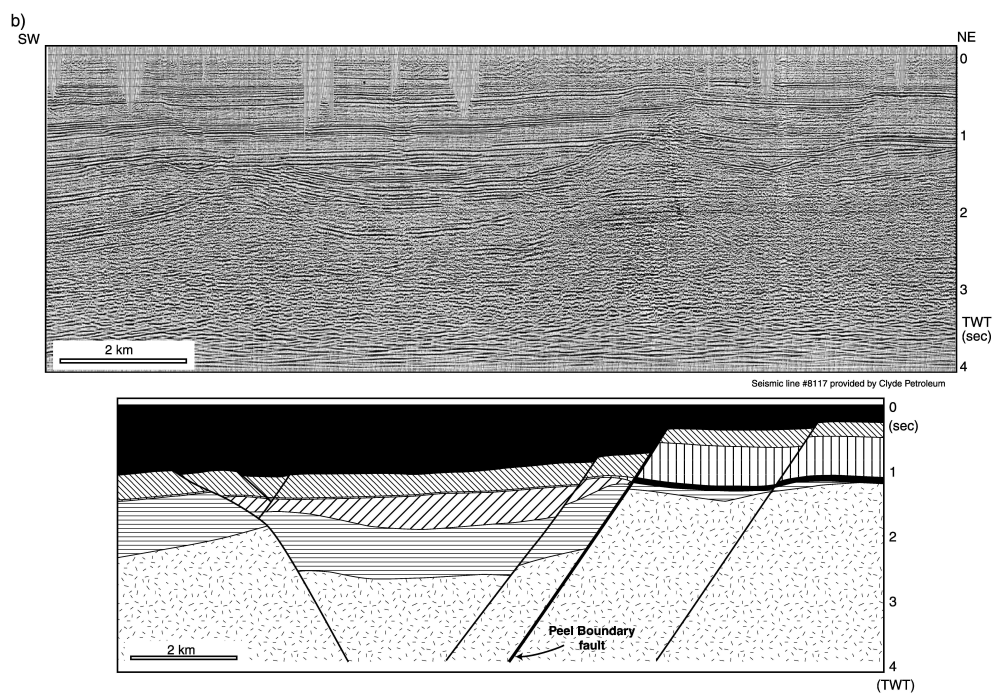


Figure 4.6: Seismic line and structural profile across the Peel Boundary fault (marked b in map embodied in figure 4.5 (Michon et al. (2003))).

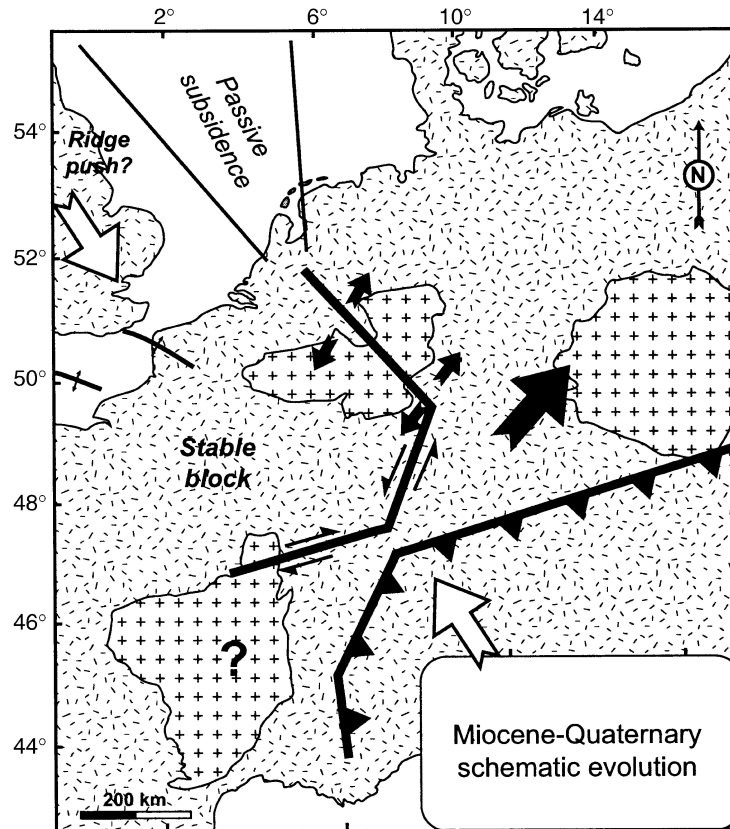


Figure 4.7: Neogene evolution of the European stress field (Michon et al. (2003)).

4.3 Recent Tectonics

4.3.1 Regional Stress Regime

Tectonic stress observed in Europe is assumed to be originated by the ridge push along the Mid-Atlantic ridge and forces along the eastern and southern plate margins along the Alpine continent-continent collision front (e.g. Grünthal and Stromeyer (1992); Müller et al. (1992); Gölke and Coblenz (1996)). For central and western Europe a large region of consistent north-west to south-east directed maximum compressional stress can be observed. This observation is consistent with the out-comings of the World Stress Map project (Zoback et al. (1989); Zoback (1992)). Figure 4.8 displays a section of the World Stress Map for Europe. The general trend as described above as well as variations can be recognized. Ahorner (1975) already discussed the existence of strike-slip faulting in the Upper-Rhine graben and normal faulting in the Lower Rhine Embayment under conditions of equivalent horizontal compressional stress. In figure 4.7 the concordance of different faulting mechanisms under the same stress field is illustrated.

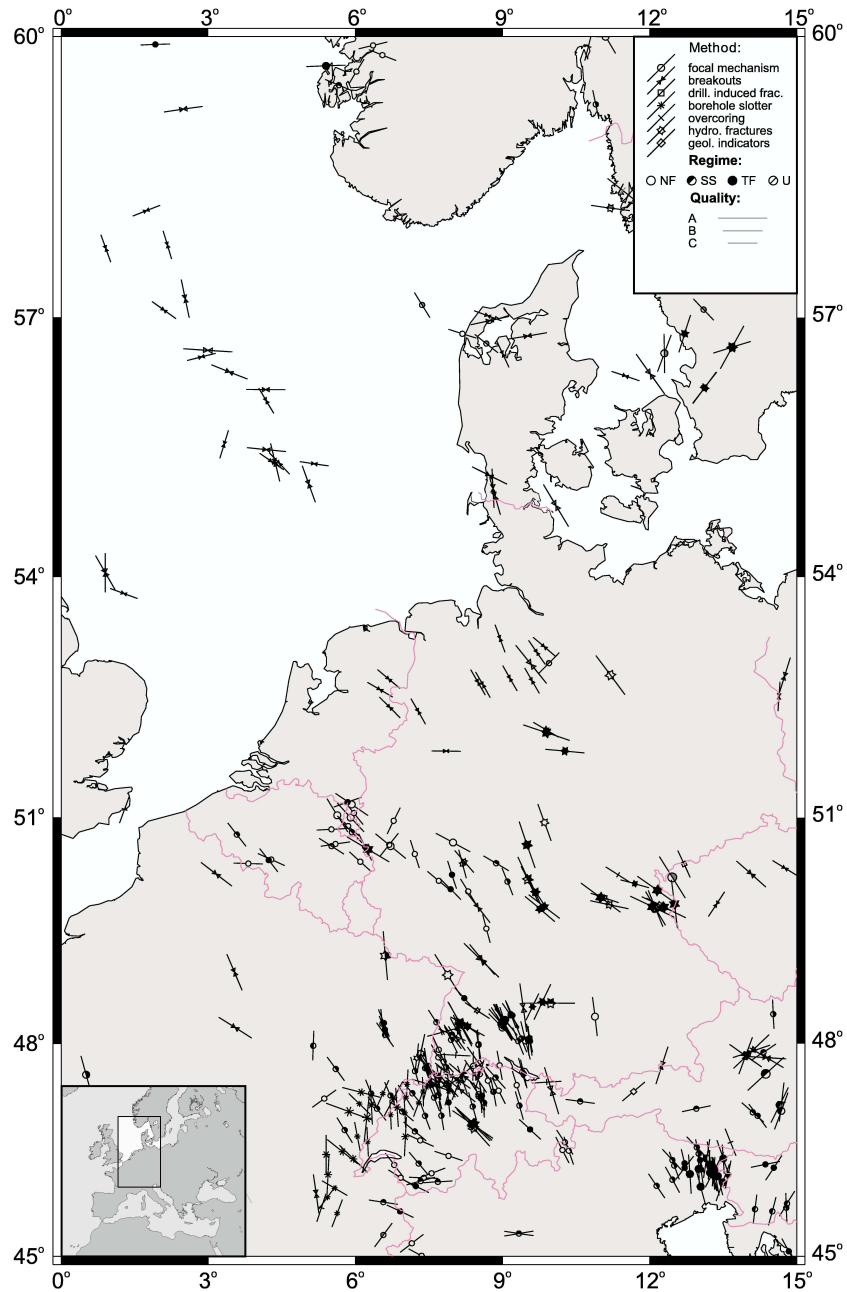


Figure 4.8: Maximum horizontal stress directions in Northwestern Europe, based on various parameters as listed in legend. A NW-SE orientation of stress in the region of the Lower Rhine Embayment can be recognized (Reinecker et al. (2003)).

4.3.2 Local Stress Regime

The local stress regime in the study area, the Lower Rhine Embayment, has been investigated by various authors (e.g. Grünthal and Stromeyer (1992, 1994); van den Berg (1994); van den Berg et al. (1994); Plenefisch and Bonjer (1994, 1997); Hinzen (2003); Worum et al. (2005)) using so different approaches as syn-sedimentation rates, digital elevation data, focal mechanism of local earthquakes and finite element modeling. These studies suggest that the local stress field in the Lower Rhine Embayment is controlled by at least three intra-plate stress fields and their interaction. These stresses are originated by the subsiding North Sea basin, the continent-continent collision along the Alpine front and the Ardennes compression. The maximum compressional stress field in the Lower Rhine Embayment is oriented NW-SE resulting in an extension regime on the main faults bordering the tectonic units of the region.

Actual movements along these fault zones appear determined by the history of the individual faults. This becomes especially clear comparing the inactive fault zones in the West Netherlands Basin and the active faulting along structures in the adjacent Roer Valley Rift System. Estimates of likelihood and mechanism of reactivation of preexisting faults incorporating their complete three-dimensional geometry constrain differences in the behavior of such structures in the associated regions (Worum et al. (2004, 2005)). Detailed investigations of focal mechanisms of local earthquakes led to consistent estimates on the stress tensors involved (Plenefisch and Bonjer (1997); Hinzen (2003)). In figure 4.9 results from both studies are compared. Both studies reveal a change in stress regime with depth associated with different stress tensors being present in upper and lower crust. However, this change appears opposite for the Upper and Lower Rhine Graben, suggesting a significantly different stress regime for these adjacent regions. The change can be explained by differences in rock composition and tectonic setting when the Upper Rhine Graben meets the Rhenish Massif. Whereas major directions of principal stresses are compatible in both parts of the Rhine rift system, magnitudes of the stress components may be altered by the buffering effect of the Rhenish Massif. Hinzen (2003) suggests that these findings can explain the ambiguity between extensional and strike slip regime that is found in this region.

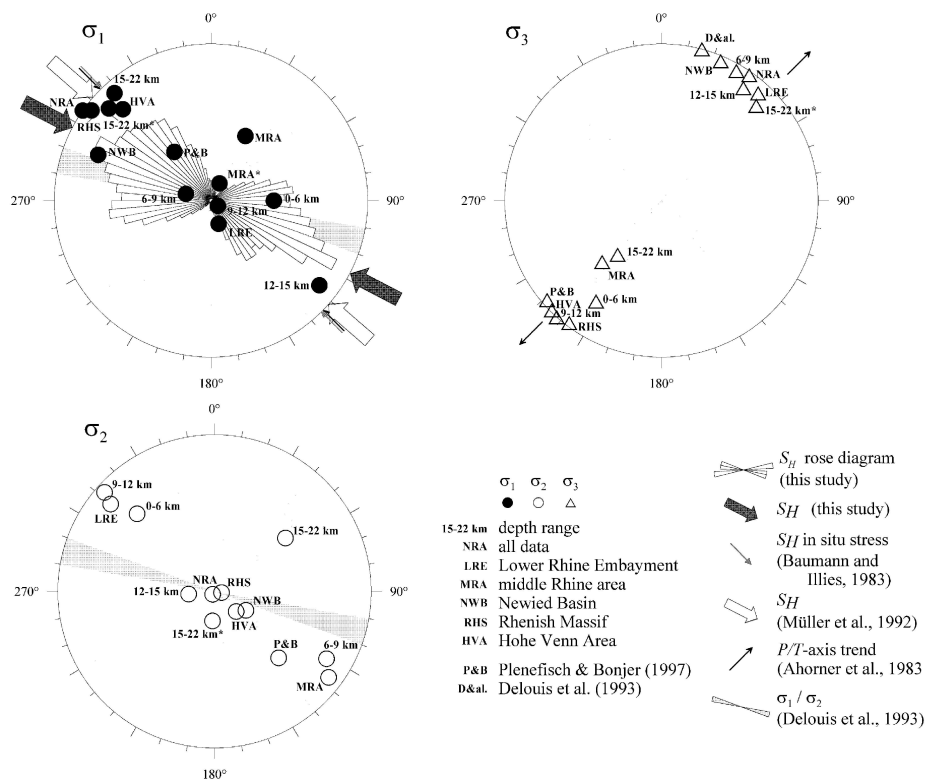


Figure 4.9: Directions of principal stresses in the region of the Lower Rhine Embayment from various studies (Hinzen (2003)).

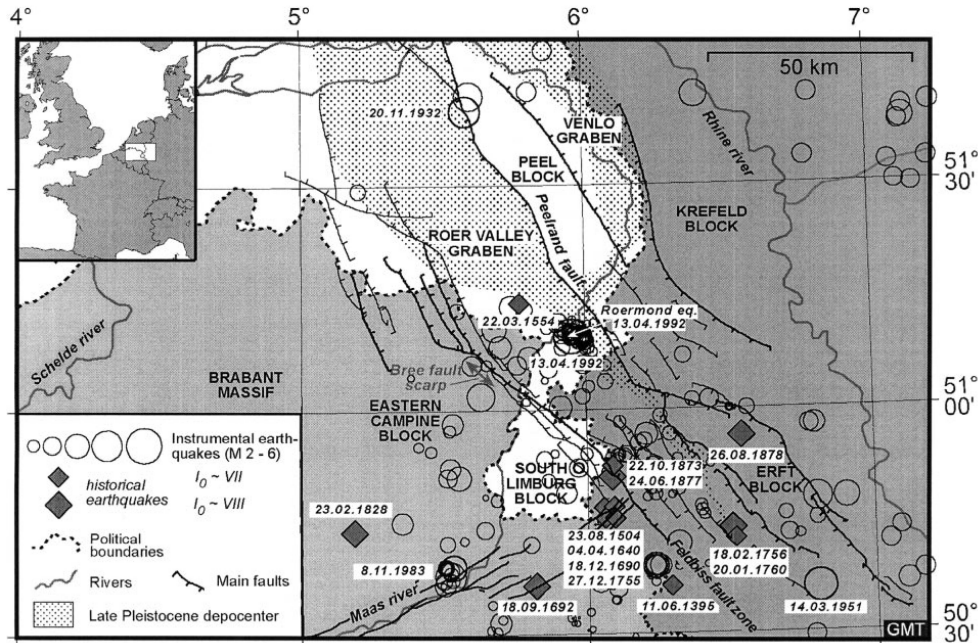


Figure 4.10: Epicentral locations for strong historical earthquakes (diamonds) and events during the 20th century (circles) in the Lower Rhine Embayment (Camelbeeck et al. (2000)).

4.4 Seismicity

From the discussion in previous sections it can be understood that the Lower Rhine Embayment is a region where active tectonics take place. The overall length of Quaternary faults in the basin amounts to more than 4000 km. Nevertheless it becomes clear that the amount of rifting is relatively small and its speed is slow compared to other rift systems. This results in a low to moderate seismicity, however with the potential of producing large earthquakes. Under conditions like these uncertainty in seismic hazard assessment is especially important as empirical observations are not sufficient in order to constrain the locations and characteristics of future earthquakes.

4.4.1 Paleoseismicity

From the work of Camelbeeck and Meghraoui (1998); Camelbeeck et al. (2000, 2001); Bommer et al. (2004) the return period of earthquakes with magnitudes between 6.2 and 6.7 is estimated as 10000 to 20000 years constrained over the last 50000 years. Assuming a similar possibility for all Quaternary faults within the Lower Rhine Embayment the recurrence period for large earthquakes can be estimated as 500 to 1000 years. These estimations are in consistence with investigations by Ahorner (1992).

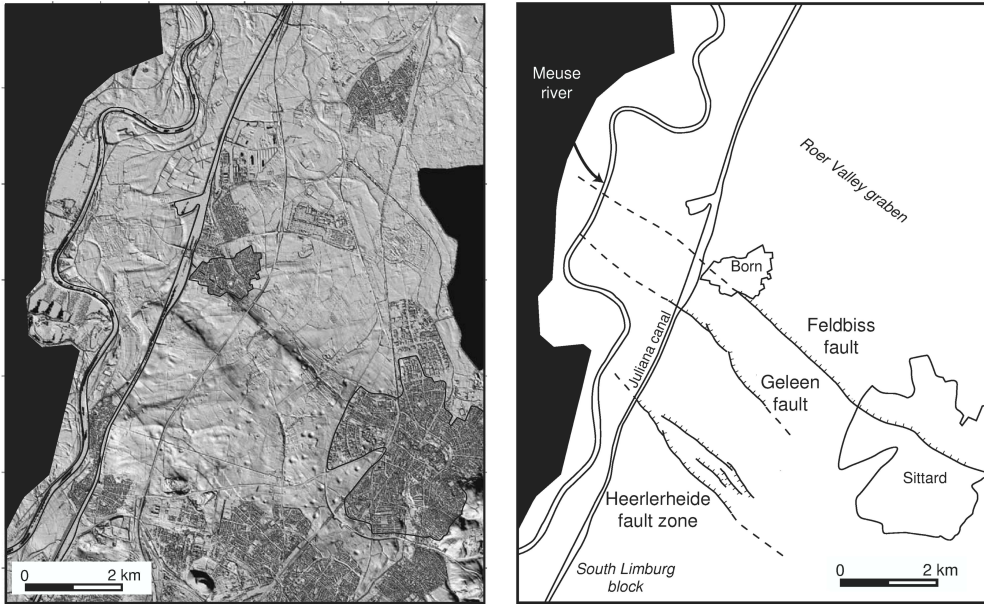


Figure 4.11: Location of the Feldbiss fault system with respect to the urban areas of Born and Sittard (Michon and van Balen (2005)).

4.4.2 Historical Earthquakes

Besides the above discussed studies on paleo-earthquakes for historical times area-wide records are available. For western Europe knowledge on reliable historical seismicity is limited to a time period of less than 700 years (e.g. Meidow (1994); Alexandre (1994)). Despite the generally considered low seismicity of the region the occurrence of at least three earthquakes with magnitudes 6.0 and greater is evident from such historical information. In figure 4.10 the distribution of historical earthquakes in the Lower Rhine Embayment and its vicinity is shown.

4.5 Urbanization and Seismic Hazard

Dense population and a high concentration of industry in the areas of northwest Europe put these regions at high risk from the occurrence of large earthquakes, although the present seismic activity appears low and destructive earthquakes are virtually unknown. Additionally, the occurrence of smaller earthquakes close to vulnerable cities and industrial habitats can result in significant damage. The dense agglomeration of both industry and private housing in the region of the Lower Rhine Embayment makes such a scenario likely. In figures 4.11 and 4.12 the location of two Netherland villages Sittard-Geleen and Uden in the vicinity to prominent tectonic faults is illustrated. In both cases the urban areas are dissected by major fault zones of the Roer Valley rift system which have shown seismic activity throughout recent times.

Assessment of seismic hazard in regions of low present day seismicity like northern Europe is evaluated on the basis of historically documented earthquakes and recently instrumentally recorded seismicity as discussed in previous section. Indications of rel-

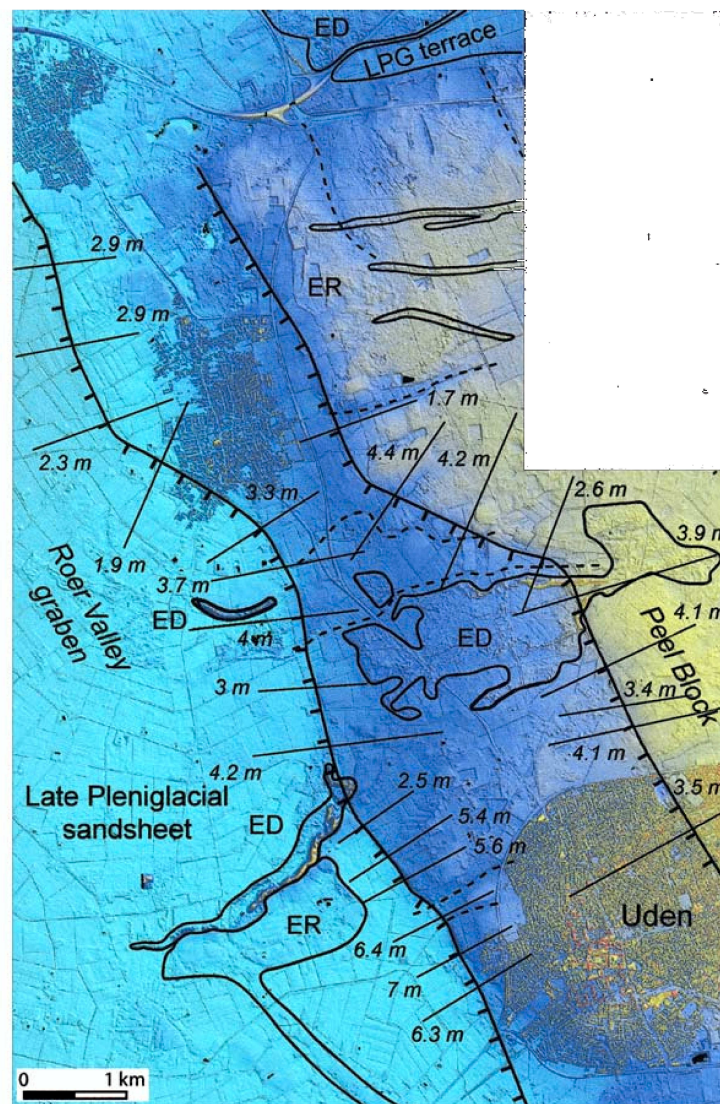


Figure 4.12: The town of Uden is located between the main and secondary fault of the Peel Boundary fault system (Michon and van Balen (2005)).

atively low levels of seismic hazard achieved by this approach lack the influence of the long-term potential for large earthquakes due to limited observation time. Enhancing the observation time into geological time scales by systematic evaluation of paleoseismicity can improve these estimations (Camelbeeck and Meghraoui (1998); Camelbeeck et al. (2001, 2000)). However, such investigations have to deal with a large number of uncertainties, including among others the identification of paleo events, estimation of their magnitude as well as possible incompleteness of the sedimentary record. Atakan et al. (2000) demonstrated the importance of systematic treatment on such uncertainties and presented an approach to account for this in the interpretation of paleoseismic data.

Commonly hazard levels achieved by probabilistic approaches are projected onto recurrence intervals or exceedance probabilities designed for individual building structures. Whereas this approach is adequate for most engineering projects problems arise in situations where extremely low levels of annual exceedance must be considered. Considering exceedance levels as low as $10^{-7} - 10^{-8}$ for the case of nuclear waste deposits has led to unphysically high levels of ground motion estimates (Corradini (2003)). Missing definition of upper limits on ground motions leads to erroneous assumption of maximum ground motion (Bommer et al. (2004)). Incorporating physically reasonable upper limits on earthquake ground motion, which can be achieved by properly designed deterministic simulations results can solve this problem. Prediction of the longterm seismic hazard in regions alike the Lower Rhine Embayment with long recurrence intervals for large earthquakes and only a limited number of observations for intermediate sized events require special treatment. An integrated approach incorporating experts of various fields is suggested (MGuire (1994); Rosenhauer and Ahorner (1994); van Eck and Davenport (1994)). The geographical location of the Lower Rhine Embayment sprawling across the borders of three European countries emphasizes the importance of international exchange of seismological data (Dost and Sleeman (1994); Haak (1994); Davenport (1994)). Incorporating new approaches and technologies in seismic hazard assessment will help improving the situation (Chen et al. (2004); Bouwkamp (1994)).

Chapter 5

Simulations of three Earthquake Scenarios in the Lower Rhine Embayment - Achievements with Improved Setups

Simulations for three earthquake scenarios presented in Ewald (2001) were repeated with improved settings in terms of model and discretization parameters. Results from these new simulations are published in Ewald et al. (2005). In this chapter a comparison of the main findings from both simulations is carried out.

5.1 Motivation

In Ewald (2001) a pilot study of basin related effects on strong ground motion in the Lower Rhine Embayment, Germany, was carried out. Elastic finite difference simulations using moment tensor point source approximations were used to study this issue. Three historical earthquake scenarios were chosen in order to study basin effects with respect to source location. The basin was represented by the most simple model consisting of a three-dimensional homogeneous sedimentary structure embedded by homogeneous bedrock. Model and source parameters as well as computational aspects are discussed in more detail below. Despite the simplified approach these simulations revealed a number of significant results:

1. Strong amplification of ground motion by the basin was observable for all scenarios.
2. Comparison of the individual scenarios showed clear sensitivity of the effects due to epicentral location.
3. In the limits of observables the results emphasized the ability of finite difference simulations in reproducing realistic ground motions in the presence of complex stratigraphy.

Reviews of this work as well as the experience from simulations of the 2002 Alsdorf earthquake presented in chapter 6 raised the question of possible improvements of the results using a more realistic basin model and an advanced simulation approach incorporating an extended source and viscoelastic attenuation. Further developments of the finite difference code described in chapter 3 as well as a improved model made it possible to carry out a new set of simulations including the above mentioned complexities and compare the results to the ones achieved by the simple-most approach. Whereas the individual effects of finite source and attenuation are discussed in detail for the magnitude 4.9 Alsdorf earthquake in chapter 6 the scope of this chapter is a broader view of differential effects adapted to the limited observational data. In the following input parameters as well as results associated with the simplified simulations are denoted as setup I, whereas the corresponding quantities of the more sophisticated simulations are referred to as setup II.

5.2 Different Setups

5.2.1 Computational Parameters

Along with improvements of the code, increased computational resources allowed the usage of an improved model representation in terms of discretization. Differences in computational parameters for setup I and II are discussed briefly in the following.

Horizontal resolution Horizontal resolution of the three-dimensional velocity model increased from 200 m to 100 m. This results in a better and smoother representation of the sedimentary basin edges. As discussed below the lowest shear wave velocity used in the model was reduced from 1400 m/s to 1000 m/s. It is noteworthy that the lowest velocity was not reduced to half of the original value as it would have been possible from the denser grid spacing. At the same time the target frequency was kept at 1 Hertz. Assuming a surface wave speed of 90 % the shear wave velocity the new setup samples surface waves with a minimum of about 9 points per wavelength (at target frequency) whereas the old simulations were carried out with a sampling of about 6 points.

In most finite difference studies concerning wave propagation at local to regional scale, involving wave propagation distances of tens to several hundreds of kilometers, a sampling of 5 points per wavelength is concerned to be sufficient in order to avoid numerical dispersion and amplitude errors. It can be found from verification that a number of 5 points per wave length at the dominant period is just at boundary between the steep part of a error versus grid spacing relation and the flat part where no significant improvement in terms of accuracy can be expected at reasonable increased computational cost. From denser sampling up to about 10 points a distinct improvement can be expected with reasonable effort.

Vertical resolution The most fundamental improvement between the two setups as for model representation concerns vertical resolution. Whereas with setup I this parameter was 200 m alike the sampling in horizontal directions, setup II has a vertical

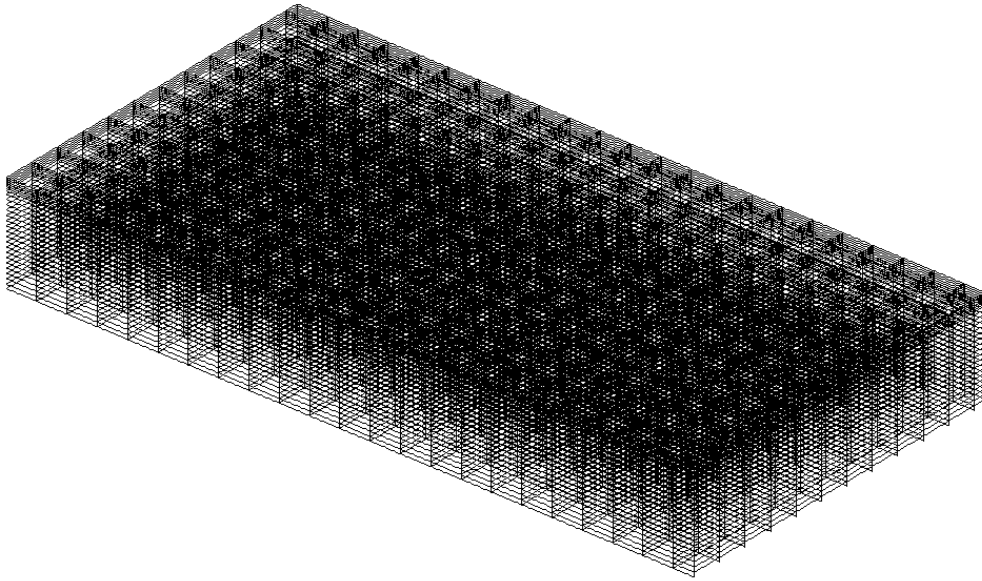


Figure 5.1: Grid representation for the new simulations. Vertical spacing increases from 50 m at the top of the model where low velocities are present, to 120 m at the bottom. For clarity reasons only every 5th grid line in horizontal direction is shown.

grid sampling of 50 m and therefore a four times denser resolution of sedimentary basin depths. A better representation of basin topography is achieved and more details of the wavefield effects should be revealed. To make this goal achievable within the limits of computational resources a varying grid spacing is used, ranging from 120 m at the bottom covering the whole range of about 20 km bedrock layers to the mentioned 50 m within the sedimentary part of the model and its surroundings. Technical aspects of this method are discussed in chapter 3. An example of the possible savings in terms of both memory and computation time can also be found in that section. Figure 5.1 illustrates the resulting grid as it was used in this study. Due to the limited graphical resolution only every twelfth grid line is shown in this plot.

It is noteworthy that the grid stretching algorithm can be applied in the other two directions, the horizontal directions x and y , in a straightforward way. Adapted to special requirements for basin simulation it is carried out only in the vertical direction where the potential of savings overwhelms the additional computation cost significantly.

Temporal discretization According to the stability criterion in finite difference simulations temporal discretization by means of time step is determined by the choice of spatial discretization by means of grid sampling and the velocities applied to the model. It is notable that the use of a fine mesh in the top layers does not necessarily lead to a proportionally smaller time step. In the setup used in this study vertically increasing velocities are applied to the bedrock representation. Therefore the highest velocities are not present at the same location as the smallest grid cells.

Absorbing boundaries The reduction of artificial reflections from the model boundaries is a general problem in numerical simulations. The Cerjan type boundaries used in the old simulations were replaced by absorbing boundaries following the approach of perfectly matched layers (PML) as described in section 3.7 in order to circumvent their main drawbacks. One drawback of the Cerjan type absorbing boundaries is the frequency dependent degree of efficiency of this method. Practically this leads to remaining reflections of the low frequency part of the wavefield. Whereas this could be tolerated for the point source approximations with very limited long period content, for finite source simulations the use of frequency independent boundary conditions becomes inevitable. The PML approach which has become popular in the seismic community in recent years provides this capability. The width of absorbing layers necessary for efficient suppression of artificial reflections is another important issue. Cerjan type boundaries work well when a width of more than 40 grid points is used. In the setup I simulations a value of 50 grid points was chosen. PML boundaries provide a better absorption for all frequencies at a width of only 20 points. Consequently, this leads to an improved ratio of computational (including the absorbing margins) to physical (without boundaries) model space. Comparing setup I and setup II with respect to this quantity demonstrates a significant improvement achieved with PML boundaries. The usage of Cerjan type absorbing boundaries inflated the model space in the old simulations from 84,000,000 grid points (physical model) to a computational model with 144,000,000 grid points. Thus, only 58.3 percent of the model were actually used for the physical model, whereas nearly half of the model was wasted in absorbing margins. With the PML boundaries a computational model space consisting of 417,000,000 grid points is necessary in order to discretize the physical model into 352,800,000 cells. The ratio of physical to computational points is 84.6 percent. Usage of resources on the reduction of artificial reflections has been reduced to about 15 percent.

Memory Despite the above discussed improvements on the code simulations using setup II require significantly larger amount of core memory than it was the case with the setup I. In fact, memory consumption is increased by a factor of about 4.5. Additional memory is necessary for three reasons. First, the number of grid points has been increased nearly threefold. Second, the memory variables necessary for the implementation of viscoelasticity are costly. The third additional field variables that must be held are the ones containing the derivative operator weights for the nonuniform grid layout. In total about 110 Gigabyte of core memory were necessary to describe the model and wavefield in the simulations with setup II. 32 nodes of the Hitachi SR8000 were used to carry out the simulations.

Computation time Using the above mentioned 32 nodes the calculation time was kept at 12 h. That means roughly only 4 times the CPU time of the setup I simulations was necessary. It is noteworthy that floating point performance was increased by a factor of 3.5 between different versions of the code. The increase in performance is mainly due to optimization of computation loops. The setup II simulations were carried out on the Hitachi SR8000 with a performance of roughly 17 percent of the theoretical peak performance.

Table 5.1: Comparison of computational parameters for the different simulation setups.

Parameter	Setup I	Setup II
Horizontal Discretization	200 m	100 m
Vertical Discretization	200 m	50 - 120 m
Time Step	0.0198 s	0.0035 s
Lowest S-wave velocity	1400	1000
Grid Size (physical model)	700×800×150	1404×1404 × 180
Grid Size (computational model)	800×900×200	1444×1444×200
Number of Time Steps	3034	16960
Simulation Time	60 s	60 s
Required Core Memory	24 GB	110 GB
Computation Time	12 h × 8 nodes	12 hours × 32 nodes

Table 5.2: Comparison of model parameters used in the different simulation setups.

Parameter	Setup I	Setup II
Sedimentary structure		
Model type	homogeneous	velocity gradient
S-wave velocity	1400 m/s	1000 - 1950 m/s
P-wave velocity	2425 m/s	1732 - 3377 m/s
Density	2200 kg/m ³	2200 kg/m ³
Bedrock		
Model type	homogeneous	layered
P-wave velocity	5000 m/s	5500 - 8000 m/s
S-wave velocity	2890 m/s	3175 - 4620 m/s
Density	3000 kg/m ³	3000 kg/m ³

Summary Above discussion gives an impression of the additional effort put into the new simulation setup. It is noteworthy that this effort was not put into higher frequency content, but into a better model representation and resolution. Simulation results using setup II should be comparable to the ones achieved with setup I and reveal how improvements on the model side affect the results. Table 5.1 gives an overview of old and new computational parameters.

5.2.2 Parameterization of Media and Source

In the section above differences in the two setups were described from a computational point of view. In this section physical model parameters are discussed. Table 5.2 summarizes a comparison of model parameters used in setup I and II.

The setup I velocity model was the simple-most three-dimensional model that can be constructed with the available data. It consists of a homogeneous sedimentary basin with a complex three-dimensional shape and topography investigated in various studies (e.g. Scherbaum et al. (2003); Hinzen et al. (2004)). This structure is surrounded

by homogenous bedrock. Both domains are modeled under the assumption of full elasticity. Consequently, the velocity model is afflicted with significant shortcomings which are briefly listed below.

1. The assumption of homogenous bedrock does not account for correct wave paths and therefore affect the incidence angle of waves entering the basin. Amplitudes and waveforms within the basin and in its vicinity can be affected.
2. P-wave velocities within bedrock are assumed too low in the setup I model. This is resulting in erroneous travel times and wrong predictions of basin response due to an underestimated velocity contrast between bedrock and sediments.
3. A homogenous sedimentary layer does not reproduce correct wave propagation within the basin. Furthermore depth dependent variations in the velocity contrasts at the interface between sediment and bedrock are neglected.
4. Sediment velocities, especially for shear and surface waves are considered too high in the setup I model.
5. Setup I does not account for viscoelastic attenuation. The basin effect consists of an amplification due to low velocities and focusing and a counteracting deamplification due to low quality factors within the sediments. The elastic simulations account only for the amplifying part.
6. The usage of a point source approximation for earthquakes of the size of the simulated scenarios appears not appropriate.

In the following paragraphs it is discussed in detail, how the new model accomplishes these shortcomings.

Velocity Model Bedrock is modeled as a layered medium with velocities ranging from 5.5 km/s to 8.0 km/s for the P-wave velocities. Associated shear wave velocities are derived using a V_P/V_S ratio of $\sqrt{3}$. The sedimentary basin is represented as three-dimensional structure with a depth depending velocity constructed according the formula:

$$V_S = 118 * (z + 1)^{0.37}$$

(Parolai et al. (2002)).

Computational limitations enforce a lowest velocity of about 1 km/s. The velocity versus depth function imposed by the given formula is therefore truncated at this value and velocities for the shallower part of the model are kept the same. Numerous studies have investigated the velocity structure in the Cologne Basin in recent years (e.g. Scherbaum et al. (2003); Hinzen et al. (2004); Ohrnberger et al. (2004); Parolai et al. (2005)). There is accordance among the various researchers that sedimentary layers show increasing velocities with depth. The reason being both increasing age and cumulative pressure of the overlying layers resulting in higher compaction of the sediments (Faust (1950)). Whereas this general behavior has been broadly accepted (Budny (1984)), the individual parameters determining the velocity versus depth relation are still a matter of debate. For the Cologne basin several models have been

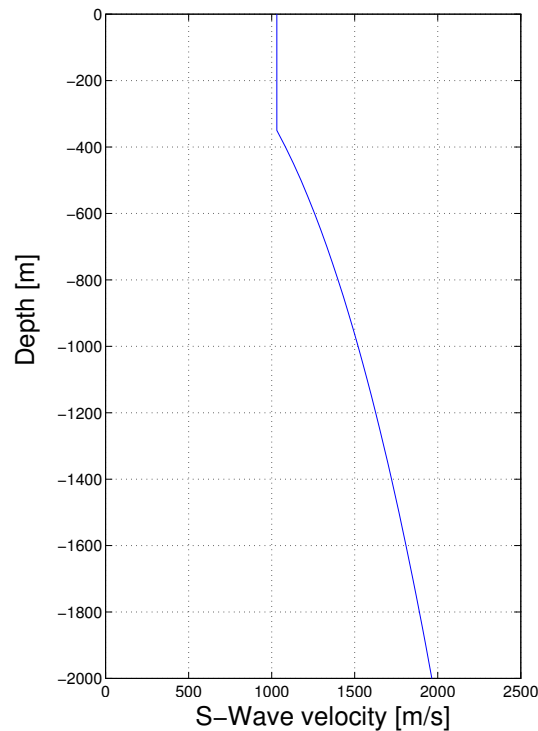


Figure 5.2: S-wave velocity vs. depth relation used for the sedimentary basin structure in this work (Parolai et al. (2002)).

proposed throughout the years. Recent investigations suggest significantly lower seismic velocities including a slower increase of shear wave velocity with depth (Hinzen et al. (2004); Scherbaum et al. (2003)) than it was commonly assumed beforehand (Parolai et al. (2002)). In this study a model incorporating relatively high velocities is preferred, as it meets the computational demands. The significant aspect of a vertical velocity gradient could be modeled using the relations given by Parolai et al. (2002). Figure 5.2 illustrates the shear wave velocity versus depth function used in this model. P wave velocities were derived assuming a V_P/V_S ratio of $\sqrt{3}$.

Increased complexity in the basin representation of setup II should allow the modeling of a number of important effects more realistically as it was the case with setup I:

1. Travel times in general and especially the time between P and S-wave onsets should be improved.
2. The use of a velocity gradient inside the basin and a layered background model leads to more realistic velocity contrasts between bedrock and sediments. Consequently, reflection coefficients at the interface between bedrock and sediments should be more realistic and the same applies to energy partitioning of reflected and transmitted waves.
3. Velocity gradient in the sediments leads to more complex wave paths for multiple reflections within the basin. Resonant shaking should be modeled more realistically.

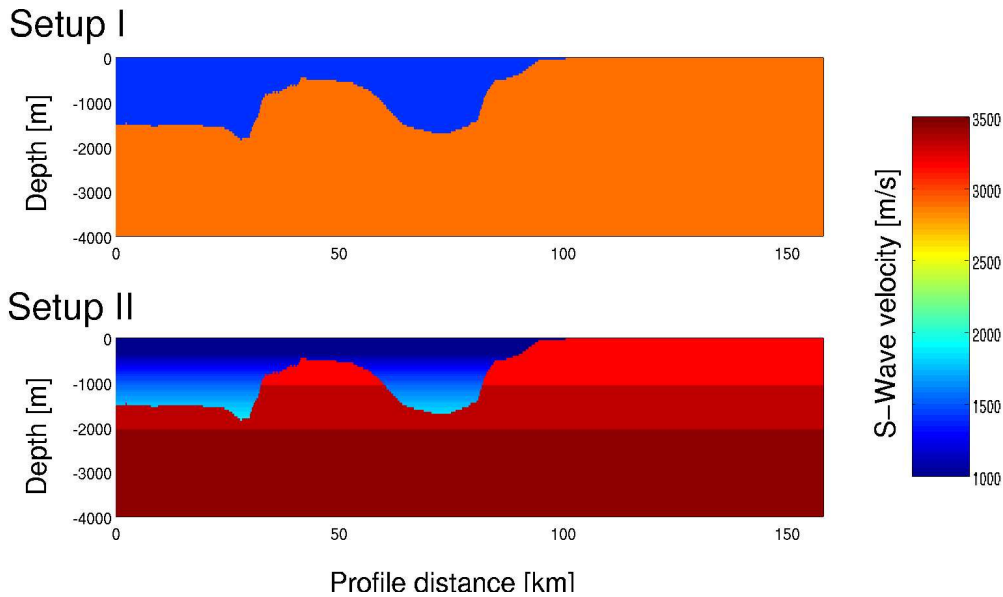


Figure 5.3: Shear wave velocity profiles for two model representations along the receiver line A - A' (see figure 5.4). Setup I: Homogeneous sediments embedded by homogeneous bedrock model, setup II: Sedimentary structure with velocity gradient embedded by layered bedrock model.

Figure 5.2 shows collocated crosssections through the basin model from the old and new simulations. This comparison demonstrates the increase in model complexity between the two setups. Comparing the crosssections with seismic lines and their geological interpretation from chapter 4 it can be understood that introducing this kind of complexity leads to a more realistic representation of the geologic structures. Nevertheless, comparing geological and model crosssections also reveals a number of distinct features with potential influence on propagating waves the model is still missing. The most obvious ones are:

1. Sediment velocities in the model are derived with a vertical gradient. Therefore there are no horizontal contrasts or gradients involved.
2. No reflectors are present within the sedimentary layer.
3. Especially inclined layers in the sediment structure would have a strong impact on wave propagation. For above discussed reasons the model is lacking such features.

The model representation used in this study, including velocity gradients in the sediment structure and layered background velocities is a large improvement compared to the simple basin model. Nevertheless, the simulation of wave propagation in the Cologne Basin would certainly gain from the construction of a real three-dimensional velocity model like the SCEC model for Southern California.

Attenuation Realistic basin effects on strong ground motion consists of two counteracting parts: An amplification due to low velocities and geometrical focusing and a deamplification effect due to the high attenuation or low quality factors within sediments. Simulations carried out under the assumption of full elasticity only account for the amplifying effect, whereas deamplification due to viscous damping is neglected. To include these effects viscoelastic behavior was implemented using the standard-linear-solid approach described in detail in section 3.3.3. For the sediments a uniform quality factor $Q_S = 50$ for shear waves and $Q_P = 100$ for P waves was used, whereas for bedrock material elastic behavior is assumed. Considering realistic quality factors for bedrock this is a valid assumption for distance ranges of tens to few hundreds of kilometers as it is the case in this study. Whereas the influence of viscoelasticity on amplitudes and waveforms is discussed in detail in chapter 6, results presented in this chapter are on a more qualitative level.

Finite Sources Previous paragraphs covered improved modeling setup concerning media and computational discretization. Another shortcoming of the simulations carried out with setup I consists in the usage of a point source approximation. It can be supposed that this results in an overestimation of peak amplitudes close to the epicenter and an overpredicted attenuation relation with epidistance. An extended source model of appropriate size is assumed inevitable in order to accurately model these features. Consequently, in the setup II simulations earthquake scenario sources were modeled as circular finite sources with source radii derived from a Brune model using an assumed stress drop of 10 bar. Details on the technical implementation are presented in chapter 3. Table 5.3 lists source radii for the individual scenarios among other parameters.

5.3 Scenarios

To examine the site effects of the sedimentary basin three historical earthquake scenarios were chosen for the simulations with respect to their location near the Lower Rhine Embayment.

5.3.1 Düren

The Düren earthquakes of December 27, 1755 and February 18, 1756 ($I_0 = \text{VIII}$, $M_L = 6.1$, $M_K = 5.5$) occurred 10 km south-west of the town of Düren between the Lower Rhine Embayment and the Hohes Venn. Their epicenters are lying close to each other and are most probably correlated with the active Feldbiss fault system, one of the south-western border faults of the Roer Valley Graben (Meidow (1994)). The earthquake of 1756, which is chosen as scenario in this study, is the strongest event in the region known from historical records.

5.3.2 Euskirchen

The Euskirchen earthquake of March 14, 1951 is located at the western border of the Lower Rhine Embayment near the town of Euskirchen. Local magnitude for the Euskirchen earthquake is $M_L = 5.7$, whereas the Karnage Magnitude is $M_K = 5.1$. The maximum observed intensities are reported to be as high as VII-VIII. The source mechanism is normal faulting on the Roer graben fault system (e.g. Hinzen and Oemisch (2001)).

5.3.3 Roermond

On April 13, 1992 the Lower Rhine Embayment experienced a moderate intraplate earthquake. The main shock occurred at 01:20:02,8 UT with the epicenter located about 5 km southwest of the Dutch town of Roermond. The hypocenter was located at a depth of approximately 15 km at the Peel Boundary fault. It was preceded about 0.2 seconds by a foreshock of local magnitude $M_L = 4.8$. The local magnitude of the mainshock was about 5.9. With this magnitude it ranges among the strongest events observed during historical time in Central Europe and especially the Lower Rhine Embayment. The earthquake was felt in large parts of Germany, Belgium, the Netherlands and France. It was subject to intensive investigations from various authors (e.g. Gariel et al. (1994); Luger et al. (1994); Meidow and Ahorner (1994); Pappin et al. (1994); Pelzing (1994)). The Roermond earthquake was a normal dip-slip event. This source mechanism fits well into the discussed tectonic model of the Roer Valley Graben, depicting a NE-SW tension with active rifting of the graben. Still, intraplate dip-slip events are rare and the estimated 70 degree dip for an intraplate earthquake in the lower crust is remarkably steep (Jackson and White (1989); Camelbeeck et al. (1994)). The return period for an event of magnitude $M_L = 5.8 - 5.9$ in the Roer Valley Graben is about 200 years. Therefore the Roermond earthquake of 1992 must be considered as a large event for this region (de Crook (1994)).

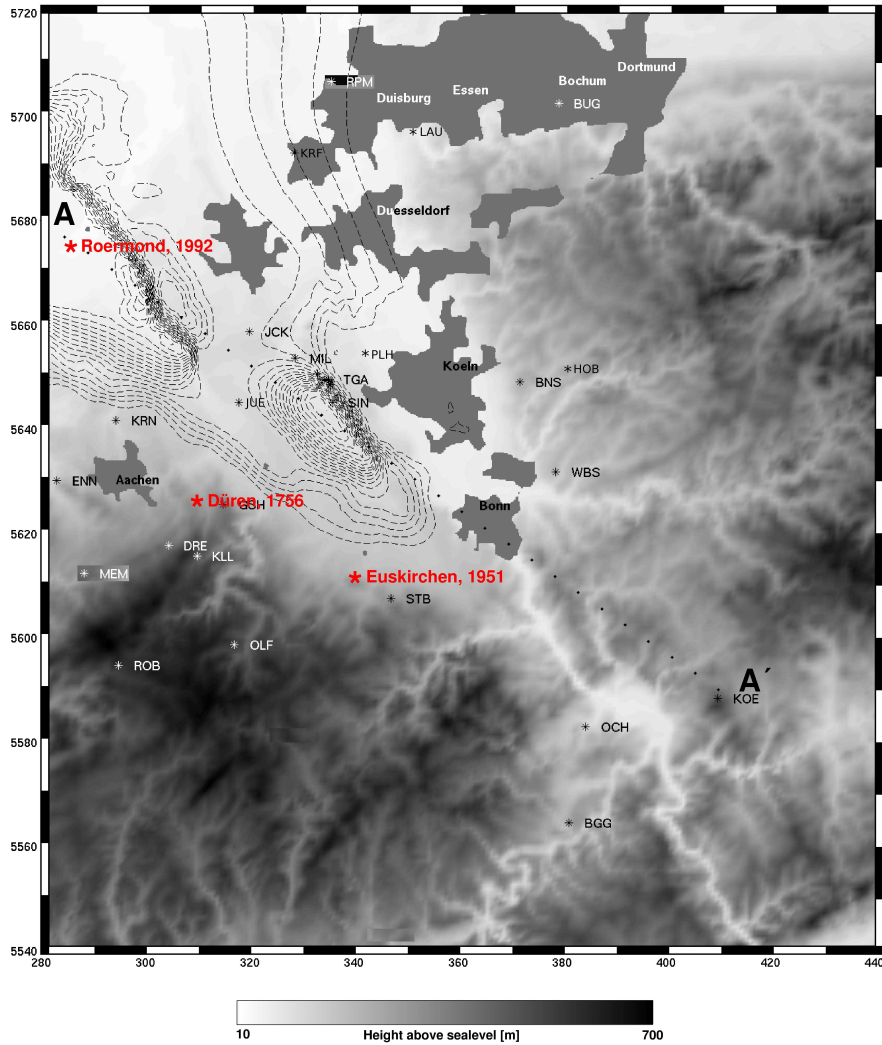


Figure 5.4: Detailed map of the study area. Dimensions and directions are given by UTM coordinates based on sector 32 U. Red stars indicate epicenters of the simulated earthquakes. Grayscale shading depicts regional topography whereas urban areas are colored in dark gray. The sedimentary basin depth is indicated by dashed isolines in 100 m intervals. The basin reaches a maximum depth of about 1900 m. Seismic network stations are marked as stars and by their station codes. A synthetic profile A-A' with 30 receivers is shown as black dots.

Table 5.3: Source parameters for the three scenarios.

	Düren	Euskirchen	Roermond
Latitude	50°45'	50°38'	51°10'
Longitude	6°21'	6°44'	5°56'
Depth	14 km	9 km	17 km
Strike	135°	110°	120°
Dip	70°	80°	70°
Rake	270°	270°	260°
Rise Time	1.0 s	1.0 s	1.0 s
Seismic Moment	14.0*10 ¹⁶ Nm	3.7*10 ¹⁶ Nm	7.5*10 ¹⁶ Nm
Radius (Setup II)	3900 m	2500 m	3200 m

5.3.4 Summary of Source Parameters

Summarized source parameters for the three simulated events of this chapter are compiled in 5.3. Values in row “Source Radius” are only valid for the simulations carried out using finite sources. Simulations with setup I are carried out using a point source approximation.

5.4 Results

Numerical simulations of seismic wave propagation account for production of the complete three dimensional wave field in complex heterogeneous structures. This leads to an enormous amount of data to be stored. Using a set of predefined wavefield parameters designed for answering specific questions make it possible to reduce requirements in terms of data storage dramatically. In the following subsections numerous key parameters are studied for the above described three earthquake scenarios with special emphasize to the different results from simple and more complex simulations.

5.4.1 Snapshots

In figures 5.5 and 5.6 snapshots of the East-West component of ground motion are shown for simulations based on setup I and setup II respectively. The wavefield is sampled at times 6, 14, 22, 30 and 38 seconds corresponding to individual rows in the plot and for the three scenarios Düren, Euskirchen and Roermond corresponding to individual columns. Each snapshot is individually scaled due to the different magnitude and scaling relation of the events. Snapshots of ground motion give a first glance of the complexity of the wavefield in the presence of a highly heterogeneous medium. They also illustrate the usefulness of numerical simulation techniques in order to understand wavefield effects in the presence of complex structures. As discussed below numerous features visible in peak ground motion maps and seismograms can be understood in regard to their origin by studying the wavefield of the associated scenario simulation displayed in these snapshots. It must be kept in mind that the velocity models of the simulation setups differ. The effect of this difference for snapshots at later times is

easily understood. The waves are simply propagating faster outside the basin for the usage of setup II. For the first snapshots taken at 6 seconds the effect is more complex. The snapshot at the surface shows a slice of the three-dimensional radiation patterns of the different phases. Taking these slices at identical time but with the usage of different velocity models is similar to slices at different depth. As a result these snapshots can look quite different.

The most prominent feature in all snapshots is the strong influence of the basin on the wavefield, its amplitudes and duration of ground motion due to multiple reflections. Nevertheless the wavefield shows distinct differences for different epicentral locations with respect to the basin and a number of similarities as well as differences from old and new simulation results. Differences in snapshots concerning the frequency content can be correlated with the individual source radii assumed for the finite source representations of the three scenarios. A notable difference in wave propagation speed due to the different velocity models. Note that the new layered background model involves a minimal wave velocity at surface that is about 10 % higher than in the old simulations. Layered nature of the bedrock model lead to further complicity in waveforms. The decreased speed of the wavefronts traveling through the small deep part of the basin, distinctly observable for the Roermond scenario with waves passing first the large deep part and than traveling south-east hitting the next depression have a good representation in the seismogram sections shown in section 5.4.4. Some prominent details of the wavefield visible in figures 5.5 and 5.6 are individually described in the following.

Both old and new simulations of the Düren scenario produce diffraction and scattering of seismic waves inside the basin resulting in a complex and lasting wavefield within basin margins. Trapped energy and reverberations inside the basin can be observed for all scenarios, especially visible for the Roermond earthquake. Wave fronts crossing the deep parts of the basin reveal amplified ground motion due to focusing effects for the Düren earthquake. Amplified ground motion in the corresponding regions can be observed in the distribution of seismic intensity presented in section 5.4.2. For the Euskirchen scenario channeling of energy within shallower basin parts along the edges is present. This results in an elevated seismic intensity to be expected in these areas, as it is discussed in section 5.4.2. The results from the Düren scenario show for both old and new simulations diffracted energy from the area between the two basin depressions acting as a secondary source and producing longlasting reverberations also notable outside the basin. A prominent raise in basin topography located just east of the main basin depression, the so called Peel High, is clearly visible in the snapshots achieved with the new simulation setup. This feature appears not that significantly in the results from the old simulation setup. This point suggests the more accurate mapping of basin topography with increased resolution.

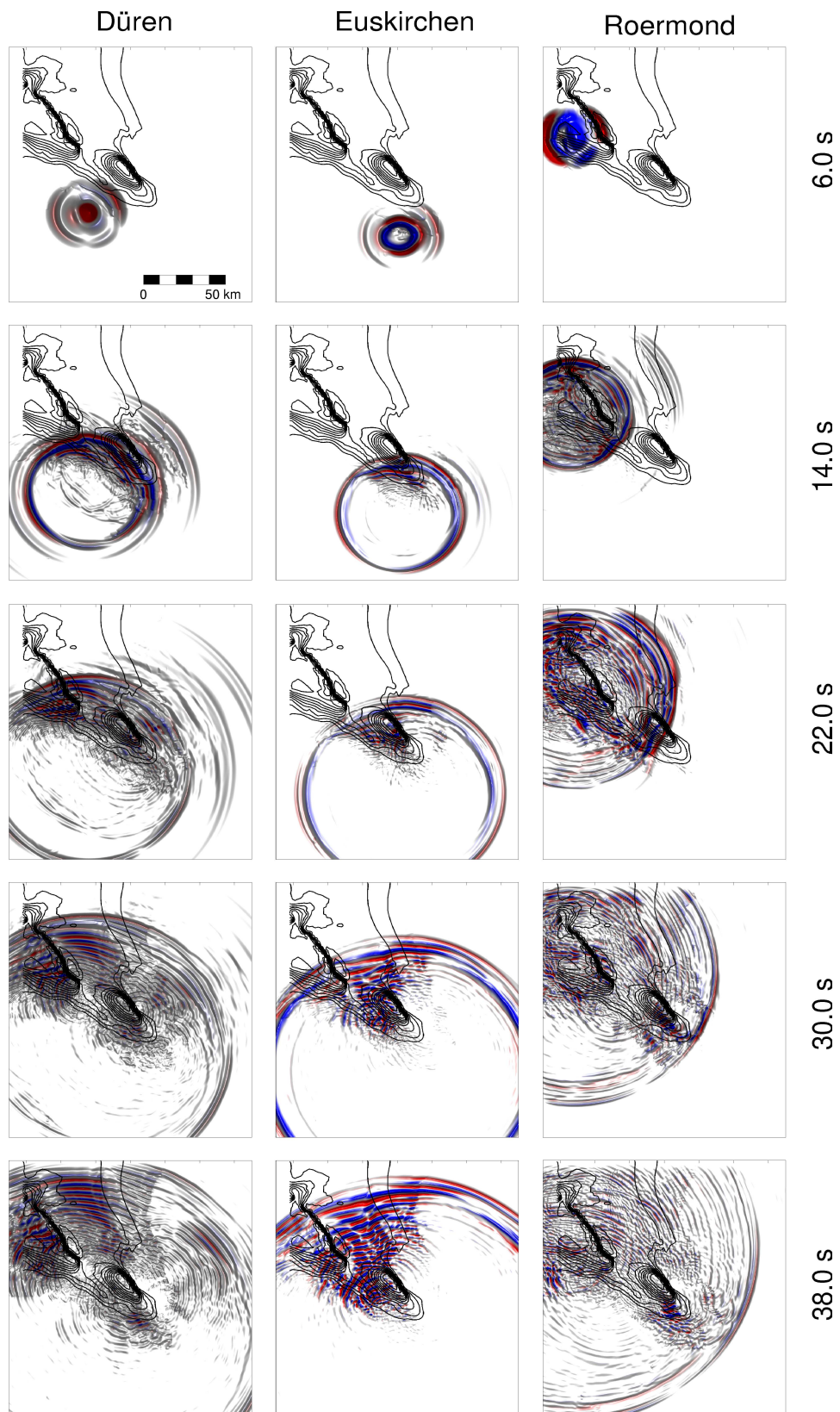


Figure 5.5: Snapshots of the East-West component ground velocity wavefield at the surface. Background contour plot indicates the depth of the sedimentary basin. Results from simulations using setup I.

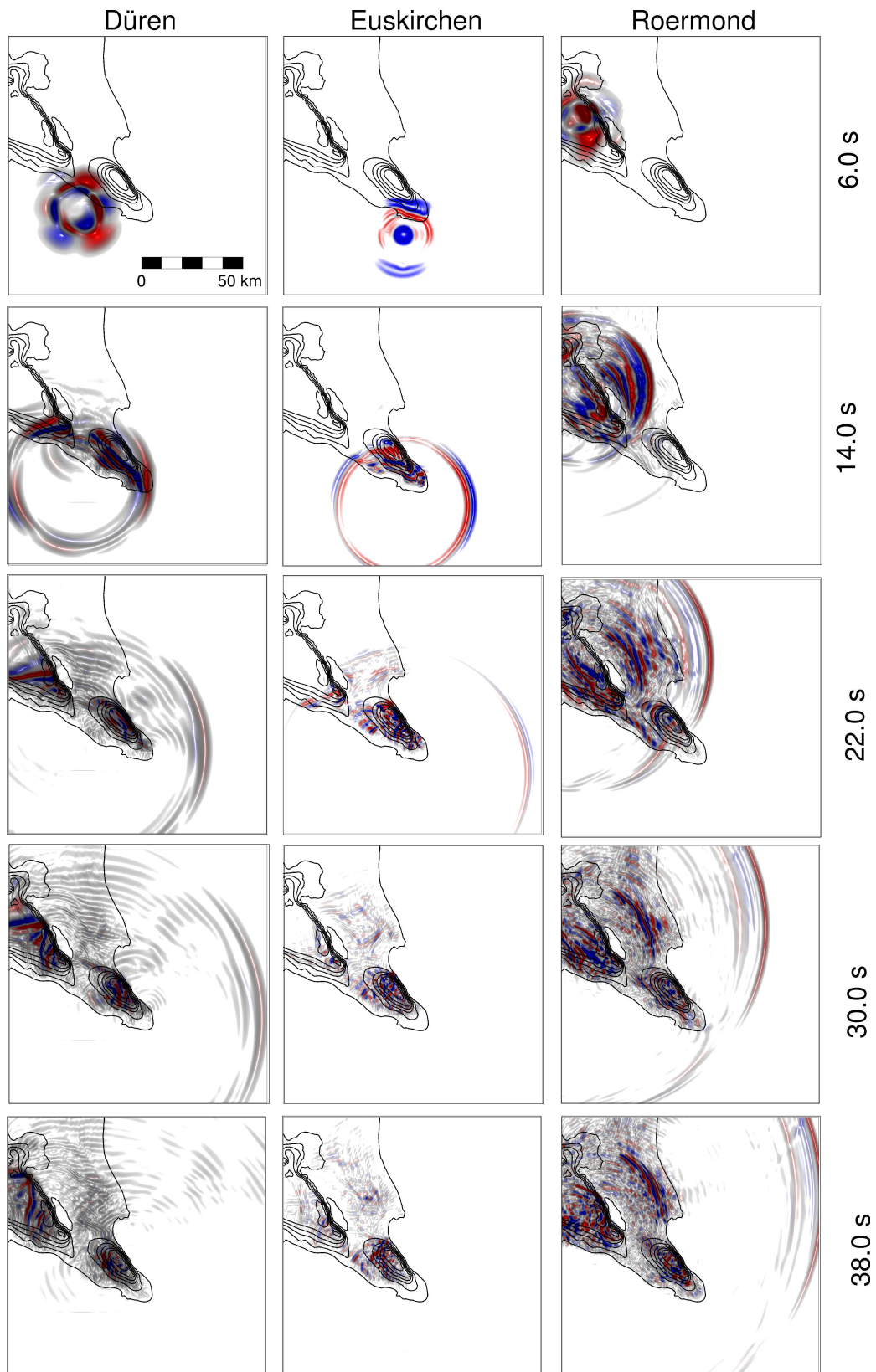


Figure 5.6: Snapshots of the East-West component ground velocity wavefield at the surface. Background contour plot indicates the depth of the sedimentary basin. Results from simulations using setup II.

5.4.2 Seismic Intensity

Numerical simulations allow an area-wide mapping of ground motion parameters such as peak ground velocity (PGV) over the whole model space. From such a PGV mapping actual values of seismic intensity can be derived and compared with observed intensities, as well as between different simulations. There are three main reasons for the usage of seismic intensity as a key parameter:

1. Seismic intensity is normally the only observable which is available area-wide, as strong motion seismometers are sparsely distributed in most areas. This accounts especially for past events, before digital seismometry was available. For historical earthquakes seismic intensity estimates from historical documents are the only source of ground motion parameters available.
2. Intensity values are derivable from simulation results by mapping peak ground motions and applying standard formulae. Estimates of seismic intensity achieved by that approach can be compared with observations. In future applications these estimations might be used in hazard assessment replacing the nowadays common estimations achieved by attenuation relations in probabilistic hazard assessment.
3. The logarithmic nature of intensity scales enables detecting key features of the ground motion distribution related to geological structures over a broad dynamic range of absolute ground motion values. It also allows a comparison of similar effects in earthquakes of different magnitudes.

The comparisons shown in this work are based on Modified Mercalli Intensity (I_{MM}) derived from Peak Ground Velocity according to the relations:

$$I_{MM} = 2.10 \log(PGV) + 3.40 \text{ for intensities below V, and}$$

$$I_{MM} = 3.47 \log(PGV) + 2.35 \text{ for intensities V and higher,}$$

where PGV is peak ground velocity given in cm/s (Wald et al. (1999)). It is noteworthy that intensities from the MSK scale are directly convertible in Modified Mercalli scale values within the interesting range (Murphy and O'Brien (1977)).

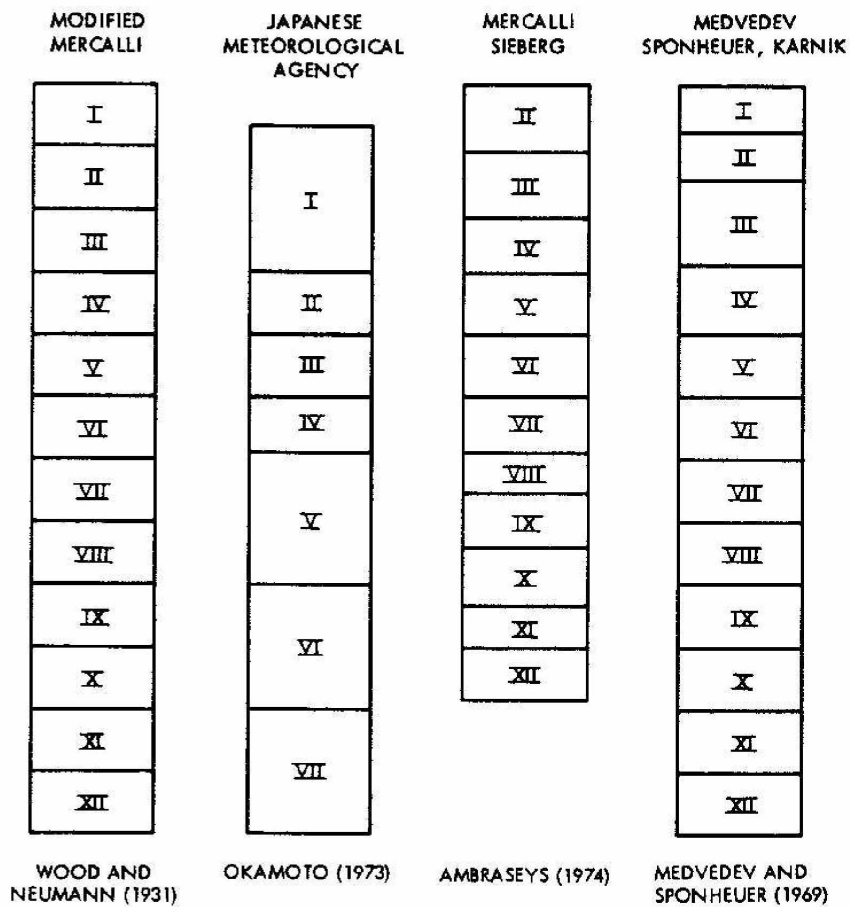


Figure 5.7: Comparison of commonly used seismic intensity scales. The MSK and Modified Mercalli scales are most commonly used for European earthquakes (after Murphy and O'Brien (1977)).

5.4.2.1 Düren 1756

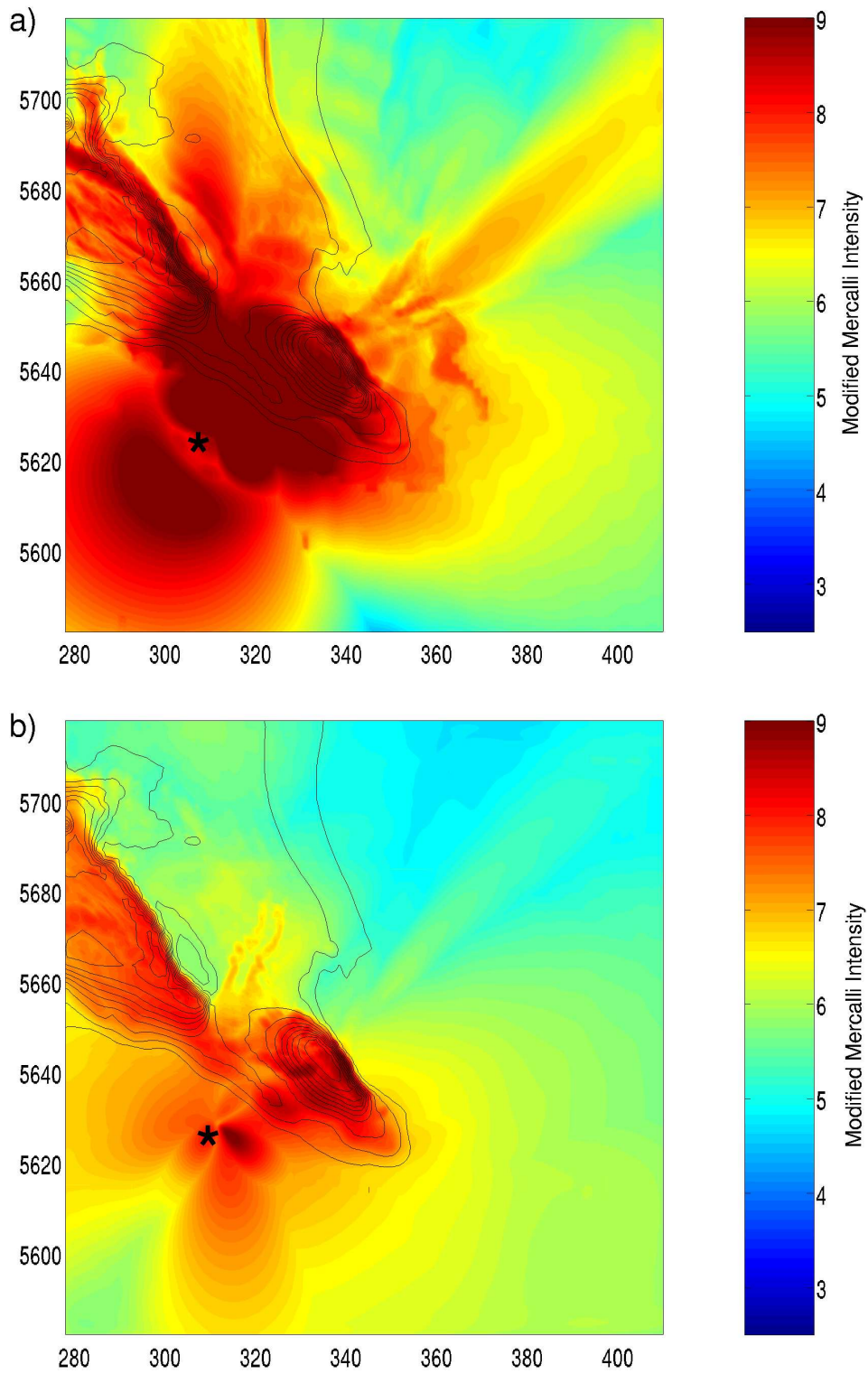


Figure 5.8: Modified Mercalli intensities for the magnitude 6.1 1756 Düren earthquake derived from simulation results using setup I (a) and setup II (b). Background contour plot indicates the depth of the sedimentary basin. Black star denotes epicentral location. Dimensions and directions are given by UTM coordinates based on sector 32 U.

With a local magnitude of 6.1 the Düren earthquake of 1756 was the strongest event in the Lower Rhine Embayment within the last 250 years. Epicentral peak intensities are estimated as VIII and above. Isoseismal radii are estimated from historical observations as 25 km for intensity VII, 55 km for intensity VI and 135 km for intensity V. In figure 5.8 Modified Mercalli intensities derived from peak ground velocities modeled using setup I and setup II respectively are mapped for the Düren 1756 earthquake. The main observations are analyzed in the following. Most prominently simulations using setup II result in significantly lower peak amplitudes and consequently degrees of seismic intensity. The expression of this effect is prominently visible in the track of amplified ground motion spreading towards north-east from the scattering center between the two basin depressions. Whereas it appears stronger for the setup I simulation results the effect can still be observed when setup II is used and can be considered as realistic. Amplified ground motion in this area is consistent with reported damage in the corresponding region. Diffracted energy that was clearly visible in snapshots in the subsection above has its signature as elevated intensity in the corresponding regions for both simulation setups. A main difference in the amplification pattern can be seen at the basin edge which acts as a boundary for amplified ground motion in presence of setup II whereas a large portion of energy is diffracted into the shallower part of the basin when setup I was used. As already discussed for the snapshots in section 5.4.1 this is due to the improved representation of the Peel High, the prominent elevation in basin topography bordering the large depression in the Northwest, with the denser model discretization. For both simulation setups a strong correlation of amplified ground motion with basin depth is observable. Additional amplification arises above the steeper basin edges. Artificial basin effect due to staircase features of the old basin representation is not visible in the simulations carried out with setup II. This feature, also visible in other scenarios clearly illustrates the improvements of the model discretization with a vertical spacing of 50 m leading to distinctly smoother basin shape.

5.4.2.2 Euskirchen 1951

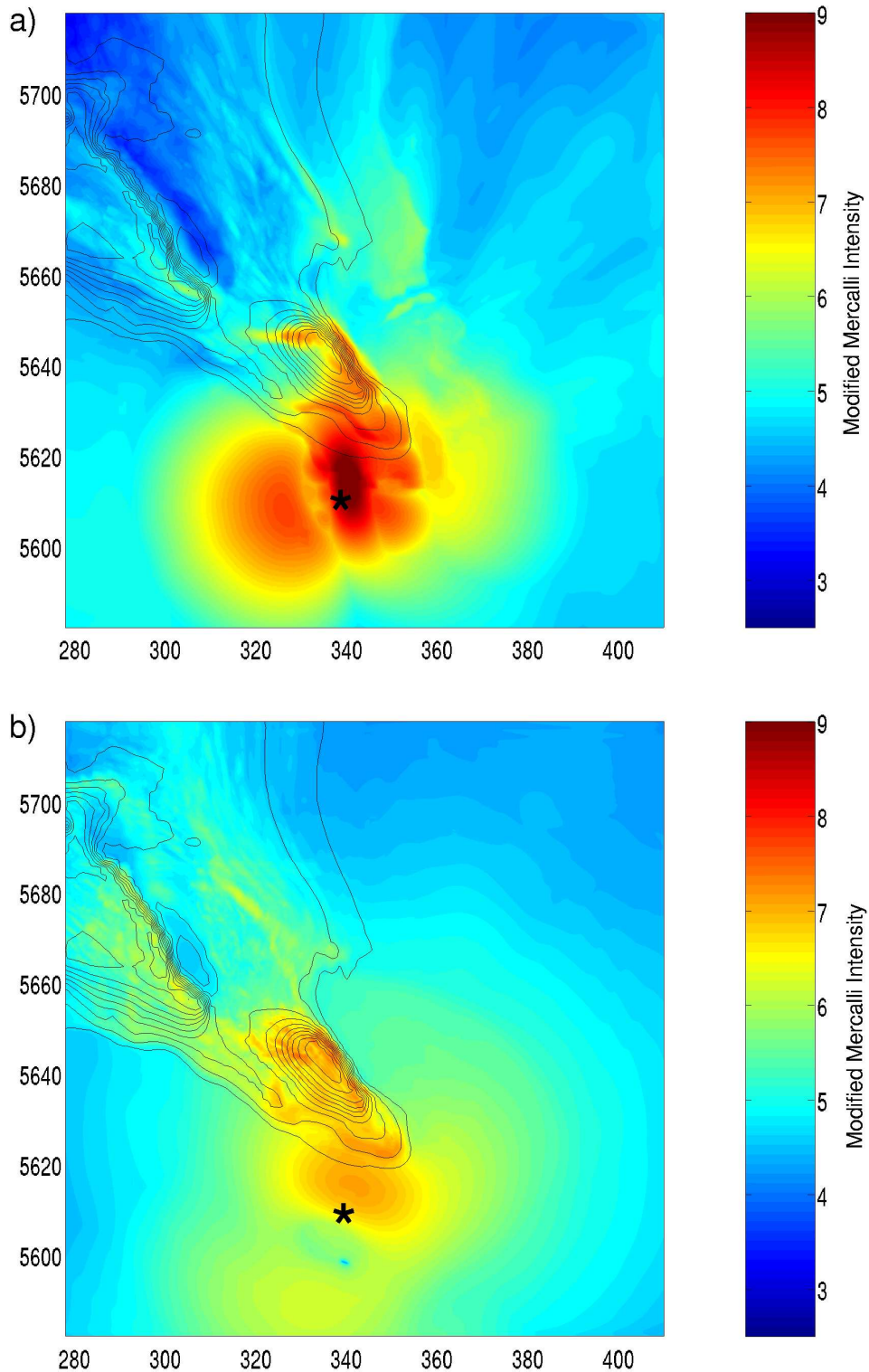


Figure 5.9: Modified Mercalli intensities for the magnitude 5.7 1951 Euskirchen earthquake derived from simulation results using setup I (a) and setup II (b). Background contour plot indicates the depth of the sedimentary basin. Black star denotes epicentral location. Dimensions and directions are given by UTM coordinates based on sector 32 U.

In figure 5.9 the distribution of seismic intensity for simulations of the magnitude 5.7 1951 Euskirchen earthquake using setup I and setup II are compared. Observations for this event suggest a peak intensity between VII and VIII. Isoseismal radii are estimated as 10 km for intensity VII, 30 km for intensity VI and 51 km for intensity V. Besides a general consistent pattern of elevated ground motion level distinct differences between these simulations can be found. Intensity mapping for the 1951 Euskirchen earthquake scenario reveals strong correlation of intensity with basin depth and shape. Differences in peak ground velocity and the derived values of seismic intensity between the different setups are not as large as it was the case for the Düren earthquake. This can be explained by the different size of both events. Whereas the incorporation of a finite source strongly affects the resulting peak amplitudes for large earthquakes with consequently large source radius, the effect is not that prominent when smaller earthquakes and source radii are considered as it is the case for the Euskirchen event. Wavefield effects like guided waves traveling along steep basin margins that were visible in the snapshots in subsection 5.4.1 result in a clear expression in the intensity pattern. These features are notable for both simulation setups and their influence on the shape of the isoseismals appears similar. Recovery of maximum intensities is improved with the incorporation of setup II, although the difference is not as significant as it was in the Düren earthquake simulations. As discussed above this is explained by the different size of the events. The finite source representation used in the new study can be seen as responsible for that gain in accuracy by smoothing the peaks in ground velocity. Isoseismal radius of intensity V is well recovered by both old and new simulation results. From this observation another characteristic of the finite source effect becomes clear: Whereas peak amplitudes are reduced the overall energy radiation is still the same and therefore the isoseismals of lower intensities are preserved. The main difference of the new simulations consists in the overall smoother picture that is drawn for seismic intensity distribution.

5.4.2.3 Roermond 1992

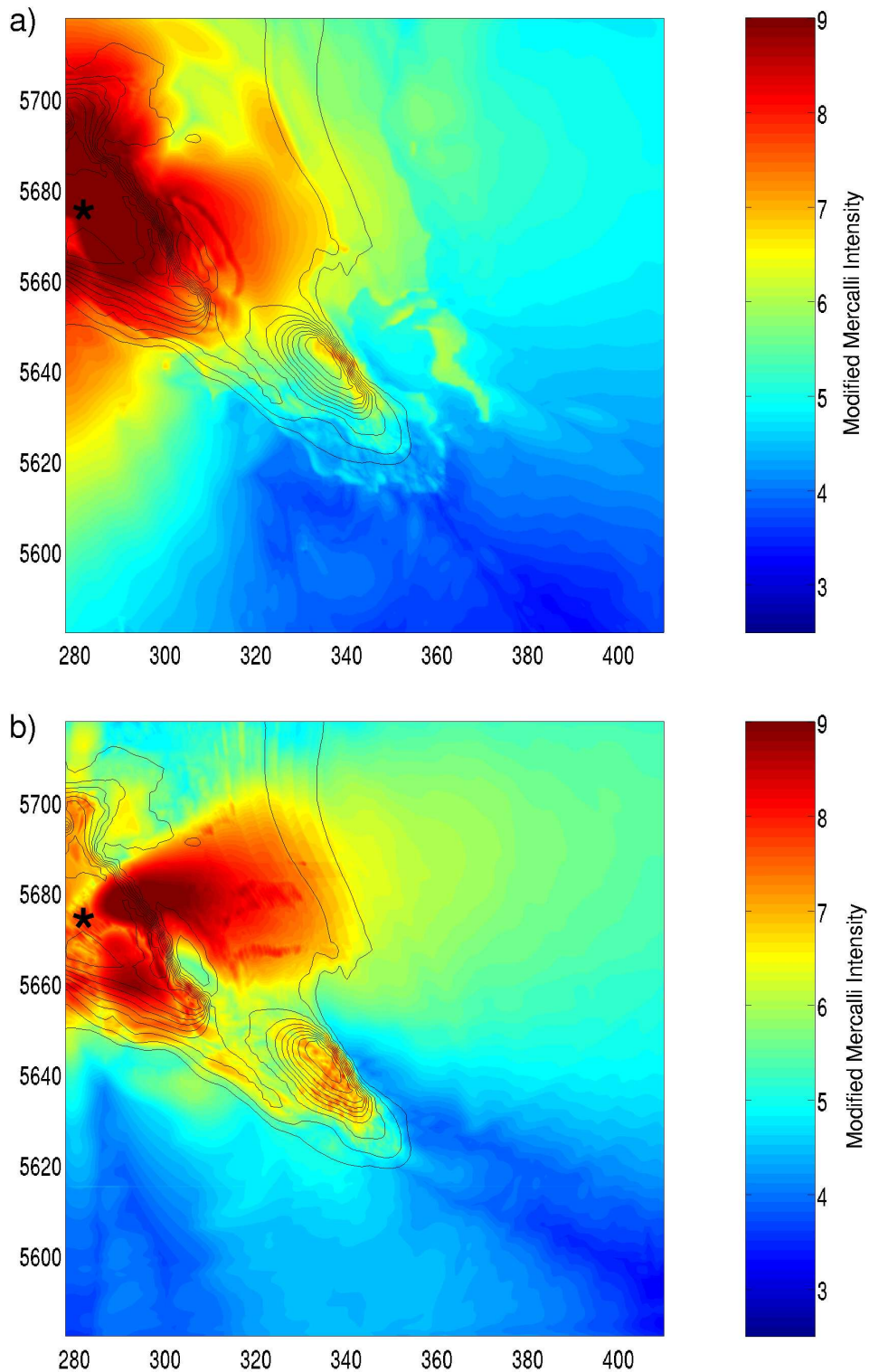


Figure 5.10: Modified Mercalli intensities for the magnitude 5.9 1992 Roermond earthquake derived from simulation results using setup I (a) and setup II (b). Background contour plot indicates the depth of the sedimentary basin. Black star denotes epicentral location. Dimensions and directions are given by UTM coordinates based on sector 32 U.

Peak intensity estimates from observations for the Roermond 1992 earthquake are still a matter of debate. A value between VII and VIII might be adequate. The isoseismal radii are estimated as 20 km for intensity VII, 55 km for intensity VI and 102 km for intensity V. Shaking hazard or intensity mapping for the magnitude 5.9 1992 Roermond earthquake scenario as shown in figure 5.10 for setup I and II, reveals similar results as for the two scenarios above. Peak values and isoseismal radii are recovered quite well, with a clearly notable improvement for the new simulations. This is due to the usage of a finite source compared to point source approximations and the partly deamplifying nature of viscoelastic sediments. The net effect of both features is a reduced peak velocity and a more balanced distribution of energy inside and outside the basin. This leads to the result of improved peak recovery by at the same time keeping the isoseismal radii at lower level. It is noteworthy that such a behavior is not producible by simple scaling of a point source. Several similarities and differences between the results from both simulation setups are briefly discussed in the following. The general strong correlation of seismic intensity with basin depth and shape is notable for both simulation setups. Simulations with both setups result in a large region of amplified ground motion in relatively shallow basin parts due to scattered energy from the source, which is located below the deepest basin part, into the corresponding regions. A spot of amplified ground motion eastward of the southern basin depression which is caused by an artificial model feature can be observed for the simulation with setup I. With the model representation of setup II the effect vanishes. This artificial effect for the setup I simulations was also notable for the Düren and Euskirchen scenario but is most prominent in this scenario. This detail is a clear indication of model improvement related to denser grid spacing. The prominent pattern of amplified ground motion and consequently higher intensity estimate in the small deep depression located roughly in the middle of the model space appears larger for the setup II simulation. This demonstrates that relatively small features with extreme geometries, concerning the edges, are better resolved in the improved model. A pattern of elevated seismic intensity just outside the basin to the south-west is not visible when setup II is used. The pattern of elevated intensity south of basin due to scattered energy is well resolved due to the usage of setup II.

5.4.3 Shaking Duration

Whereas intensity mapping shown in the previous subsection represents the distribution of peak ground motion, a second parameter with significance to possible building damage is missed: the duration of strong shaking. This parameter can be retrieved by recording the first and last time a certain threshold value is exceeded. In this work a value of 4 cm/s is chosen as threshold, corresponding to an intensity step from IV to V. This method is adopted from Olsen (2000). The time between these two exceedings is referred to as shaking duration in this study. This procedure is illustrated in figure 5.11. To illustrate the effects on shaking duration values are recorded over the whole model surface and displayed as color-coded isoline plots.

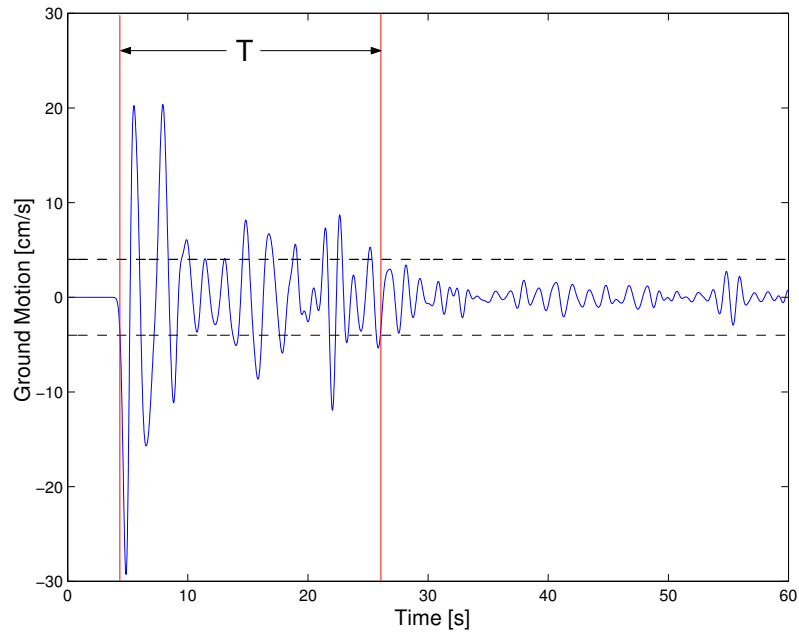


Figure 5.11: Shaking duration is defined in this study as the interval between first and last exceedance of a certain threshold value (4 cm/s).

5.4.3.1 Düren 1756

Figure 5.12 shows a mapping of shaking duration for the simulations of the 1756 Düren earthquake using setups I and II, respectively. Both plots display a strong correlation of this parameter with the presence of low velocity sediments. A closer view reveals significant relation of prolonged shaking with basin depth. Nevertheless, for this earthquake a few sole spots of prolonged shaking outside the basin are visible as well. In the following similarities and differences between the results for the different simulation setups are described. The mentioned correlation with basin depth is equivalently recognizable for both simulation setups. An interesting feature shown by both pictures is the splitting of the long duration areas at the Peel High, into two spots of similar size and amplitude. This distinct raise in basin topography located east of the main depression was already discussed in the previous section. Its effect was already prominent in snapshots of the wavefield and peak amplitude considerations and it also appears in the distribution of shaking duration. The simulation using setup II results in smoother shaking duration maps and only the new results show a clear relation of shaking duration and epicdistance. That is clearly due to the influence of viscoelastic attenuation, whereas in the elastic simulations only geometrical spreading is responsible for reduced amplitudes. This effect is not significant for trapped waves and reverberations. Interestingly the new setup produces larger areas of prolonged shaking for the Düren earthquake, whereas the maximum duration is lower. This behavior coincides with the expectations for a finite source and viscoelastic attenuation within the medium. The overall smoother picture achieved with setup II is due to both the reduced frequency resulting from finite source effects as well as a signature of the better model resolution.

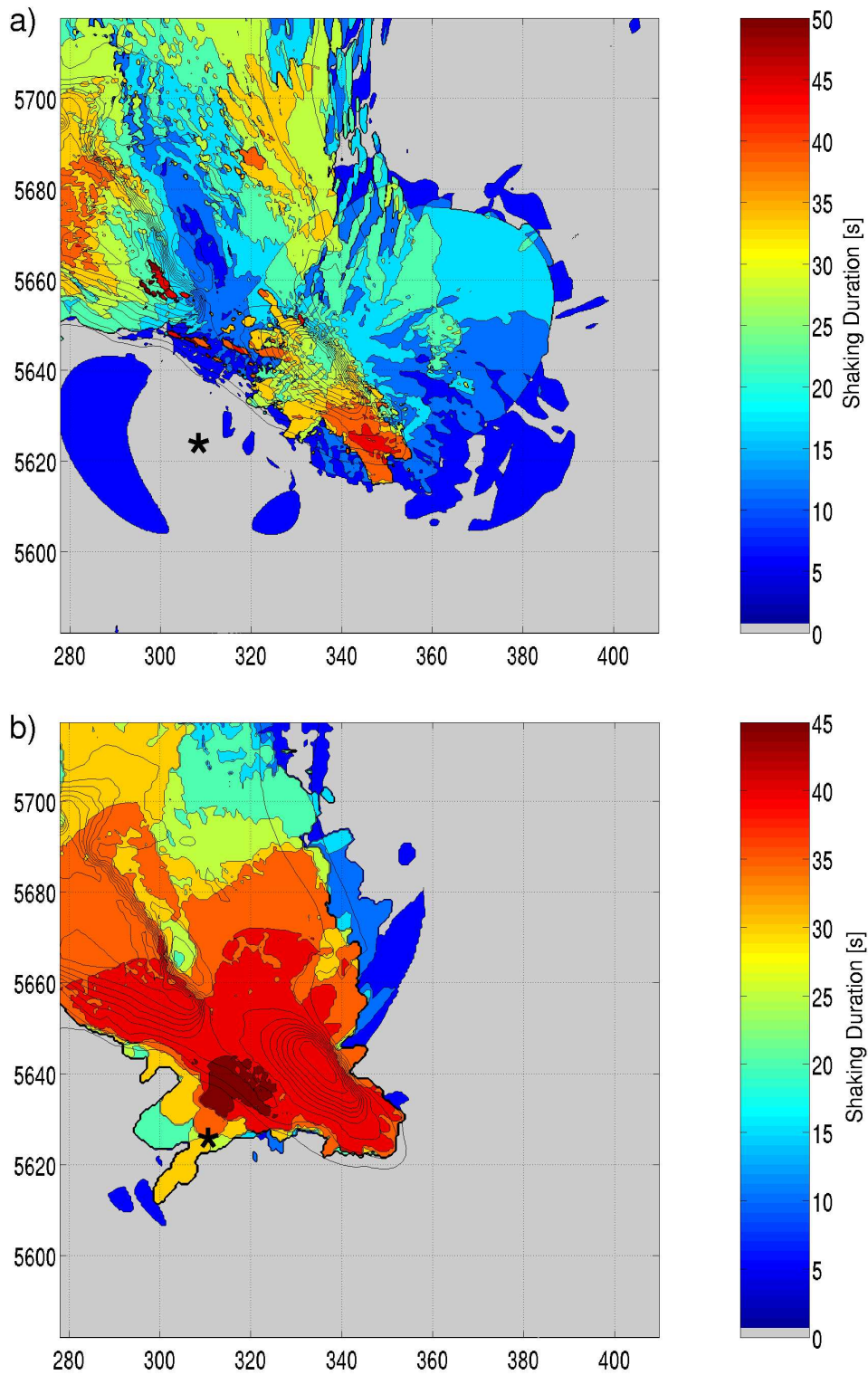


Figure 5.12: Shaking duration for the magnitude 6.1 1756 Düren earthquake scenario from simulation results achieved with setup I (a) and setup II (b). Background contour plot indicates the depth of the sedimentary basin. Black star denotes epicentral location. Dimensions and directions are given by UTM coordinates based on sector 32 U.

5.4.3.2 Euskirchen 1851

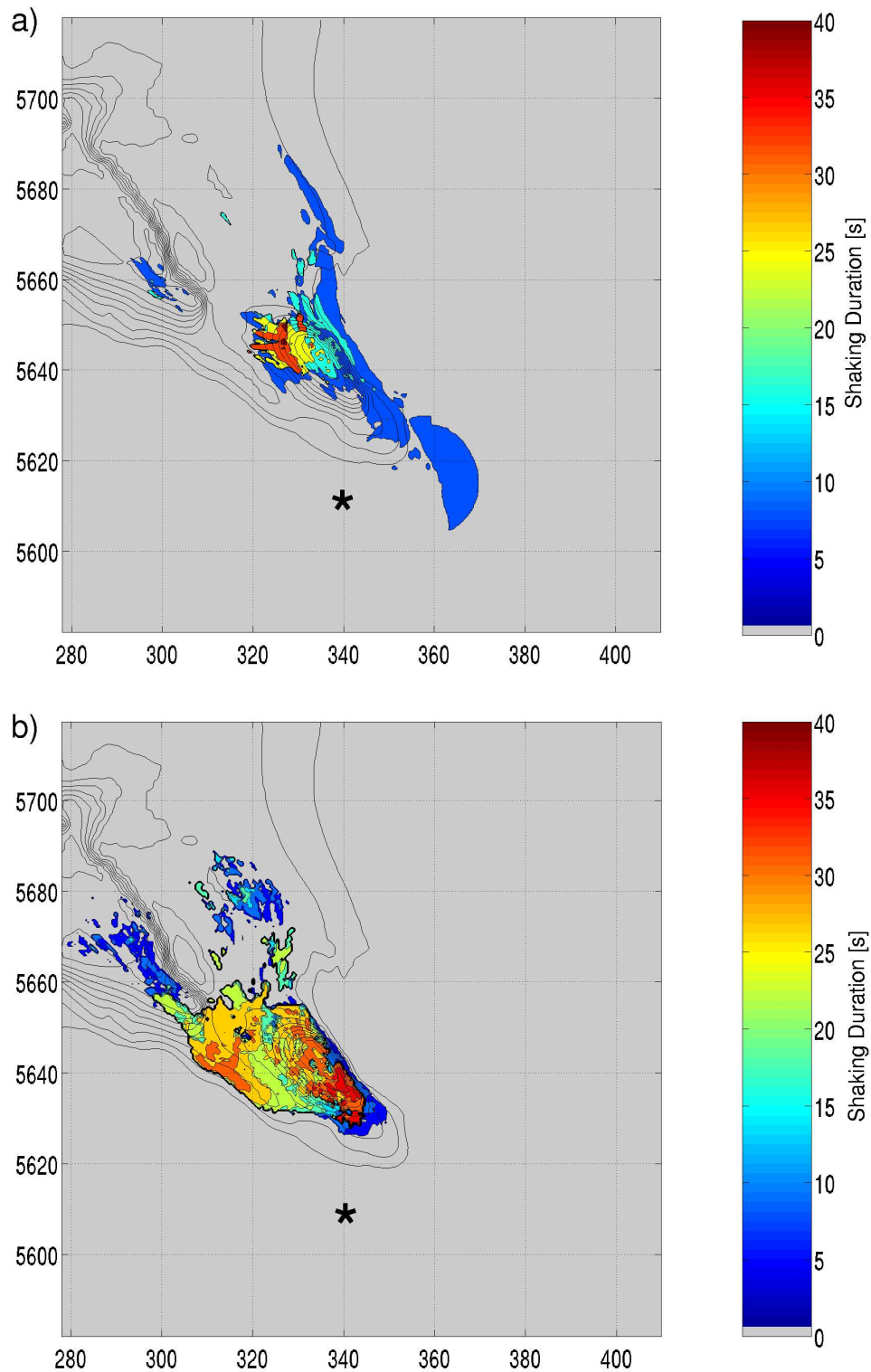


Figure 5.13: Shaking duration for the magnitude 5.7 1951 Euskirchen earthquake scenario from simulation results achieved with setup I (a) and setup II (b). Background contour plot indicates the depth of the sedimentary basin. Black star denotes epicentral location. Dimensions and directions are given by UTM coordinates based on sector 32 U.

Mapping of shaking duration for the 1951 Euskirchen earthquake scenario simulations using setup I and II reveals in general smaller areas of prolonged shaking due to the lower magnitude of the event. The resulting shaking duration maps are shown in figure 5.13 for both setups. Although not the whole sedimentary area is associated with enhanced shaking duration according to the definition and threshold value used in this study, significant correlation with basin depth can be recognized for this event as well. More discrete spots in this case make it easy to detect a strong correlation between prolonged ground motion and steep basin edges. This accounts in particular for the simulation carried out with setup II. Comparison with the results from the Düren earthquake scenario simulations in the previous section clearly demonstrates that the spots with long duration time are significantly smaller for this event. It is notable that the peak values are not so much different from the ones associated with the larger event near the town of Düren. It is evident from the simulations that long lasting ground motion can be produced by a magnitude 5.7 earthquake in the presence of a sedimentary structure. In the following prominent features of the shaking duration distribution are discussed. Coincidence of simulation results for both setups can be recognized. Spots of enhanced shaking duration can be observed above the steep basin edges for both simulation setups. It is remarkable that the geometric effect of basin edges does not only affect peak amplitude but also the duration of strong shaking. The effect can be explained by wave energy which is guided along the basin contours and results in strong ground motion. However, significant differences between results achieved using setup I and II can as well be observed. Most prominently the half-circle shaped feature is missing when setup II is used. This feature is caused by large amplitudes in the relatively undisturbed wave field south of the basin. With the use of a finite source it does not appear due to overall lower peak amplitudes. Nevertheless maximum values inside the basin are significantly higher for discrete and relatively small areas. The pattern of shaking duration resulting from simulations carried out using setup II show a more intuitive attenuation behavior with epicentral distance. Very strong heterogeneities in this parameter are reduced compared to the simulations with setup I. The correlation of basin depth with enhanced shaking duration for the deep basin depression in the south-east appears realistic.

5.4.3.3 Roermond 1992

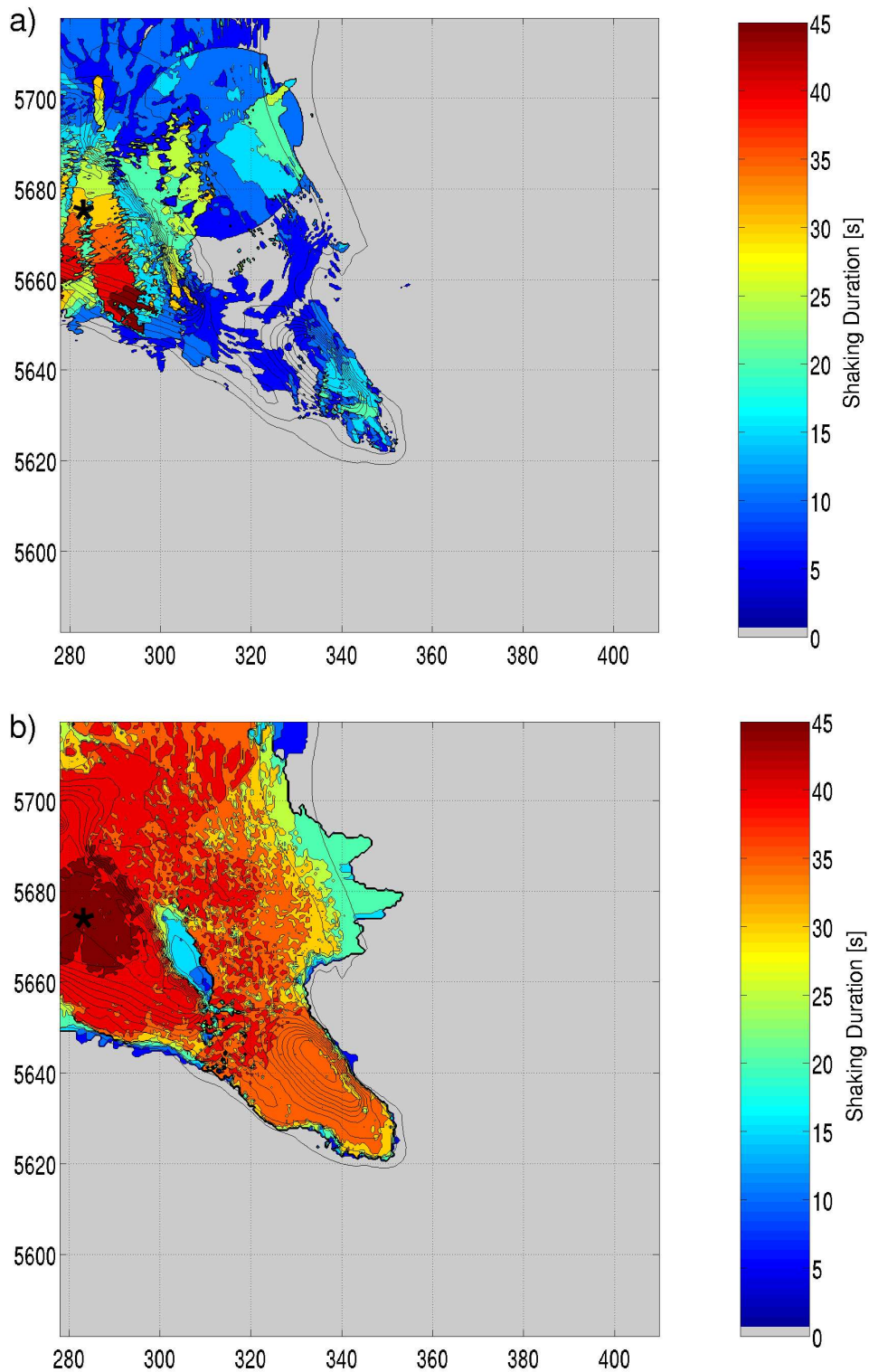


Figure 5.14: Shaking duration for the magnitude 5.9 1992 Roermond earthquake scenario from simulation results achieved with setup I (a) and setup II (b). Background contour plot indicates the depth of the sedimentary basin. Black star denotes epicentral location. Dimensions and directions are given by UTM coordinates based on sector 32 U.

Shaking duration maps for the simulations of the 1992 Roermond earthquake as presented in figure 5.14 show the strongest correlation with basin depth of the three scenarios.

A striking similarity between results achieved with both simulation setups consists in the very similar maximum values of shaking duration. However as the distribution of this parameter over the model area appears quite different this may be considered an artificial effect due to the simple derivation of shaking duration with a threshold value. Whereas the pattern of shaking duration within the basin significantly varies both simulations produce a strict limitation of enhanced shaking period to the basin area. The most prominent difference between simulation results achieved with different setups consists in the smoother distribution of prolonged shaking when setup II is used. As discussed above this can be explained with a better resolution of the basin model and the influence of attenuation and a finite source incorporated in this simulation. This setting also results in a good correlation of shaking duration with epicentral distance that is hardly recognizable when setup I is considered. The raise in basin topography, the Peel High, mentioned for the Düren scenario, is mapped very clearly by the improved model representation.

5.4.4 Seismograms

Whereas the above shown parameters of maximum amplitudes - expressed as seismic intensity - and shaking duration give an impression of the distribution of energy over the whole model space, distinct phenomena and their origins can only be seen on seismograms. Numerical simulations allow recording of ground motion on any location within the model space. Typically such synthetic receivers are placed on the surface at equidistant positions or following the station distribution given by a real seismic network. In this subsection two kinds of seismogram plots are presented: Seismogram sections along a profile and a single station comparison of synthetic and observed ground motion.

5.4.4.1 Profiles

In this paragraph seismogram sections along a profile labeled A - A' (see figure 5.4) are presented. Each section consists of 30 equally spaced receivers on which three component seismograms are plotted. For each component the resulting seismograms for the three earthquake scenarios achieved with the different setups are compared. Seismogram sections for each event are scaled individually to the maximum amplitude. A black curve below the sections indicate the individual depth of the sedimentary basin at the receiver location. From this a good correlation of the observable effects with basin topography can be achieved. Key features of the presented seismograms are labeled with capital letters and are individually discussed in brief.

East/West component First seismograms of the East-West horizontal component are investigated. Figure 5.15 shows the described seismogram sections resulting from simulations using setup I, whereas figure 5.16 displays the equivalent plot for simulations with setup II.

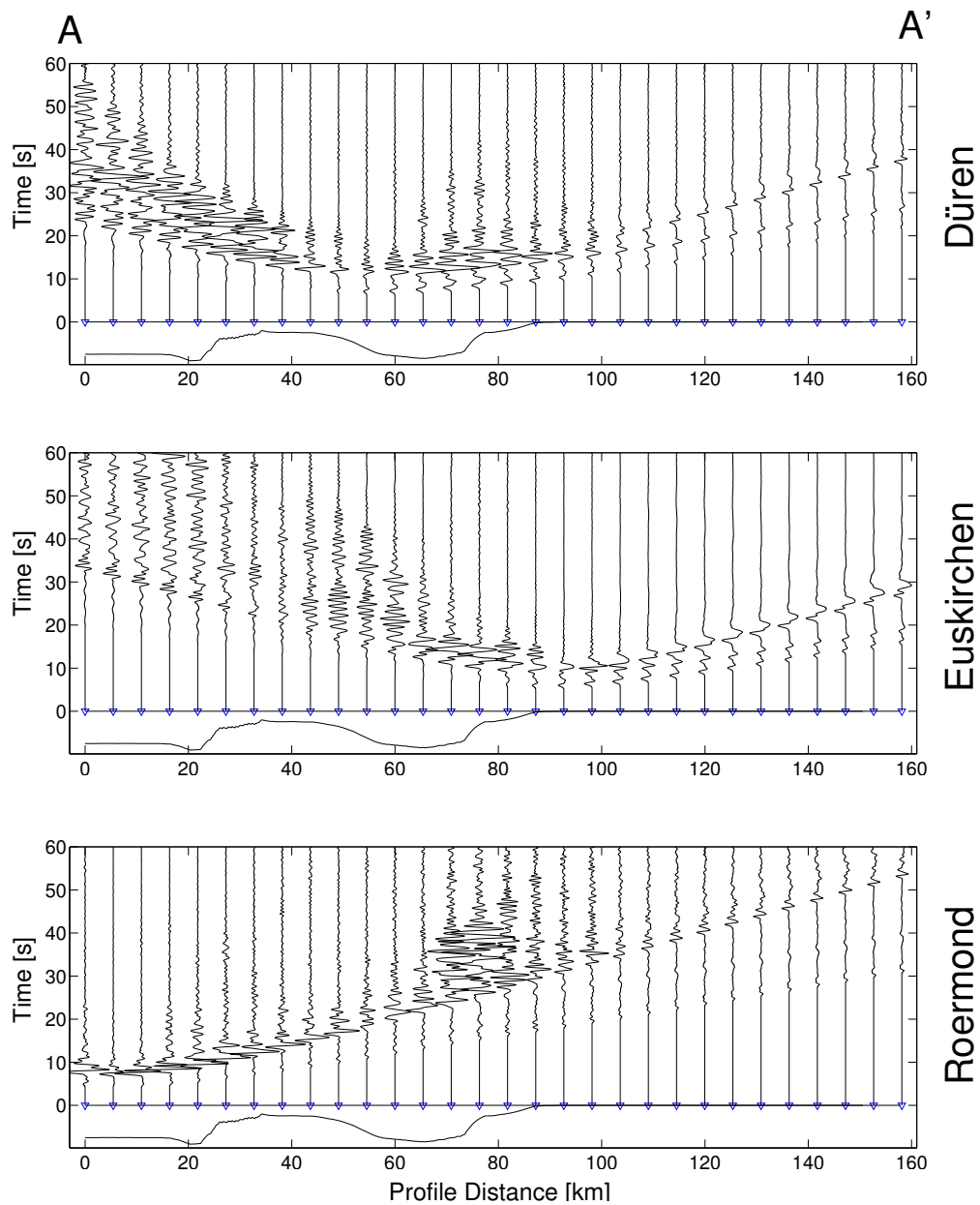


Figure 5.15: Seismogram section of the east-west velocity component along the profile A-A' (5.4). Synthetics for the three earthquake scenarios are produced using setup I.

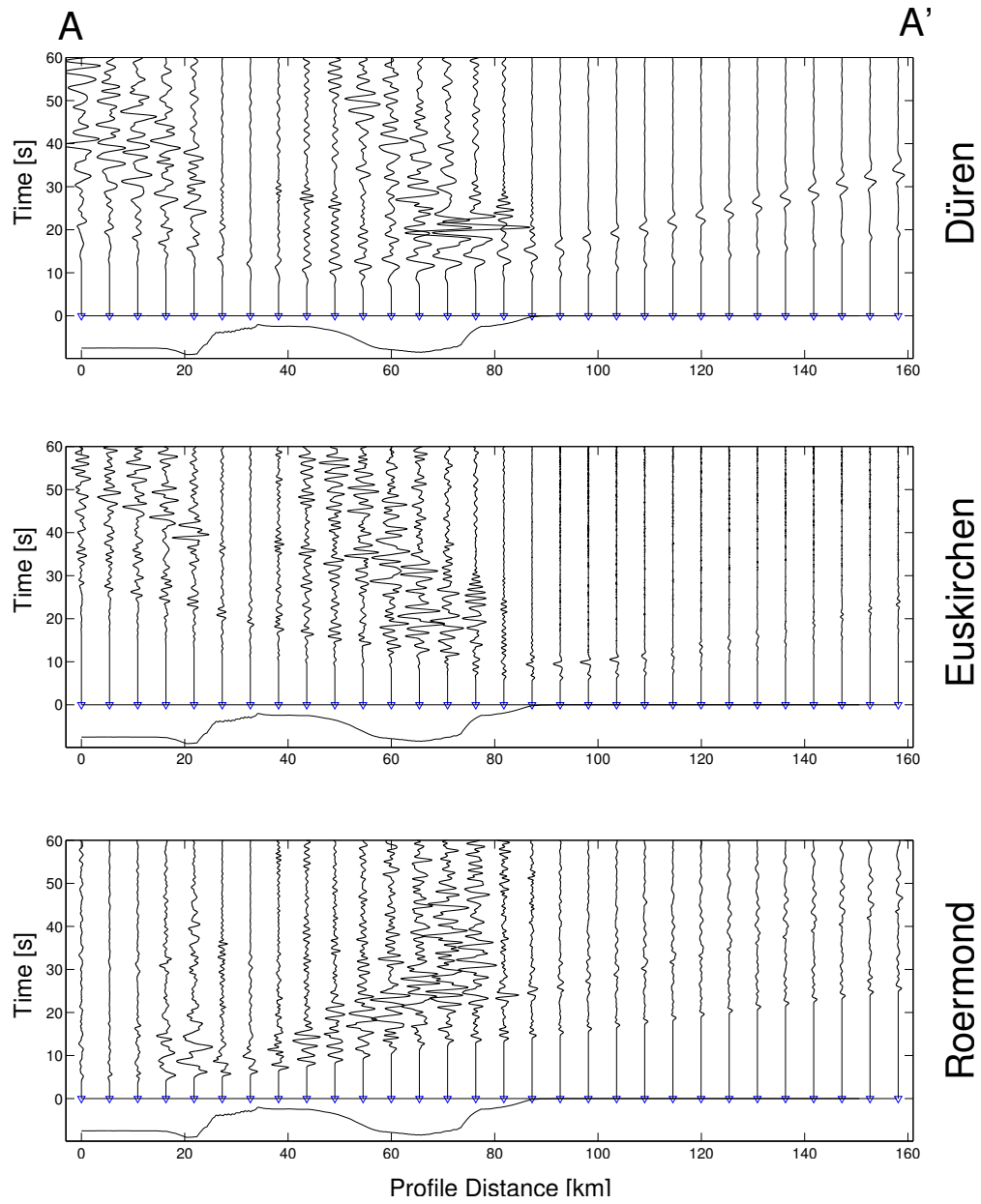


Figure 5.16: Seismogram section of the east-west velocity component along the profile A-A' (5.4). Synthetics for the three earthquake scenarios are produced using setup II.

A clear travel time signature of the sedimentary basin is observable for the first arrivals on the Roermond section, especially for the seismogram section achieved with setup II. In general, the difference in travel times outside the basin due to the different velocity models is clearly visible. Considering the assumed low velocity in the homogeneous bedrock model used in the old setup travel times achieved with the model used in setup II appear much more confident. For the Düren scenario a single large amplitude appears above the steep basin edge. It is notable that this coincides with significant effects seen on intensities and snapshots as well as shaking duration maps. This feature is not observable when setup I is used. It is notable that a similar effect can be seen in the North-South component for the Euskirchen event. A diffuse pattern of late arriving energy within the deepest part of the basin is present for simulations of the Euskirchen earthquake with both setups. The multiple reflected waves causing these onsets are also prominent in the snapshots.

Strong reflected phases originating at the middle of the basin structure can be observed for the Euskirchen earthquake in simulations using setup I and II. A single phase of this can be identified in both simulation results. From the snapshots of the wavefield it can be understood that the area between the two main basin depressions acts as a secondary resonant source. Significantly prolonged ground motion without significant correlation between neighboring receivers inside the basin area can be observed for the Düren earthquake. This observation appears consistently in the results for both simulation setups. For both setups a clear correlation between basin depth and peak amplitude can be observed for the 1992 Roermond earthquake scenario simulations. This is consistent with the effect of the basin of waves entering the basin at steep incidence angles, like it is the case for this scenario.

North/South component Figures 5.17 and 5.18 present seismogram sections of the North-South component horizontal ground velocity. In general similar observations can be made as it was the case for the East-West component.

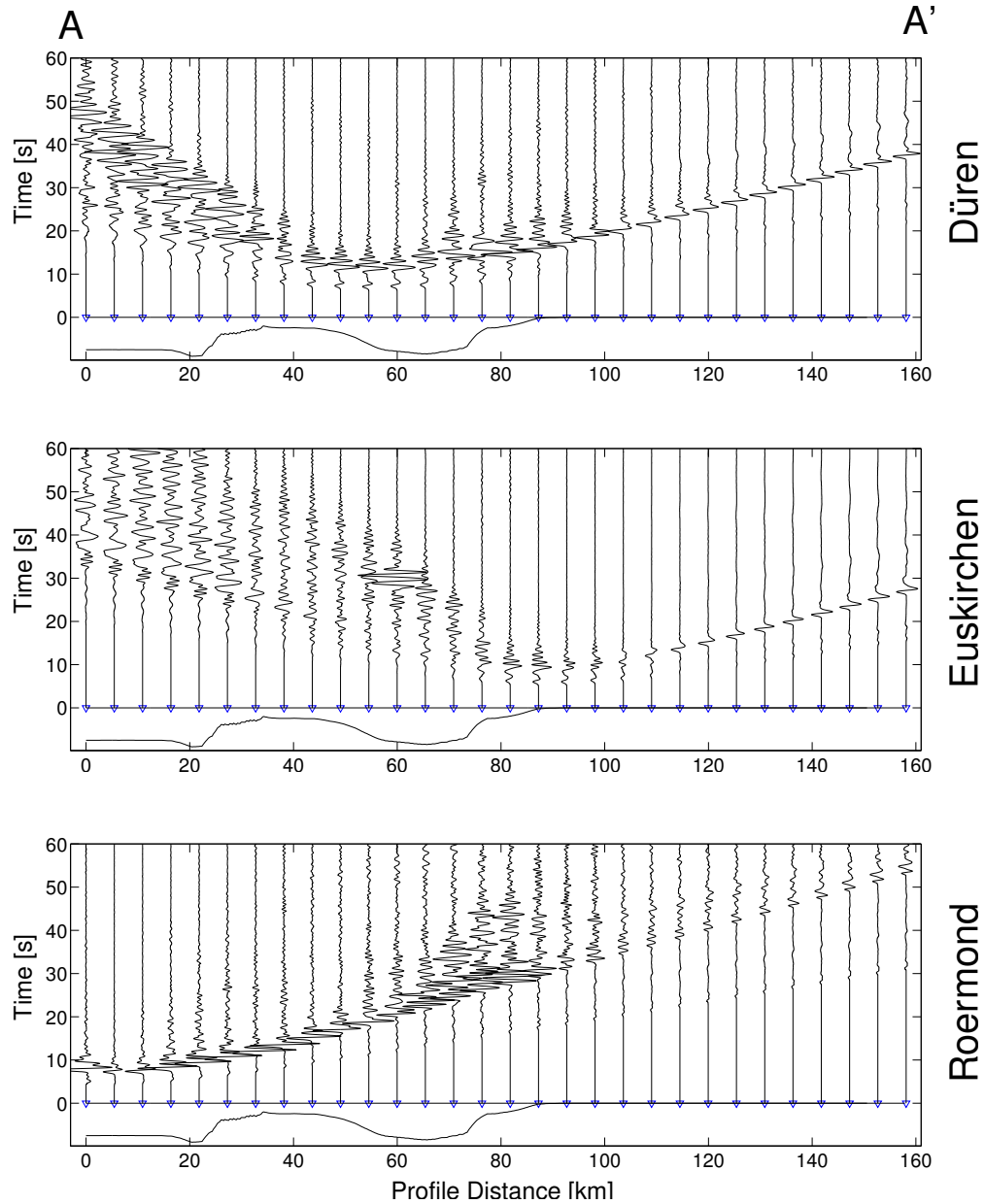


Figure 5.17: Seismogram section of the north-south velocity component along the profile A-A' (5.4). Synthetics for the three earthquake scenarios are produced using setup I.

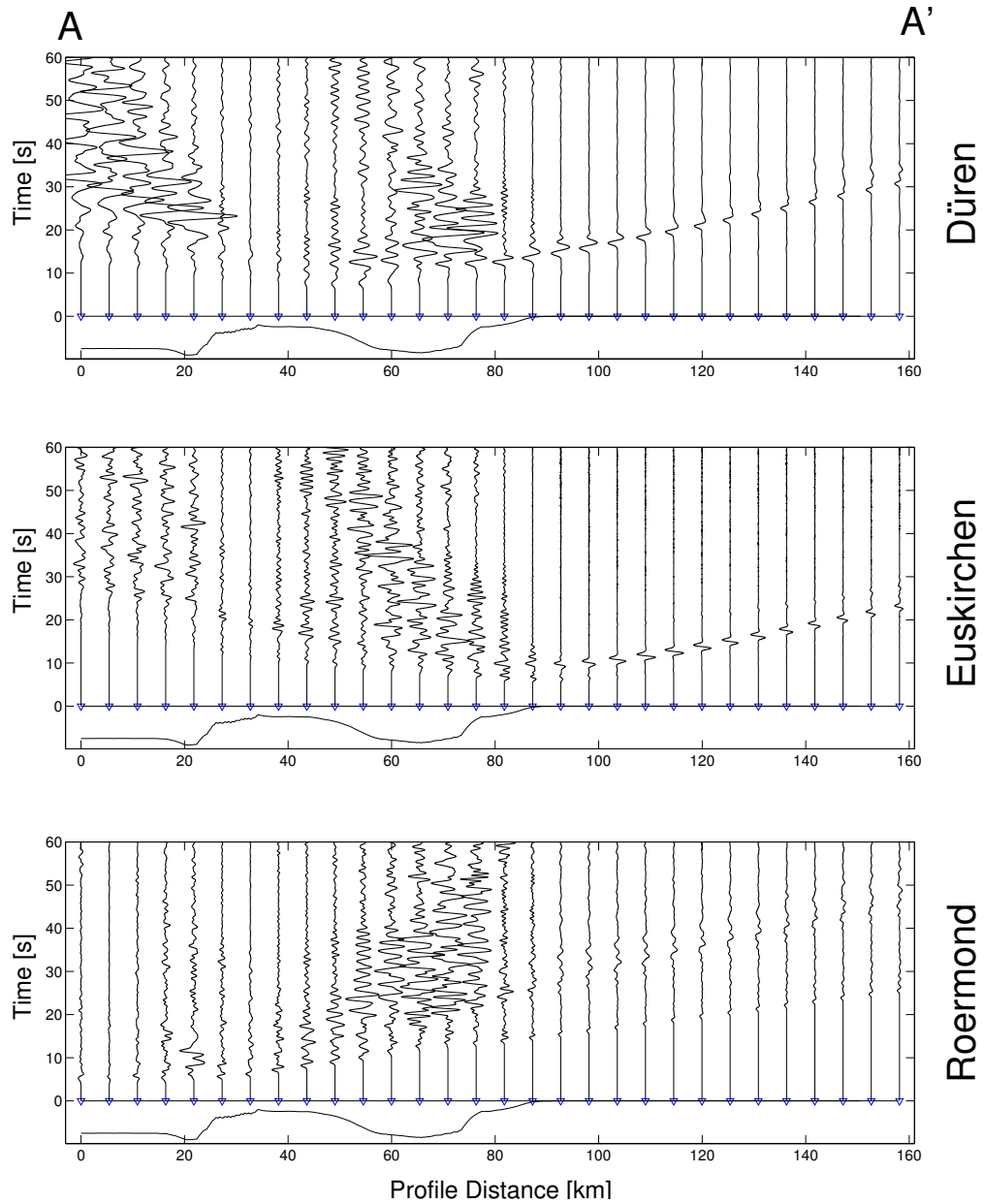


Figure 5.18: Seismogram section of the north-south velocity component along the profile A-A' (5.4). Synthetics for the three earthquake scenarios are produced using setup II.

However, several effects and their signature can be observed prominently on this component and are discussed in the following.

A single onset with very large amplitude is visible for the Euskirchen event. When the model representation of setup II is used it appears not as solitary as it is the case for the simpler model, but still there is no coherent signal observable at the neighboring stations. Additionally, the onset is observable at significantly later times when this model is applied.

For the Roermond simulations concentration of energy above the basin edges, especially at the southern small depression with its steep flanks is recognizable for the setup I simulation. Simulations employing the refined model reveal a more basin depth correlated distribution of large amplitudes. It is a well known fact that both basin depth and geometric effects due to steep basin walls play an important role when basin related amplitude effects are considered. However, the focusing effect above the steep edges might be overpredicted by simulations with setup I due to the point source approximation which simplifies geometrical relations between source, structure and receiver. A contiguous pattern of longlasting ground motion with large amplitudes is observed for the Düren earthquake. Individual phases have comparable velocities and characteristics for both simulations.

Vertical component Profile sections for the vertical component are presented in figures 5.19 and 5.20 for simulations using setup I and setup II. The seismograms show similar features as observed on the horizontal ones. It is notable and in consistence with theory that the effects on the vertical component are qualitatively the same as on horizontal components whereas quantitatively the horizontal ones show much stronger amplitude variations as the vertical ones.

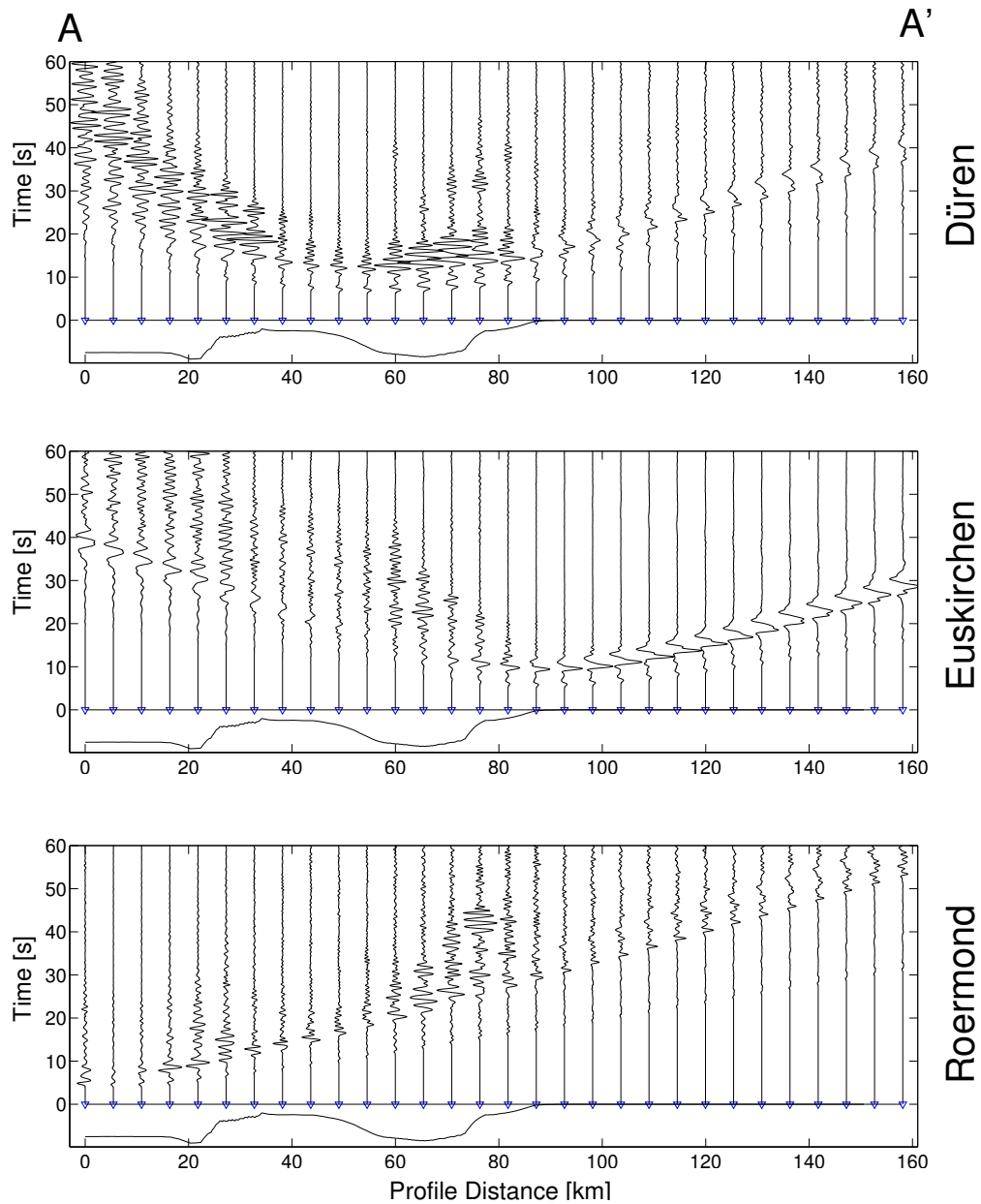


Figure 5.19: Seismogram section of the vertical velocity component along the profile A-A' (5.4). Synthetics for the three earthquake scenarios are produced using setup I.

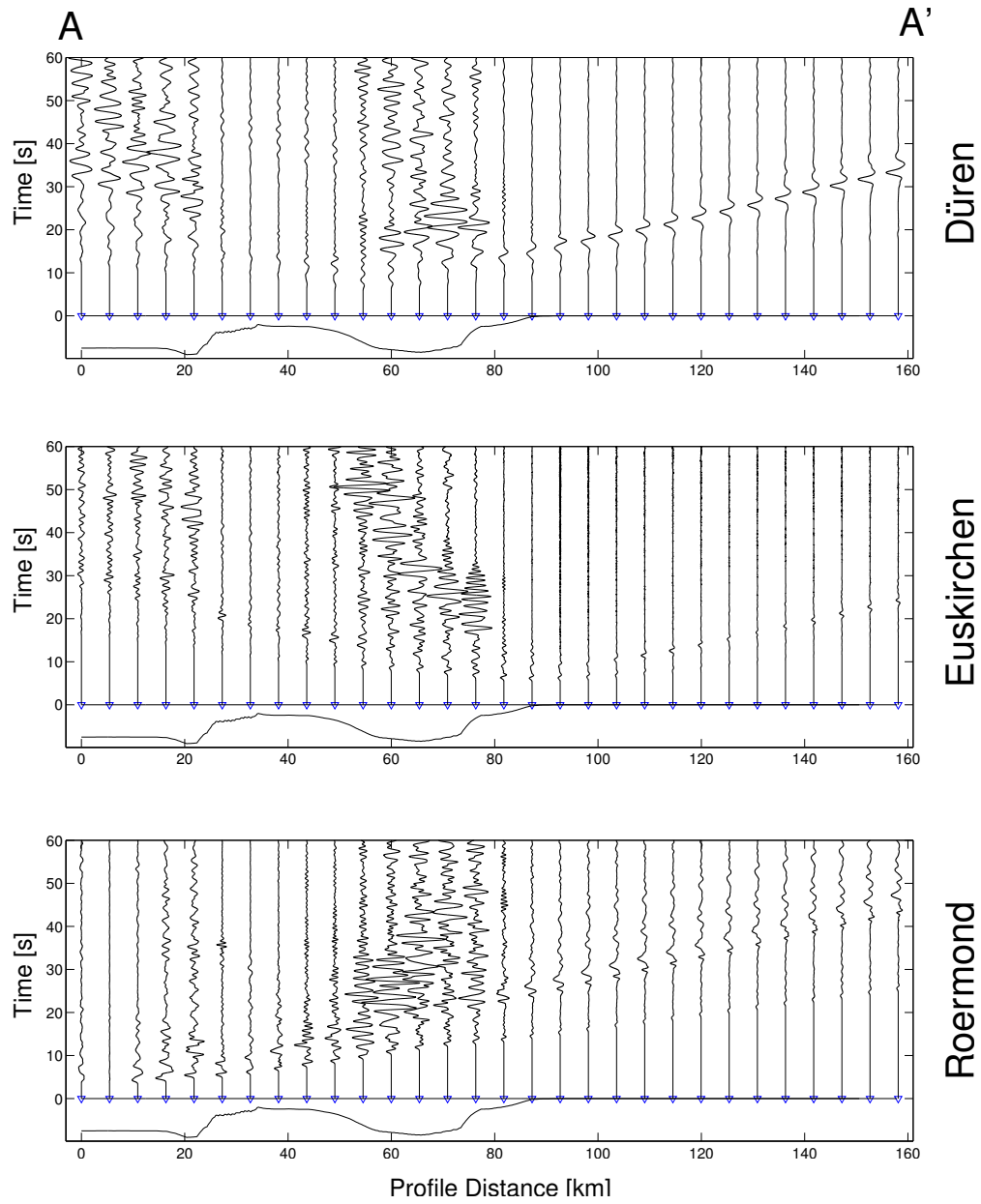


Figure 5.20: Seismogram section of the vertical velocity component along the profile A-A' (5.4). Synthetics for the three earthquake scenarios are produced using setup II.

5.4.4.2 Comparison with observed ground motion

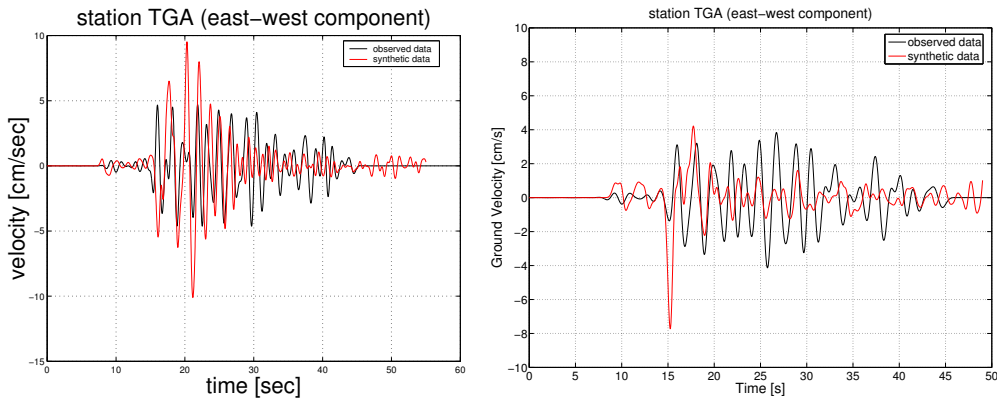


Figure 5.21: Comparison of east-west component seismograms at station TGA for the 1992 Roermond earthquake. Synthetics achieved with setup I (left) and setup II (right) are plotted in red along with observed ground motion (black).

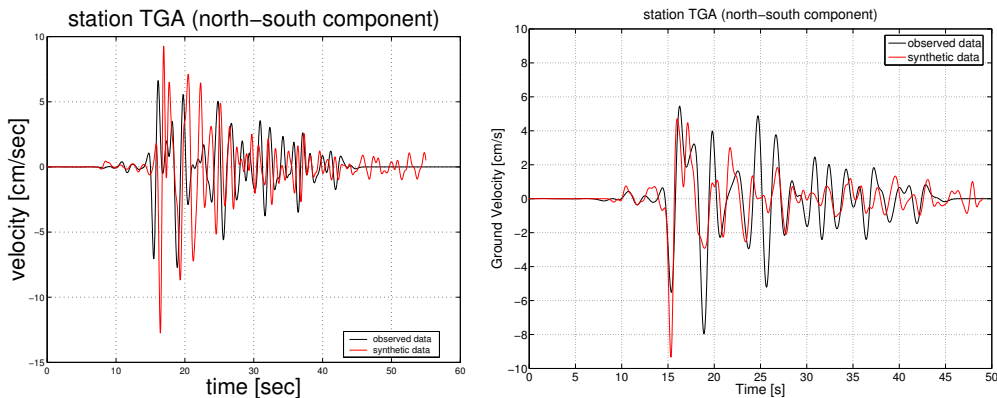


Figure 5.22: Comparison of north-south component seismograms at station TGA for the 1992 Roermond earthquake. Synthetics achieved with setup I (left) and setup II (right) are plotted in red along with observed ground motion (black).

As already discussed the dataset of ground motion observations for large earthquakes in the Cologne Basin area is very sparse. The 1992 Roermond earthquake is the only instrumentally recorded one of the three simulated scenarios. Unfortunately only one station (TGA, see map 5.4) provided unclipped strong motion data. Direct comparisons of synthetics from simulations using both setups and observed seismograms are presented for three components of ground motion in figures 5.21, 5.22 and 5.23. For both setups some similarities are achieved and outlined in the following.

1. Peak values of ground motion are matched with a misfit of about 50 to 60 percent.
2. Envelopes of the observed seismograms are quite well reproduced for all components.

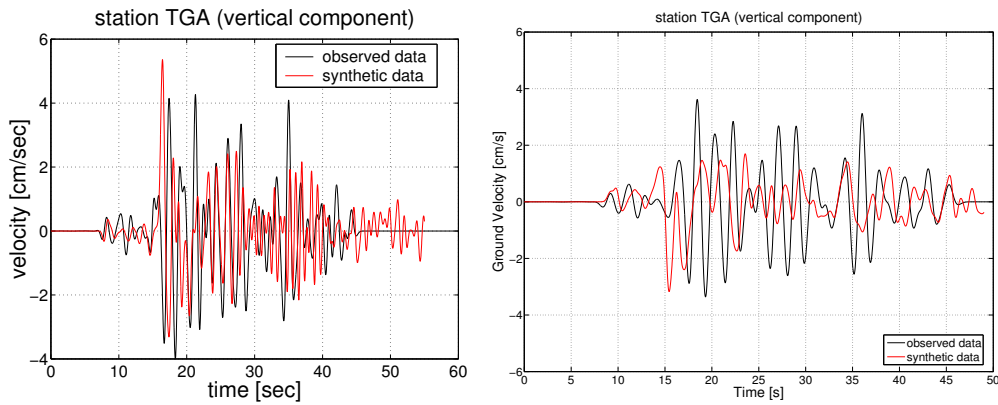


Figure 5.23: Comparison of vertical component seismograms at station TGA for the 1992 Roermond earthquake. Synthetics achieved with setup I (left) and setup II (right) are plotted in red along with observed ground motion (black).

Nevertheless, incorporating more complexity in the model with the use of setup II lead to some significant improvements on the wave forms.

1. P and S-wave arrival times are better matched with the use of setup II. This is clearly a benefit of the more realistic velocity model.
2. Amplitude ratio of P and S-waves are matched quite accurately when setup II is employed.
3. For the horizontal components several individual phases of the synthetic seismograms achieved with the setup II simulations appear to match the observation.

5.4.5 Cumulative Intensity

In order to get an impression of future potential usage of numerical scenario simulations in shaking hazard assessment a simple approach is made to produce a cumulative intensity map based on the series of three scenarios. Peak ground velocities resulting from the individual scenarios are averaged with an equal weight. Afterwards the Modified Mercalli intensity is calculated according to the formulas given above.

The resulting maps of cumulative intensities are shown in figures 5.24 for the setup I simulations and in figure 5.25 for setup II. It is notable that after this series of only three earthquakes the source related intensity distribution already starts to dissolve into a basin correlated shape. To link the results to available ground motion estimates the maps are compared with the shaking hazard map for the Cologne Basin for a recurrence rate of 0.001 per year (Rosenhauer and Ahorner (1994)). A qualitatively good agreement in the shape of isoseismals can be recognized. Absolute values are difficult to compare as no recurrence interval is considered for the cumulative intensity map of this work. Nevertheless, the resulting values are comparable due to the fact that three large events within a period of time of 250 years coincide roughly with a recurrence of 0.001 per year. Simulation results using setup I and setup II produce nearly equal distributions of cumulative intensity. From the discussion in previous sections it is understood that most of the differential effects resulting from improved model representation with setup II are associated with local heterogeneities that are better resolved with this model. Consequently, these small-scale features are leveled when a stacking is performed in order to achieve cumulative values.

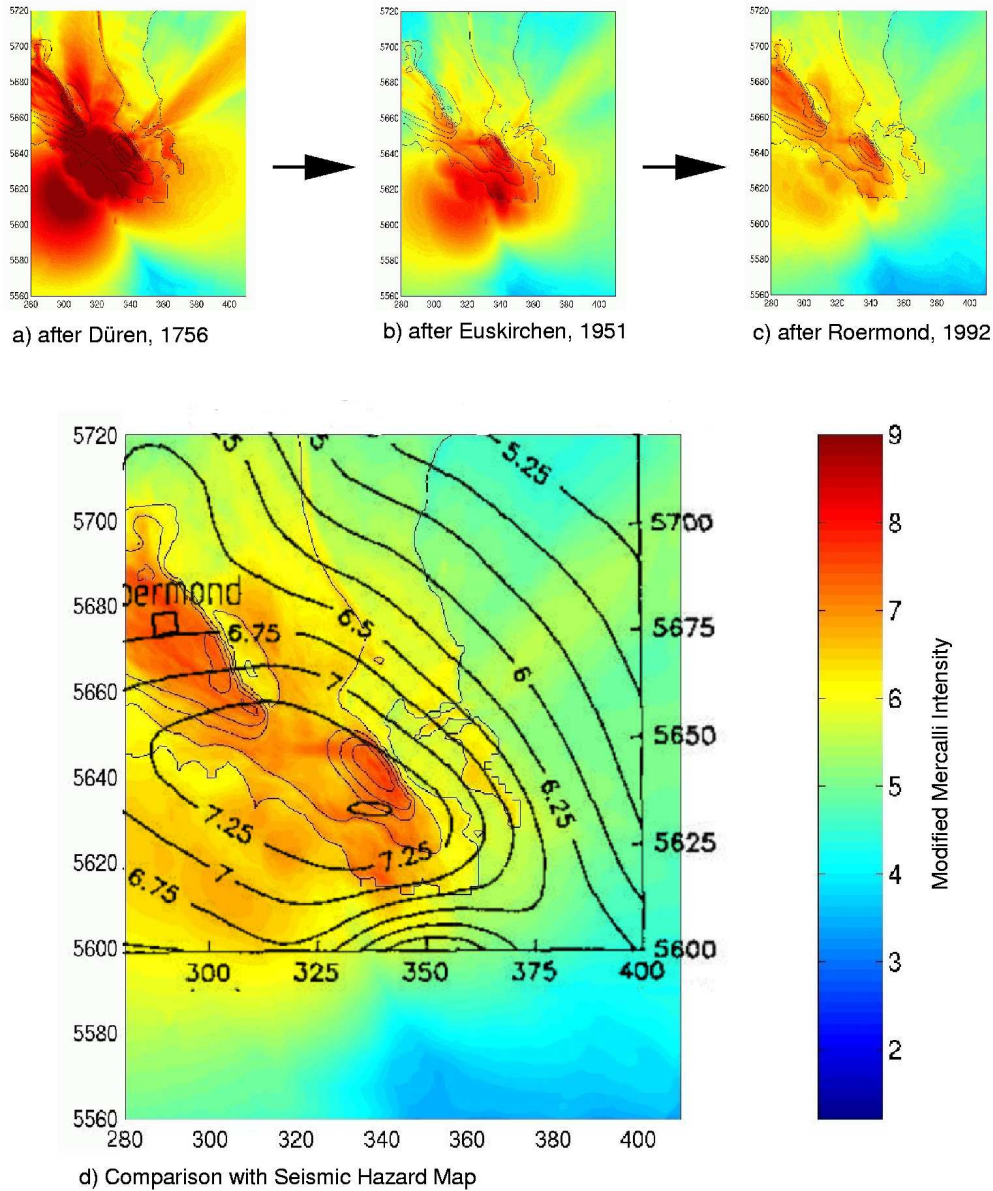


Figure 5.24: Evolution of combined intensities achieved with setup I throughout the sequence of the simulated three scenarios (a - c) and comparison with the current seismic hazard map for the study area (d). The black lines with numbers indicate the probabilistic earthquake intensity isolines with an occurrence rate of 0.001 per year (after Rosenhauer and Ahorner (1994)). Dimensions and directions are given by UTM coordinates based on sector 32 U.

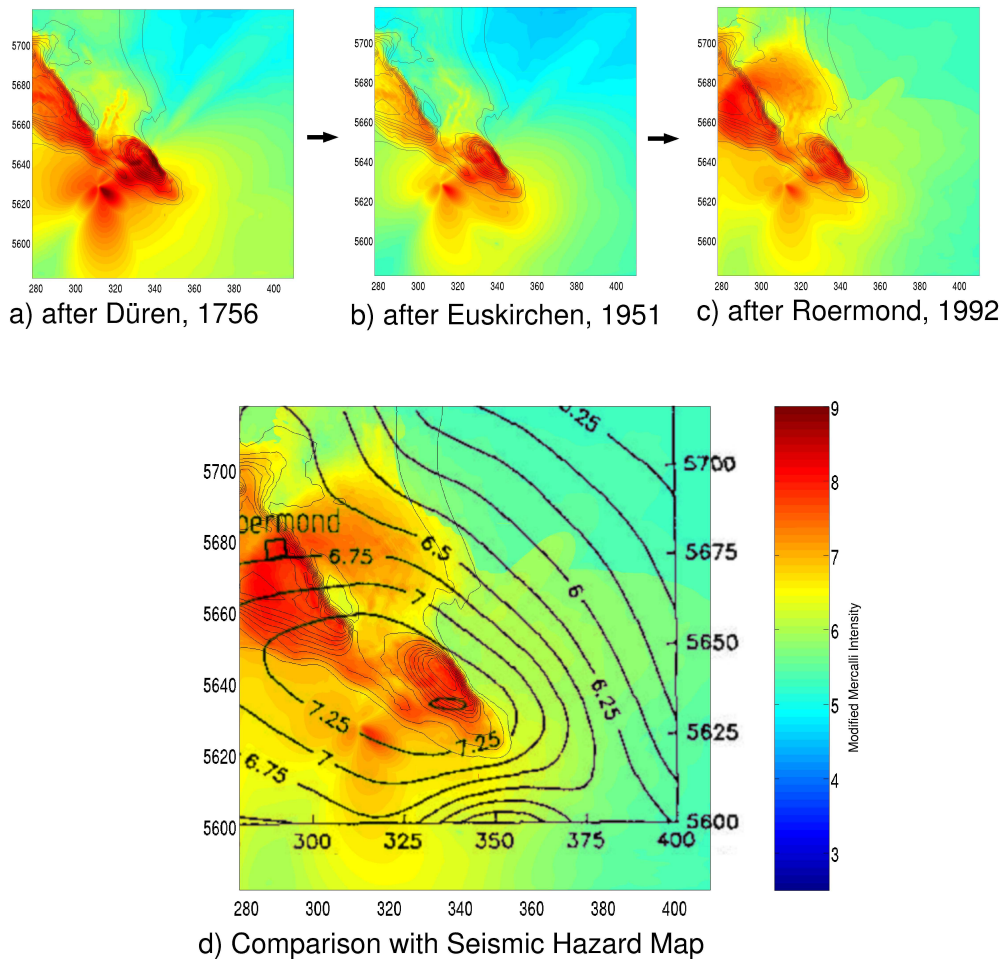


Figure 5.25: Evolution of combined intensities achieved with setup II throughout the sequence of the simulated three scenarios (a - c) and comparison with the current seismic hazard map for the study area (d). The black lines with numbers indicate the probabilistic earthquake intensity isolines with an occurrence rate of 0.001 per year (after Rosenhauer and Ahorner (1994)). Dimensions and directions are given by UTM coordinates based on sector 32 U.

5.5 Discussion

In the previous sections results from numerical simulations for three earthquake scenarios in the Cologne Basin were presented. Two setups varying significantly in terms of model complexity were compared with respect to key parameters of seismic ground motion. The main findings are:

1. Mapping peak ground velocities by means of associated seismic intensity leads to comparable distributions of ground motion levels for both setups. However, there are numerous details in which intensities achieved with the more advanced setup II differ significantly from the ones resulting from the simpler setup. Most of these local distinctions can indeed be traced back to shortcomings of the model. Therefore results from the setup II simulations are more reliable. Nevertheless the overall distribution of seismic intensities reveal a clear signature of amplified ground motion due to the sedimentary basin comparable in amplitude and shape for both setups.
2. Shaking duration mapping derived from setup I simulations show highly heterogeneous patterns for all scenarios, making the figures hard to interpret. Clear improvement has been achieved with the use of setup II. There are indications that these gains are linked directly to the use of finite sources and the incorporation of viscoelastic attenuation in the model. Results from setup II are easier to interpret and more confident. This applies in particular for the distribution of shaking duration.
3. Seismogram sections along a profile intersecting both of the deep basin depressions which are considered the main features of the velocity model reveal an interesting mixture of general similarities and clear improvements using setup II. Such improvements involve a realistic signature on travel times as well as enhanced shaking duration in some parts of the basin.
4. Waveform comparison of observed and synthetic data for one station and scenario where observations are available has been carried out. Significantly better fitting synthetics are achieved by the use of setup II. Due to the use of finite source and viscoelasticity in combination with an advanced and better resolved velocity model results in correct onsets for P and S waves, a good fit in amplitudes and an overall similar envelope of the seismograms. It is noteworthy that the first guess fit achieved from setup I has already shown some similarities.
5. A cumulative intensity map was derived for the three scenarios by simply stacking and averaging peak ground velocities and converting the result into Modified Mercalli Intensities. As can be expected, considering the above discussion, the results are very similar for both setups. This result is due to the fact that small-scale features in which the improvements of setup II appeared were disguised by the averaging procedure.

From the discussed points the conclusion seems valid, that full elastic simulations with the simplest basin model are capable of modeling main features of basin amplification adequately. Such simulations can be considered useful in order to produce

estimates on amplified ground motion in the presence of highly heterogenous geometries, such as sedimentary basins. However, in order to retrieve more realistic seismograms that can be analyzed in details and not only in terms of peak amplitudes a more complex approach, incorporating both finite source effects and viscoelastic attenuation seems to be more appropriate.

Chapter 6

Effects of Finite Source and Viscoelasticity for the M_L 4.9 2002 Alsdorf Earthquake Scenario

In this chapter results from numerical simulations and comparison with observational data for a magnitude 4.9 earthquake taking place on July 22, 2002 near the village of Alsdorf are presented. Special emphasize is given to variabilities of ground motion parameters due to the use of different source models and the effect of viscoelastic attenuation.

6.1 Motivation

Results presented in the previous chapter have demonstrated the significance of the effects of finite sources and viscoelasticity on wave propagation in the presence of sedimentary basins. Due to the dearth of observational data analysis of these effects remained on a qualitative level. In 2002 an earthquake took place near the village of Alsdorf close to the Cologne Basin, just after a network of strong motion receivers was completed. This event provides an excellent dataset in order to quantify effects of increased complexity in ground motion simulations demonstrated for the three scenarios of Roermond, Euskirchen and Düren. In this chapter the results are presented. Complexity of the simulation setup was increased in four steps, starting with a perfectly elastic point source approximation and ending with a viscoelastic finite source simulation. The resulting combinations are:

1. Point source / Elastic model
2. Point source / Viscoelastic model
3. Finite source / Elastic model
4. Finite source / Viscoelastic model

Table 6.1: Computational parameters for the simulations of the 2002 Alsdorf earthquake.

Parameter	Value
Spatial Discretization (horizontal)	100 m
Spatial Discretization (vertical)	50 - 120 m
Time Step	0.0035 s
Lowest S-wave velocity	1040 m/s
Grid Size (physical model)	1404 x 1404 x 180
Grid Size (computational model)	1444 x 1444 x 200
Number of Time Steps	16960
Simulation Time	60 s
Required Core Memory	110 GB
Computation Time	12h * 32 nodes

For each station location within the strong motion network therefore a set of four synthetics plus observational data is available and differential effects as well as similarities with observations were studied.

6.2 Setup

The setup chosen for the four simulations is the same as described in chapter 5 for the new setup. The most important parameters are briefly recapitulated in the following:

The model is discretized onto a computational grid with a spatial sampling of 100 m in horizontal direction in order to get a well resolved basin representation. In vertical direction a nonuniform discretization is applied. The grid size varies from 50 m in the sedimentary structure to 120 m in bedrock. The nonuniform grid was designed in order to have good resolution of basin depth and at the same time restrict the number of grid nodes for the simulations that have to be carried out. The technique is described in detail in chapter 3. In order to inhibit artificial reflection of wave energy from the model boundaries a 20 grid points wide region of perfectly matched layers (PML) is added to the physical model.

The overall size of the computational grid is $1444 \times 1444 \times 200$ grid points. 120 gigabytes of core memory are needed to carry out these simulations. The model is distributed over 32 nodes of the Hitachi SR8000 supercomputer at the Leibniz Rechenzentrum. A single simulation run of the described parameters consumes 12 hours at this machine. The code is parallelized using message passing between the individual nodes and automatically parallelized on the 8 processors within each node taking advantage of the OpenMP standard. The overall CPU time can therefore be calculated as $12 \times 8 \times 32 = 3072$ hours. A single processor of the SR8000 has a nominal peak performance of 1.5 GigaFlops. The code used for the simulations reaches about 17% of this theoretical performance. This is well within the range of performance expected for finite difference simulations. The computational parameters are compiled in table 6.1.

Table 6.2: Media parameters for elastic and viscoelastic models.

	Elastic Model	Viscoelastic Model
Sediment		
P-wave velocity	1732 - 3118 m/s	1732 - 3118 m/s
S-wave velocity	1040-1800 m/s	1040-1800 m/s
Quality factor P-wave	∞	100
Quality factor S-wave	∞	50
Bedrock		
P-wave velocity	5500 - 8000 m/s	5500 - 8000 m/s
S-wave velocity	3175 - 4619 m/s	3175 - 4619 m/s
Quality factor P-wave	∞	∞
Quality factor S-wave	∞	∞

All simulations are carried out using a delta function as source time function, therefore it is possible to filter the synthetic seismograms in different frequency ranges and study the frequency-dependent effects.

6.3 Model

The velocity model used for the simulations presented in this chapter is equivalent to the one described in detail the previous chapter. Key parameters are resumed in table 6.2.

6.4 Scenario

Subject to the investigations presented in this chapter is a recent earthquake within the Lower Rhine Embayment. The event occurred on July 22, 2002 at 5.45 UTC. Its epicenter was located near the town of Alsdorf, about 14 km northeast of Aachen and 54 km away from Cologne. In figure 6.1 the location of the epicenter is shown in relation to the geographic setting of the region. The 2002 Alsdorf earthquake was the strongest event since the 1992 Roermond earthquake, which was presented in the previous chapter and it also was the first damaging event since then. Slight building damage is reported from villages close to the epicenter such as Herzogenrath and Würselen, in the area of Düren chimneys on tenements collapsed. Figure 6.3 gives an impression of typical damage on roofs and chimneys.

The earthquake was felt in the whole area of the Lower Rhine Embayment as well as in large parts of surrounding areas in Germany, Belgium, the Netherlands, Luxembourg and France. The seismological survey of the Netherlands received nearly 4000 felt reports within one week after the event. The intensity map shown in figure 6.4 illustrates the extent the area where ground motion was felt. Isoseismal radii can be estimated as 10 km for Intensity VI, 25 km for intensity V, 50 km for intensity IV and 100 km for intensity III, which serves as the threshold value for human recognition of seismic

Table 6.3: Source parameters for the M_L 4.9 2002 Alsdorf earthquake as used in this study.

Parameter	Value
Latitude	50.885° N
Longitude	6.189° E
Depth	14 km
Strike	138°
Dip	55°
Rake	-73°
Seismic Moment	$8.4 \cdot 10^{15}$ Nm
Source radius	1.45 km

ground motion. Comparing this map with the well known basin outline reveals strong influence of local ground conditions on the observed intensities.

The surrounding area of the epicenter showed a raised microseismic activity with a number of magnitude 2.5 earthquakes a few kilometers to the south. This activity migrated northwards, before the earthquake of Alsdorf took place. Nevertheless there are no clear precursors associated with this earthquake. More than 25 aftershocks with maximum magnitude 2.6 have been observed in the days after the Alsdorf event. The source mechanism of the 2002 Alsdorf earthquake have been investigated by the Bensberg Seismological Observatory and the Seismological Central Observatory of the German Regional Seismic Network and the Gräfenberg Array (SZGRF). The event took place on the Rur boundary fault in a depth of about 14 km, the source mechanism was normal faulting. The source parameters for the Alsdorf earthquake are listed in table 6.3. Figure 6.2 shows the fault plane solution for this event.

6.5 Observations

The seismological observatory of Bensberg (University of Cologne) maintains a network of more than 20 permanently recording stations. Short period seismometers are attached to these stations recording three-component (East-West, North-South and vertical) of ground motion for local and remote earthquakes. Figure 6.1 shows the station distribution in a topographical context of the study area.

As a consequence of the poor data coverage on the occasion of the Roermond earthquake in 1992 and the obvious impact of sedimentary structure on ground motion characteristics stations were condensed within the margins of the basin. In figure 6.5 the coverage of sediments by the receiver distribution is illustrated. Black lines in this graph indicate isolines of sediment depth. Receivers of the Bensberg seismic network are shown as red crosses with their individual station code attached. From this plot a good coverage of different basin depth as well as prominent features of the basin topography such as steep flanks of the basin can be recognized.

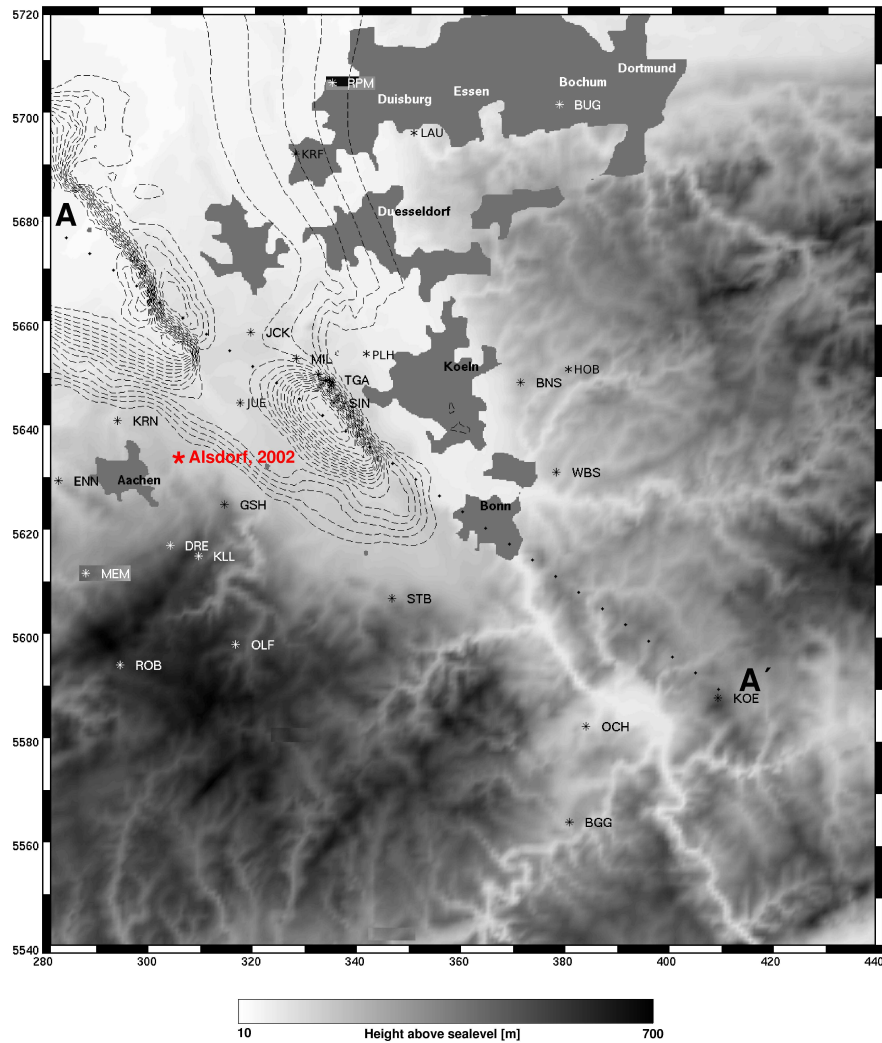


Figure 6.1: Location of the 2002 Alsdorf earthquake (M_L 4.9) in its geographic context. Dimensions and directions are given by UTM coordinates based on sector 32 U. Grayscale shading depicts regional topography. The sedimentary basin depth is indicated by dashed isolines in 100 m intervals. The basin reaches a maximum depth of about 1900 m. Seismic network stations are marked as stars and by their station codes. A synthetic profile A-A' with 30 receivers is shown as black dots. Urban areas within the Lower Rhine Embayment are colored dark-gray.

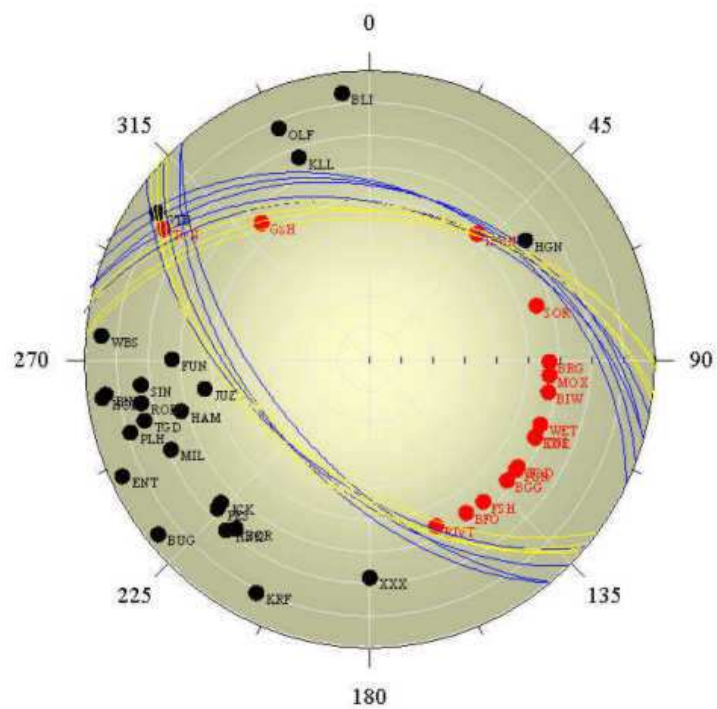


Figure 6.2: Fault plane solution for the M_L 4.9 2002 Alsdorf earthquake (after Hinzen (2002)). Black and red dots indicate stations observing positive and negative amplitudes of the first arrivals, respectively.



Figure 6.3: Slight damage onto buildings (broken chimneys and damaged roofs) could be observed in the epicentral region of the M_L 4.9 2002 Alsdorf earthquake (after Hinzen (2002)).

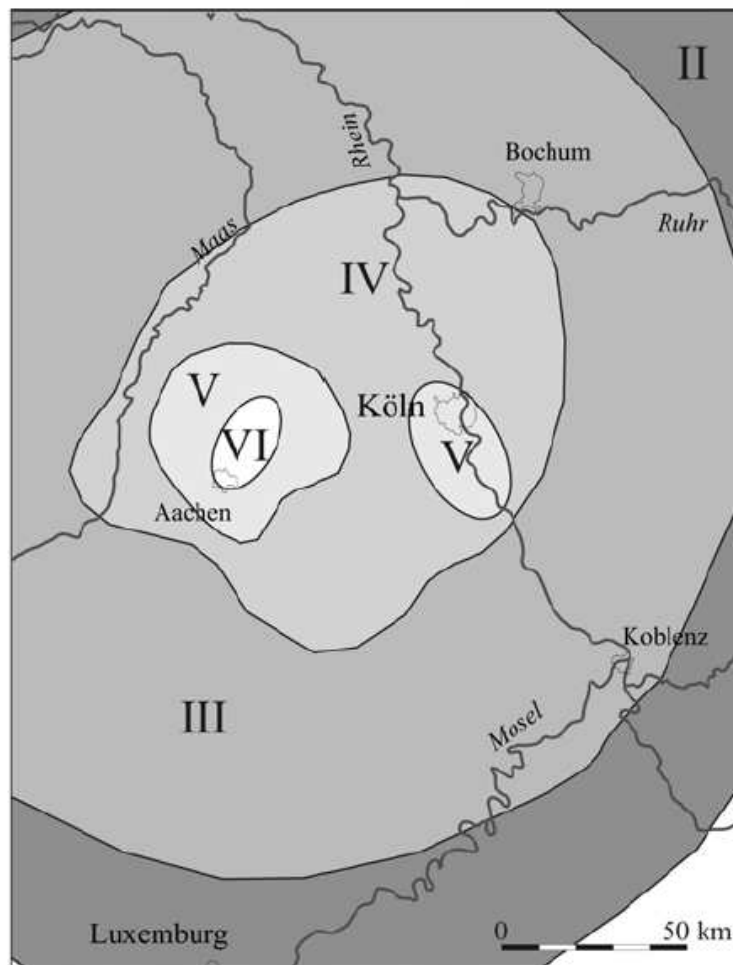


Figure 6.4: Map of observed seismic intensities for the M_L 4.9 2002 Alsdorf earthquake (after Hinzen (2002)).

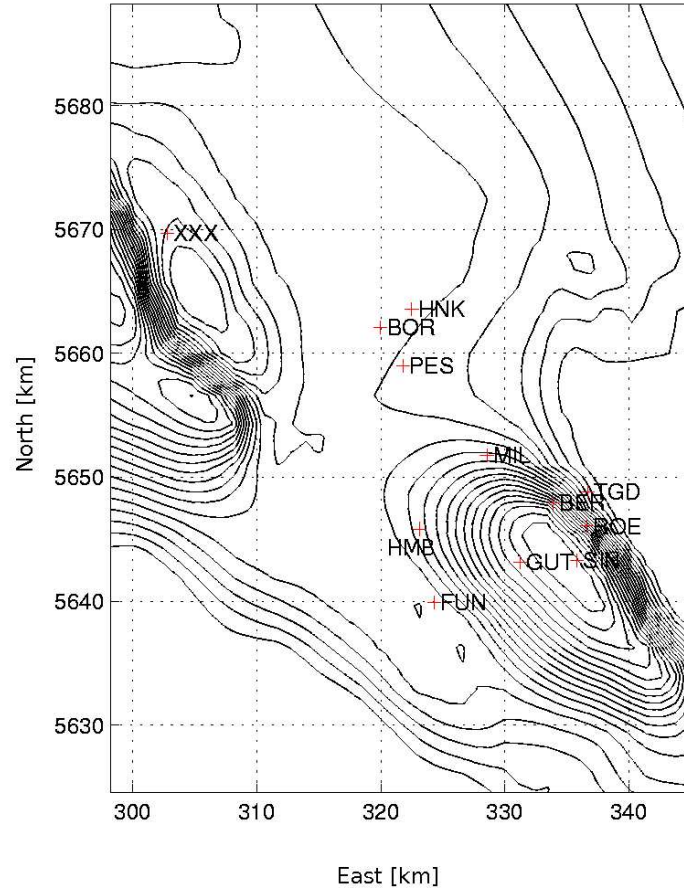


Figure 6.5: Isoline plot of basin depth showing the distribution of seismic stations of the recently employed subnet. Stations are demarked as red crosses attached with their abbreviated names.

Besides sedimentary depth another factor was influencing the choice of station locations in this network. The main faults within the Lower Rhine Embayment are well known as can be recognized from figures in chapter 3. These faults are the origin of tectonic earthquakes in this region. The seismic stations were arranged in order to have a good coverage of epicentral distances with respect to any fault.

When the 2002 Alsdorf earthquake took place on the Rur boundary fault (see figure 6.1) a range of 20 to 120 km epicentral distance was documented by recordings. In table 6.4 site parameters for the stations are presented. Column “Epidistance” embodies distances calculated with respect to the epicenter of the Alsdorf event, whereas column “Sitecondition” indicates whether the station is located within the basin margins or on bedrock.

Table 6.4: Stations of the Bensberg seismic network with their individual site conditions and epidistance to the Alsdorf, 2002 earthquake.

Code	Station Name	Lat.	Long.	Epidistance	Sitecondition
BER	Bergheim	50.959°	6.636°	32.2 km	Sediment
BNS	Bensberg	50.964°	7.176°	68.3 km	Bedrock
BOR	Borschemich	51.082°	6.430°	27.6 km	Sediment
FUN	Funkhaus	50.884°	6.502°	21.7 km	Sediment
GMA	Gut Margaretenhöhe	50.915°	6.599°	28.7 km	Sediment
HMB	Hambach	50.937°	6.483°	21.2 km	Sediment
HNK	Hochneukirch	51.096°	6.465°	30.3 km	Sediment
KOE	Köppel	50.425°	7.732°	120.0 km	Bedrock
MIL	Millendorf	50.992°	6.557°	28.2 km	Sediment
PES	Pesch	51.055°	6.457°	26.5 km	Sediment
ROE	Roetschberg	50.943°	6.674°	34.4 km	Sediment
SIN	Sindorf	50.918°	6.664°	33.3 km	Sediment
STB	Steinbachtalsperre	50.594°	6.840°	55.9 km	Bedrock
TGD	Tagebau	50.968°	6.674°	35.1 km	Sediment

6.6 Results

In this section results from simulations of the four described setups with increasing complexity are compared with one another as well as with data. Emphasize is put on the overall accuracy in reproducing observed data and in differential effects between the different setups. Using a delta shaped source time function it is possible to study effects due to finite sources and viscoelasticity in different frequency ranges and make some conclusions about the limits in which approximations are considered to be valid.

6.6.1 General Problems of Quantification

General problems arise when synthetic seismograms of high frequency content are compared with data. At frequencies above 0.5 Hz significant texture of the Earth at all length scales below 10 km affects the observed time series (Wilson and Pavlis (2000)). Complexities including scattering at topographic structures (Petersen et al. (1994); Ashford et al. (1997)), the influence of unconsolidated material in the uppermost layers (Anderson et al. (1996)) as well as complex three-dimensional effects (Rial (1996)) result in individual signatures on the seismogram. The combination of all these effects at the same time is currently still beyond the ability of deterministic ground motion modeling. Visually comparing the model cross sections shown in the previous chapter with geological profiles presented in chapter 4 reveals a number of simplifications on the model: 1) The model does not include any inclined structures besides the sediment-bedrock interface. 2) In horizontal direction there are also no steps in velocity modeled. Such features are apparent at practically all fault zones in the model space and can be considered to affect both the wave propagation and the wavefield emanating from a source located on such a fault (e.g. Ben-Zion and Andrews (1998); Ben-Zion (2001);

Ben-Zion and Huang (2002)). 3) The homogenous gradient in velocity is only a second level approximation to the real complexity of a vertical velocity profile. 4) Restricting seismic velocities in the uppermost layers prohibits a modeling of site effects.

Taking into account the wavefield complexity corresponding to the model as it is obvious from the snapshots it is clear, that such features would have an impact on waveforms in a frequency range of 1 Hz and slightly above as is the case in this simulations. Therefore synthetic seismograms will always reveal an idealized picture of the realistic data. Directly comparing such synthetics with observed seismograms can result only in a fit in terms of a similar seismogram from a similar event. A strict wiggle-by-wiggle accordance cannot be expected. Alternatively in this study seismograms are characterized by a number of key parameters, which are considered to be associated more with the whole trace than with single onsets. Such parameters contain peak ground velocity, envelope and frequency content. Synthetic seismograms coinciding with observations by means of this parameterization can be considered equivalent to observed seismograms for the use in seismic hazard estimations.

6.6.2 Profiles

To get a first impression of the extent of conformity and variability of the results from the four described setups seismogram sections are shown on the following pages. The profiles are constructed as described in the previous chapter. A profile of 30 receivers is dissecting both deep basin depressions which are ranked as the most prominent features of the sedimentary structure and therefore are expected to produce the strongest effects. The basin topography is indicated in black below the zero line in order to ease affiliating effects in waveforms to the underlying structure. In order to ease the recognition of individual effects on waveforms blow-ups of prominent phases are embedded in the plots.

Point Source Elastic / Finite Source Elastic Figure 6.6 shows a comparison of seismograms from elastic simulations using a point source (plotted in black) with ones produced by a finite source (red). Seismograms are scaled equally for the different simulation types, but individually for different components. The comparison is carried out for three components and the most prominent features are described in the following.

Most obviously the point source simulations produce much higher amplitudes. Peak amplitudes for the point source simulations are often caused by a strong resonance effect within the basin. The interpretation is that this is due to the idealized geometric conditions of point source and basin margins which lead to an overestimated amplification of seismic waves. For the finite source simulations, already with a relatively small source radius as is the case for this scenario earthquake, these resonance effects are reduced significantly due to more realistic superposition of waves at the source region.

The resulting wavefield has not the idealized shape that tends to result in resonant shaking. The point should be emphasized here that already for source radii of only 1450 meters the point source approximation seems not valid anymore in the presence of strong heterogeneities interacting with the wavefield. Certainly, resonant amplification plays an important role in the understanding of basin amplification. Point source approximations appear to be too likely in producing these effects. The finite source simulations as well as later presented observational data both show the same effects but distributed more sparsely and much weaker.

Point Source Elastic / Point Source Viscoelastic In figure 6.7 three component seismograms from point source simulations are presented. In this graph results from pure elastic modeling (black traces) are compared with viscoelastic ones (red traces). Both simulations produce resonant reverberations as discussed in the paragraph above. Therefore it is also made clear that this effect is an intrinsic feature of the point source and not due to the elastic modeling of the sedimentary basin structure. Nevertheless the effect is damped strongly by viscoelastic attenuation in the respective traces. It will be demonstrated in subsection 6.6.3 by means of peak ground velocity considerations this leads to an overrating of the attenuation effect.

The increasing effect of attenuation with seismogram time can be seen clearly. A closer view reveals the correctly modeled dispersion effect and therefore change in

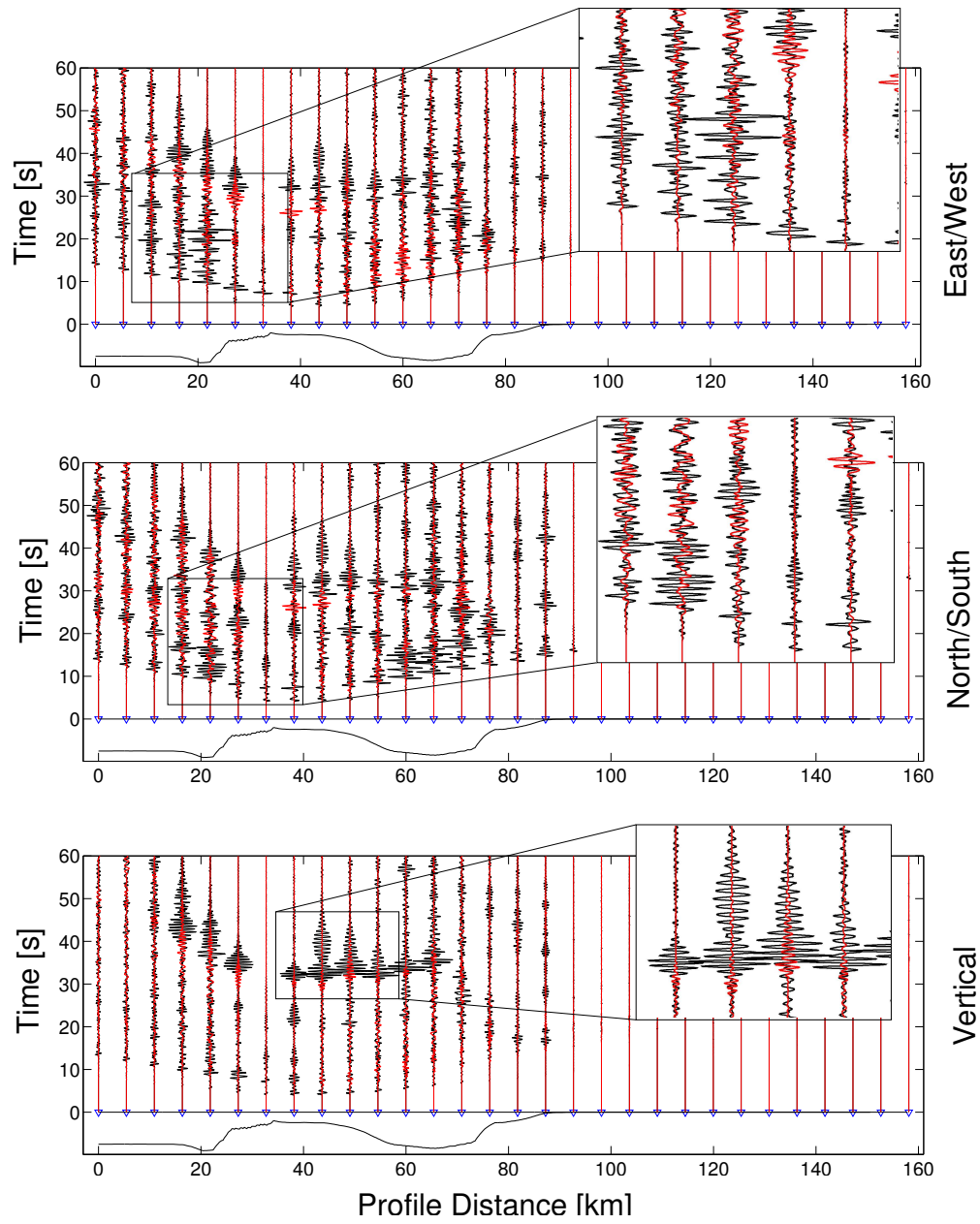


Figure 6.6: Profiles of synthetic three component seismograms. Black trace: Point source elastic simulation, red trace: Finite source elastic simulation. Embedded blow-ups clarify the effects on the waveforms.

waveform due to the use of standard linear solids. A simple damping factor as suggested by Graves (1996) for the use in finite difference ground motion simulations in the presence of attenuating structures would not be capable of modeling this behavior. It is also notable that amplitudes of early arrivals are therefore slightly modified by the incorporation of viscoelasticity. The strong impact of finite source effects on these as it has been observed in the comparison above is a possibility to distinguish both in first order damping effects. It will be discussed later that both mechanisms are necessary in order to reproduce realistic amplitudes over a broad range of epicdistances and site conditions.

Finite Source Elastic / Finite Source Viscoelastic Seismograms in the profile sections presented in figure 6.8 are both produced by a finite source. Traces achieved by pure elastic simulation are plotted in black, whereas red traces refer to viscoelastic modeling. The effect of viscoelastic damping is significantly observable for all traces within the basin, whereas outside only the red overlying traces are visible. From the change in color it can be recognized at a first glance that the viscoelastic effect increases with seismogram time. Whereas the first arrivals are apparently plotted in red, because traces are identical and so only the overlying color is recognizable, black color becomes more and more visible with increasing time.

On the vertical component still reverberations are recognizable, however amplitudes caused by this are in a reasonable range and the modeled effect is much more trustworthy as it was the case for point source simulations. The seismograms also reveal strong influence on the frequency content. Traces recorded above the deepest parts of the basin show significant long period waveforms due to superposition of individual phases within the wavefield.

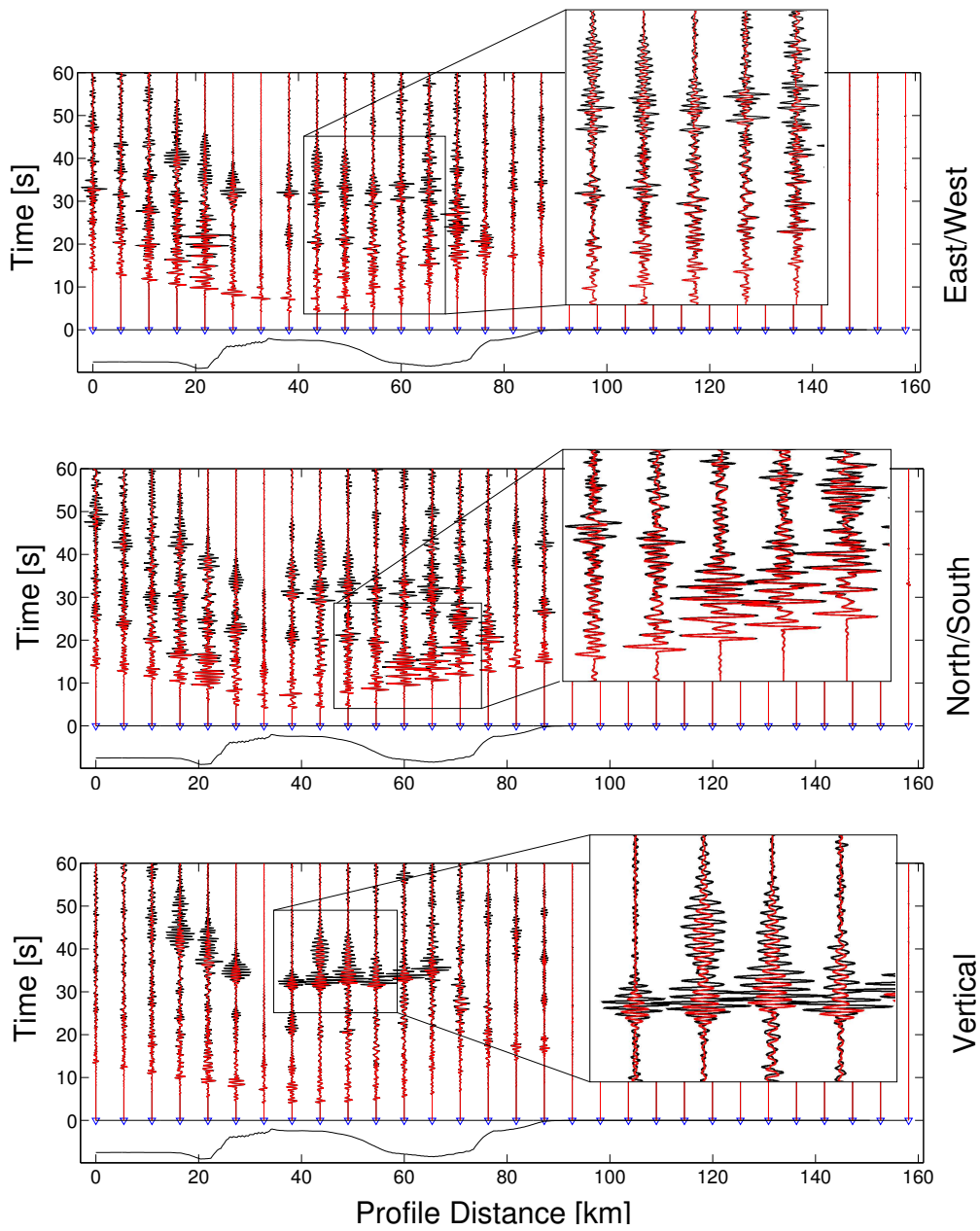


Figure 6.7: Profiles of synthetic three component seismograms. Black trace: Point source elastic simulation, red trace: Point source viscoelastic simulation. Embedded blow-ups clarify the effects on the waveforms.

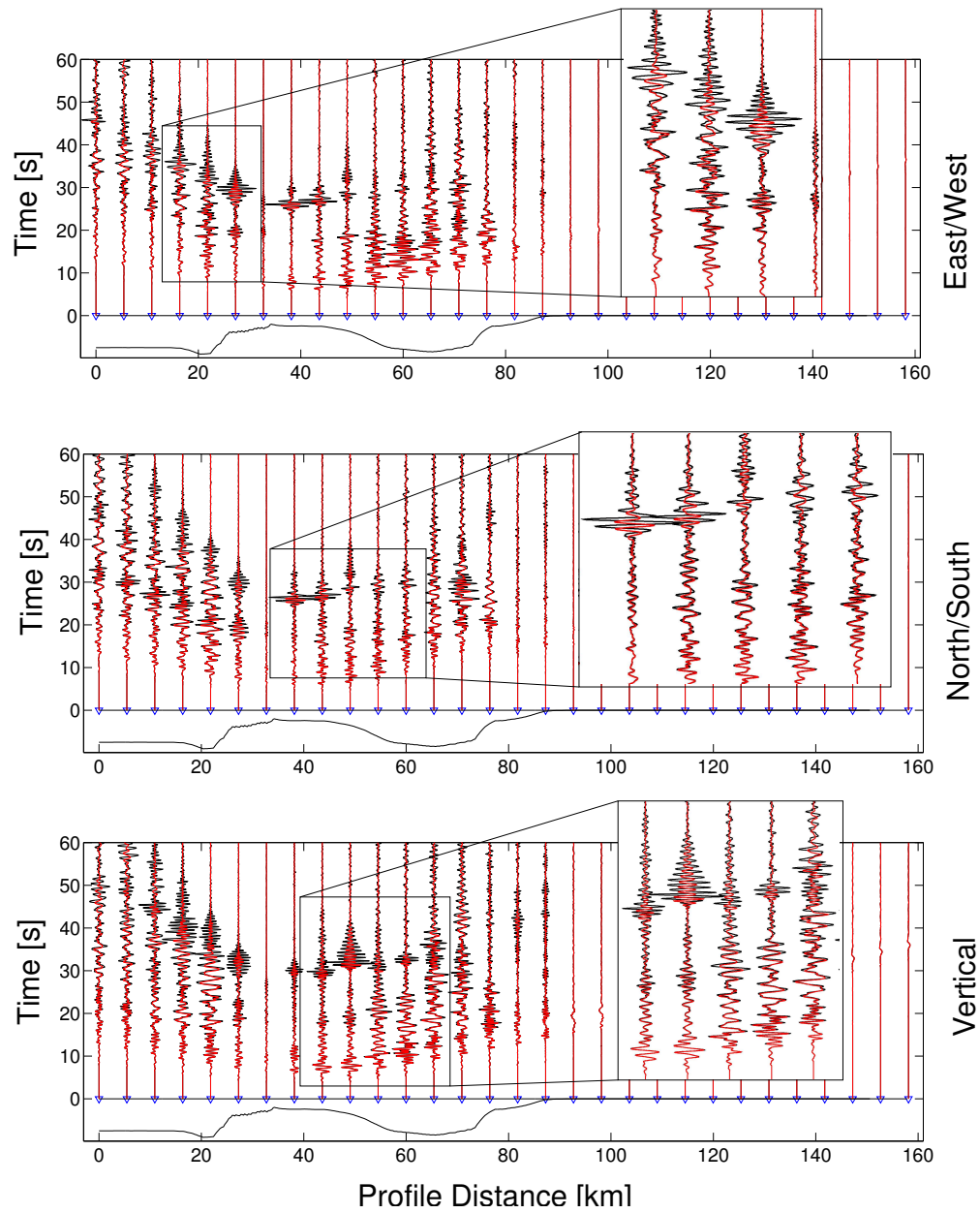


Figure 6.8: Profiles of synthetic three component seismograms. Black trace: Finite source elastic simulation, red trace: Finite source viscoelastic simulation. Embedded blow-ups clarify the effects on the waveforms.

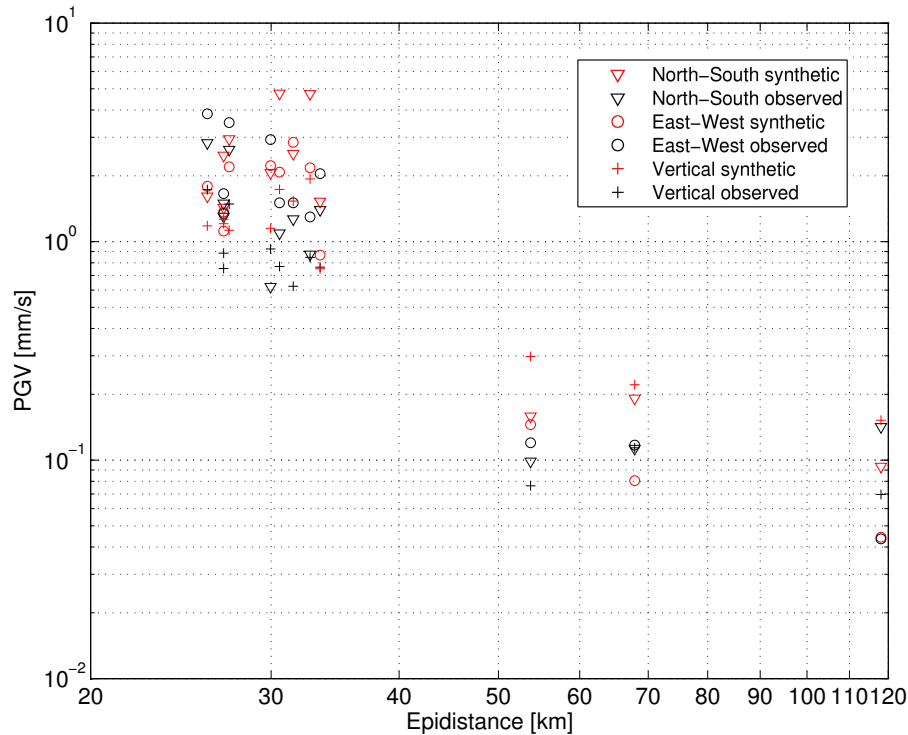


Figure 6.9: Logarithmic plot of observed (black) and synthetic (red) peak ground velocities vs. epicdistance. Synthetics are achieved using a finite source model and including viscoelastic attenuation in the simulations. Horizontal East-West and North-South component are demarked as circles and triangles, respectively. Crosses indicate vertical ground motion.

6.6.3 Peak Ground Velocity

When numerical simulations are considered as a tool for the improvement of shaking hazard estimation peak ground velocity (PGV) is one of the most important parameters of the synthetics. Therefore special emphasize is put onto this issue.

6.6.3.1 Peak Ground Velocity versus Offset

For the Alsdorf earthquake, the station distribution of the Bensberg seismic network provides receiver offsets ranging from 20 to 120 km for the comparison of peak amplitudes. As the stations with the largest epicentral distances are located on bedrock a disproportional strong amplitude decrease compared to the closer ones is apparent.

The range of observed and synthetic PGVs for the 2002 Alsdorf earthquake is illustrated in figure 6.9 in a logarithmic plot. Observed values are plotted in black, whereas synthetic results achieved with the use of a finite source and a viscoelastic model are plotted in red. For each station three components of ground motion are shown: Triangles demark East-West horizontal component, the North-South component is plotted as circles and crosses demark vertical ground motion. It can be recognized, that observed and synthetic values coincide well within the variability of the observations.

This result is encouraging when the use of finite difference simulations as a potential tool in hazard assessment is concerned. Nevertheless a more accurate quantification of the misfit between simulated and observed data is inevitable.

6.6.3.2 Ratio of Synthetic and Observed PGV versus Offset

To quantify the fit between data and synthetics in terms of peak amplitudes over a large range values a simple approach is made. The ratio of synthetic to observed PGV is calculated for each station and plotted in a half logarithmic plot against the epicdistance. Individual stations are labeled in the plots by their station code. These comparison are carried out applying a low pass filter with 1 Hertz cut-off frequency to each component. The results are discussed in detail in the following paragraphs.

East-West component In figure 6.10 ratios off synthetic to observed PGV are plotted. Colors indicate individual simulation setups:

Red: Point source - Elastic

Blue: Point source - Viscoelastic

Green: Finite source - Elastic

Black: Finite source - Viscoelastic

In the following improvements with increased simulation complexity are described.

The maximum misfit for point sources is 5.5, for finite source elastic 5.3 and for finite source viscoelastic it decreases to 3.3. Apparently for one station misfit between observed and synthetic peak amplitudes has increased with complexity of the simulation. However the overall variation in PGV ratios is significantly lowered by the introduction of a more realistic model.

North-South component Figure 6.11 shows the analog plot for the North-South component seismograms. The results demonstrate clearer improvement as on the East-West component.

Maximum misfit decreases from 10.7 for the point source approximations to values below 4 for the finite sources. Finite source seismograms lead to an underestimation of peak ground velocity (in this frequency band) for most of the stations. The variation is significantly smaller for the finite source approximation. The underestimation could therefore be solved with a static correction factor. In the next section the significance of this point in terms of waveform modeling is discussed in more detail. PGVs from finite source simulations are in reasonable agreement with the observed ones over a range of 100 km epicentral distances. Finite source simulations are capable of modeling both PGVs inside the basin and on bedrock.

Vertical component PGV ratios of observed and synthetic vertical ground motion recordings are shown in 6.12. The results manifest the ones obtained by the horizontal components.

Maximum misfit for point source approximations is close to 13, the finite source ones lay below 5. Whereas on the North-South component point source simulations result

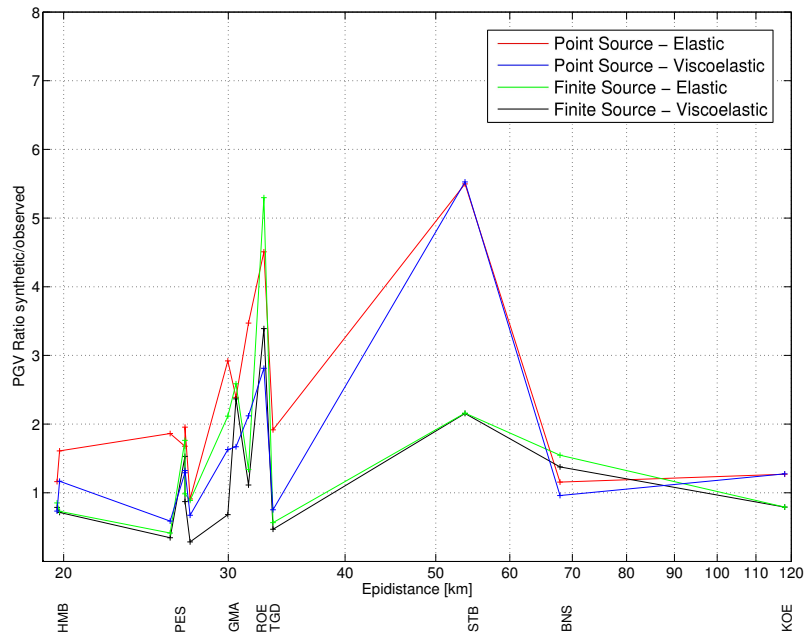


Figure 6.10: Ratio of synthetic to observed peak ground velocity at Bensberg seismic network stations. Values are derived from East-West component seismograms filtered at 1 Hz. Red: Elastic simulation with point source, blue: Viscoelastic simulation with point source, green: Elastic simulation with finite source, black: Viscoelastic simulation with finite source.

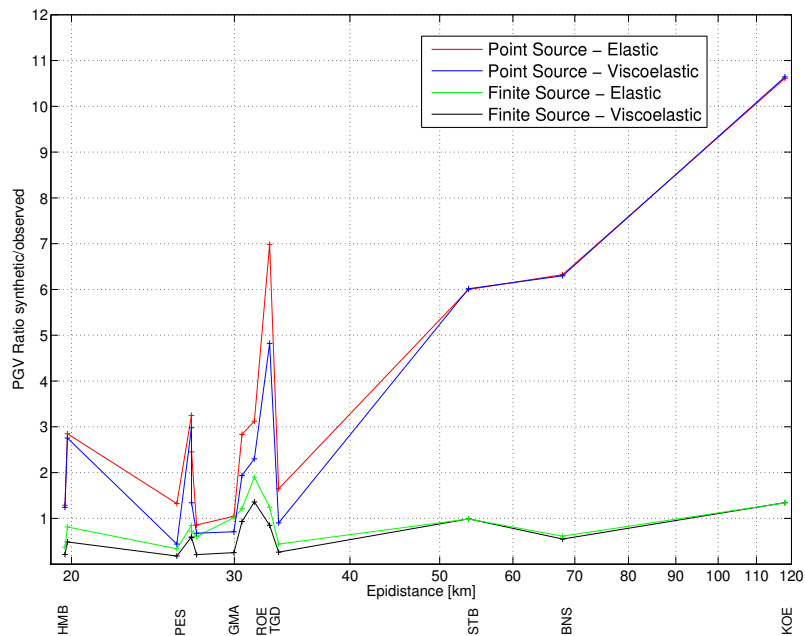


Figure 6.11: Same as figure 6.10 for the North-South component.

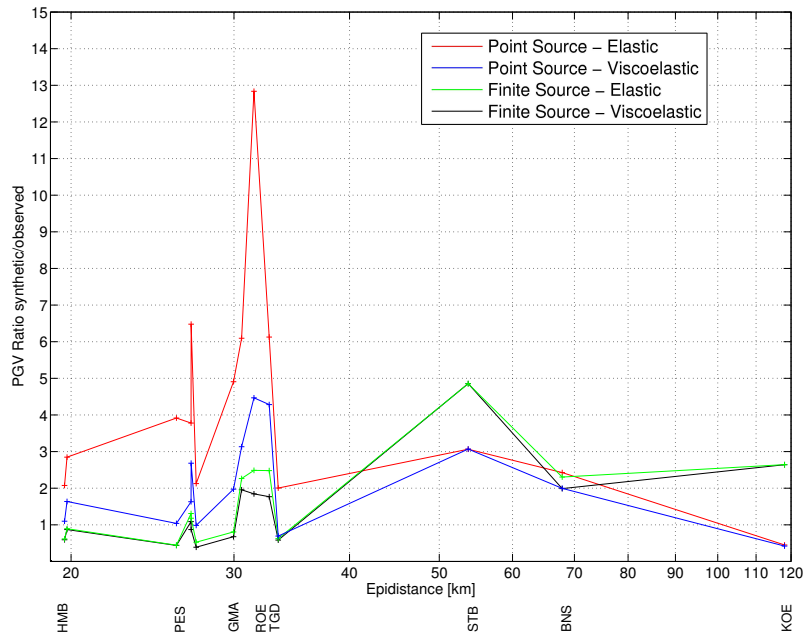


Figure 6.12: Same as 6.10 for the vertical component.

in a clear overestimation of amplitudes at large epicentral distances and on bedrock stations, the result for the vertical component is opposite. Stations within the sedimentary basin are overestimated significantly in terms of peak amplitudes. The finite source simulations show largest misfits for the stations far from the source and on bedrock. Nevertheless, variation in PGV ratios is distinctly smaller for finite source simulations.

Combined investigation of PGV ratios between observed and synthetic seismograms shows clear improvements due to the incorporation of viscoelastic attenuation and finite source effects in the simulation. The main issues are:

1. The overall misfit in peak ground velocity has been significantly reduced.
2. The simulations show a reasonable variation of misfit over the whole range of epicentral distances and site conditions.
3. Only the finite source viscoelastic simulations are capable of reproducing amplitudes within reasonable error margins for all stations and all components.

6.6.3.3 Ratio of Synthetic and Observed PGV versus Frequency

In order to analyze the frequency dependency of the effects of finite source and viscoelasticity, PGV ratios like the ones shown above are averaged over all stations in a frequency range from about 0.15 to 1.25 Hz. The frequency range used in this study is limited on the high frequency side by the grid per wavelength criterion. On the low frequency side a limitation is introduced through the seismogram length.

East-West component In figure 6.13 the above described plots are presented derived from East-West component seismograms. For both finite source and point source simulations the signature of viscoelastic attenuation is clearly evident in the frequency characteristics of PGV ratio. Starting with very little impact at the lowest frequencies the impact of attenuation increases continuously with frequency. This signature is in agreement with the expectations from the characteristics of standard linear solids. The frequency dependence for finite source simulations differs significantly from that obtained by point source simulations. Whereas the point source starts with a reasonable fit a clearly increasing misfit with frequency is observable. This is in good correspondence to the expectation that point source approximations yield valid results for a low frequency approximation whereas they lack correct high frequency content. PGV ratio versus frequency behavior for the finite source simulations shows an interesting overprediction of the low frequency content, whereas the high frequency part is accurately matched. The nearly flat part for frequencies from 0.6 Hz to the maximum frequency of 1.25 Hz proves accurate modeling of the short-period ground motion by the finite source viscoelastic simulation.

North-South component In figure 6.14 the same kind of plots are shown derived from North-South component seismograms. As expected from the results shown in 6.11, the best fit with data is obtained for this component of motion. Whereas a clearly increasing misfit with frequency is prominent for the point sources, the finite source simulations yield good agreement over the whole frequency range expressed in ratios close to one for a large part of the spectrum. Nevertheless, elevated low frequency content can be observed for the finite source simulations. Interestingly this peak coincides roughly with the one observable for the East-West component between 0.2 and 0.3 Hz. Clear signature of viscoelastic damping can be found for all simulations. The increasing difference with frequency between elastic and viscoelastic simulations is in agreement with the expectations from the underlying physics.

Vertical component Figure 6.15 displays PGV ratio values plotted versus frequency for the vertical ground motion.

Point source simulation results show a clear trend of increasing errors with higher frequencies. The ratio of synthetic to observed PGVs reach an average over all stations of more than 8. For the finite source results the low frequency peak already observed on the two horizontal components also appears on the vertical component. To higher frequencies PGV ratio derived for the finite source simulations becomes stable above about 0.7 Hz and values are close to one. The effect of viscoelasticity is visible for

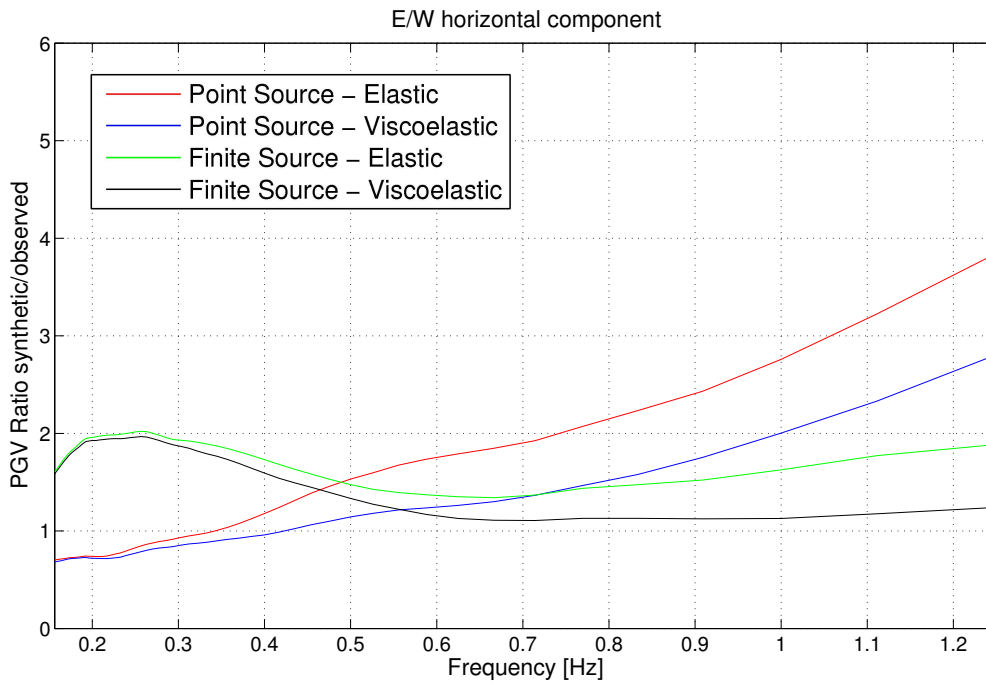


Figure 6.13: Frequency dependence of the ratio of synthetic to observed peak ground velocity for the East-West component averaged over all stations.

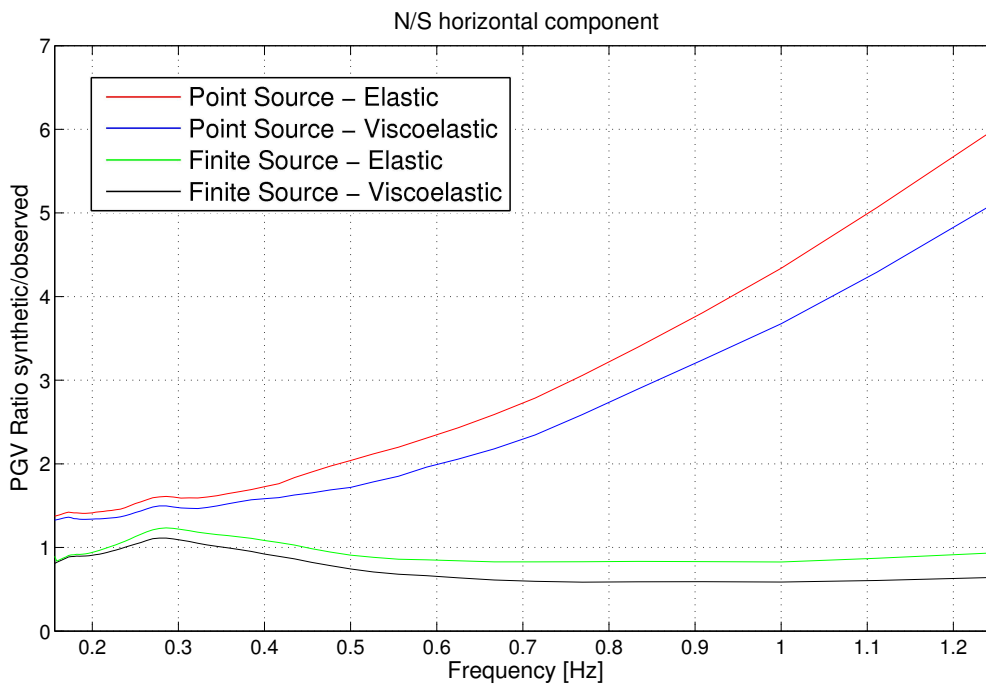


Figure 6.14: Frequency dependence of the ratio of synthetic to observed peak ground velocity for the North-South component averaged over all stations.

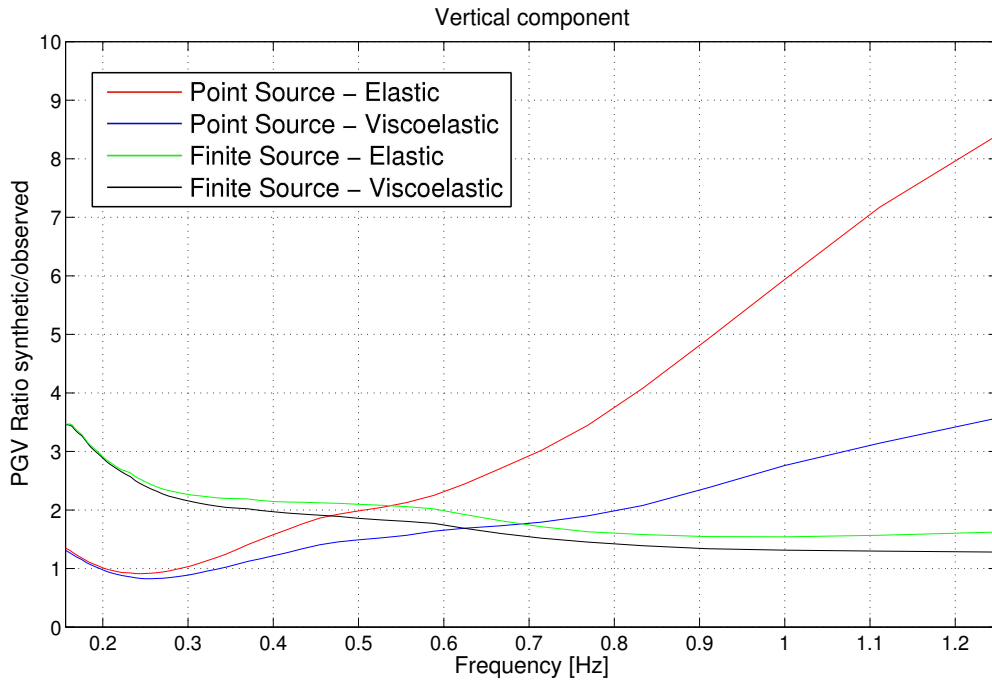


Figure 6.15: Frequency dependence of the ratio of synthetic to observed peak ground velocity for the vertical component averaged over all stations.

the finite source simulations as it was for the other components. This effect additionally improves the ratio of synthetic to observed peak ground motion for the finite source model. Whereas for the attenuation signature in the components above was in agreement with the physics, this is not the case for the vertical component of point source simulations. The large difference between viscoelastic and elastic simulations is caused by artificial reverberations as can be seen on the corresponding seismograms. These signals are affected strongly by the viscoelastic attenuation. Their appearance is restricted to the simulations carried out with point source approximation.

Combining the results for all three components of motion leads to the following conclusions:

The incorporation of finite sources into the simulations results in a clear improvement on the high frequency part of the seismograms. Point source approximation results in significantly overrated amplitudes in the higher frequency parts. Combination of finite sources with viscoelasticity is capable of producing reasonable flat ratios of synthetic to observed peak ground velocities with distance. The finite source plots showed for all components a significant overprediction of amplitudes in the long period range.

This behavior can be explained by the idealized finite sources used in this study. The model of a homogeneous circular fault appears to overestimate the effect of finite sources at a given radius. Due to optimal superposition of excited waves a large part of the high frequency content is deleted and the energy is shifted into the long period part of the spectrum. Therefore the influence of source extent appears overrated. As the plots shown above are based on a comparison between synthetics and observations the result can be interpreted as shortcoming of the model. Finite source radii estimated

from observations are based on a model which includes intrinsically heterogeneities in the source. The best fitting idealized uniform source as is used in this study must be significantly smaller than these. Another way of dealing with this problem would be the incorporation of random heterogeneities into the source area. For example the rupture velocity or the individual portions of seismic moment associated with the single point sources on the plane could be randomly undulated. This effect is significant already for the source dimensions and magnitudes in this study.

6.6.4 Seismogram Comparison

As discussed in section 6.6.1 a wiggle-by-wiggle coincidence of synthetic and observed seismograms can not be expected given the limitations of the simulation approach. Nevertheless a number of stations from the Bensberg seismic network are chosen in order to reveal waveform effects due to the incorporation of both finite sources and viscoelasticity. In figure 6.5 the distribution of stations within the basin is shown. The following stations have been chosen in order to show effects due to different location with respect to the basin:

BNS - Seismic station at Bensberg. This station is located on bedrock at a distance of 68 km from the epicenter of the 2002 Alsdorf earthquake.

PES - Station Pesch is located on sediments in a shallow part of the basin at an epicentral distance of 26 km.

GMA - The seismic station at Gut Margaretenhöhe is placed above one of the deepest parts of the basin. Its epicentral distance is about 29 km.

MIL - The seismic station at Millendorf is interesting due to its location above one of the basin flanks 28 km away from the epicenter of the 2002 event.

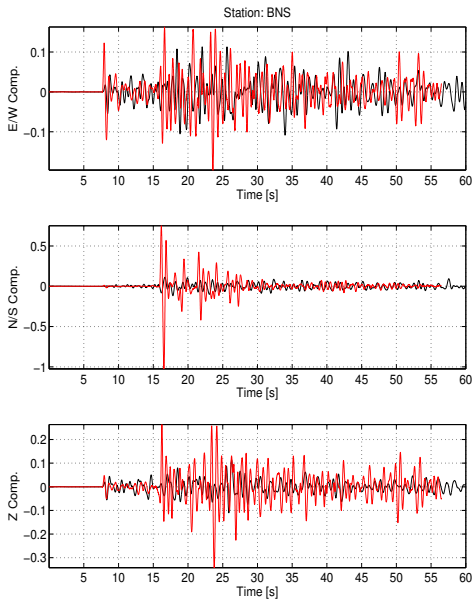
On the following pages three component seismograms for the four simulation types (point source - elastic, point source - viscoelastic, finite source - elastic, finite source - viscoelastic) are shown for these receivers. In order to illustrate differential effects between these simulation types as well as a comparison with observations for each station two kinds of plots are presented.

1. The first figure displays four sets of seismograms including the two horizontal components East/West and North/South as well as vertical ground motion. For all components synthetics, plotted in red, are compared with observed data which are represented by black lines.
2. The following two figures show a closer view. Each plot contains three seismograms: observed data and two different simulations in order to focus on individual effects. First the effect of finite source is considered. The traces shown in this graph are: black - data, blue - point source elastic, red - finite source elastic. In the second graph the effect of viscoelastic attenuation is examined, displaying the following traces: black - data, blue finite source elastic, red - finite source viscoelastic.

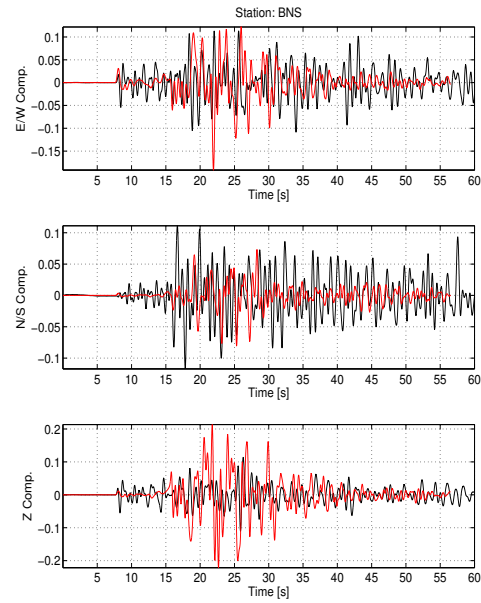
Results for the individual stations are discussed in the following paragraphs.

Station BNS A comparison of seismograms of the four different simulation types as it is shown in figure 6.16 for station BNS (Bensberg), which is located on bedrock at a epicentral distance of 68 km reveals several significant effects. Arrival times for both P and S-waves are matched properly for both finite source and point source simulations. Due to the site nature as a bedrock site and the direct path propagating only through bedrock, which is not object to viscoelastic damping amplitudes of first arrivals, both P and S-waves are not affected by the incorporation of viscoelasticity into the model. In contrast, amplitudes and waveforms within the coda are strongly affected by attenuation. This is recognizable for both finite source and point source simulations. The reason is that these onsets are related to surface waves generated within the basin and secondary reverberations which can be seen on the snapshots for all scenarios in the previous chapter. This is illustrated in figure 6.18. It is obvious that amplitudes are affected strongly by the source model. Whereas amplitudes for the East-West and vertical component are in rough agreement with the observations for the point source model shown in the left column, the North-South component seismograms show significantly overrated amplitudes. The finite source simulations, shown in the right column, are capable of producing roughly matching amplitudes for all components of ground motion. Figure 6.17 illustrates clearly, that amplitudes on two components (horizontal East-West and vertical) which are already matching for the point source approximation are kept at the same level whereas the ones on the North-South component are affected distinctly by the use of a finite source. This differentiated effect on individual components is important in order to achieve an improved general fit. Seismograms produced by the finite source simulations are not only linearly scaled representations of the ones achieved with a point source. Similar observations can be made for the overrated P-wave amplitude visible on the East-West component seismogram produced by a point source. The usage of a finite source model reduces these phases to a more realistic level, while keeping the roughly matching amplitudes on shear and surface waves. From the comparison of seismograms on this station it already becomes clear that the finite source model results in a more realistic representation of ground motion which could not be achieved by an adjusted point source.

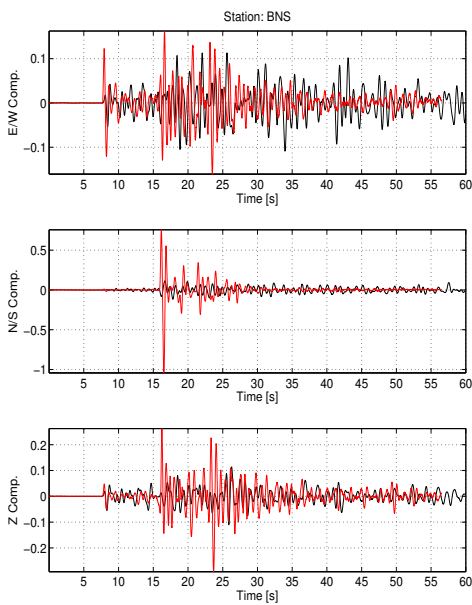
a) Point Source / Elastic



b) Finite Source / Elastic



c) Point Source / Viscoelastic



d) Finite Source / Viscoelastic

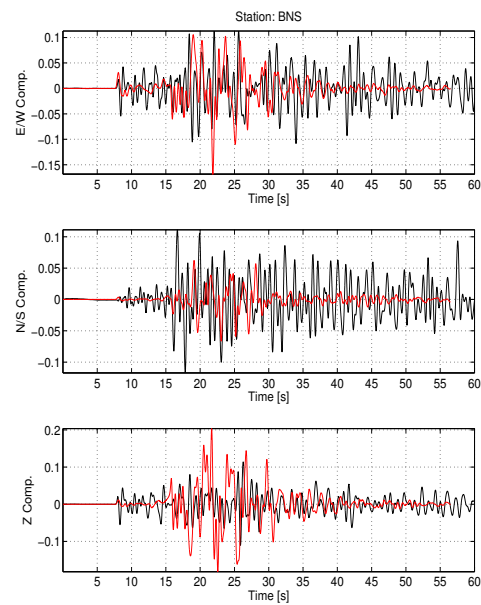


Figure 6.16: Seismogram comparison at station BNS. Synthetics (red traces) from four simulation types (as indicated) are compared with observed data (black). Amplitudes are given in cm/s.

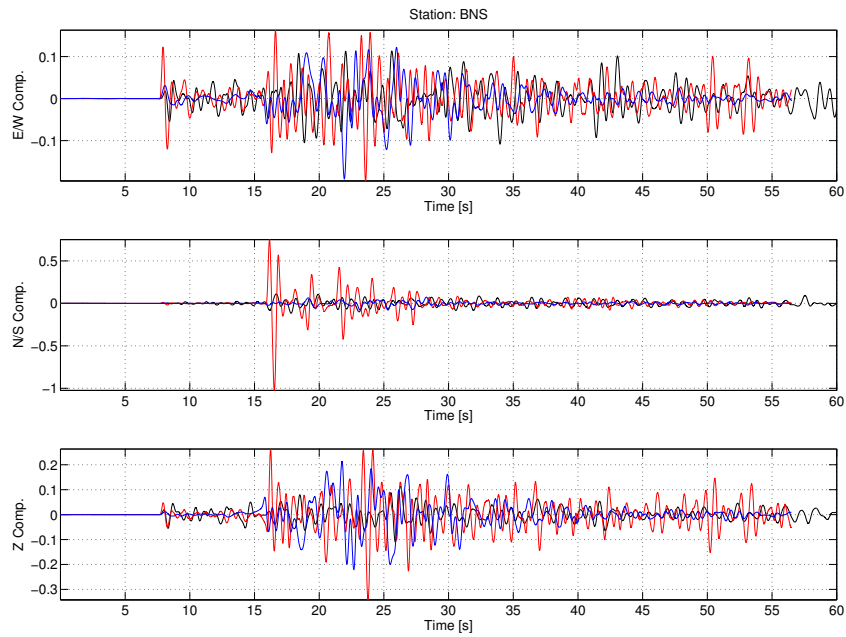


Figure 6.17: Comparison of point source (blue traces) and finite source (red traces) synthetics, both achieved with an elastic model, with data (black) at station BNS. Amplitudes are given in cm/s.

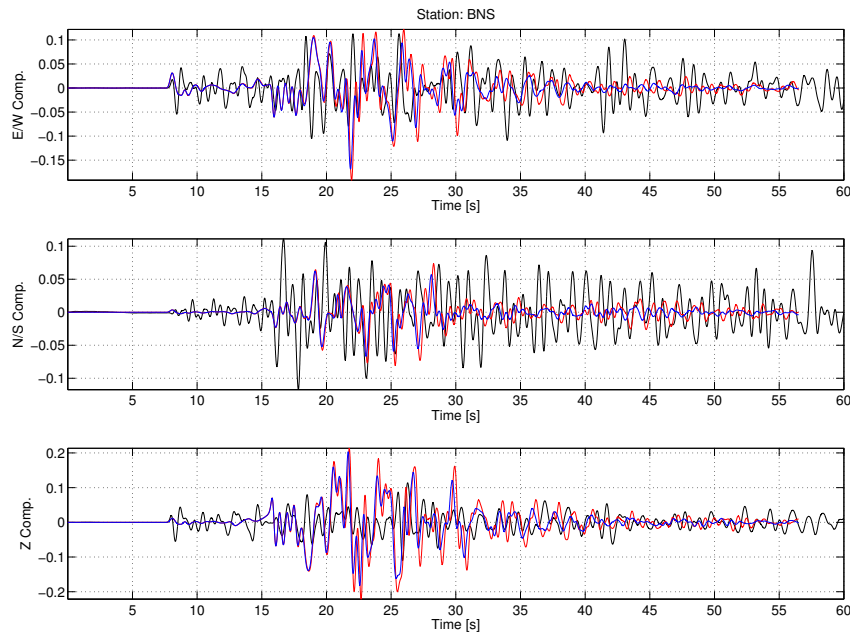


Figure 6.18: Comparison of elastic (blue traces) and viscoelastic (red traces) synthetics, both achieved with finite source simulations with data (black) at station BNS. Amplitudes are given in cm/s.

Station PES Performing the analog comparison at station PES (Pesch), located at an epicentral distance of 26 km on sediments within the basin shows similar results due to different reasons.

Taking the vertical component as example, although this component of ground motion is of less impact on shaking hazard considerations, an excellent fit of early arrivals in amplitude and waveform is recognizable for the point source simulations. However, this achievement is completely disguised by strongly overrated modeling of basin reverberations resulting in resonant shaking starting around 38 seconds simulation time. These waves are producing the highest amplitudes within the seismogram and would therefore dominate peak ground velocity estimations. Incorporation of viscous damping helps reducing this effect as can be seen on the left column of figure 6.19 which covers point source elastic and viscoelastic simulations. Nevertheless the distortion of the seismogram still obvious. Key parameters such as PGV or shaking duration derived from these seismograms would lead to erroneous results. Although the finite source simulations reveal problems in the reproduction of realistic amplitudes for that station the overall similarity is higher due to the lack of these strong resonances. Differential analysis of the effects of both finite source and viscoelasticity presented in figures 6.20 and 6.21, respectively, demonstrates the strong impact of the finite source on reverberation amplitudes. Consequently, the late part of the seismogram is reproduced significantly better when a finite source is incorporated. The match with observations in this part of the time series is additionally improved including viscoelastic attenuation. However, early arrivals appear to be affected too strongly by the finite source representation used in this study. Consistently with the investigations of peak ground velocities presented in the previous section a smaller source radius for an effective homogeneous finite source can be suggested.

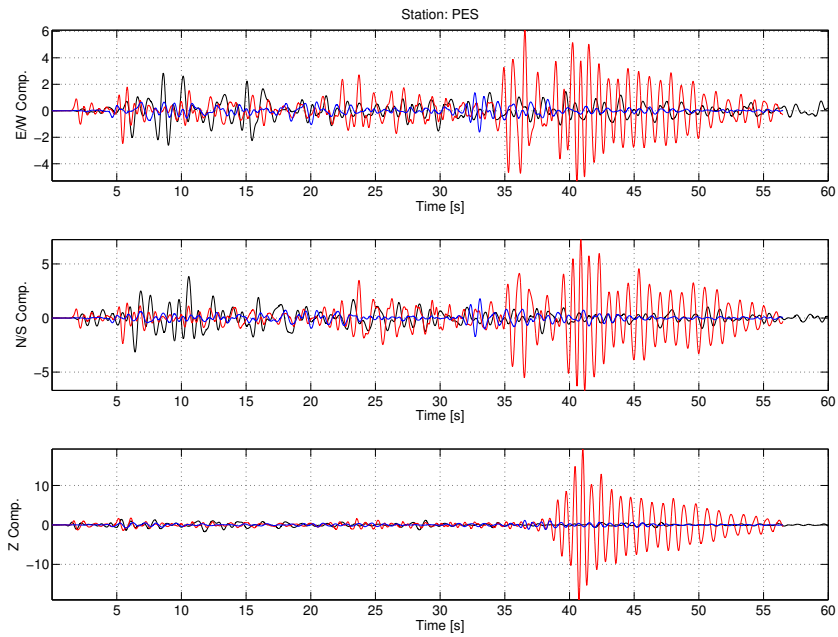


Figure 6.20: Comparison of point source (blue traces) and finite source (red traces) synthetics, both achieved with an elastic model, with data (black) at station PES. Amplitudes are given in cm/s.

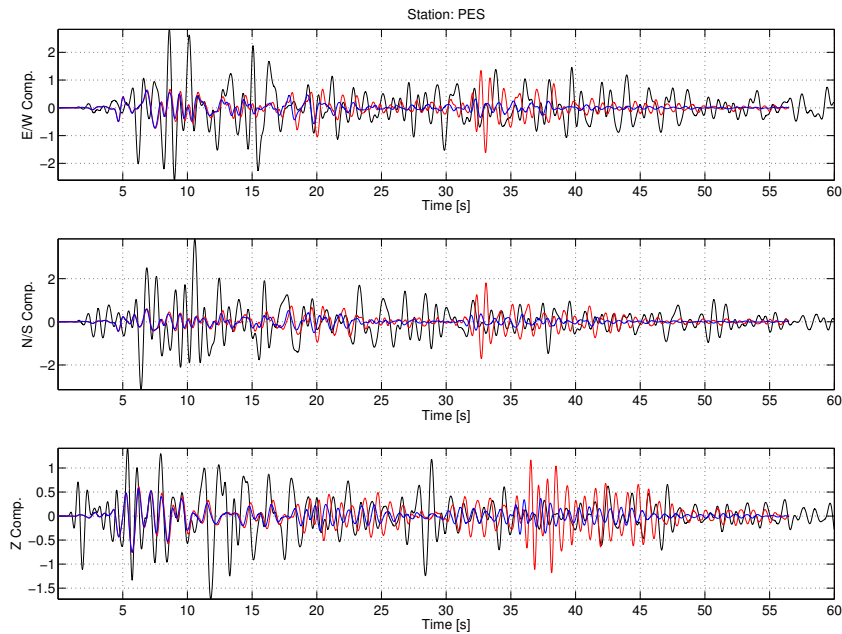
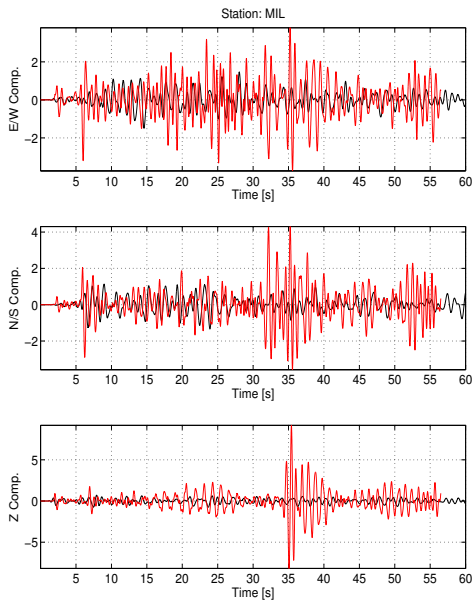


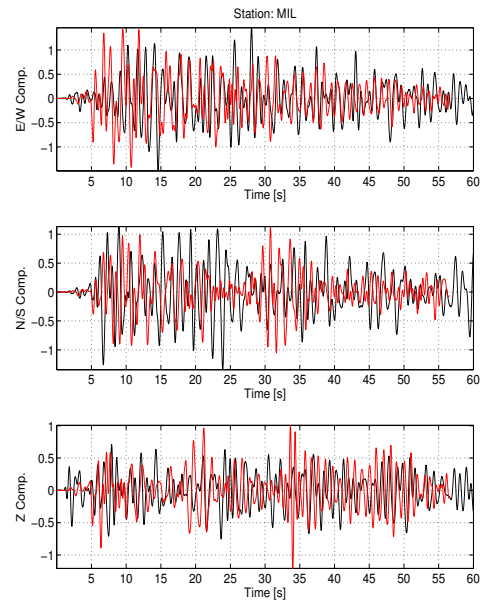
Figure 6.21: Comparison of elastic (blue traces) and viscoelastic (red traces) synthetics, both achieved with finite source simulations with data (black) at station PES. Amplitudes are given in cm/s.

Station MIL Seismogram comparison for station MIL (Millendorf), located at the end of a prominent depression in basin topography are presented in figure 6.22. Point source simulations in the left column reveal strong reverberations, especially on the vertical component and at late times. On this component of ground motion the maximum amplitudes can be assigned to these reverberations which are significantly damped when viscoelasticity is involved. This effect was already mentioned in the discussion of PGV ratio plots where the influence of viscoelasticity on vertical ground motion was overestimated. Seismograms from the finite source simulations shown in the column on the right do not show these strong reverberations at all. As already discussed simplified geometric conditions between source location and geologic structure by the use of a point source approximation favors resonant reverberations. In fact, seismograms of the North-South component show a similar effect, although to less extent. As this is also recognizable from the data it is considered to be a realistic feature in opposite to the ones mentioned above. In general amplitudes are better fitted with the finite source simulations, shown in the right column, than by the ones using point source approximation which are displayed in the left column. The effect of viscoelasticity further improves amplitudes on the early arrivals whereas the coda amplitudes are significantly lower than on the observed seismograms. A more detailed analysis of the individual effect of finite source and attenuation presented in figures 6.23 and 6.24 respectively, reveals the improvement on seismogram fit that is achieved through the combined influence of finite source and viscoelasticity. Whereas the finite fault reduces specific large seismogram amplitudes which are caused by resonance effects, attenuation diminishes the overall level of amplitudes. It can be observed how the damping effect becomes stronger with time.

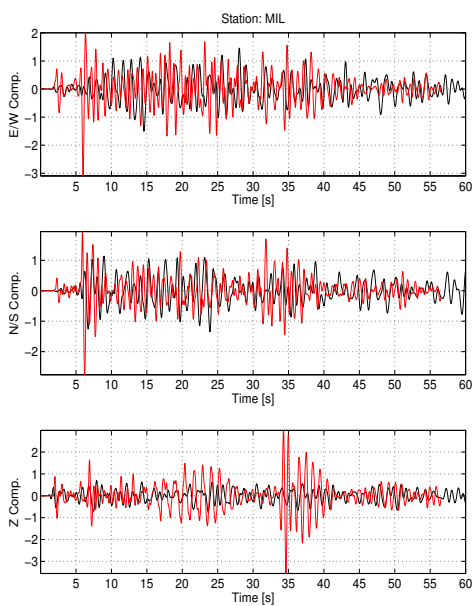
a) Point Source / Elastic



b) Finite Source / Elastic



c) Point Source / Viscoelastic



d) Finite Source / Viscoelastic

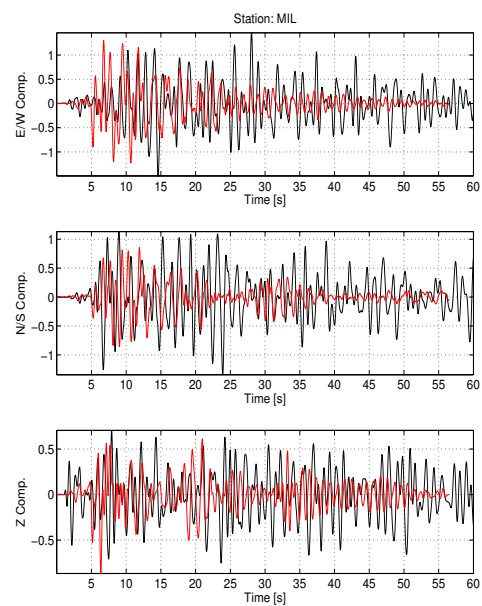


Figure 6.22: Seismogram comparison at station MIL. Synthetics (red) from four simulation types (as indicated) are compared with observed data. Amplitudes are given in cm/s.

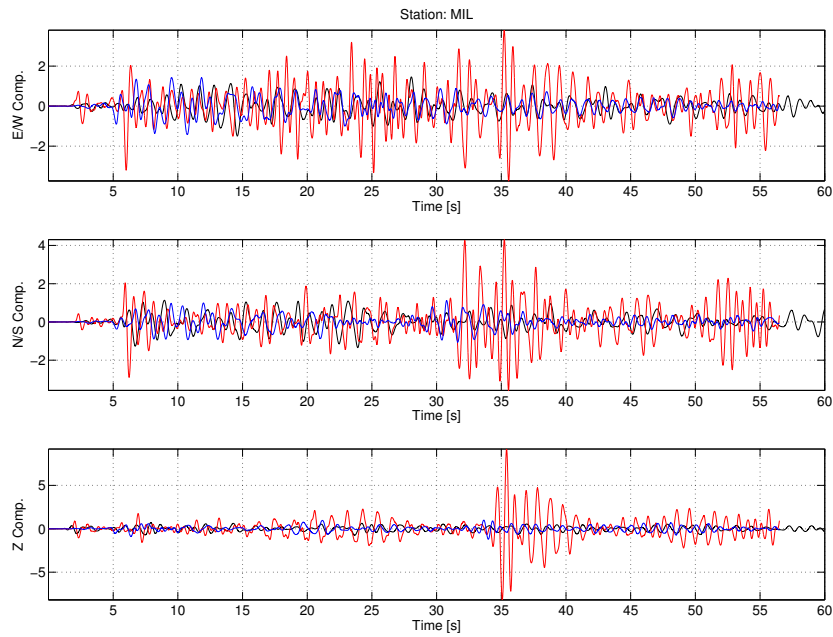


Figure 6.23: Comparison of point source (blue traces) and finite source (red traces) synthetics, both achieved with an elastic model, with data (black) at station MIL. Amplitudes are given in cm/s.

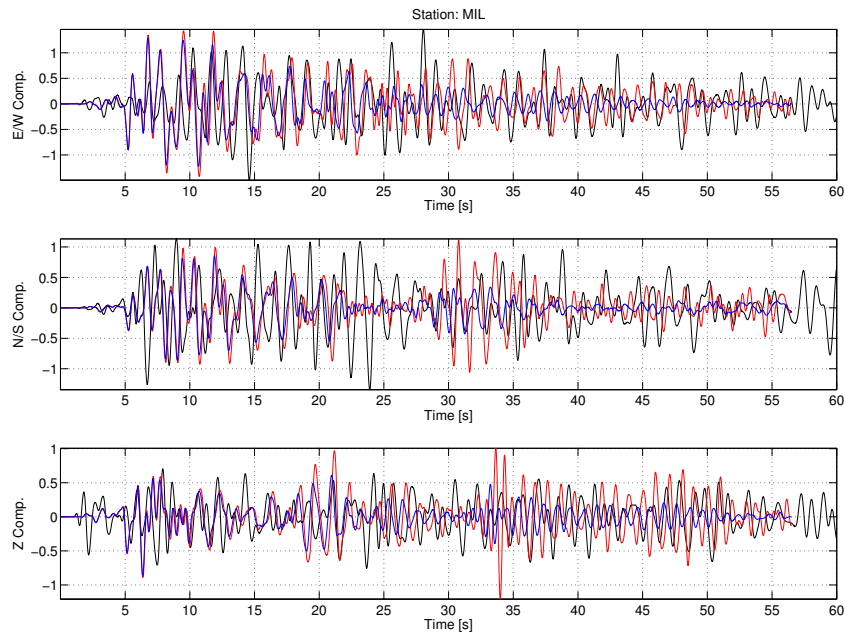


Figure 6.24: Comparison of elastic (blue traces) and viscoelastic (red traces) synthetics, both achieved with finite source simulations with data (black) at station MIL. Amplitudes are given in cm/s.

Station GMA Station GMA (Gut Margaretenhöhe) with an epicentral distance of 29 km was chosen as it is located above the maximum depth of the sedimentary basin. As for the previous stations seismogram comparisons are presented in figure 6.25, 6.26 and 6.27.

For this station the point source simulations produce a quite accurate fit with the data for the East-West horizontal component. A clear improvement is recognizable when viscoelastic attenuation is included. This fit is slightly improved by incorporation of finite sources. It is interesting that the effect of viscoelasticity seems overrated for the coda at this station. This can be explained in the location of the station above the thickest sediment layer. As a first model representation a constant Q value for the whole sediment structure was applied in these simulations. More realistically attenuation should be higher in the uppermost layer and significantly lower in the lower sediments. The fact that attenuation acts too strong on this station supports a lower average value of attenuation. A better fit in terms of amplitudes is achieved with the finite source simulations. Also amplitudes within the coda are matching the observed ones well. From the comparison of elastic simulations with viscoelastic ones it can be understood that the optimal fit in terms of amplitude ration between peak values and coda lies in between the elastic and viscoelastic ones. The reasons have already been discussed for the point source seismograms. Consequently, an improved attenuation model can be suggested from these results.

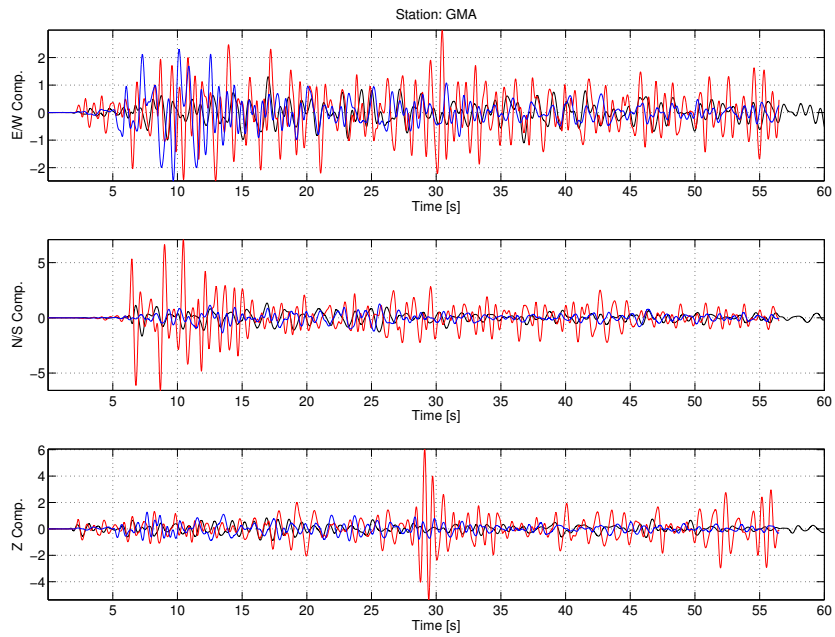


Figure 6.26: Comparison of point source (blue traces) and finite source (red traces) synthetics, both achieved with an elastic model, with data (black) at station GMA. Amplitudes are given in cm/s.

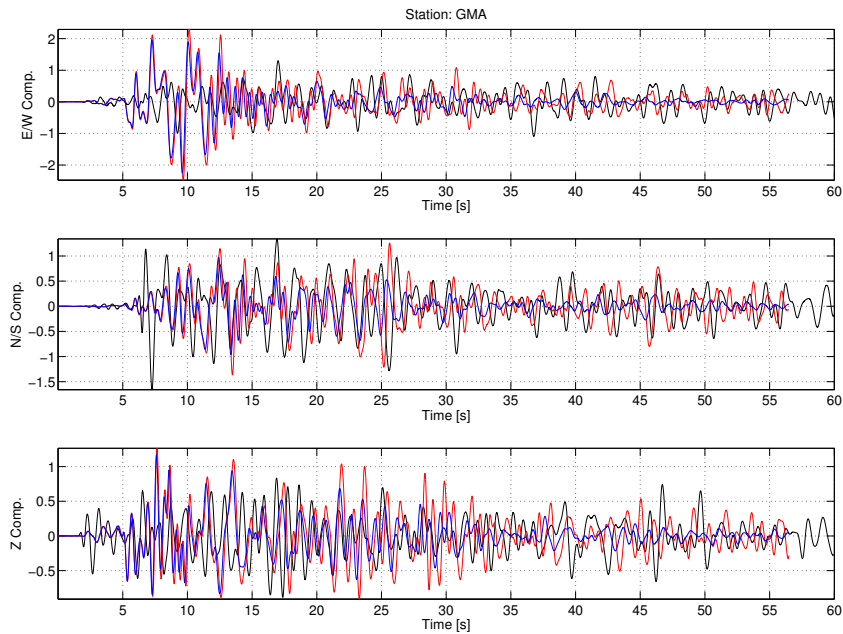


Figure 6.27: Comparison of elastic (blue traces) and viscoelastic (red traces) synthetics, both achieved with finite source simulations with data (black) at station GMA. Amplitudes are given in cm/s.

6.6.5 Envelopes

In the sections above synthetic seismograms are compared with observed ones with a strong focus on amplitudes. To quantify effects of finite sources and viscoelasticity on waveforms without the ascendance of amplitudes a different approach must be made. In this section normalized envelopes are used to study the pure influence on waveforms. The envelope Y of a seismogram X is defined as:

$$Y(t) = \frac{\text{abs}(X(t) + j * \text{hilbert}(X(t)))}{\text{max}(\text{abs}(X(t) + j * \text{hilbert}(X(t))))}$$

In this definition j is the unit imaginary number and *hilbert* represents the Hilbert transform of the time series X . From a practical point of view the envelope of a time-series is an unsigned lowpass of the original signal. The normalization erases any influence from the amplitude in order to ease recognition of similarities in the waveforms. Nevertheless relative amplitudes within the trace are kept, allowing for example analysis of amplitude ratio of P to S-waves or relative amplitudes within the coda. It is instructive to carry out the comparison of envelopes in different frequency ranges to study similarities in the low frequency part achievable already with point source approximations, the improvements in the higher frequency part by more complex simulations as well as the influence of viscoelasticity which is also intrinsically frequency dependent.

On the following pages comparisons of normalized envelopes are presented for an assortment of stations. The individual plots are arranged in a similar way as the ones used for the seismogram comparisons of the previous subsection. Results from point and finite sources are facing each other in left and right columns, whereas elastic and viscoelastic simulations appear in the top and bottom row, respectively. For each simulation type envelope comparisons were carried out in a range of periods from 0.8 seconds which is associated with the highest achievable frequency in these simulations to 3.6 seconds in 8 equally spaced steps. For each period range a low pass with appropriate cut-off frequency is applied to observed and synthetic traces. The following paragraphs outline main results for the stations chosen.

Station BNS Comparing the relative amplitudes of P and S-waves at station BNS (Bensberg) in figure 6.28 reveals a quite complex behavior. Whereas for the highest frequencies this ratio is better matched by the point source simulations the opposite holds true for the range of other frequencies. Analyzing the match in P-wave amplitudes for the finite source simulations reveals a clear improvement with increasing period. For the point source simulations the opposite is the case. Long period P-wave amplitudes appear herein strongly overrated. The overall characteristics of the frequency dependent envelopes reveal a much smoother picture for the finite source simulations. As expected considering the location of station Bensberg on solid rock the effect of viscoelastic attenuation does not appear significantly. However, it is visible within the coda.

Station GMA Envelope comparison at station GMA (Gut Margaretenhöhe) located at an epicentral distance of 28 km on sediments as shown in figure 6.29 reveals al-

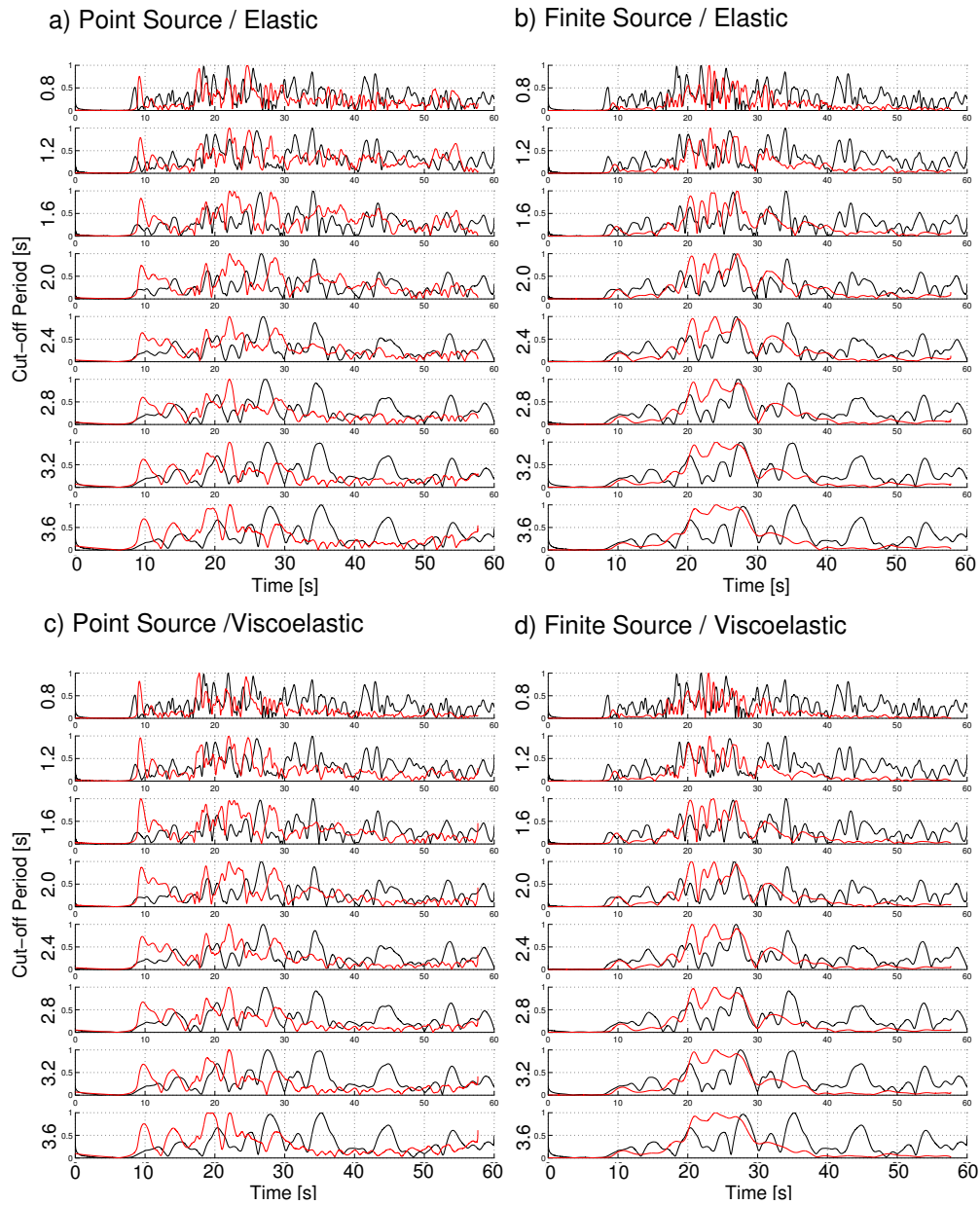


Figure 6.28: Normalized envelopes of East-West component seismograms at station BNS (Bensberg). Traces are low pass filtered with a cut-off period ranging from 0.8 seconds to 3.6 seconds. Observed data is plotted in black against synthetics (red) achieved with different simulation settings as indicated.

ready a quite good match for the simplest simulations. This fit can not be improved significantly by increased complexity in the simulations. In fact, relative amplitudes of early arrivals and coda waves reveal overrated damping for this station. As station GMA is located atop the thickest sediment accumulation of the stations available it becomes clear that the assumed uniform quality factor of 50 for the complete sedimental structure is too high. Whereas for most of the stations located on thinner sediment layers the amplitude ratio between early arrivals and late arrivals, which are affected more strongly by attenuation is improved, for this station the opposite is the case. Envelopes shown in figure 6.29 support the assumption that a depth dependent quality factor could improve the overall fit of the seismograms.

Station MIL Figure 6.30 shows a comparison of envelopes at the basin station MIL (Millendorf), located at an epicentral distance of 28 km. It clearly demonstrates improvements in waveform fitting achieved with the use of finite source modeling. Whereas the point source simulations result in a sharp peak at about 7 seconds simulation time, envelopes derived from finite source simulations show a much broader distribution of energy. This observation holds for the whole frequency range covered in this investigation. However, it is also notable that incorporation of viscoelasticity does not improve the relation of peak and coda amplitudes, in fact it has negative impact on that parameter. Due to the above mentioned normalized nature of the envelopes shown here this feature can be recognized quite clearly. Again the observation emphasize a more detailed attenuation model for the sedimentary structure.

Station PES At station PES (Pesch), located at a epicentral distance of 26 km on sediments, improvements achieved by the usage of finite source and viscoelasticity is remarkably clear. Figure 6.31 illustrates the improved reproduction of observed envelopes for the different simulation settings over a range of dominant frequencies. Comparing the results columnwise in order to focus on the attenuation effect demonstrates improved ratio between amplitudes observed in the coda and on earlier arrivals. This opposite behavior to the above discussed results for station GMA favors a depth dependent attenuation model alike the velocity model used in this study. The mentioned amplitude ratio and therefore the envelope could be kept for stations placed above smaller sediment thickness and at the same time the coda for stations on deeper parts of the sedimental basin are improved. The overall shape of the envelopes, especially the first part is modeled better by the finite source simulations. Combining both complexities leads to an accurate fit in relative amplitudes as well as waveform.

In figure 6.32 the improvements in terms of envelopes at station PES with increasing complexity of the simulation are illustrated for the highest frequencies contained in the simulations. Clearly it can be seen how the fit in terms of envelope shape improves with the incorporation of the finite source model. Furthermore with additional viscoelastic attenuation the relative amplitudes of individual peaks coincide.

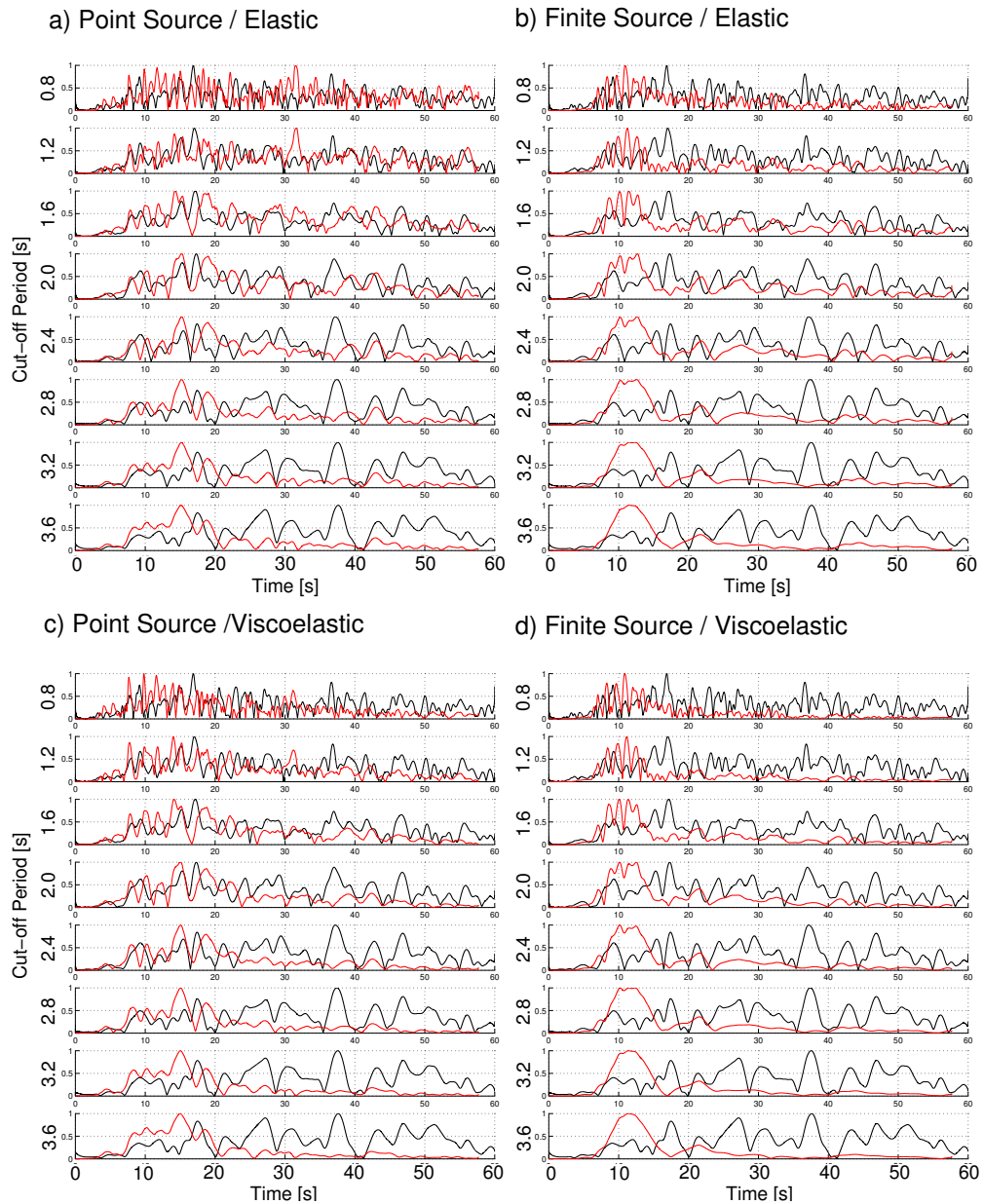


Figure 6.29: Normalized envelopes of East-West component seismograms at station GMA (Gut Margaretenhöhe). traces are low pass filtered with a cut-off period ranging from 0.8 seconds to 3.6 seconds. Observed data is plotted in black against synthetics (red) achieved with different simulation settings as indicated.

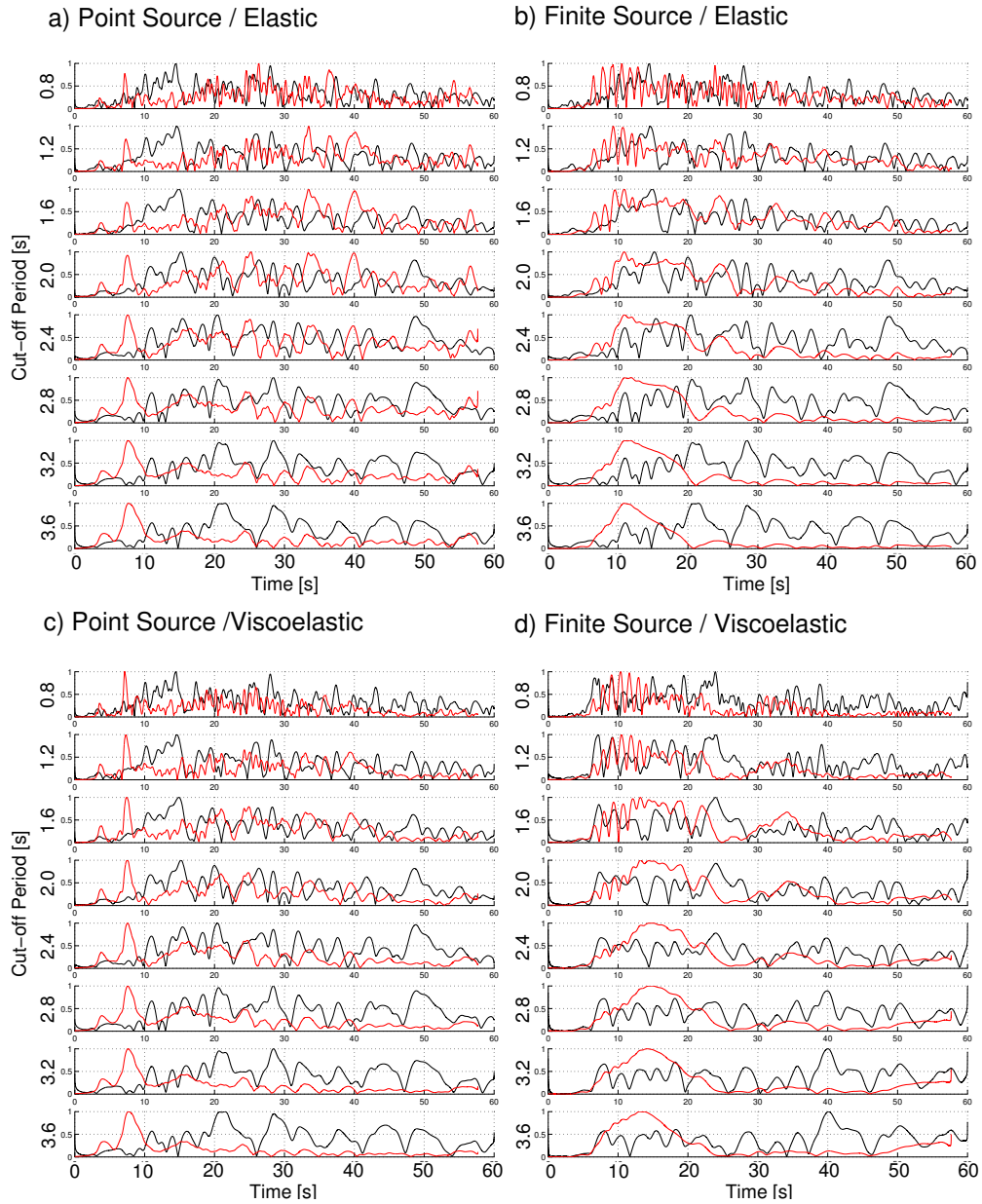


Figure 6.30: Normalized envelopes of East-West component seismograms at station MIL (Millendorf). Traces are low pass filtered with a cut-off period ranging from 0.8 seconds to 3.6 seconds. Observed data is plotted in black against synthetics (red) achieved with different simulation settings as indicated.

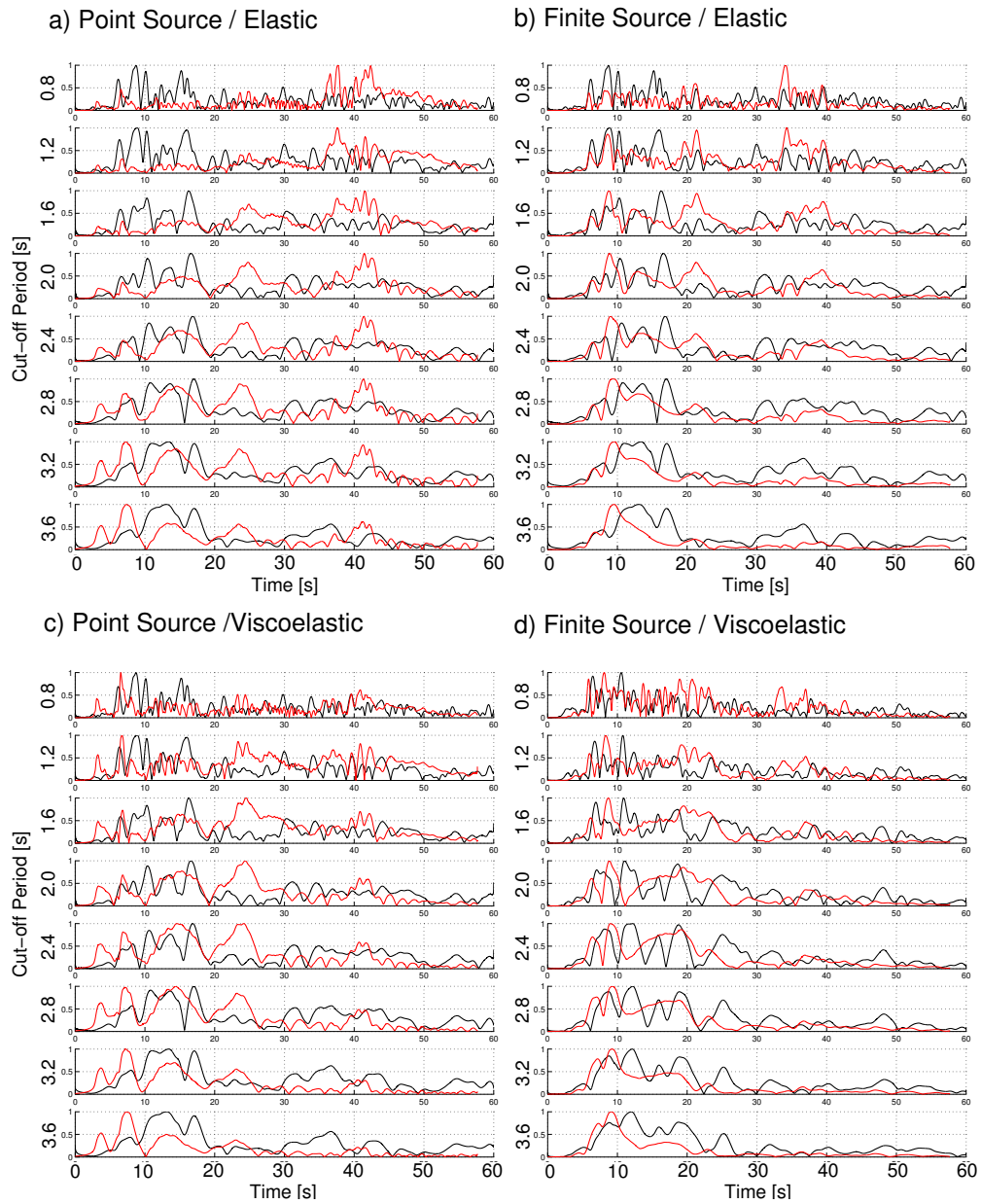


Figure 6.31: Normalized envelopes of East-West component seismograms at station PES (Pesch). Traces are low pass filtered with a cut-off period ranging from 0.8 seconds to 3.6 seconds. Observed data is plotted in black against synthetics (red) achieved with different simulation settings as indicated.

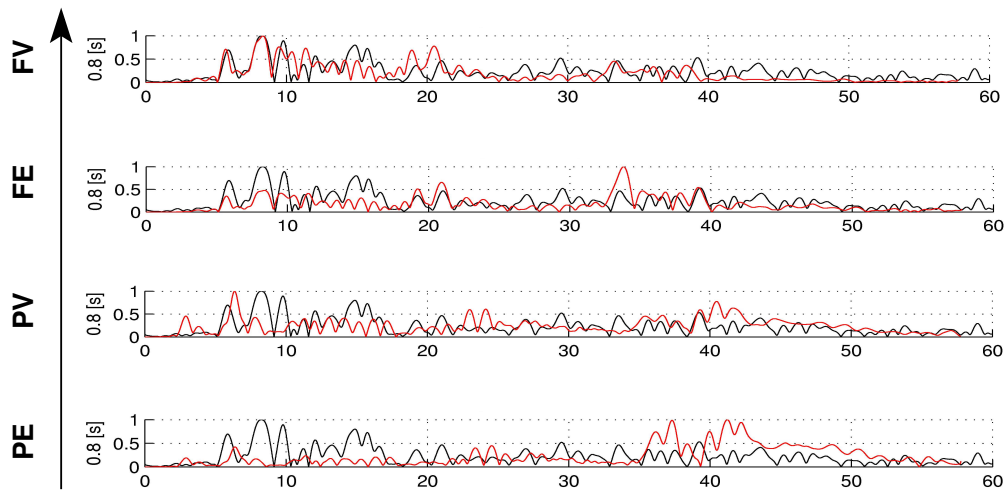


Figure 6.32: Envelopes of synthetic (red) and observed (black) seismograms low pass filtered with 0.8 s cut-off period at station PES. Synthetics result from simulations with point source and elastic model (PE), point source and viscoelastic model (PV) finite source and elastic model (FE), finite source and viscoelastic model (FV). Introduction of complexities into the simulation setting results in an improved agreement of envelopes.

6.6.6 Spectra

Parameterizations of seismograms presented in the previous subsections, covering maximal amplitudes and waveform similarity suggested a clear frequency dependence in the effects of finite source and viscoelasticity. In order to further investigate this behavior, another characterization of seismograms is chosen focusing on individual frequency content. Amplitude spectra are derived from synthetic and observed seismograms using different lowpass filters. Results for the synthetics produced by the four simulation types (point source - elastic, point source - viscoelastic, finite source - elastic, finite source - viscoelastic) are individually compared with observations and differential effects are discussed. Results are presented for the same four stations chosen in the above sections plus an additional station showing the effects remarkably clear. To avoid distortion of the results by differing absolute amplitudes all spectra are normalized to their respective maximum. Graphs for the individual stations are arranged in the same scheme as it was done for the previous section. Point source and finite source simulations are facing each other in left and right column, whereas elastic simulations are contained in the top row and viscoelastic ones in the bottom row. For each simulation type a spectral comparison is carried out in the same 8 frequency bands used in the previous section, ranging from a period of 0.8 seconds to 3.6 seconds. Spectra derived from observations are plotted in black to be compared with the synthetic ones plotted in red.

Station BNS Amplitude spectra from observed and synthetic seismograms at station Bensberg (BNS), a bedrock station located at 68 km epicentral distance are shown in figure 6.33. The observed spectrum characterized by two clear peaks in the high frequency range at 0.8 and between 0.9 and 1 Hz. The lower frequency part shows a broader distribution of energy in the range below 0.3 Hz and a few characteristic peaks between 0.3 and 0.5 Hz.

Comparing these with the synthetic spectra from point source simulations reveals a good coverage of the low frequent distribution. Nevertheless, this similarity is distorted by a artificial zero frequency content in these synthetics. This can be explained by the artificial cutoff of a resonant wavetrain visible in the seismograms resulting in static displacement. From the mentioned peaks between 0.3 and 0.5 Hz two peaks are reasonably matched by the synthetics, whereas the lower one at 0.3 Hz is shifted to lower frequencies and underestimated in amplitude. The high frequent peaks are not well reproduced in the synthetics. Numerous spikes in the spectra from point source simulations happen to occur in the right frequency range, but there is no consistent coincidence with the peaks from observations. Relative amplitudes in this part of the spectrum appear also too high in the point source simulations. This observation of an overrated part of energy contained in the high frequencies is in agreement with the observations from seismogram comparisons. The influence of attenuation is hardly visible in the amplitude spectra, which is in agreement with expectations considering the site condition of this station.

Comparing the point source spectra with ones obtained using a finite source reveals a number of significant differences. First of all, the general shape of the spectra is much smoother when a finite source is involved. The smooth distribution in the long period

part of the spectra is capable of covering most of the real spectral content in that range. A dominant peak just below 0.4 Hz is still well within this distribution. The zero frequency content that was observable with the point source has vanished. This effect is in consistency with the interpretation of reduced reverberations in the presence of finite sources. Note that although the station BNS is located on solid rock reverberations from within the basin are indeed affecting the late part of the seismograms due to secondary source effects discussed in chapter 5 for the snapshots of the complex wavefield simulated for three earthquake scenarios in the study area.

However, investigating the spectra derived with different lowpass filters it becomes obvious that the low frequent part is overrated in the synthetics from finite source simulations. This is consistent with the estimations achieved by frequency dependent PGV considerations. Nevertheless the overall relation between high frequency and low frequency content of seismic energy is improved distinctly by the incorporation of finite source effects. Spectra achieved with this simulation type are also matching the numerous peaks in the frequency band from 0.8 to 1.2 Hz. It has to be noted that spectra displayed in this section contain frequencies higher than those estimated by the given lowpass corner period indicated on the left of each plot. This is due to the limited steepness of the filters flanks used in this study.

Station GMA Spectra derived from observations at station GMA (Gut Margaretenhöhe), located about 29 km away from the epicenter on sediments show numerous characteristic peaks, as can be seen in figure 6.34. In the long period part of the spectrum these are located at 0.15 and 0.25 Hz as well as a broader one around 0.4 Hz. Very strong energy is present at 0.6 Hz whereas the higher frequencies show a more complicated pattern of smaller peaks. The low frequency peak at 0.15 Hz is not matched by any of the simulation types, the same accounts for the dominant peak at 0.6 Hz. This one is contained in the pattern produced by the point source simulations but nevertheless these simulations result in a number of equivalent peaks around that frequency. Therefore the dominating affect of the energy of this period can not be matched with the point source approximation seismograms. The point source simulation are also not capable of reproducing the sharp peak at 0.25 Hertz and the broader one around 0.4 Hz which are forming the energy distribution in the lower frequency part of the observed spectra. In contrast, the finite source simulations result in spectra which are matching the observation in this part. The amplitude ratio between these two peaks is well matched by the synthetics. Spectra derived from these simulations also reproduce the numerous peaks in the high frequency range. However, the dominating peak at 0.6 Hz is missed also when finite source effects are involved. Additionally, the finite source spectra reveal an overrating of the long period part of the wavefield, as it was the case for the bedrock station BNS above.

Comparing the spectra columnwise in order to investigate the effects of viscoelastic attenuation demonstrates that the observations made on the seismogram comparisons and PGV considerations have a clear signature in the related spectra. For each simulation type the uppermost graph, which is low pass filtered at 0.8 seconds contains all frequencies the simulations allow for. Examining the relative amplitudes within this spectrum reveals the strong effect on high frequencies that is expected by an attenuation with a constant Q . As station GMA is located over a thick sedimental structure

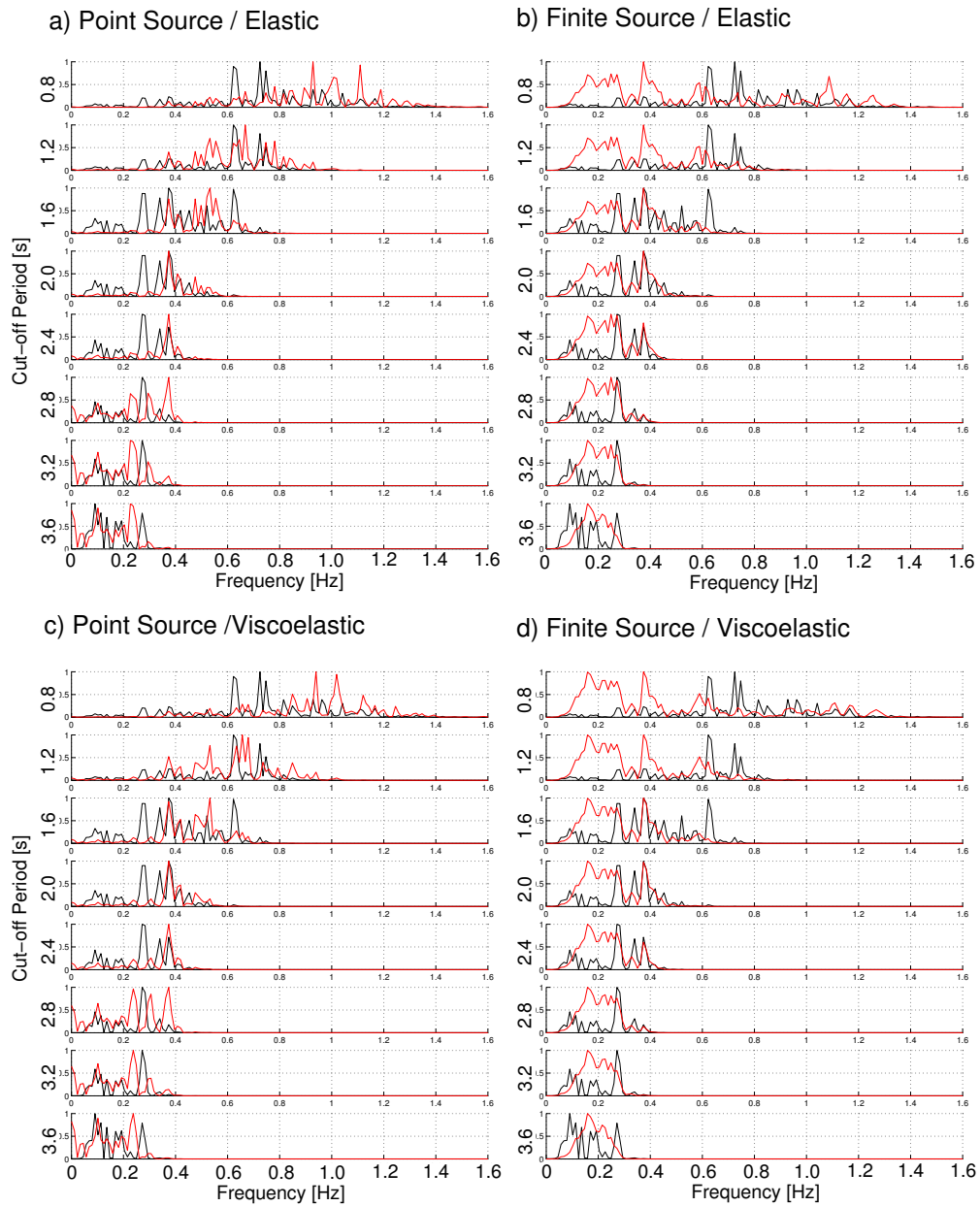


Figure 6.33: Normalized amplitude spectra of East-West component seismograms at station BNS. Traces are low pass filtered with cut-off periods from 0.8 to 3.6 s. Synthetics with setups as indicated are plotted red, observed data is plotted black.

this effect is prominent at this location.

Station FUN In figure 6.35 normalized amplitude spectra at station FUN (Funkhaus), located at an epicentral distance of 21.7 km on sediments are shown. The plots reveal distinct improvements in terms of frequency content of the seismograms achieved by the more complex simulations.

The observed amplitude spectrum is characterized by two peaks, a sharp one at 0.9 Hz and a more broad distribution of energy between 0.4 and 0.5 Hz. The above discussed observation of finite source simulations producing smoother spectral energy distributions also applies for this station. Nevertheless, sharp peaks from point source simulations coincide with some of the peaks derived from observed seismograms for the low frequency part of the spectrum. However, as filter frequency is enhanced it becomes obvious, that relative amplitudes of the individual peaks do not match the observations. In fact the highest frequency contained seems to dominate the spectrum for the point source simulations. This holds true also when viscoelastic attenuation is modeled. In opposite the finite source spectra show a smoother low frequency distribution in the spectrum which is containing all observed frequencies at a roughly matching relative amplitude. For the higher frequency part this is still the case. Spectra obtained from finite source synthetics are reproducing both the peaks at 0.9 Hz and around 0.45 Hz. When viscoelasticity is incorporated in the simulations the amplitude ratio between both peaks is improved significantly. All synthetics contain a peak just below 1.2 Hertz, which is not supported by the observation. However, the impact of this on the complete spectrum can be reduced distinctly by the usage of viscoelasticity.

Station MIL At station Millendorf (MIL), which is located at an epicentral distance of 28 km within the sedimentary basin the observed spectra are again dominated by a single peak at 0.7 Hz. The lower frequency content is distributed over numerous peaks between 0.1 and 0.5 Hz. Comparison of observed and synthetic spectra for this station is shown in figure 6.36.

Simulations using a point source appear capable of reproducing this spectra quite accurately, besides a shifting of the strongest peak to 0.75 Hz. Again incorporation of viscoelasticity results in a better fit of relative amplitudes within the individual spectra by damping the otherwise overrated high frequency part. For the viscoelastic point source simulations the amplitude ratio of the short and long period peaks is matched remarkably well. However, spikes in the spectra above 0.8 Hz are overrated and not in the correct locations. This part of the spectrum is not coinciding with observations at all. Similarly to the previous stations spectra derived from finite source simulations show smoother distribution of energy over the frequency range. This smoother shape is not capable of matching individual peaks in the observed spectra, nevertheless it contains all frequencies involved. Again the low frequency part of the spectra appears overrated strongly. Additional damping due to viscoelasticity adds to this misfit in the spectra. The dominating peak at 0.7 Hz in the observations is found not until 0.8 Hz in these synthetics. The higher frequency part seems matched in terms of amplitude.

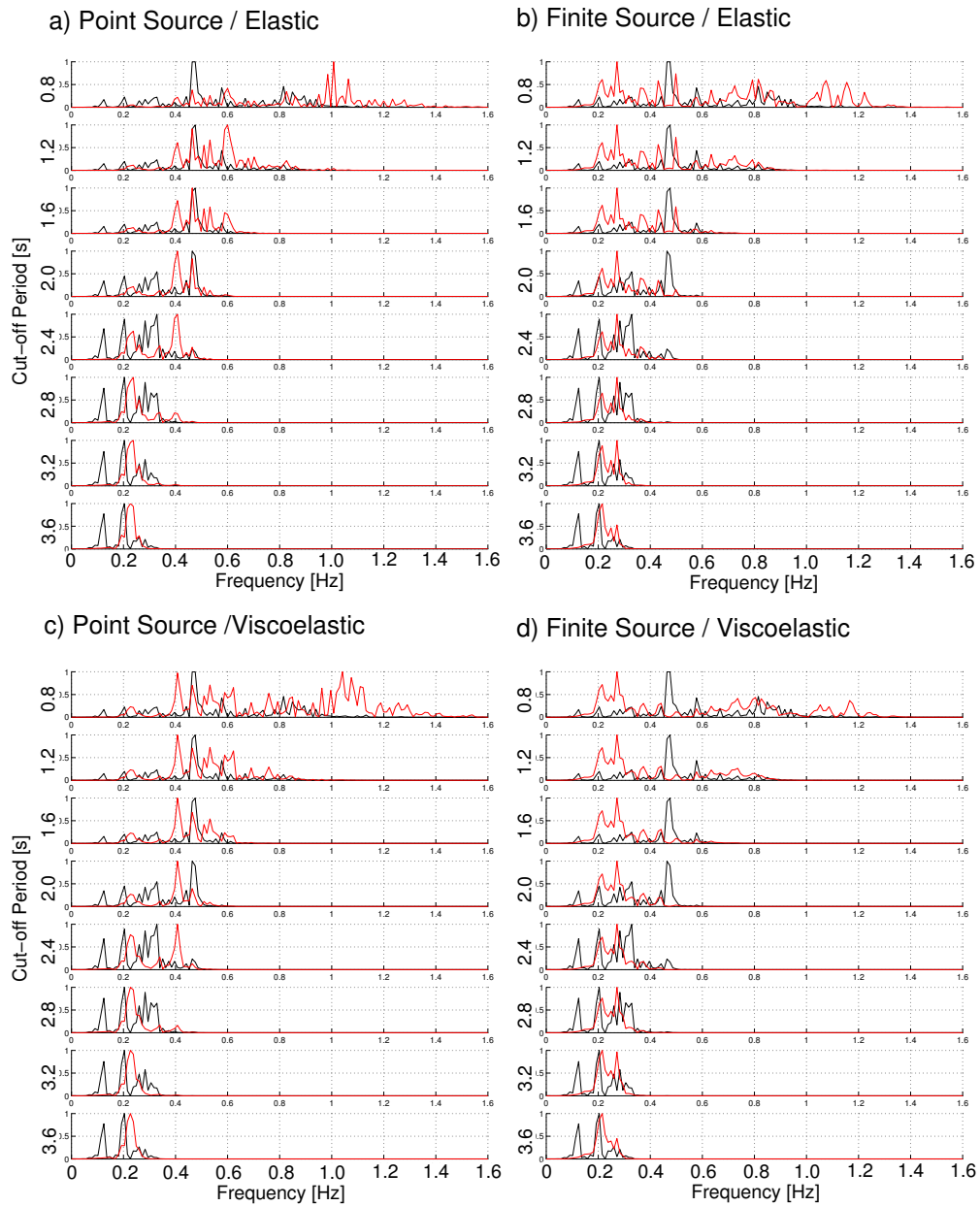


Figure 6.34: Normalized amplitude spectra of East-West component seismograms at station GMA. Traces are low pass filtered with cut-off periods from 0.8 to 3.6 s. Synthetics with setups as indicated are plotted red, observed data is plotted black.

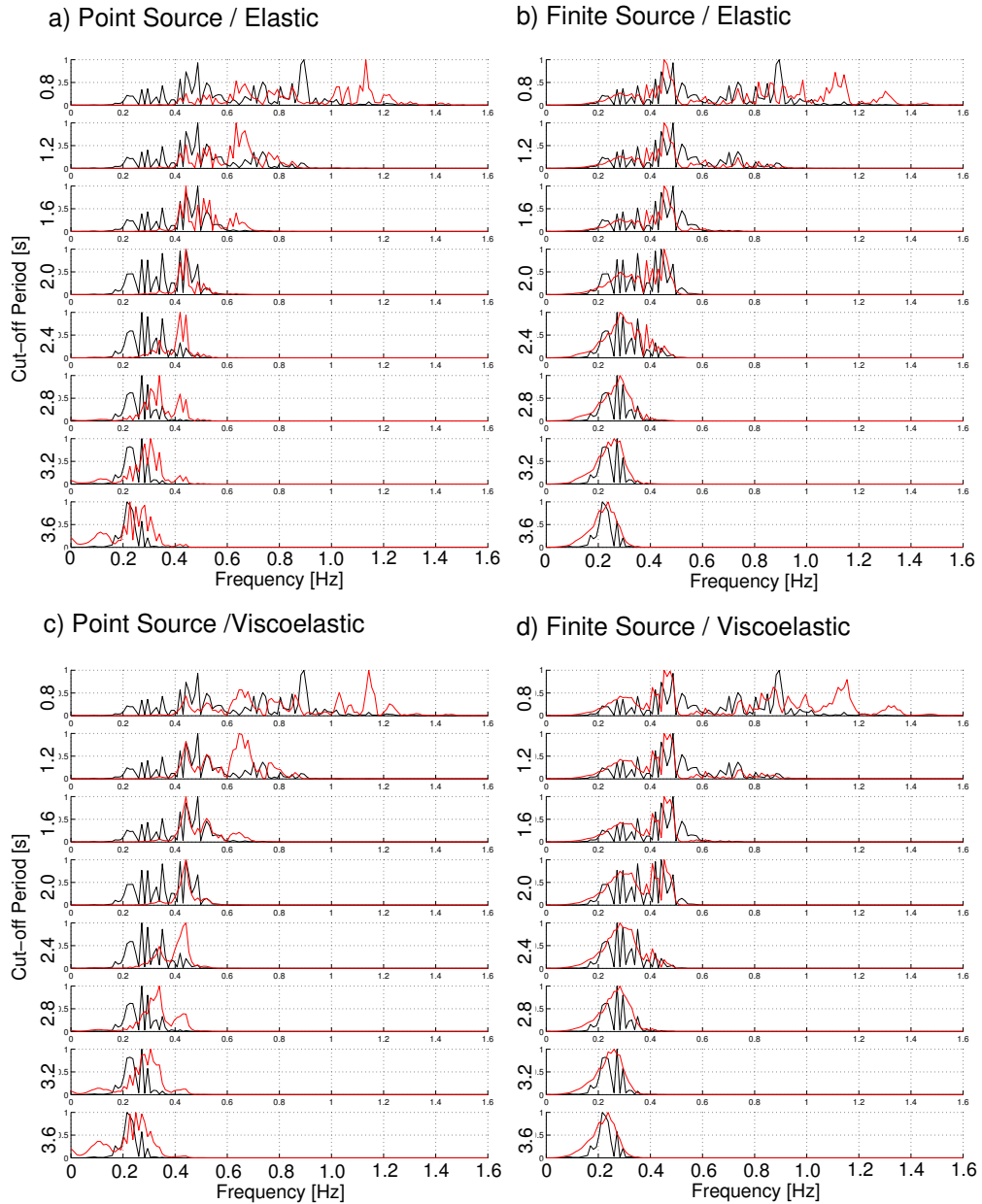


Figure 6.35: Normalized amplitude spectra of East-West component seismograms at station FUN. Traces are low pass filtered in a period range from 0.8 seconds to 3.6 seconds. Synthetics with setups as indicated are plotted red, observed data is plotted black.

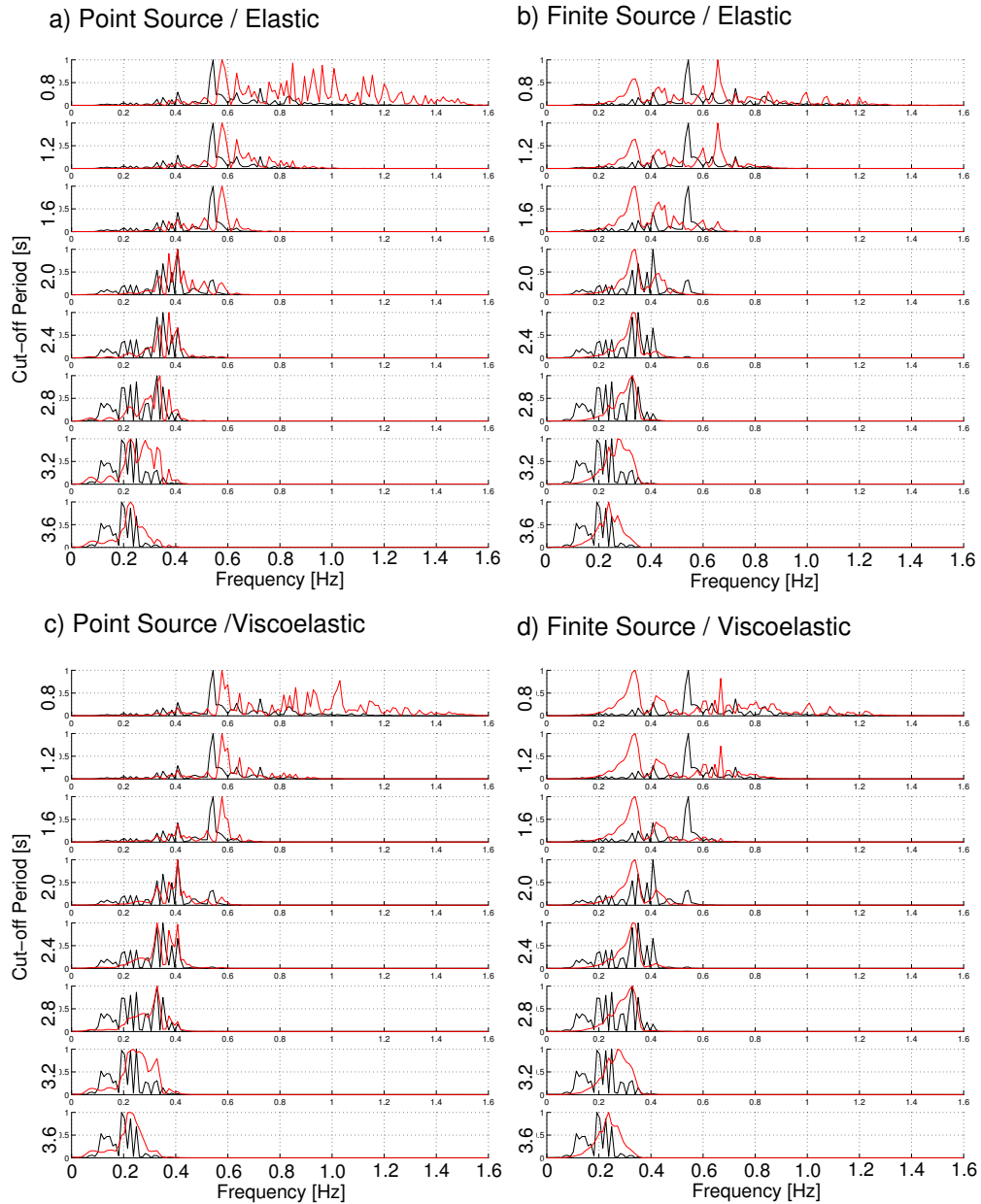


Figure 6.36: Normalized amplitude spectra of East-West component seismograms at station MIL. Traces are low pass filtered in a period range from 0.8 seconds to 3.6 seconds. Synthetics with setups as indicated are plotted red, observed data is plotted black.

Station PES Envelope comparisons at station Pesch (PES), located at an epicentral distance of 26.5 km on sediments have revealed striking similarities to observations and distinct improvements with enhanced model complexity. This findings are supported further in terms of spectral content as recognizable in figure 6.37.

Spectra derived from observed seismograms reveal a complicated pattern for this stations with a number of significant peaks around 0.3 Hz, between 0.4 and 0.6 Hz and in the higher frequency part as well prominently around 1 Hz. Point source simulations both of elastic and viscoelastic type result in spectra that are matching the observations only until a period of 3.2 seconds has been achieved. The high frequency part of the spectra is distributed in numerous peaks without correspondence in the observations. The overall short period amplitudes are overrated. Introducing a finite source leads to some significant improvements in the spectral content. The finite source spectra are capable of reproducing all important peaks in the observations. The prominent one at 1 Hz is found also in synthetics, however with introduction of viscoelasticity it is reduced in amplitude so that the fit appears better in the pure elastic modeling. Consistently with the previous considerations at other stations and of different parameters this supports the estimation of the overall damping nature of the sediments being slightly overrated in these simulations. Comparisons at a degree of similarity like the ones at station PES can be used for tuning of model parameters and may result in an overall better recovery of observations. The low frequency part is represented by a smooth distribution of energy in the synthetics covering the important peaks in the observations.

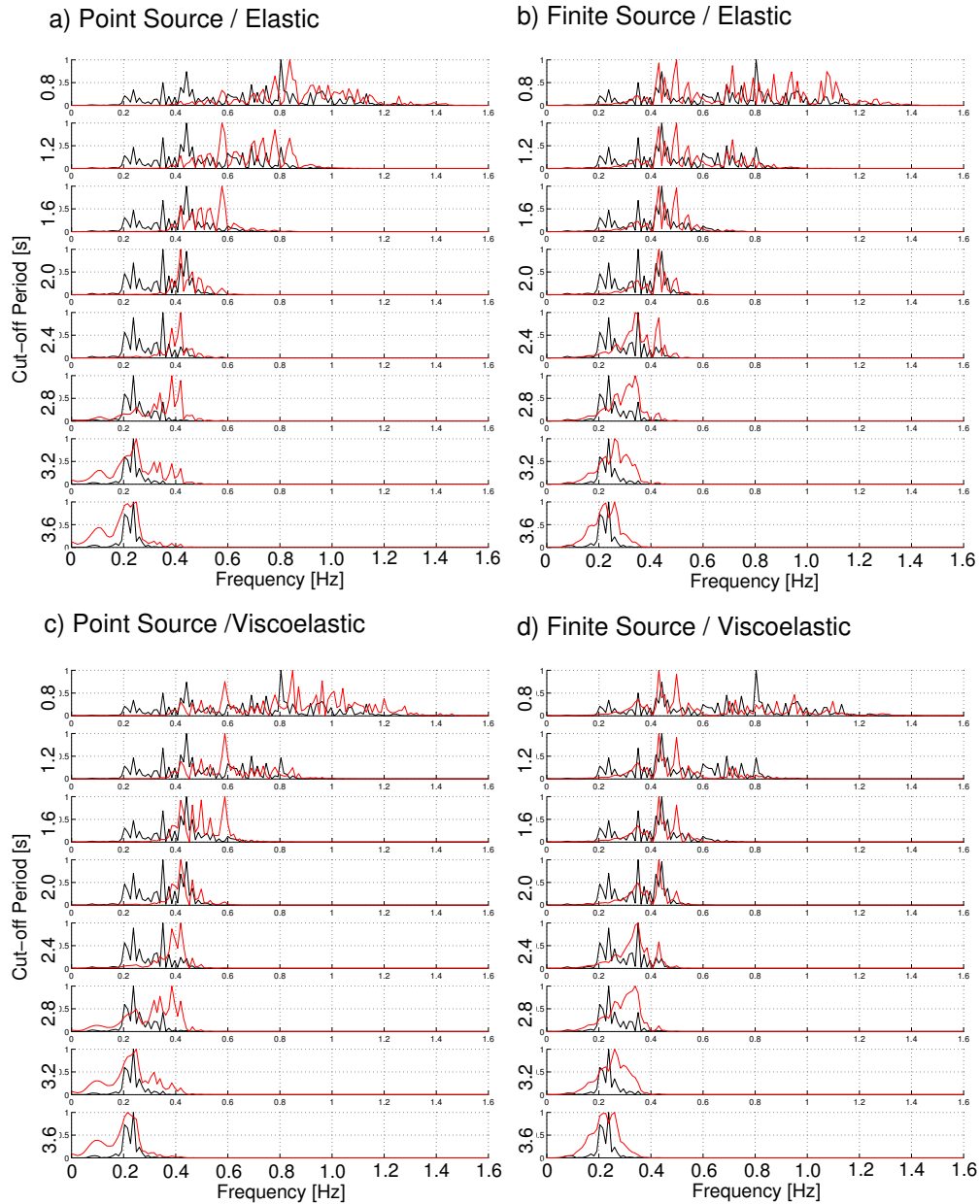


Figure 6.37: Normalized amplitude spectra of East-West component seismograms at station PES. Traces are low pass filtered in a period range from 0.8 seconds to 3.6 seconds. Synthetics with setups as indicated are plotted red, observed data is plotted black.

6.6.7 Spectrograms

In contrast to the spectra investigated in the previous section, spectrogram plots are capable of adding information on the time dependence of the spectral content of seismogram traces. As an example spectrograms for station PES (Pesch) are shown in figure 6.38 for the four types of simulations and observations.

This station has revealed a high degree of similarity in envelopes as well as spectral content for the finite source viscoelastic modeling. Additionally, it has demonstrated prominently the improvements achievable by adding more complexities into the simulations. Therefore it is ideal in order to check the abilities of retrieving information throughout a spectrogram plot. In analogy to figure 6.32 the subplots refer to individual simulation types and are arranged in an ascending manner with increasing complexity of the model. Starting at the bottom with the point source elastic simulation, attenuation is added in the second row. Using the finite source incorporated in an elastic model is the next step before finally finite source and viscoelastic modeling of attenuation are combined. The subplot at the top shows the spectrogram derived from the observed seismogram, serving as reference. In order to reveal origins of individual spots within the spectrograms the respective seismograms are plotted below each graph. The spectrogram for the point source elastic simulation shows strong spots within a narrow frequency band at late times. The related seismogram reveals prominent resonances as origin for this. Amplified ground motion due to this effect dominates the seismogram and consequently the spectrogram as well. Adding viscoelasticity to the simulation reduces the amplitudes of resonant shaking significantly as the figure above demonstrates. Nevertheless the effect appears still strong enough to disguise the remaining content of the spectrogram. With the incorporation of finite source effects as additional complexity into the modeling the resulting picture changes significantly. The monofrequent signal is still observable, but there is no distinct prolongation of shaking due to resonant effects at this point. Consequently, the remaining amplitudes become visible in the spectrogram. Viscoelastic attenuation adjusts the relative amplitudes within the trace to better fit the observed data. The final spectrogram plot reveals striking similarity with the one derived from observations. Seismograms plotted below the two graphs at the top prove this similarity.

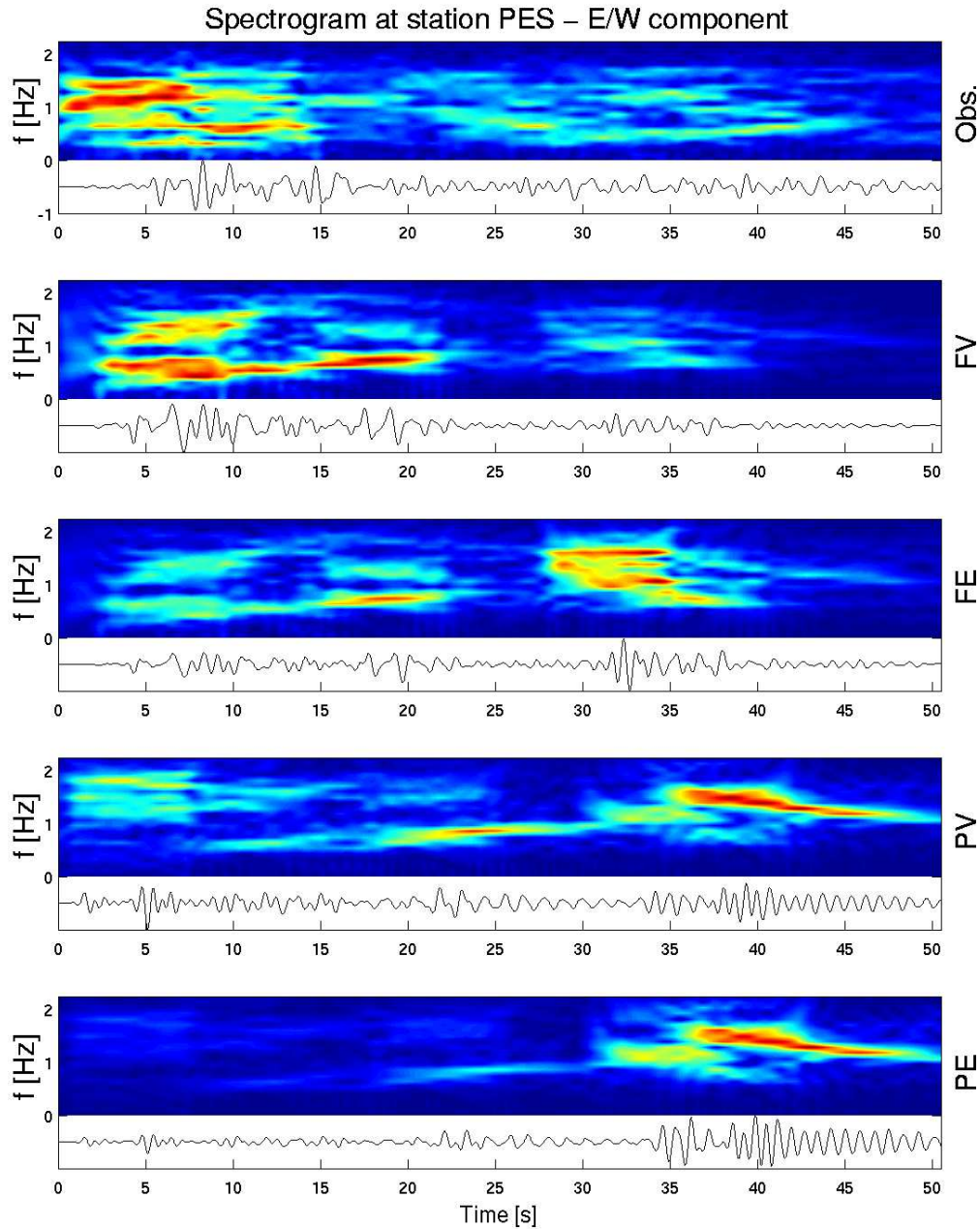


Figure 6.38: Spectrograms of observed and synthetic seismograms at station PES (Pesch). From bottom to top: Point source elastic, point source viscoelastic, finite-source elastic, finite-source viscoelastic, observation. Increasing similarity with enhanced simulation complexity can be recognized.

6.7 Discussion

In the following the main results from the various comparisons presented above are summarized and some conclusions are made.

Profiles:

1. Simulations using point source approximations are prone to result in resonant reverberations at high frequencies.
2. These resonances can produce artificial high amplitudes, even if the remaining seismogram appears realistic.
3. Using finite sources reduces this tendency towards resonances. Still observed reverberations have realistic amplitudes.
4. Incorporation of viscoelasticity in combination with point source approximations results in an overestimated attenuation effect due to strong damping of the above discussed resonant phases.
5. Finite sources and viscoelastic attenuation both result in lower amplitudes. However, the effect of finite sources on the first break amplitudes provides a possibility to distinguish it from attenuation effects.

PGV and PGV ratio:

1. Numerical simulations are capable of reproducing peak amplitudes of seismic wavefield within reasonable error margins for hazard estimation.
2. Introduction of complexity into the model by means of finite sources and viscoelastic attenuation leads to significantly improved results.
3. Frequency dependent investigation of PGV shows that the high frequency part is modeled more realistically when a finite source is involved.
4. The idealized nature of the kinematic finite source used in this study leads to an overestimation of the finite source effects.
5. For a best fitting idealized finite source a smaller source radius should be chosen than it is estimated from data by magnitude and frequency characteristics. This is due to the fact that in the real estimation rupture heterogeneities are involved intrinsically.
6. Another attempt to deal with this problem consists in modeling such heterogeneities, for example through a random undulation in rupture speed or moment rate for the individual points on the finite source plane.
7. The variation in misfit between individual stations is significantly reduced.

Seismogram Comparison:

1. General improvements in terms of similarity between synthetics and observed seismograms are recognizable due to the usage of viscoelasticity and finite sources
2. From the seismogram comparisons it becomes clear that the viscoelastic attenuation modeled in this study acts not as a single damping factor. Stations which have shown distinctly overestimated ground motions are reduced in their amplitudes whereas others stayed at the same level.
3. Some stations show clear overestimation of attenuation. This is especially the case for stations located on the thickest basin parts and can be related to the simple attenuation model with a uniform quality factor over the whole sedimentary structure.

Envelopes

1. In terms of envelope comparison improvements due to the use of finite sources become clearly visible.
2. Attenuation adds to a better match of amplitudes in early and late parts of the seismograms for most of the stations.
3. Finite source effects appear overestimated for some stations.
4. As discussed above for the seismograms itself also the related envelopes show overestimated attenuation effects for some of the stations.

Spectral content

1. Simulations carried out with a finite source result in smoother spectra.
2. Spectra obtained from point source simulations contain the low frequency part, but they lack in reproducing the higher frequencies contained in the observed seismograms.
3. Some of the point source spectra appear to be dominated by artificial high frequency peaks at the limit of the individually applied low pass filter.
4. For some stations a clear overrating of the low frequency part is observable for the finite source synthetics.

Interpretation In this chapter synthetics achieved by four types of simulations with increasing complexity were presented. Starting with point source elastic simulations, complexity was introduced in terms of the model by incorporating viscoelastic attenuation as well as introducing source complexity by the usage of a simple kinematic finite source model. The individual seismograms are compared to observations in terms of a set of key parameters, such as peak amplitude and spectral content. Observations were available for stations located on bedrock and within the sedimentary basin at

epicentral distances ranging from 20 to 120 km. Characterization of synthetics into a number of key parameters can help quantifying the fit with observed data and quantify improvements achieved by different simulation setups.

Overall, the fit with data is improved significantly with increasing complexity in the simulations. Especially the usage of finite source results in improved amplitude ratio between stations located in different site conditions and at different epicentral distances. To first order the effect of a finite source consists in a reduced amplitude and lower frequency of the resulting seismogram. However, the amount of this impact varies with site location. Improved amplitudes on 15 stations shows clearly the site dependence of the finite source effects. It is important to point out that this result could not be achieved by an adjusted point source, where the scaling factor would affect all stations in a linear way.

However, the simplified kinematic finite source model used in this study appears to overestimate these finite source effects. The finite sources in this study consist of a circular fault with the hypocenter in the middle. Moment rates are homogeneously distributed over the fault plane and released with identical source time functions delayed by a rupture front which is homogeneously emanating from the hypocenter to the rims of the fault. Combining this idealized source model with the source radius derived from observations, where source complexities such as heterogenous moment release and rise time are intrinsic, results in an overrating of finite source effects. Investigations presented in this chapter therefore support a reduced radius for the usage of idealized finite source models. Alternatively introduction of artificial heterogeneities into the finite source model could possibly account for that. This could be achieved by a randomized rupture time or moment release. Certainly, the optimal degree of randomization would have to be found by performing numerous simulations for a well documented earthquake scenario. The same applies for the optimal source radius for a idealized homogeneous source as mentioned before.

Incorporating viscoelasticity has led to an improved amplitude between early and late arrivals within a single trace. This results in better matching waveforms and envelopes. The simple attenuation model used in this study results in overestimated attenuation effects for some of the stations. Taking advantage of the characterization methods presented in this study a parameter search for the best fitting attenuation model seems possible. Complexities incorporated in the numerical simulations of earthquake scenarios seem necessary in order to produce realistic ground motion estimates. The above discussed results make clear that such complexities have to be introduced both in terms of the source by the usage of finite source models, as well as in terms of the model by including attenuation into the simulations. When the effects of both are considered synthetic seismograms can be obtained with similar envelopes and frequency content to the observations.

The above discussed limitations in terms of the attenuation model and the kinematic source representation suggest further development of the model. Performing numerous simulations may help in refining the attenuation model and achieve general rules for the design of appropriate kinematic finite source models.

Chapter 7

Variability of Simulation Results Depending on Uncertainties in Input Parameters

In this chapter results are presented obtained by a coarser discretization of the Cologne basin and the usage of the 2002 Alsdorf earthquake scenario as described in detail in the previous chapter. The model is varied in a number of parameters within realistic margins of uncertainties as they can be associated with data. Variability of the results due to these uncertainties is investigated in terms of peak ground velocity, derived intensity and waveforms.

7.1 Motivation

The main results presented in the previous chapter have demonstrated significant effects on the seismic wavefield caused by distinct changes in the simulation setup. Whereas these changes were intentionally introduced into the numerical simulations in terms of source and velocity model the question arises on the variability of synthetic results related to uncertainties in the input data. Uncertainties of any kind of input data on the media such as model velocities, attenuation or structural geometry as well as on the source parameters, such as hypocenter location, especially depth, source mechanism or magnitude are subject to uncertainties and therefore a range of valid values exist which are incorporated into the model.

Besides restrictions in the theory itself like an assumed linear or isotropic behavior, inaccuracies in synthetic seismograms can be separated with respect to their origin into three parts: 1) errors arising from approximations in the theory of the approach, such as grid dispersion in the case of finite difference methods, 2) errors caused by a simplified or coarsely discretized model of both source and media and 3) inaccuracies resulting from erroneous input data which projects into the simulation results. Errors of the first category can be addressed by application of more accurate algorithms and are subject to a large number of publications throughout recent years (e.g. Geller and Takeuchi (1998); Takeuchi and Geller (2000, 2003)). Errors of the second category

are commonly minimized by the usage of the best model description which is possible within the computational limitations. The influence of varying input parameters is seldom discussed when numerical simulations are used. Recent work by Graves and Wald (2004) on the impact of different velocity models on strong ground motion synthetics for the Southern Californian region has shown significant effects. However a systematic investigation of errors or uncertainties resulting from multiple input data sets for deterministic wave propagation simulations has not been undertaken. The main reasons being: 1) The large number of input parameters for ground motion simulations results in a tremendous number of degrees of freedom, when these parameters are considered to be erroneous. Consequently, a large number of simulations with only gradually differing setups has to be performed in order to characterize the individual influences of variations. 2) Whenever multiple simulations are carried out it is normally the goal to fit some data. From the whole amount of synthetics only the best fitting end member is then presented as sole error-free solution.

In this chapter a heuristic approach is shown on how to qualitatively and quantitatively map the effects of varying input parameters on simulation results. Due to limited computational resources simplifications and restrictions are inevitable. This work can be understood as a pilot study for future studies that can be done with the computational capabilities expected in the next years. With a set of simulations like the ones presented here it is possible to define limits of linear behavior, which can be obligatory for applying inversion techniques to a problem.

7.2 Setup

To make a reasonable number of simulation runs possible it was necessary to reduce the computational effort for the single simulation. The basin model for the Lower Rhine Embayment is discretized into a coarser grid compared to the one used in chapter 6. The study area was also restricted to the basin itself and its close vicinity as the most interesting results are expected from the basin representation and its interaction with the other parameters. In table 7.1 calculation parameters are summarized. They are briefly discussed in the following. The grid size was limited to 800 times 724 times 200 grid points, resulting in a total of about 116 million grid points. About 32 GB of core memory were necessary to describe the model and wavefield parameters onto that grid. The model was distributed over 8 nodes of the Hitachi SR8000 supercomputer at the Leibniz Rechen Zentrum. Total computation time is about 8 hours for a problem of this size. The resulting CPU time is therefore 64 node hours.

Table 7.1: Computational parameters for the simulations in this chapter.

Parameter	Value
Grid size	$800 \times 724 \times 200$
Computation time	8 h \times 8 nodes = 64 node hours
Memory	32 GB
Timestep	0.008 s
Number of timesteps	5047
Horizontal discretization N-S	145 m
Horizontal discretization E-W	132 m
Vertical discretization	102 m

7.3 Model

Whereas differential effects depending on slight changes in a velocity model can be quantified easily as long as one-dimensional amplification factors are concerned, the situation is more complicated when the full three-dimensional wavefield must be taken into account. The complex interaction between a realistic geometry with a realistic source results in a very complex seismic wavefield with large heterogeneities in peak amplitudes as can be understood from the previous chapters. Such heterogeneities are prone to show significant sensitivity to relatively small changes in the structure that is generating them. In order to account for such complexities a realistic three dimensional sedimentary structure is chosen as model in this study. For the above discussed reason of computational demands the model was discretized into a coarser grid. Additionally, the model space was restricted to the close vicinity of the basin structure. Figure 7.2 a) shows an isoline plot of the basin depth resulting from the discretized reference model. This basin model is consequently altered in order to account for possible uncertainties of the basin depth. As the studies presented in this chapter focus on differential effects caused by small variations on a reference model, the reference model is kept simple. Similar to the homogeneous basin model presented in chapter 5 it consists of a homogeneous sedimentary structure embedded into a uniform bedrock model.

Table 7.2: Source parameters for the 2002 Alsdorf earthquake (M_L 4.9).

Parameter	Value
Latitude	50.885° N
Longitude	6.189° E
Depth	14 km
Strike	138°
Dip	55°
Rake	-73°
Seismic Moment	$8.4 \cdot 10^{15}$ Nm

7.4 Scenario

The M_L 4.9 2002 Alsdorf earthquake was chosen as scenario earthquake for this study. The earthquake is described in detail in the previous chapter. This scenario was ideal for the sensitivity study presented here for a number of reasons: Due to the discussed need for a small model it was necessary to choose an earthquake which is located very close to the basin. The fact that the Alsdorf earthquake is located directly on the basin border adds to its suitability. In contrast to the Roermond earthquake with its source located underneath the sedimentary structure, the wavefield emanating from the Alsdorf source location splits in a part not affected by the basin structure, the first arrivals at least, and a significantly altered part. This makes it possible to distinguish between effects associated with the source and ones that are subject to interactions between source pattern and geometry of the structure.

In the previous chapter effects of finite source and viscoelasticity on the wavefield were discussed. Nevertheless for a simplified model as it is used in this study, the size of the Alsdorf earthquake justifies the usage of a moment tensor point source as a first order approximation. The usage of a realistic source mechanism is assumed obligatory for a general estimate on variations. Whenever simple sources such as pure strike slip or explosion sources are considered a part of the complexity in interactions with geometric settings are neglected and results are artificially simplified. As an example the surface expression of the source pattern could be asserted. A pure strike slip source would not show the sensitivity in this issue to variations in source depth as it is the case for arbitrary oriented moment tensors. Last but not least, availability of observations for this earthquake makes it possible to validate the results obtained by the reference model and relate the observed variations in a realistic framework. Summarized source parameters for the 2002 Alsdorf earthquake used as reference setting in this study are given in table 7.2.

7.5 Error axes

The main concept of the investigations presented in this chapter is a so called error space which is defined by a number of error axes. Each of these axes is associated with one simulation parameter which is considered to be erroneous. Its reference value is placed in the origin and it is consequently varied along the axis. The whole error

space therefore represents the complete set of possible parameter sets where each is varied within its predefined error margins, including all possible combinations. A well defined quantity must be chosen in order to reveal variations caused by differing input parameters. In this study peak ground velocity (PGV) and seismic intensity as derived quantity was chosen. The main benefits of this quantity are briefly summarized.

- Peak ground velocity can be considered the most important parameter in seismic hazard estimation. Knowledge about the limits of variation of this quantity and an estimation of its intrinsic uncertainty are therefore of definite interest and can improve the expressiveness of simulation results.
- Peak ground velocity can be obtained by simply recording the largest amplitude at each point on the surface. An area-wide mapping of this quantity is convenient.
- Due to their logarithmic nature derived seismic intensity values are favorable in revealing differential effects over a large range of absolute values.
- Results from the previous chapters have proven the complex relation between seismic intensity and underground structure. It can be expected that differences are significant in these plots.

PGV or seismic intensity is mapped for each altered scenario and differences can be derived both in terms of absolute values as well as relative errors. Additionally, seismograms are presented for a choice of stations on locations of interest identified by the inspection of the PGV maps. These waveforms can explain the origin of complex behavior affecting PGVs. In figure 7.1 the error space concept is illustrated by means of the realization used in this study. The three error axes considered are: basin depth, source depth and strike orientation angle of the moment tensor source. These quantities are varied along the axes and an intensity plot is given for each resulting model representation. A closer view of the individual plots already reveals slight variations in the intensity pattern. In the following subsections individual model variations are described in detail.

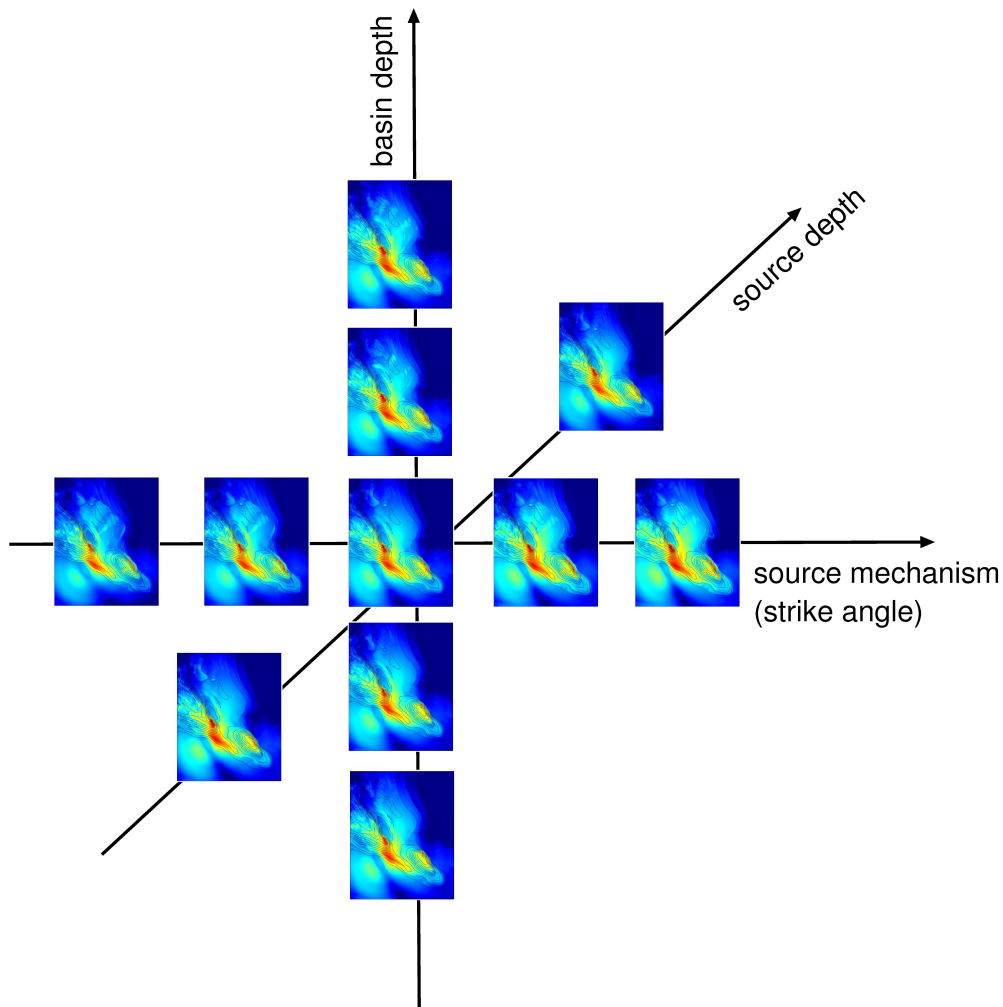


Figure 7.1: Three axes (basin depth, source depth and source mechanism) defining the three dimensional error space investigated in this study.

7.5.1 Basin Depth

The sedimentary basin is certainly the most prominent feature of the model used in this study and causes significant variations in the resulting wave field. Basin depth can be considered the most important parameter characterizing this structure and therefore it was chosen as subject to variations. The real basin model is derived from various investigations compiled into a depth to basin map. Naturally it is difficult to estimate real uncertainty margins for such a map. In order to find a compromise between a realistic estimate on errors and a definite variation an simple assumption is applied: The basin depth at each point is varied with plus/minus 10 percent serving as a conservative assumption on the uncertainty and with plus/minus 5 percent providing a optimistic error estimation.

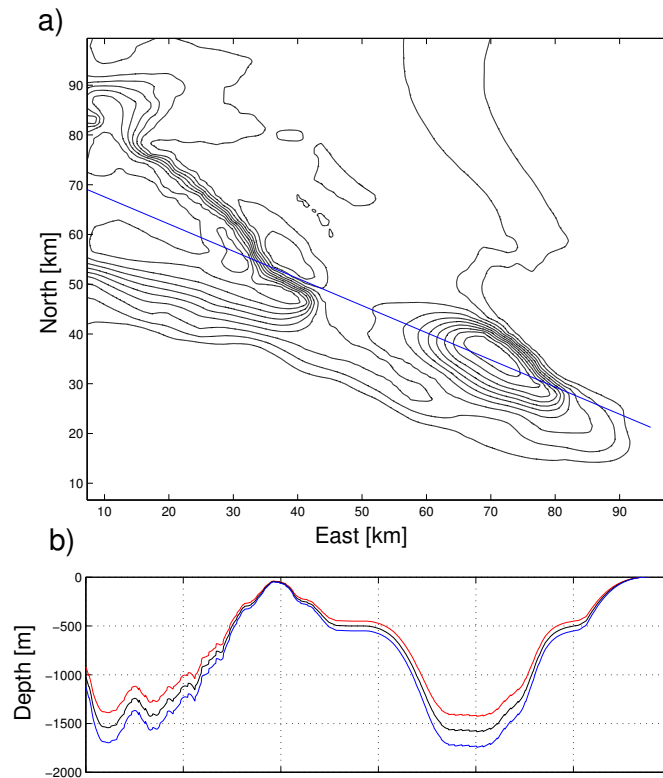


Figure 7.2: Variation in basin depth by +/- 10 percent. The blue line in a) indicates the location of a depth-profile which is shown in b).

In figure 7.2 the resulting impact on the velocity model is illustrated. Subfigure a) shows an isoline plot for the basin model with the blue line indicating the position of a cross-section which is provided in subfigure b). In this inflated profile the reference model of the basin is plotted in black against the two endmembers of variation. The plus 10 percent model is plotted in blue and the minus 10 percent one in red. Whereas the general characteristic of increasing uncertainty with depth may be a realistic assumption it becomes clear that this approach simplifies the real situation in a number of ways. The basin margins are fixed in the model as they refer to a depth to bedrock value of zero and therefore are not affected by the variations applied herein. In reality these margins are given typically by geologic mapping which definitely is subject to uncertainties. Increasing error with depth may be a realistic assumption as general behavior, nevertheless it is certainly not a linear relation as imposed in this realization. Certainly, there are specific error free points within the model, namely the locations, where well logs are present. The realistic variation of uncertainty on basin depth is much more complex than it is modeled by this approach. Nevertheless it can be considered as a valid first order approach in order to reveal complexities in the impact of depth to bedrock variations on the seismic wavefield within the basin.

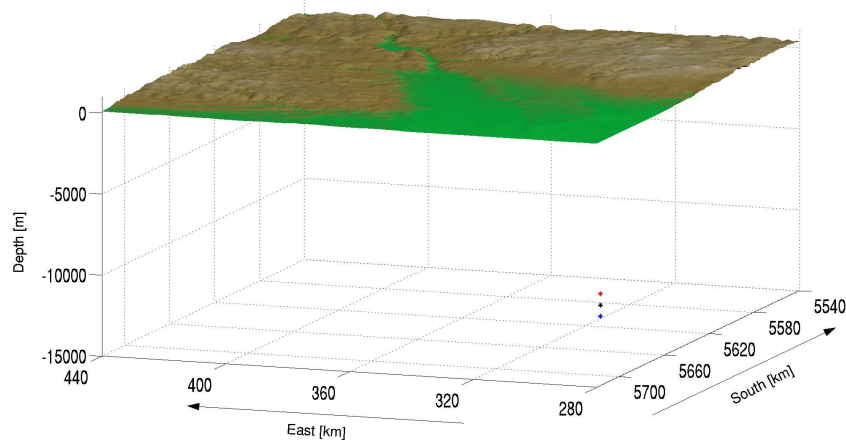


Figure 7.3: Uncertainty in hypocenter location for the 2002 Alsdorf earthquake modeled by a variation of ± 5 percent on source depth.

7.5.2 Source Depth

From parameters of the hypocenter location source depth is typically the one which is least confident. This is due to the fact that by the source depth estimation the velocity model used has the greatest impact. For the 1992 Roermond earthquake source depth estimates from different authors vary by more than 40 percent (Ahorner (1994); Braunmiller et al. (1994); Paulssen et al. (1992); Dziewonski et al. (1993)). On the other hand uncertainty estimates given in individual studies are typically much more optimistic. The reason for that may be the use of a consistent model when the error is estimated. For example travel time residuals are minimized within a fixed velocity model and from the remaining residual the error margins are derived. There is also a tradeoff between source depth and magnitude estimations recognizable from comparing various studies. Parameter studies by Scherbaum (1994) using a stochastic approach have demonstrated the ambiguity among various source parameters.

The above discussed issues make a realistic estimate of the uncertainties concerning source depth difficult. In this study an approach is made on the optimistic side of error estimation. As the velocity model is not subject to variations typical error estimates from within one study are assumed to be in the range of some percent (typically 1 or 2 %). This value has been enlarged to 5 percent and been taken as variation on source depth. To illustrate the different hypocenter locations figure 7.3 shows a surface plot of topography with the hypocenters resulting from the variation demarked as stars. Alike the previous section positive variation is colored blue, whereas the negative one appears red.

7.5.3 Source Mechanism

Besides the depth of the hypocenter coefficients of the moment tensor derived from observations are object to uncertainties. Typically these values are given in the strike, dip and rake angle of the best fitting double couple. Due to the non double couple part of the source and sparse observations these angles can be distinctly erroneous. To quantify the effects of uncertainties in source mechanism parameters in this work the angle of strike orientation is varied. With respect to the reference value it is changed by 5 and 10 degrees in both directions. In figure 7.4 the five resulting fault plane projections to the surface are illustrated.

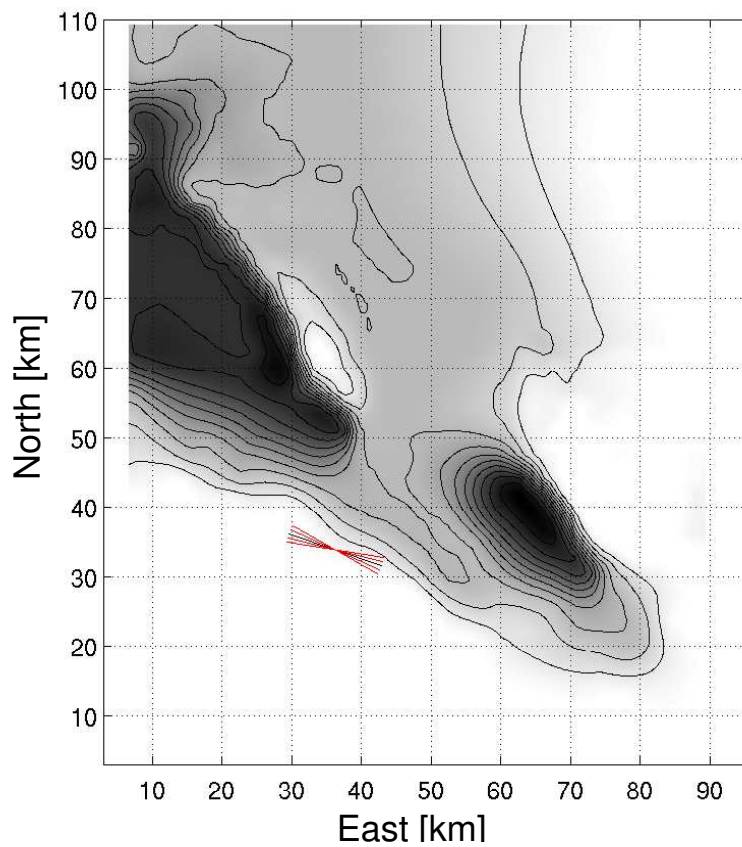


Figure 7.4: Variation in strike orientation is used to identify the effects of uncertainties in source mechanism parameters.

7.6 Results

In this section the resulting variations from the differing models described beforehand are presented.

7.6.1 Reference Solution

Figure 7.5 presents a comparison between isoseismals observed from the 2002 Alsdorf earthquake with the seismic intensity map derived from synthetic PGVs. Besides an overprediction of peak values in the vicinity of the epicenter the overall shape of isoseismals for degree V and IV are well matched. The island of intensity V around and south of the city of Cologne is reproduced well in the simulation results. This intensity map serves in the following sections as a reference solution from which differential effects with varying models are described.

The figures in the following sections are arranged in a similar way. First the relative and absolute differences to the reference solution are shown as maps for the whole model space. Consequently, seismograms on a number of points of interest are presented in order to understand the origin of variations. In figure 7.6 a map is presented showing the distribution of virtual receivers over the study area. Stations are distributed in an equidistant grid in order to cover both source and basin effects. Additionally, denser station distributions are applied to specific areas of interest like the sharply defined depression southeast of the main basin structure.

7.6.2 Basin Depth

As first parameter the depth to bedrock map is varied by an amount of -10 percent to +10 percent in equally spaced intervals of 5 percent. In figure 7.7 the resulting variations in terms of peak ground velocities with their variations relative to the reference model are mapped for the individual simulations. The reference solution is located in the middle as indicated. To the top basin depth is increased, whereas to the bottom results achieved with a reduced basin depth are presented.

In the left column the resulting distributions of seismic intensity derived from peak ground velocities are shown. At a first glance the maps look very similar. However, variations can be recognized visually from these plots. In order to clarify extent and location of differences between the individual model representations differential maps are plotted in the middle and right columns.

The column in the middle presents mapping of relative differences of the individual peak ground velocities to the reference solution. Colorbars indicate maximum differences of up to 50 percent in positive and negative direction. It also becomes clear that the distribution of relative aberrations is highly heterogeneous and includes a number of details that are not intuitively understood. In order to reveal the importance of individual spots of high variation as well as to get a clearer picture of the overall distribution the plots in the right column are shown. These are mapping the absolute difference in terms of seismic intensity between varied models and reference solution.

It becomes clear that the maximum aberration in terms of intensity can reach about half a degree on the Modified Mercalli scale. Some spots of strong variation are coinciding

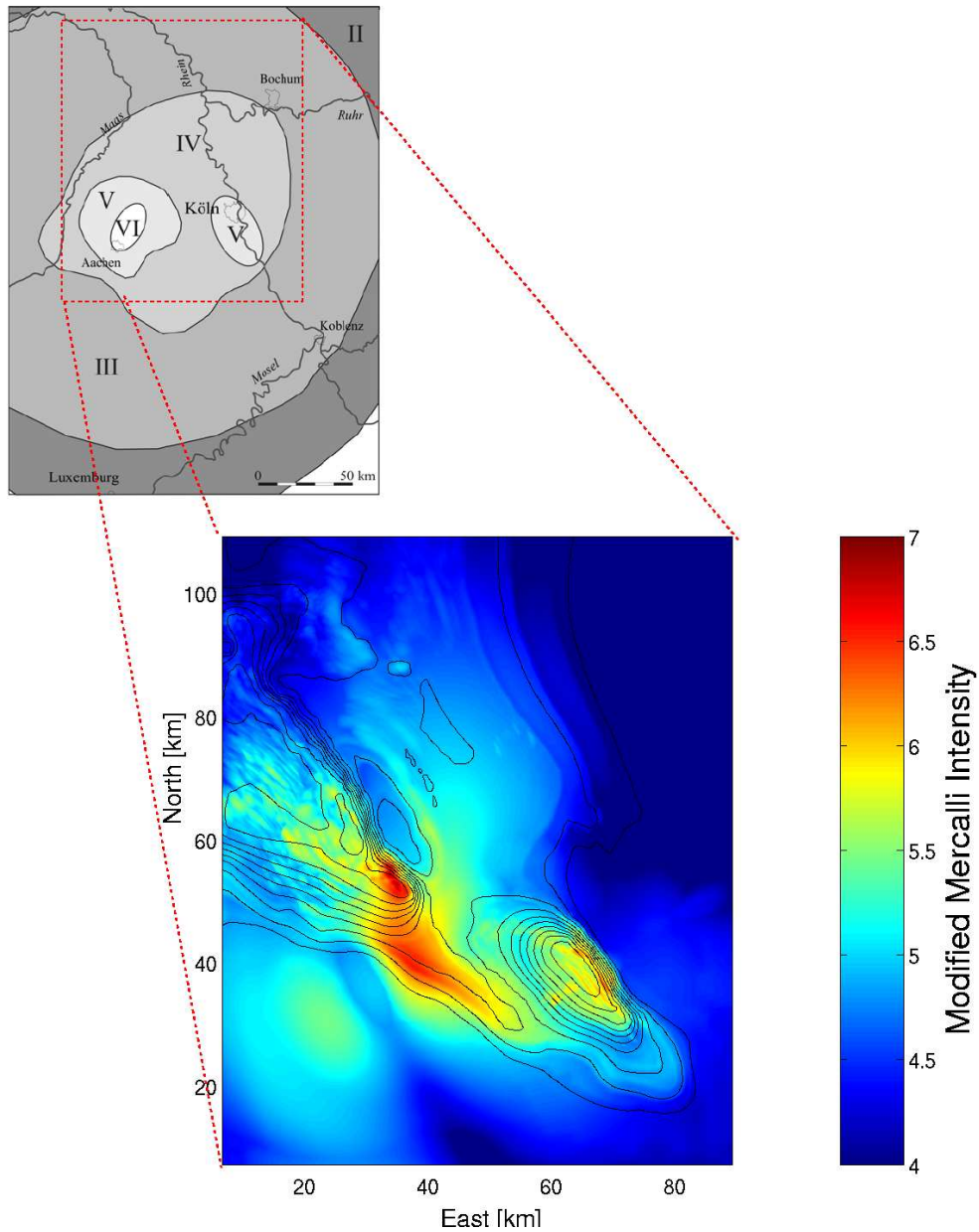


Figure 7.5: Comparison of observed seismic intensities (grayscale map) to simulated intensity distribution of the reference model.

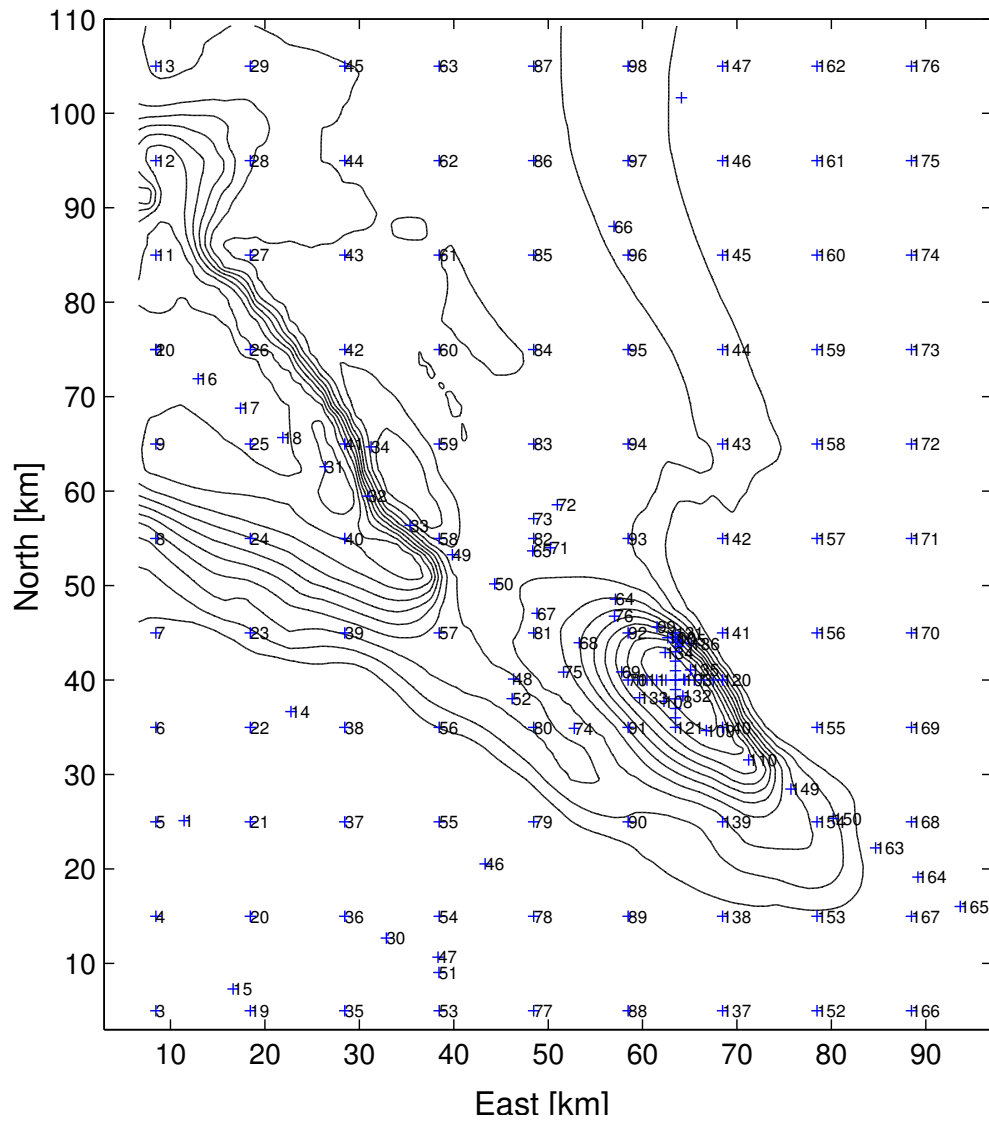


Figure 7.6: Distribution of virtual receivers used in this study to detect variabilities depending on changes in input datasets.

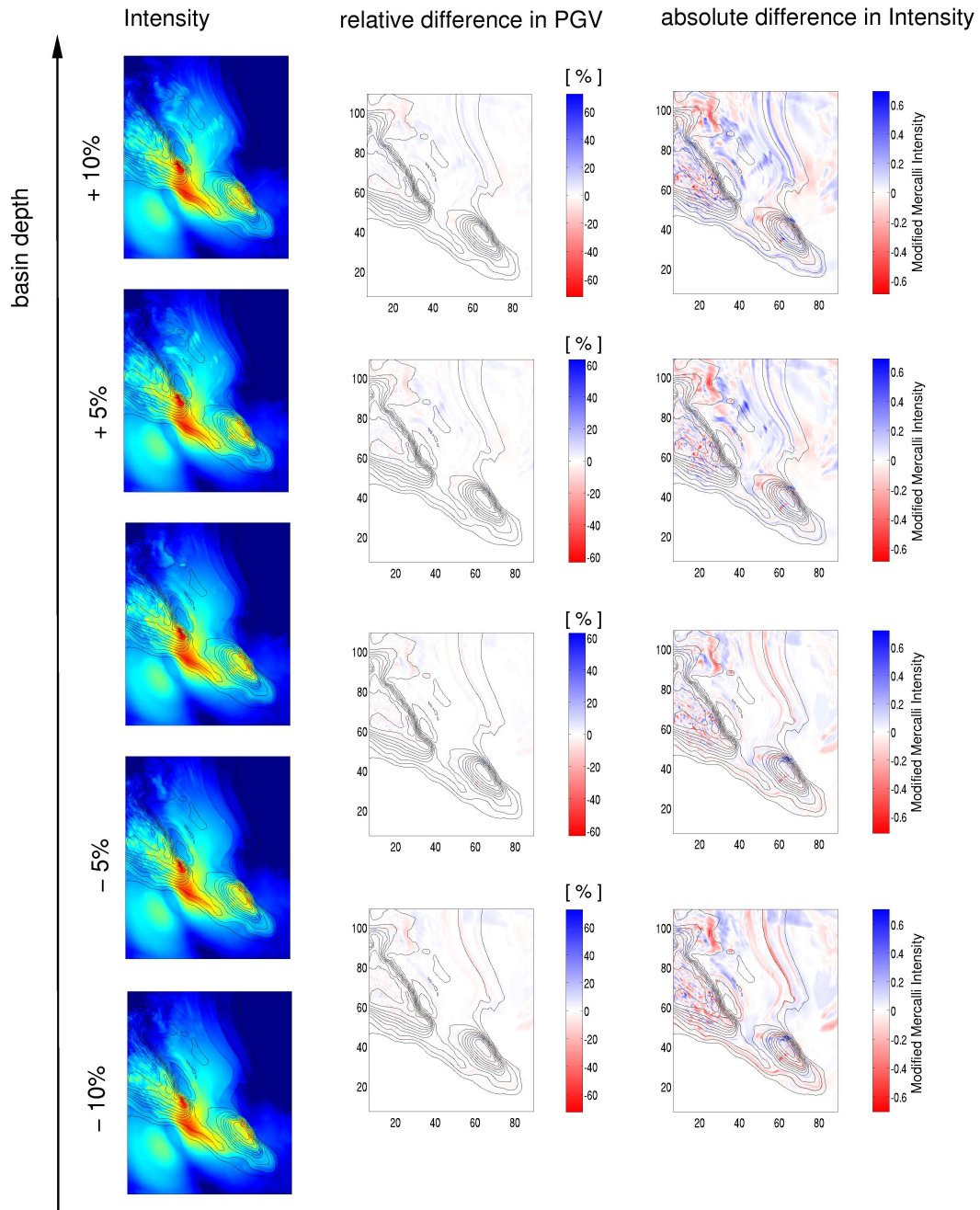


Figure 7.7: Seismic intensities from simulations with varying basin depth (left column). The relative difference between the individual models is shown in the middle, whereas the right column shows differences in resulting seismic intensity.

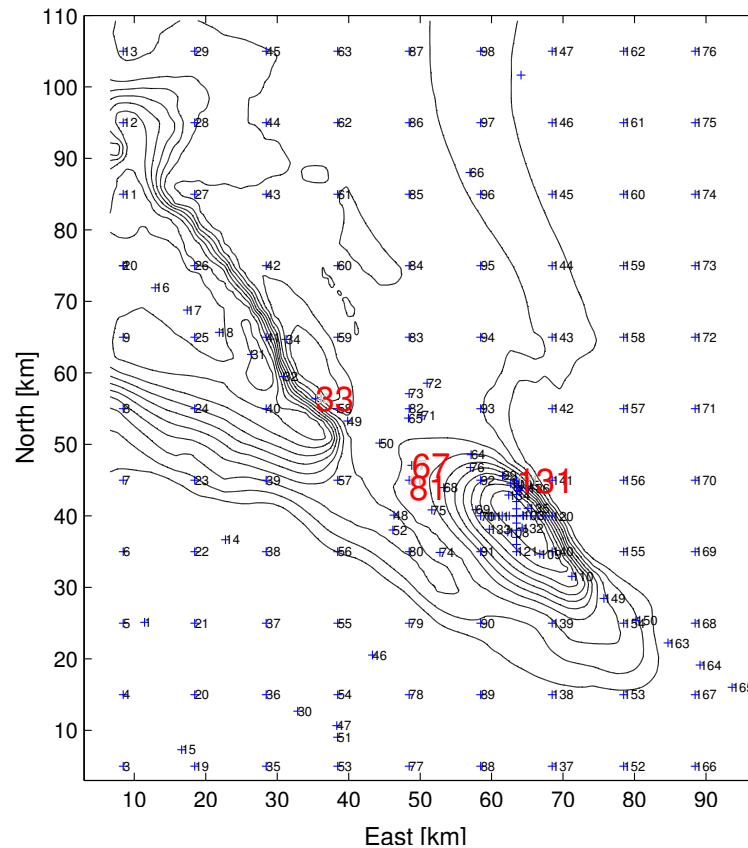


Figure 7.8: Distribution of virtual receivers used in this study. The four stations from which seismogram comparisons are presented in this section are demarked with large red numbers.

with expectations such as the pattern along the isolines of basin depth, where the direct influence of a modified basin depth is clearly expressed. However, within the basin a complex pattern of amplification and deamplification with varied basin depth can be found. It is noteworthy that there are several parts of the basin where both an increased and a reduced basin depth result in amplified ground motion with respect to the reference model. There are also regions where the opposite is true.

A dense distribution of virtual receivers is applied to the study area in order to understand details in variation of peak ground motion from the seismograms. Figure 7.8 displays the receiver locations with respect to the reference basin model. On the following pages East-West horizontal component seismograms are presented for a choice of receivers and the observed effects are described. In order to clarify the net effect on peak ground velocity the maximum amplitudes of individual phases are picked and plotted.

Station 33 Station 33 located within a shallower part of the basin shows nearly linear relation of amplitudes with increased basin depth. Seismograms of the East-West component ground motion for the five different basin models are shown in figure 7.9

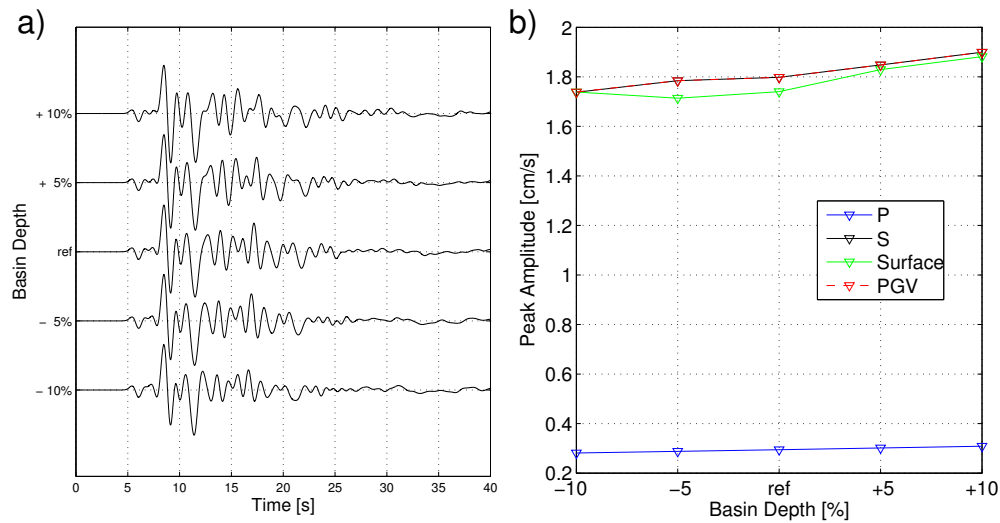


Figure 7.9: East-West component seismograms at station 33 (see 7.8 for location) achieved using models with basin depth variations from -10 % to +10 % as indicated (a). Maximum amplitudes for individual phases and the resulting peak ground velocity of the traces are plotted in (b).

a). From bottom to top the seismograms refer to models with basin depth decreased by 10 percent to a model with a 10 percent increased basin depth as indicated on the individual traces. From the waveforms it can be estimated that shaking durations derived from these seismograms would also reveal a linear increase with basin depth. This station illustrates an example where the assumption of linearity can be considered valid and an inversion based on this assumption would produce reasonable results. Figure 7.9 b) shows the maximum amplitudes for the individual phases of P-waves, S-waves and surface waves, as well as the resulting peak ground velocity for the whole traces. The discussed nearly linear dependence is clearly recognizable.

Station 67 Seismograms recorded at the virtual station 67, as presented in figure 7.10 a), show a quite different relation of amplitudes and waveforms with basin depth. This station is located between the two main depressions in basin topography. Whereas the first arrivals of shear waves appear to have the largest amplitude for the reference model, amplitudes are smaller for both the models with increased and reduced basin depth. The opposite relation can be recognized from the later arrivals. Increased as well as reduced basin depth results in stronger amplitudes in this part of the seismograms. However these maximal coda amplitudes appear at different times and due to different mechanisms. Whereas reduced basin depth results in strong resonant phases at around 15 seconds seismogram time, very large amplitudes appear for the deeper basin models at late time around 20 to 25 seconds in a pair of resonant reverberations. Maximum amplitudes for individual phases are shown in figure 7.10 b). The net effect in terms of peak ground velocity (PGV), where arrival time is hidden, consists in larger amplitudes compared to the reference solution for models with deeper and shallower basin representation. However, a 10 percent increase in basin depth results in lower amplitudes. This relation is also recognizable from the PGV and intensity maps

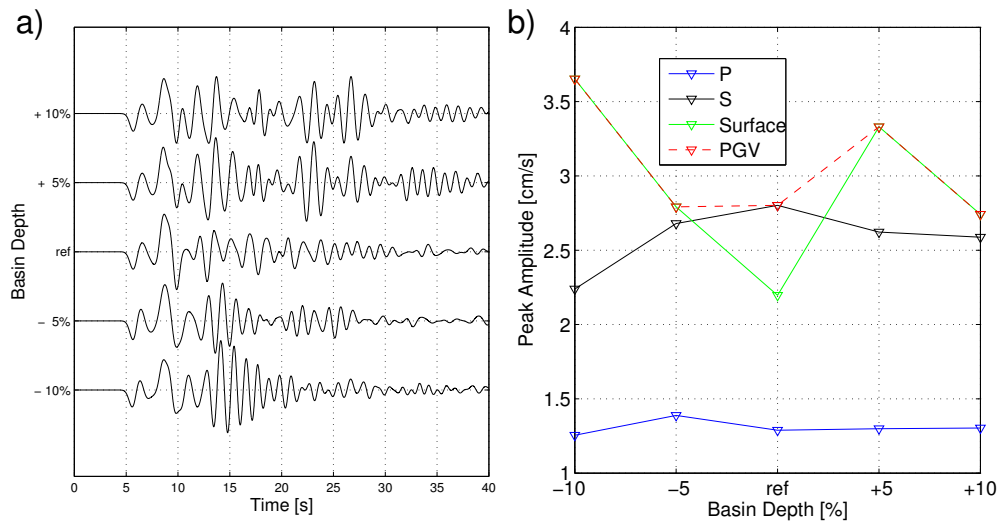


Figure 7.10: East-West component seismograms at station 67 (see 7.8 for location) achieved using models with basin depth variations from -10 % to +10 % as indicated (a). Maximum amplitudes for individual phases and the resulting peak ground velocity of the traces are plotted in (b).

presented in figure 7.7 above.

Station 81 Whereas station 67 showed amplified ground motion for all but one model variations the opposite behavior can be recognized from station 81. It can be recognized from map 7.8 that these stations are located closely to each other. From figure 7.11 b) it can be understood that the reference model produces the highest level of ground motion at this location. The related seismograms are shown in figure 7.11 a). The top three model representations result in amplified ground motion due to resonances between 12 and 16 seconds seismogram time. For the models with reduced basin depth these phases are not prominently observable. Considering only the peak values results in the mentioned behavior of highest values for the reference solution and decreasing amplitudes for both senses of basin depth variation. This observation is consistent with the mapping of PGV and derived seismic intensity at the respective location as can be seen in figure 7.7.

Station 131 Similar observations can be made on station 131 which is located above one of the steep basin edges. Seismograms for all model variations at this station are shown in figure 7.12 a). From figure 7.12 b) it can be recognized that the resulting peak ground motions are related to surface waves and have the maximum value for the reference model. Resonant amplification of ground motion can be observed for all models at very late seismogram times around 30 to 35 seconds. An additional resonance with smaller amplitudes appears for the three traces at the top around 20 seconds. Whereas peak ground velocities for the reference model and the model with 5 percent increment on basin depth are determined by the late resonance, the early resonance appoints the maximum for the uppermost trace. The net effect consists in

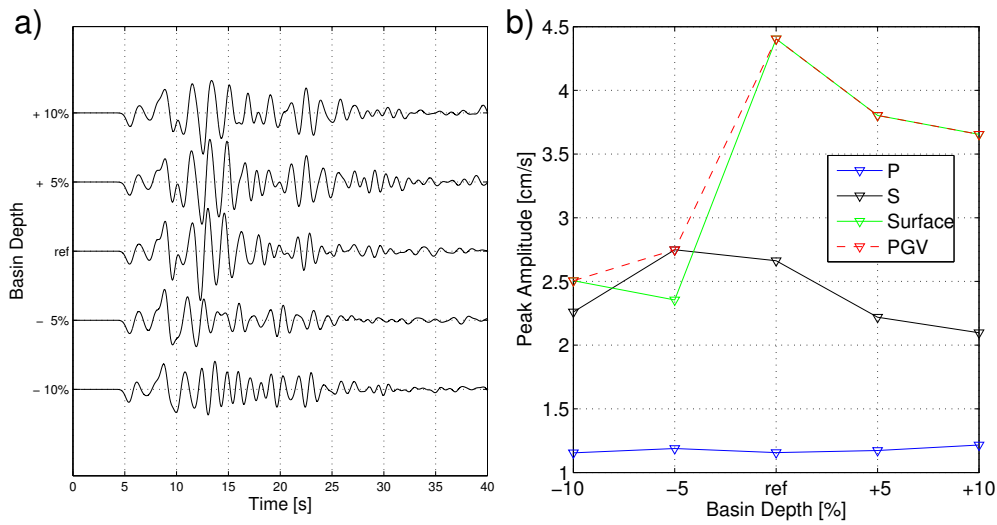


Figure 7.11: East-West component seismograms at station 81 (see 7.8 for location) achieved using models with basin depth variations from -10 % to +10 % as indicated (a). Maximum amplitudes for individual phases and the resulting peak ground velocity of the traces are plotted in (b).

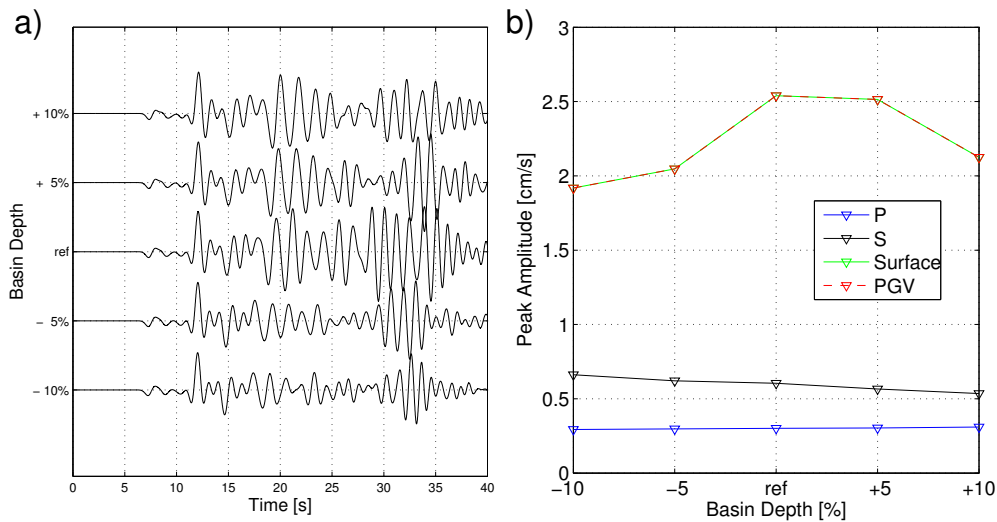


Figure 7.12: East-West component seismograms at station 131 (see 7.8 for location) achieved using models with basin depth variations from -10 % to +10 % as indicated (a). Maximum amplitudes for individual phases and the resulting peak ground velocity of the traces are plotted in (b).

decreasing PGV with all model variations and is observable in the PGV and intensity plots as it was the case for the station above.

7.6.3 Source Depth

Hypocenter depth is investigated as a second parameter that is considered to be significantly erroneous. Herein the reference source depth of 14 km is altered by an amount of 5 percent towards smaller and larger depth. In figure 7.3 the varying location of the hypocenter is illustrated. Effects due to the differing source depth are considered to be less heterogeneous as it was the case when the velocity model was varied. Therefore two simulations plus the reference one are assumed to be sufficient in order to reveal the characteristic effects of these changes.

In figure 7.13 variations on peak ground velocity and seismic intensity are presented when a modified source depth is considered. Like in figure 7.7 in the left column intensity maps derived from synthetic peak ground velocities are shown for different hypocenter depths. Again, the overall pattern looks quite similar. However, a change in size is easily observable for example for the green region in the southwestern corner. For a quantification of the variation relative differences in terms of peak ground motion (mid column) and absolute differences in terms of seismic intensity (right column) are presented.

The column in the middle shows the relative variation in terms of PGV in percent with respect to the reference solution. Intuitively, the effect of a deeper source is expected to be an overall smaller amplitude at any location within the model area and the opposite if the source is located more shallow. On first order the pictures assert this assumption. Differential PGV mapping for a 5 percent reduced source depth show 10 to 20 percent amplified ground motions over large parts of the model space. The opposite is the case when source depth is increased. Here differential PGV maps display deamplification of peak surface ground motion by 20 percent over a large portion of the model. However, a closer view reveals interesting and non intuitive details. A large area south of the epicenter shows an alteration of peak ground velocity with opposite sign than it is observed for most of the model area and is intuitively understood from the previous considerations. This effect can be understood as an expression of the varying projection of the source pattern from the moment tensor point source included. It is noteworthy that this area coincides roughly with the nodal plane of minimum amplitudes visible at the PGV plots. Therefore the effect can be considered as less important in terms of hazard estimation. A very important effect is visible within the basin margins in areas where large ground motion with strong lateral heterogeneities is observed.

In the shallow part of the basin large areas near the source appear to be not sensitive in terms of PGV to a increased source depth. In fact for this region a reduced source depth results in weaker ground motion, a behavior which can be considered not intuitive. The same accounts for a shadow region northeast of the basin depression on the right hand side. Both areas show this contradicting behavior due to interactions of the source pattern with the geometry of the basin. Waveform comparison shown later in this section gives a explanation to this result. Inside the deepest depressions of the basin things get even more complicated. Due to the highly heterogeneous nature of the peak ground velocity distribution a change of source depth can have amplifying or

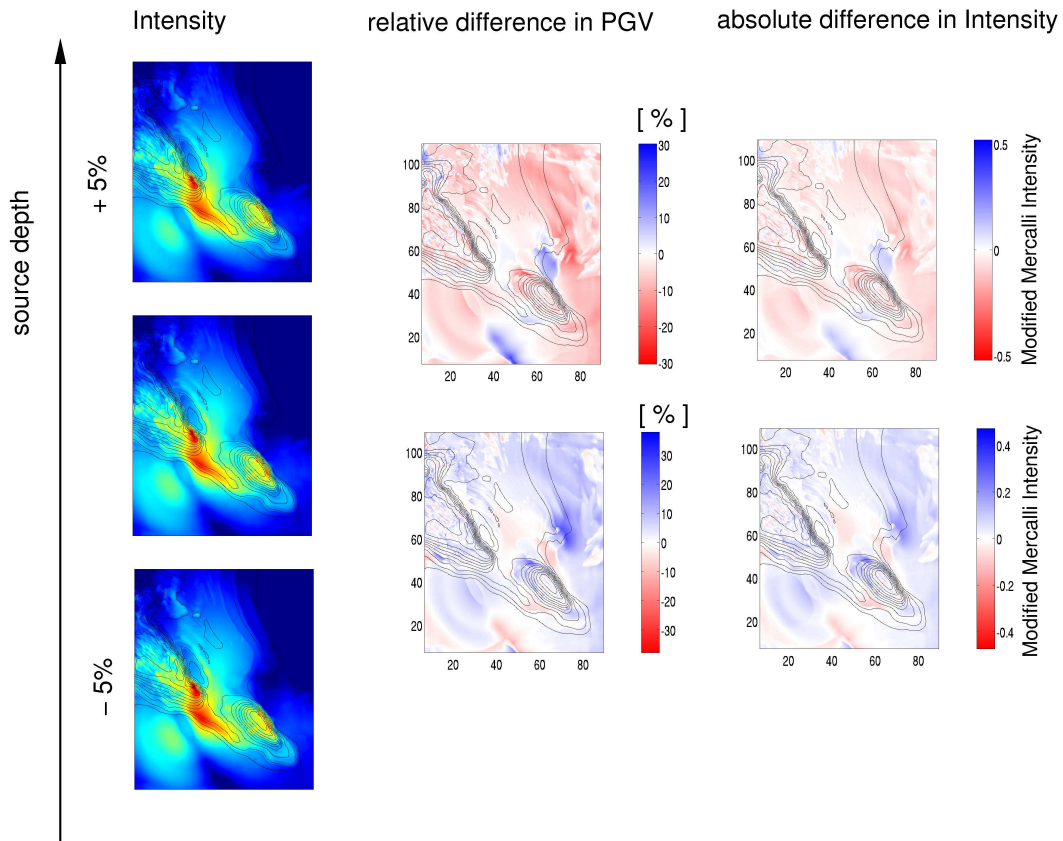


Figure 7.13: Seismic intensities from simulations with varying source depth (left column). The relative difference between the individual models is shown in the middle, whereas the right column shows differences in resulting seismic intensity.

deamplifying effects with small scale variations over the deep basin parts. Maps in the right column show the differences between models in terms of seismic intensity. The above discussed variations result in maximum variations of about half a degree on the seismic intensity scale.

For the investigation of amplitude effects due to a variation in source depth the same distribution of stations was used as in the previous section. In figure 7.14 locations of these virtual receivers are displayed. The ones chosen for the following discussion are demarked with large red numbers.

Station 73 This station is located in the shallow part of the basin with a relatively flat topography underneath. In this context it is important to consider the wave path from the hypocenter to the receiver location. For this station there is no distinct basin topography recognizable along this path. Amplitude comparison for the East-West horizontal component as shown in figure 7.15 a) reveal very similar waveforms when a change in source depth of 5 percent to greater or lesser values is introduced. The onsets of P and S-waves show the travel time influence of the altering source depth. Peak amplitudes are scaling linearly with source depth as shown in figure 7.15 b).

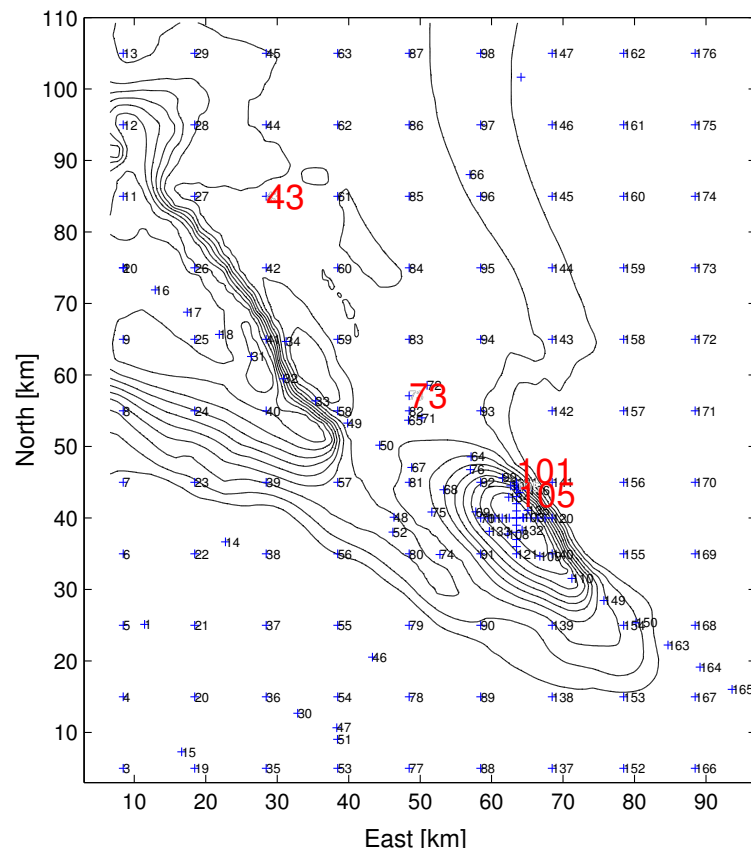


Figure 7.14: Distribution of virtual receivers used in this study. The four stations from which seismogram comparison is presented in this section are demarked with large red numbers.

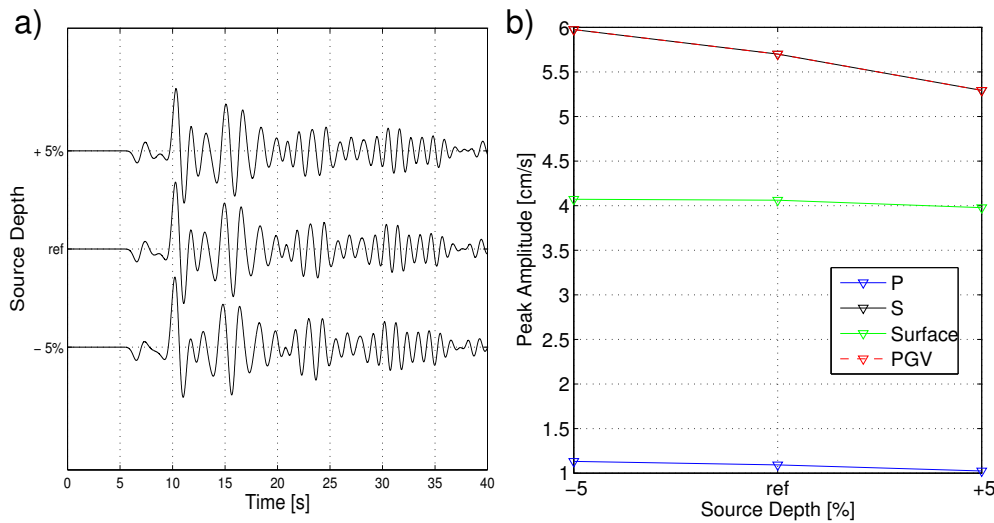


Figure 7.15: East-West component seismograms at station 73 (see 7.14 for location) achieved using models with variations in source depth of -5 % and +5 % from the reference value as indicated (a). Maximum amplitudes for individual phases and the resulting peak ground velocity of the traces are plotted in (b).

Station 43 Like the station before this receiver is set in a shallow part of the basin with no strong topography apparent underneath. However, reconsidering the wave path from source to receiver reveals a distinct difference. From a point of view located at the epicenter station 43 is lying behind one of the most prominent features of basin topography. This different setting has a clear expression in the waveform differences. Seismograms at this station achieved with varying source depth are shown in figure 7.16 a). Whereas the first arrival of P-waves still show linearly decreasing amplitudes with increased source depth, the shear wave onsets exhibit a disproportionately high amplification with reduced depth. The surface waves show a very complex behavior. The first large amplitude which is determining the overall peak ground motion is increasing with source depth, that means it reveals a non-intuitive dependence on this parameter. The contradicting dependence of shear wave and surface wave amplitudes with source depth is obvious in figure 7.16 b). The late coda again exhibits a roughly linear scaling of amplitudes with decreasing source depth as it is intuitively understood.

Station 101 For station 101 located above the deepest basin part northeast of the epicenter a similar behavior can be observed as for station 43. Figure 7.17 a) presents seismograms of the East-West component horizontal ground motion recorded at this station. Again first arrivals of P-waves show a weak dependence on the source depth. The shear wave amplitudes appear strongly related to source depth in the intuitive way, that means a deeper source results in lower amplitudes. The first part of the surface waves appears not affected by this parameter. However, later arrivals which include the peak amplitudes due to constructive interference show a contradicting dependence on source depth. Consequently, a deeper source results in higher amplitudes, as visible in figure 7.17 b). The explanation for this behavior can be found in the fact that these amplitudes are not a function of only the source and receiver location, but also depend

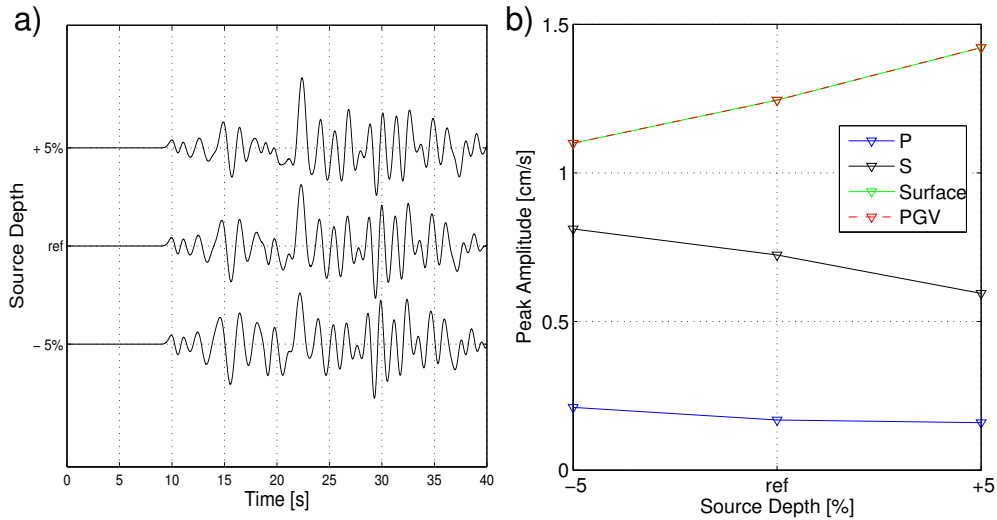


Figure 7.16: East-West component seismograms at station 43 (see 7.14 for location) achieved using models with variations in source depth of -5 % and +5 % from the reference value as indicated (a). Maximum amplitudes for individual phases and the resulting peak ground velocity of the traces are plotted in (b).

on the surrounding wavefield. That means a point that shows the kind of behavior like on station 43 with amplification due to a deeper source in the early arriving surface waves can have its expression in the late arrivals on a different receiver.

Station 105 Similar to the example above station 105 located close to station 101 demonstrates the same behavior. From the seismograms shown in figure 7.18 a), it can be seen clearly that the whole trace shows an intuitive dependence of amplitudes with source depth. This is the case for the first arrivals as well as for the last surface wave onset at 35 seconds seismogram time. However, the peak amplitudes are again determined by constructive interference between 25 and 30 seconds. This interference works better for the seismogram associated with the deepest source location and consequently peak ground velocity becomes amplified with increasing source depth. The effect has its clear expression in terms of peak ground velocities shown in figure 7.18 b).

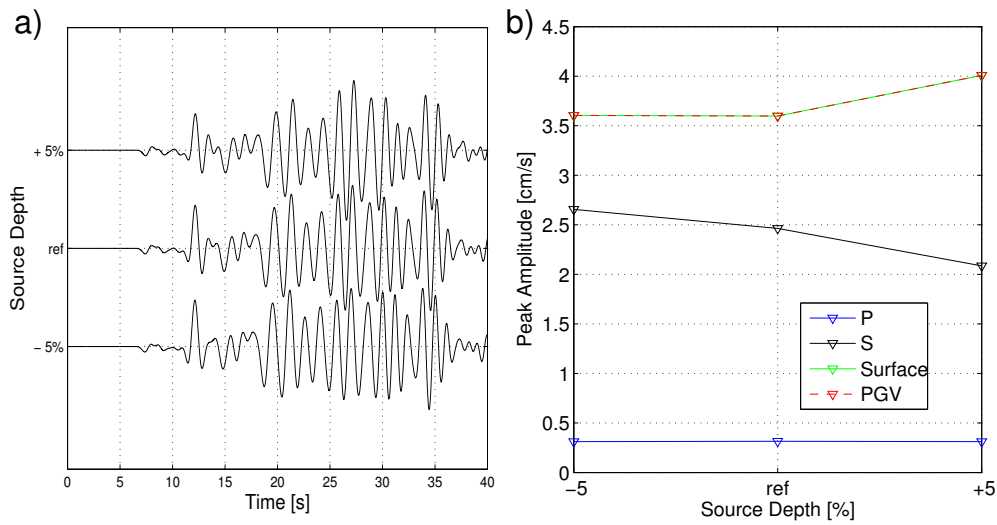


Figure 7.17: East-West component seismograms at station 101 (see 7.14 for location) achieved using models with variations in source depth of -5 % and +5 % from the reference value as indicated (a). Maximum amplitudes for individual phases and the resulting peak ground velocity of the traces are plotted in (b).

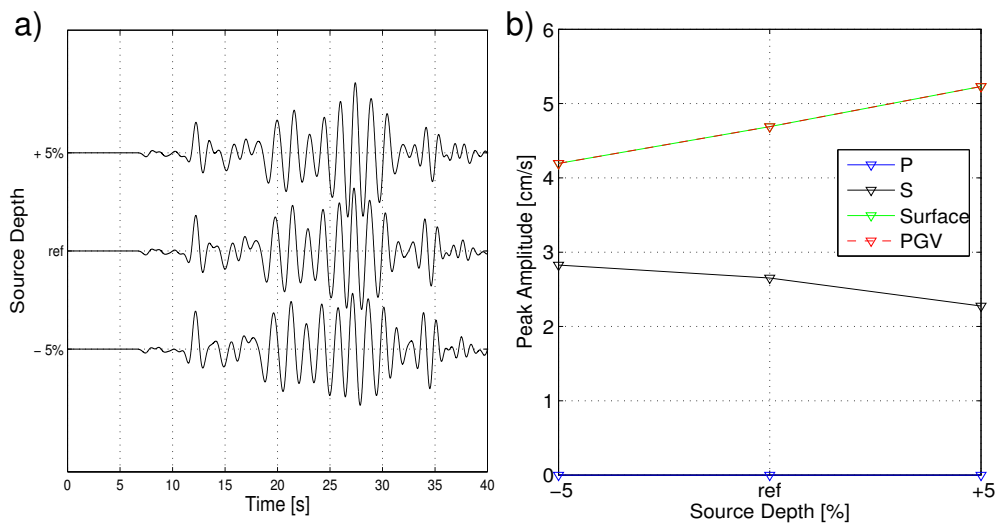


Figure 7.18: East-West component seismograms at station 105 (see 7.14 for location) achieved using models with variations in source depth of -5 % and +5 % from the reference value as indicated (a). Maximum amplitudes for individual phases and the resulting peak ground velocity of the traces are plotted in (b).

7.6.4 Source Mechanism

In a homogeneous model effects caused by a change in strike angle of the moment tensor source can be estimated directly. The source pattern is rotated by a certain degree and the resulting amplitude differences can be calculated. However, in the presence of a complex three-dimensional structure like the sedimentary basin in this study the relations become more difficult. From the results of the previous section concerning changes in source depth it can be understood that resulting amplitudes at the surface are depending on complex interaction between wave radiation from the source and the subsurface geometry. In order to investigate the influence of uncertainties on the estimation of the source tensor the strike angle is varied in 5 degree steps from minus 10 degrees to plus 10 degrees from the original value which serves again as reference solution. The resulting source plane orientations are shown in figure 7.4. From this graph it can be understood that the resulting variation in incidence angles at the bedrock to sediment interface results in nonlinearly affected amplitudes.

In figure 7.19 the individual distribution of seismic intensity for the resulting five scenarios is presented in the left column. The column in the middle illustrates the resulting relative differences in peak ground velocity whereas the column on the right hand side presents absolute differences in the derived quantity seismic intensity. The most striking result is that the expected pattern of areas with amplification and deamplification is present only for a small part of the model in the south. For this region the wavefield is determined by the homogeneous background model. Due to the source location close to the sedimentary basin the rest of the study area is affected strongly by the basin itself or its interaction with the changed source radiation pattern. The overall effect is an amplifying one when the strike angle is turned towards the basin and a deamplification when it is turned in the other direction. An overall variation in peak amplitudes of 15 percent for a 5 degree change in strike angle and as high as 25 percent for a 10 degree change in strike angle can be observed over large parts of the model. The amplification and deamplification have roughly the same amount.

Regions with opposite behavior can be recognized in shadow parts of the model behind strong topographies in the sedimentary basin with respect to the epicenter. These areas coincide with similar observations presented in the previous sections for the interaction of source depth variations with basin structure. Inside the basin disproportionately high amplification and deamplification effects are observable in different regions: between the two deep basin depressions and above the steep basin edges, and above the deepest part of the basin in the north west. The differences can be as high as 25 percent in terms of PGV resulting in a variation in seismic intensity of half a degree. The mentioned differential source radiation pattern is observable south of the basin on bedrock.

For the investigation of amplitude effects due to a variation in source orientation the same distribution of stations was used as in the previous section. In figure 7.20 locations of these virtual receivers are displayed. The ones chosen for the following discussion are demarked with red numbers.

Station 35 This station is located on the southern model edge upon bedrock. Seismograms recorded at this station are shown in figure 7.21 a). Despite the fact that it is located only 20 km away from the epicenter amplitudes recorded on this station show

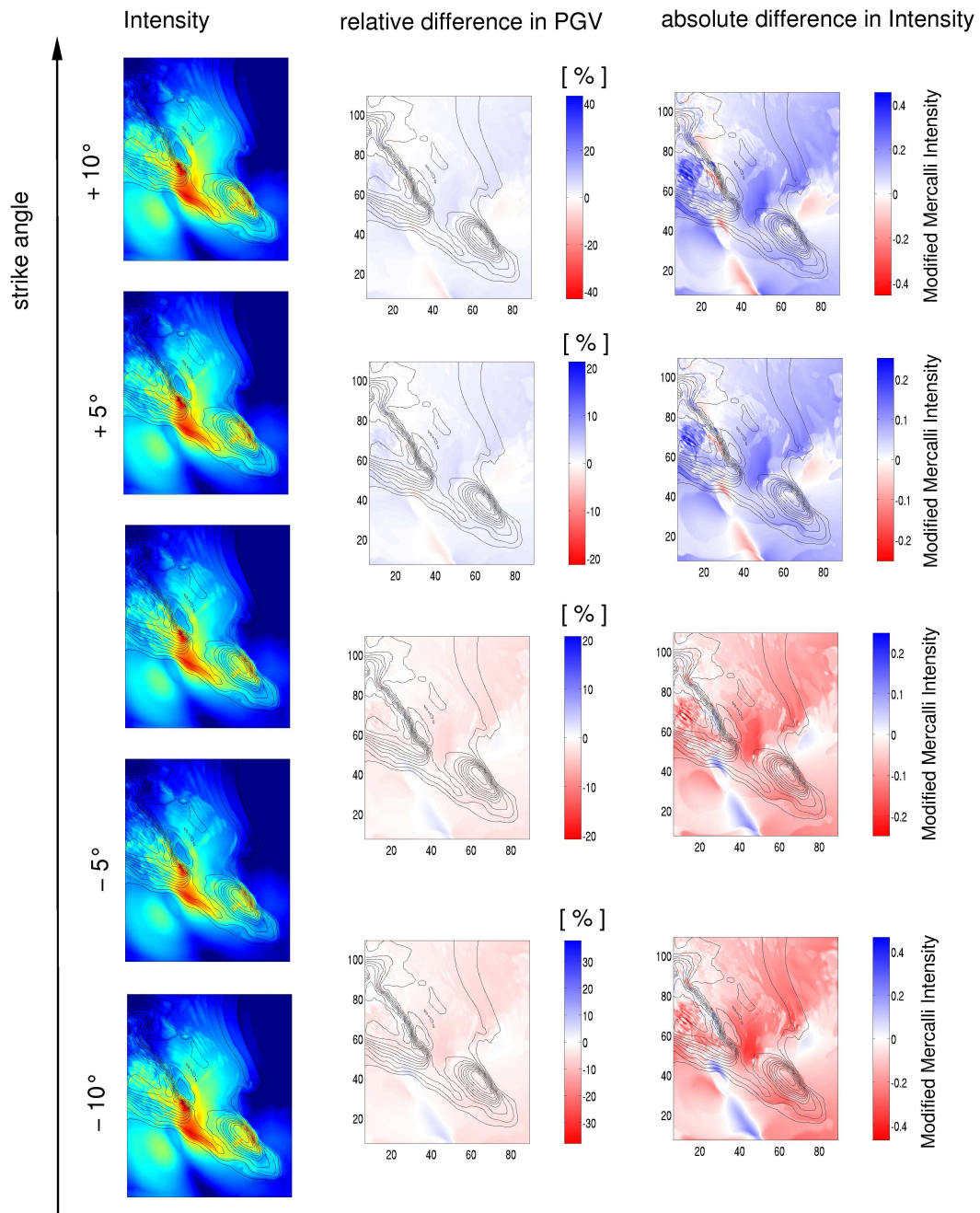


Figure 7.19: Seismic intensities from simulations with varying strike orientation (left column). The relative difference between the individual models is shown in the middle, whereas the right column shows differences in resulting seismic intensity.

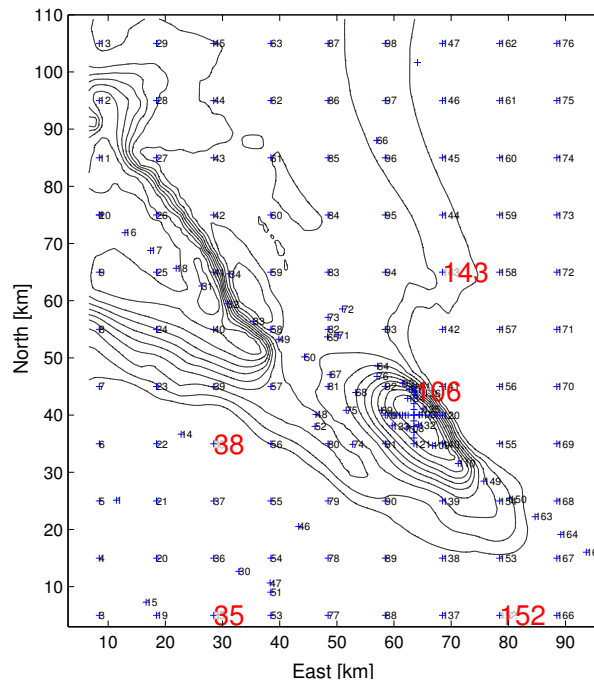


Figure 7.20: Distribution of virtual receivers used in this study. The five stations from which seismogram comparison is presented in this section are demarked with large red numbers.

only weak sensitivity to the changes in strike angle that has been applied in this study. The slight linear decrease in peak amplitudes can be recognized in figure 7.21 b).

Station 38 Station 38, also a bedrock station, is located close to a nodal plane of the reference source radiation pattern for shear waves. The effect on the seismograms recorded at this receiver are easily understood from figure 7.22 a). Whereas the P wave amplitude remains nearly constant for the changes in the strike angle the shear wave amplitudes are highly sensitive to those. A change in positive direction increases amplitudes as the energy radiation beam turns towards the station. A negative change of the strike angle changes the sign of the shear wave onset and with further decreasing angle the amplitude rises. Clear expression can be found in the peak ground velocities presented in figure 7.22 b). As in the example above the coda of the seismograms is not affected by the changing strike angle, as this part consists of scattered energy from the basin structure.

Station 152 For the bedrock site 152 a linear dependence of amplitudes on strike angle can be found for a single onset of surface waves. Seismograms displayed in figure 7.23 a) appear nearly identical besides this phase. As this phase produces the strongest amplitudes in the traces it determines the peak ground velocities shown in figure 7.23 b).

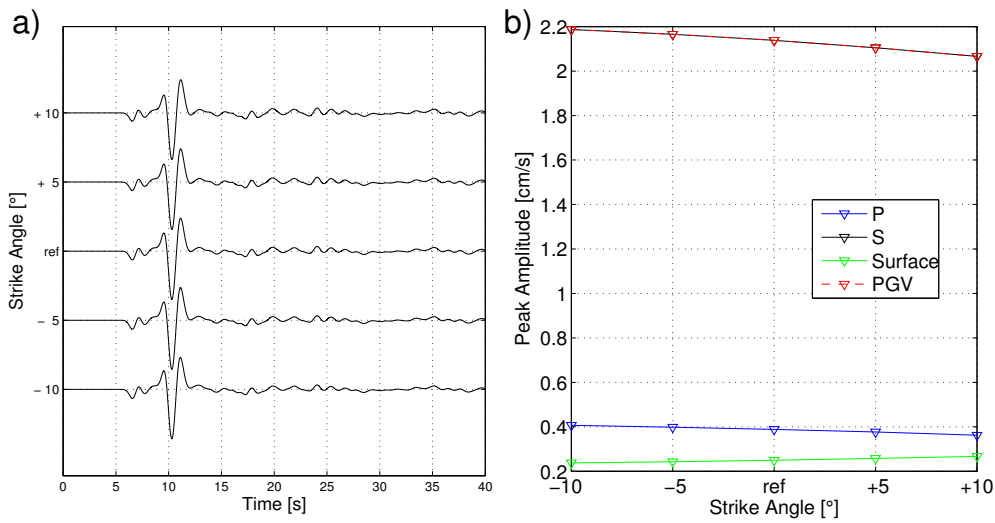


Figure 7.21: East-West component seismograms at station 35 (see 7.14 for location) achieved using models with variations in strike orientation of -10° to $+10^\circ$ from the reference value as indicated (a). Maximum amplitudes for individual phases and the resulting peak ground velocity of the traces are plotted in (b).

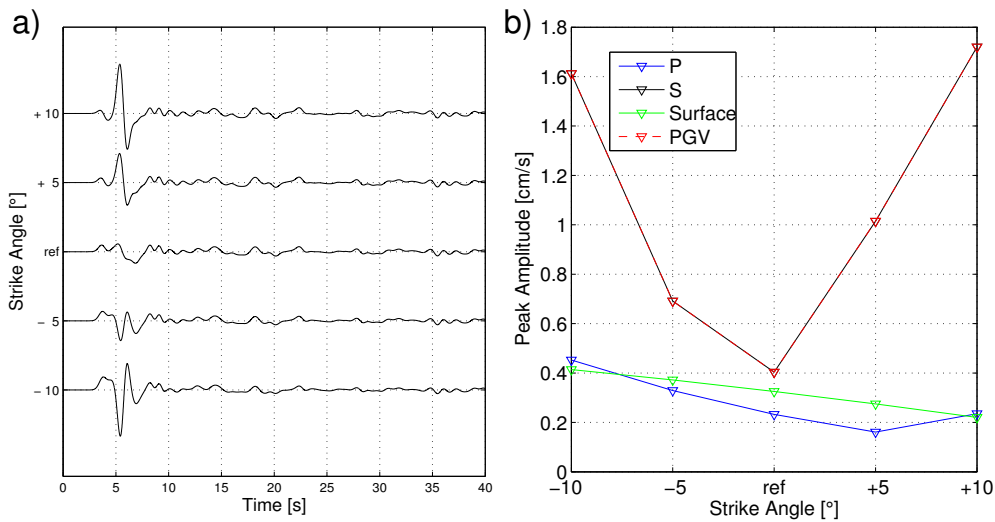


Figure 7.22: East-West component seismograms at station 38 (see 7.14 for location) achieved using models with variations in strike orientation of -10° to $+10^\circ$ from the reference value as indicated (a). Maximum amplitudes for individual phases and the resulting peak ground velocity of the traces are plotted in (b).

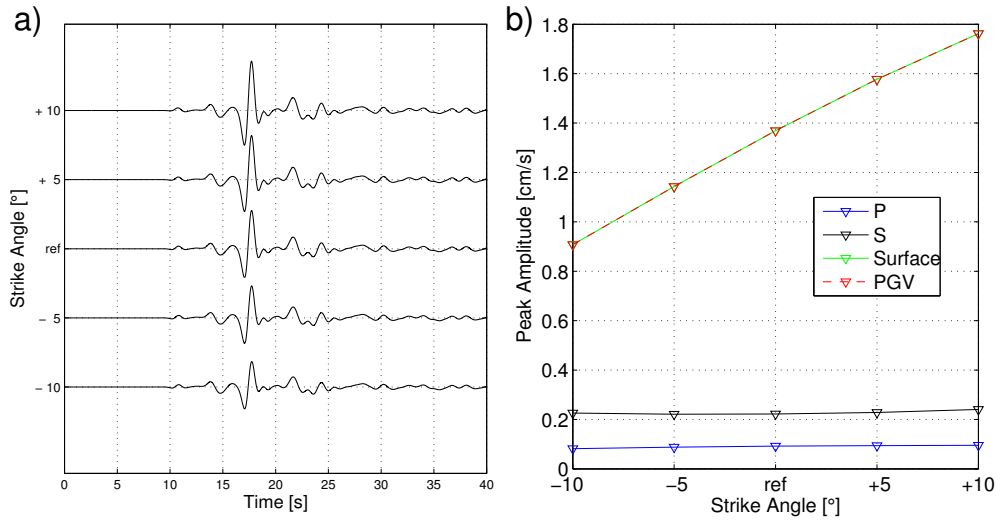


Figure 7.23: East-West component seismograms at station 152 (see 7.14 for location) achieved using models with variations in strike orientation of -10° to $+10^\circ$ from the reference value as indicated (a). Maximum amplitudes for individual phases and the resulting peak ground velocity of the traces are plotted in (b).

Station 143 Inside the basin relations become complex. Seismograms recorded at virtual receiver 143 in a shallow part of the basin close to the steep flanks of the southern deep depression are presented in figure 7.20 a) and reveal a complex behavior. This originates from the superposition of different waves which are depending differently on the strike angle. For this location, shown in figure 7.24, the first arrivals as well as the last part of the traces between 35 and 40 seconds show weakly increasing amplitude with increasing strike angle. Arrivals in between, however, exhibit a disproportionately strong dependence on this parameter. As these onsets are dominating the peak ground velocities in this region the strong change observable in the PGV maps can be understood. The varying dependence of amplitudes with strike angle for the different phases are illustrated in figure 7.24 b).

Station 106 This station is located above the deep depression in basin topography southeast of the main basin structure. The seismograms presented in figure 7.25 a) demonstrate clear sensitivity in the P and S-wave amplitudes on strike angle. Nevertheless, the dominating reverberations in the later part of the trace are affected only weakly by this parameter. These wavefronts are reverberating energy trapped within this part of the basin. It can be understood that there is no significant sensitivity to the path of the wave energy when entering this structure. As the peak amplitudes of the region can be found in this part of the seismograms it becomes clear, why the deepest parts of this confined structure do not show distinct sensitivity to the strike angle in the PGV maps. Plots of maximum amplitudes shown in figure 7.25 b) prove this weak dependence on strike angle compared to the previous station.

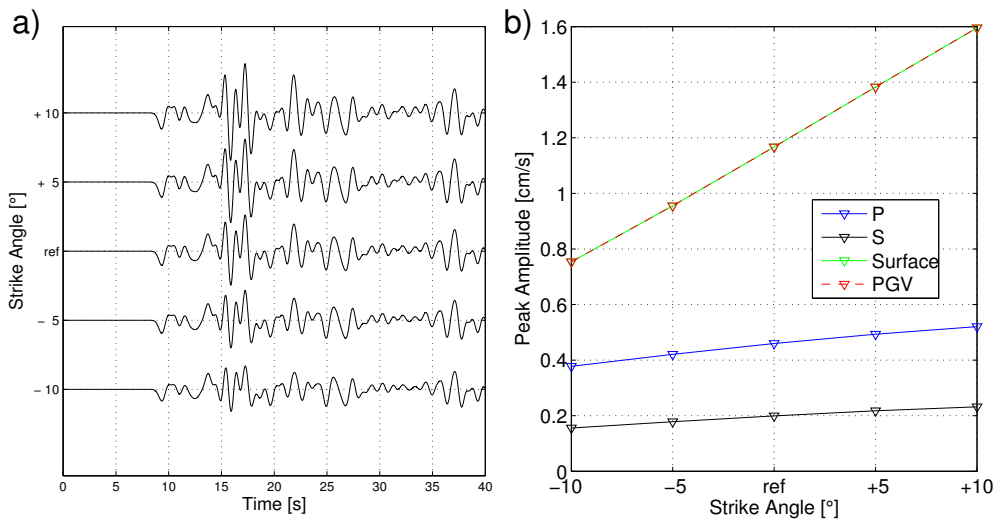


Figure 7.24: East-West component seismograms at station 143 (see 7.14 for location) achieved using models with variations in strike orientation of -10° to $+10^\circ$ from the reference value as indicated (a). Maximum amplitudes for individual phases and the resulting peak ground velocity of the traces are plotted in (b).

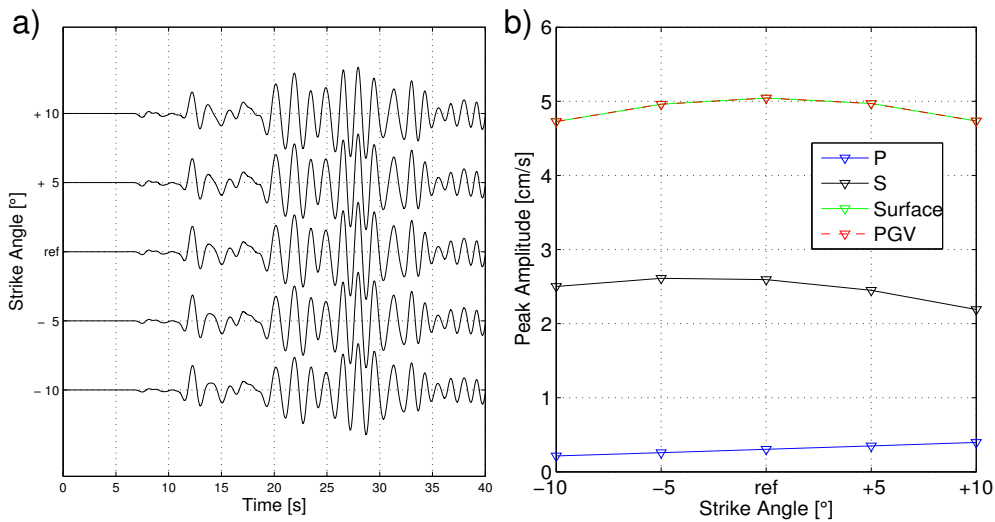


Figure 7.25: East-West component seismograms at station 106 (see 7.14 for location) achieved using models with variations in strike orientation of -10° to $+10^\circ$ from the reference value as indicated (a). Maximum amplitudes for individual phases and the resulting peak ground velocity of the traces are plotted in (b).

7.7 Combination of Variabilities

In previous sections variability of simulation results due to marginal differences in three individual input parameters have been shown. In this section a possible application interface for variability results is suggested. As this has the character of a pilot study a number of simplifications is made and individually discussed on appearance. The procedure consists of the following steps:

1. For an chosen simulation parameter a probability curve is applied to the individual variations. In this context a simple Gaussian uncertainty relation is assumed. Figure 7.26 displays a sample probability curve which is used in the following. In a realistic approach it will be a crucial task to find appropriate estimates on the probability for individual parameter uncertainties. These relations are not necessarily independent from location. For example the accuracy of a basin depth estimate shows typically a large variation over a study region, ranging from errorfree values at locations, where well-logs are available to distinctly erroneous values in between.
2. Using the above discussed uncertainty probability it is possible to compute a best guess simulation result on each point using weighted averaging of the individual results.
3. From this average result the extent of variations can be quantified for each point. The result consists of a best guess value with errorbars attached.

As example the basin depth variation is chosen. Figure 7.27 displays a possible output format for such an application. For an arbitrarily chosen position within the study area an averaged resulting value is provided along with its variations. Mapping of both the average value as well as the variations in positive and negative direction allow identification of regions of interest. Additionally, seismograms for all simulations available can be displayed.

7.8 Discussion

In this chapter the influence of uncertainties in input parameters on results from numerical ground motion simulations was investigated. The concept of an error space defined by a number of error axes is developed. Limited computational resources restrict the character of this work to the one of a pilot study. The model was varied in three parameters and no combinations of variation in different parameters at the same time was considered. Consequently, these models were located along the axes of the error space. As parameters were chosen:

1. Basin depth as the most prominent parameter defining the velocity model of the study area.
2. Hypocenter depth of the scenario earthquake.

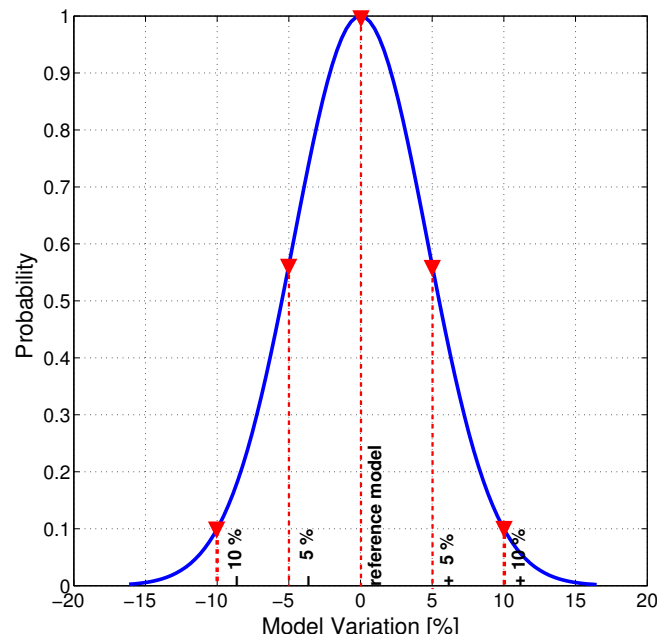


Figure 7.26: Assumed Gaussian probability relation for individual model variations.

3. Strike angle of the moment tensor given by the earthquake scenario.

Peak ground velocity (PGV) and seismic intensity as derived quantity were chosen as output values on which variations due to a change in the input parameters were studied. The main results are summarized in the following:

- For all parameters a variation in a realistic range of plus/minus 10 percent result in a local variability of peak ground motion up to 50 percent.
- All parameter variations result in a heterogenous distribution of resulting variations in PGV.
- Clear interaction between a change in source depth or mechanism with the structural geometry of the model can be observed.
- For the variation in basin depth it can be seen that there is no general relation between this parameter and the sign of change in result. There are locations within the study area, where both a reduced as well as enhanced basin depth result in amplification and vice versa.

From a technical point of view the simple approach to achieve this goal used in this study has a number of advantages:

- A striking feature of the approach is its straight forward character. The input parameters are varied and the results stored as they come.

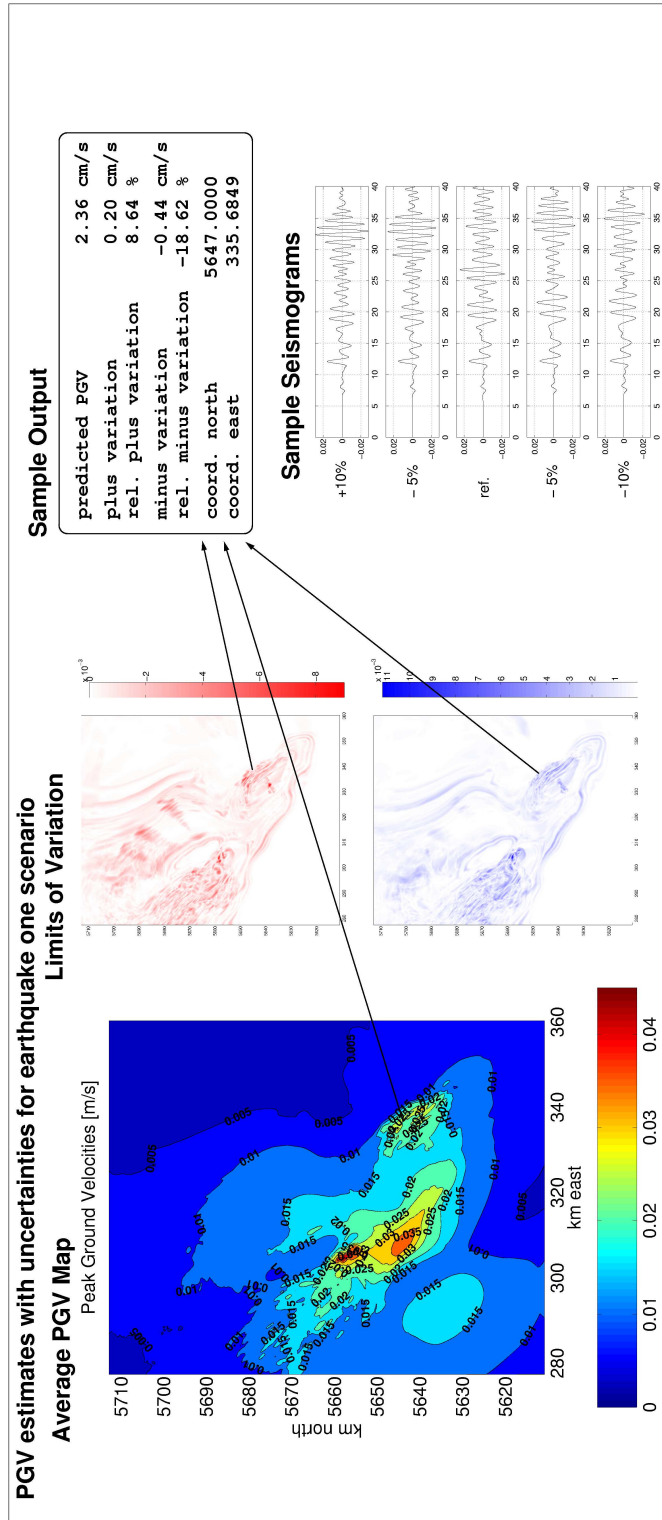


Figure 7.27: Possible output format displaying combined results from multiple simulations with variable input datasets.

- The availability of complete solutions using different input parameter sets account for diverse post processing. For example the probability relations can be modified both locally or over the whole model area to account for new findings.
- Also it is possible to enhance an existing dataset alike the one presented in this chapter to investigate other parameters.
- Most importantly this approach accounts for the correct realization of interaction between different parameters.

However, achieving these goals using the straight forward approach suggested in this chapter is affiliated with large computational effort:

- A complete exploration of the error space may need the individual simulation for all possible combinations of parameters within the error space.
- Output datasets for all simulations have to be stored and be postprocessed. As discussed several times in this thesis the amount of data produced by numerical simulations for three dimensional wave propagation tends to be very large.

The approach proposed in this chapter may serve as possibility to estimate limits of linear behavior in wave propagation simulations. Such limits are necessary to know before an inversion technique based on the assumption of linearity such as adjoint state methods can be employed.

As discussed in 7.2 due to limitations of computational requirements no combination of these variations has been performed. In a future step the whole error space defined by error axes has to be explored in order to reveal the combined influence of uncertainties along more than one error axis. Large heterogeneities revealed in the spatial distribution of variations already impose a strong coupling effect between changes on source parameters with structural geometry of the model. From this result a complex behavior can be expected when both model and source are object to changes. Variations may behave, multiply or zero out. As a next step the question has to be answered whether and in which limitations variations away from the error space axes can be estimated from a combination of results along the axes. Figure 7.28 illustrates the principle by means of a two-dimensional error space determined by two arbitrary input parameters. Squares demark positions in the error space where variations are known. They therefore represent the status of this work. Circles demark positions of unknown behavior. The key question is whether these positions can be evaluated through a combination of known results (squares) or if all possible simulations have to be performed. From this two-dimensional example it already becomes clear that in the latter case the number of necessary simulations is increasing rapidly.

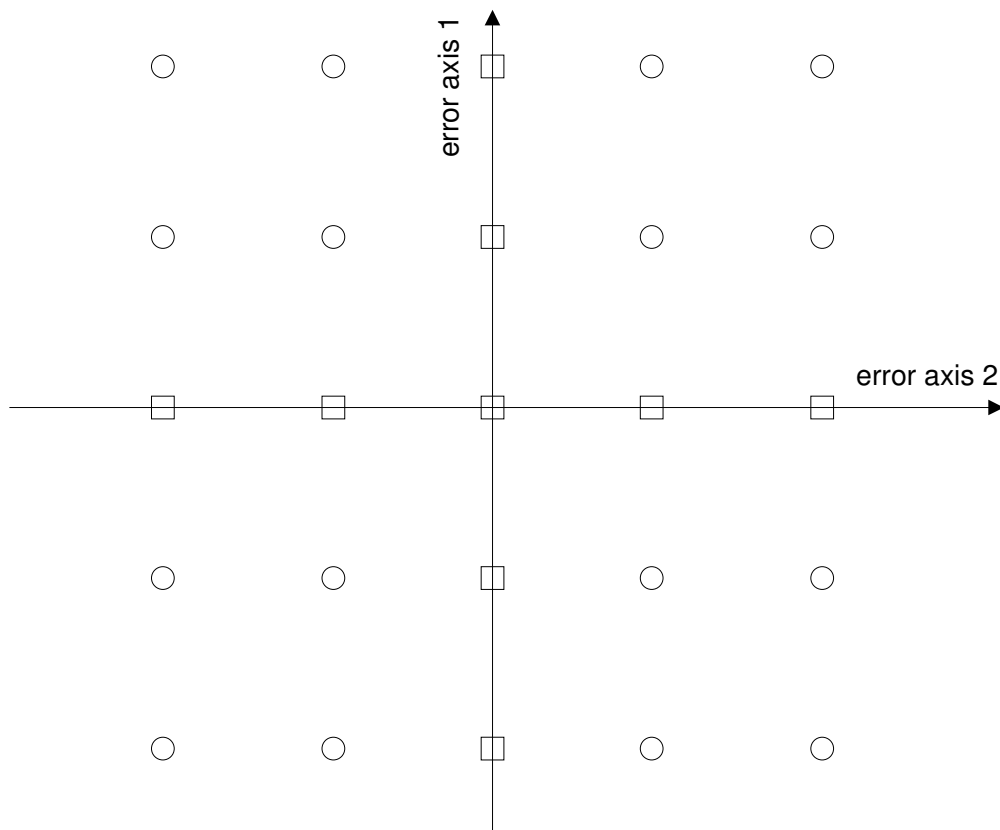


Figure 7.28: Principle of combination of uncertainties. Squares indicate positions within the error space where variability is known, circles combinations with unknown result.

Chapter 8

The WWW Scenario Database

The WWW scenario database is a web based tool designed for visualization purposes of synthetic seismic data produced by numerical simulations. The implementation is based on a PHP code developed by Kim B. Olsen at St. Barbara. This code was enhanced in its capabilities with special emphasize to the online derivation and visualization of ground motion key parameters, such as seismic intensity or static displacement. Whereas the practical usage of the WWW Scenario Database is described in Rieger (2005), in this chapter guidelines are given concerning the appropriate design of output routines in simulation codes and data processing necessary to add new scenario results to the database.

8.1 Motivation

A general characteristic of numerical simulations of earthquake scenarios is the excessive consumption of both computational time and core memory. Additionally, a lot of man power is needed to implement additional complexities in existing codes, get codes running and prepare useful models for the production of synthetic data. Once this operational effort is being completed it is a natural desire of programmers to retrieve as much information as possible from the single simulation run. Fulfillment of this wish results in the production of huge amounts of data to be stored. From the whole data set produced by individual simulation runs typically only a small percentage is actually used in order to answer specific questions. From this contradiction the idea of a scenario database arose with the goal of taking advantage of such datasets as a whole at very little additional effort. The data should be available for longterm use in a format that makes it easy to access, possibly from any place and still with the data quality necessary to answer scientific questions. From these objective targets a set of requirements on the nature of the database application can be constructed:

- Data should be kept in a central database, with the possibility of uploading new scenario results and retrieving information from the existing ones.
- Data should be compressed to a reasonable size.
- The interface for both uploading and retrieving data should be web based.

- Formats have to be standardized in order to make longterm increase of the database feasible.
- Not only downloading data, but also visualization procedures should be web based.

The presented WWW scenario database is an attempt to meet most of these requirements.

8.2 Technique

For the implementation of the WWW scenario database the PHP script language was chosen. PHP stands for “PHP: Hypertext Preprocessor”. Using this language meets most of the requirements:

- PHP is an open-source tool, so no expensive software or software licenses have to be bought.
- PHP is a server-side scripting language, that means that the - partly - expensive calculations necessary to process data and create visualizations from it are carried out on the server and a user from a slow machine can still use the database interfaces.
- The PHP approach is suitable for the modularization of the functionalities of the database into a number of scripts with - more or less - manageable length.
- Due to above points it is ensured that the database is relatively easy to enhance in terms of functionality as well as maintainable for the longterm usage.
- PHP supports a large number of mathematical functions necessary for producing secondary data (such as intensity maps).
- The possibility to handle external programs is also given and used for processing expensive calculations.
- Additionally, figures once created can be stored and loaded directly when accessed again.
- PHP supports production of figures designed for the usage with common web browsers.

A detailed description of the individual modules and their capabilities is given in Rieger (2005). A screen shot from the running application in a web browser is shown in this context to serve as example for further explanations.

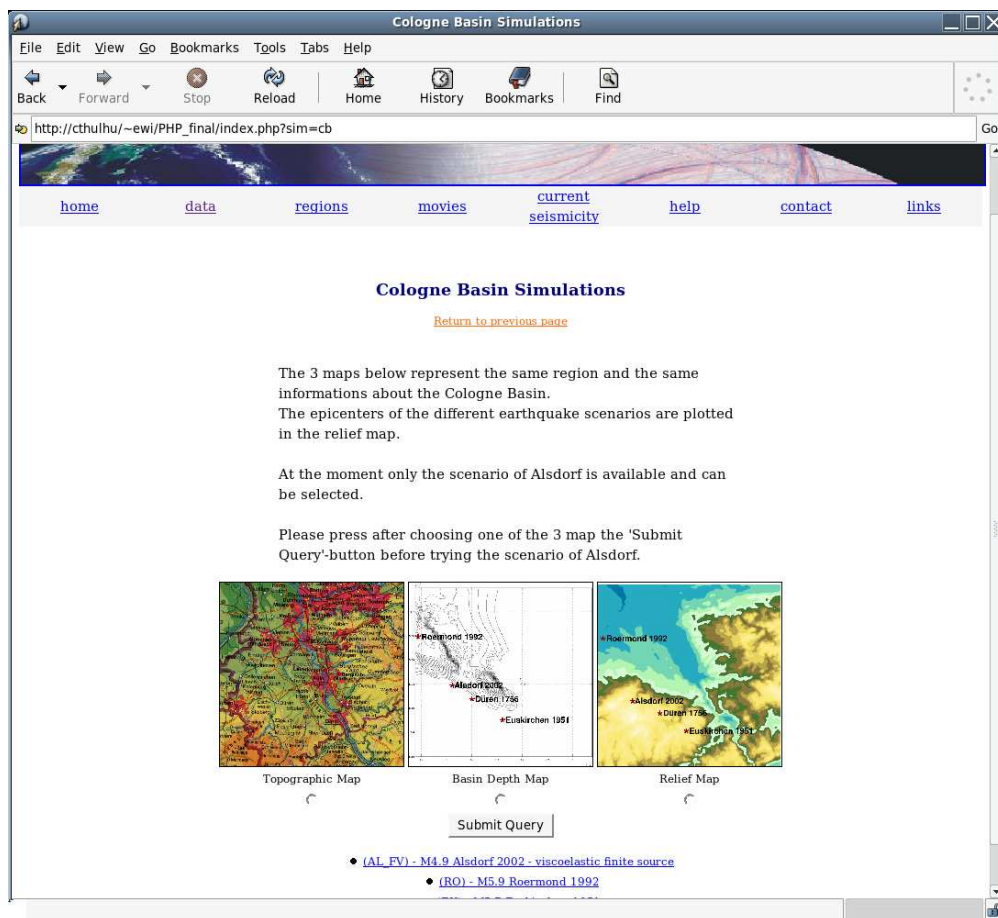


Figure 8.1: Screen shot from scenario earthquake database entry page.

8.3 Creation of a New Scenario Earthquake Entry

In this section all steps necessary to create a new entry in the scenario earthquake database are covered.

8.3.1 Database Structure

The database itself is designed as an ordinary LINUX/UNIX directory tree. An example is shown in figure 8.2. The philosophy of the database design is to keep the directory and filenames short for the items that are automatically generated or contain raw data. Only parameter files which can and should be edited by the user have self-explanatory names.

Top level directories contain what should be called a scenario region. In the example **cb** is an abbreviation for Cologne Basin. It is necessary to highlight the point that such a scenario region is defined not only through the regional aspect as it may be imposed by the choice of names. Instead the definition scenario region also covers the dataset design contained herein. That means, all datasets in a specific directory must have the same number of receivers, identical receiver geometry and so on. These parameters are passed to the application through a number of configuration files identifiable by the common beginning **.sim_**. The filenames are completed by a syllable characterizing the file content. This set of parameter files is associated with the scenario region and therefore all scenarios contained must fit into that description. The individual files are explained below.

The next level consists of the individual scenario earthquakes available for one specific scenario region. In the example tree **a1** stands for the Alsdorf earthquake. Individual setups can and should be explained in detail using the configuration files explained below. The choice of the directory name itself is arbitrary, nevertheless it is recommended to use short but somehow self-explanatory names.

There are three entries to each scenario directory containing the three components of seismograms in binary format. Generation of files recognizable for the database is explained in 8.3.5. The special directory **.www_files** is created and accessed by the application itself to store figures and temporary data. It should not be accessed or changed in any way by the user. The top level directory also contains a number of picture files in Graphics Interchange Format (GIF). These files contain maps serving as an interface for the user in order to access data at specific locations.

```
cb
|-- .sim_coordstr
|-- .sim_name
|-- .sim_params
|-- .sim_scenarios
|-- al
|   |-- x
|   |-- y
|   `-- z
|-- cb1.gif
|-- cb1.txt
|-- cb2.gif
|-- cb2.jpg
|-- cb2.txt
|-- cb3.gif
|-- cb3.jpg
|-- cb3.txt
|-- cbgrid1.gif
|-- cbgrid1.png
|-- cbgrid2.gif
|-- cbgrid2.png
|-- cbgrid3.gif
|-- cbgrid3.png
|-- du
|   |-- x
|   |-- y
|   `-- z
|-- ek
|   |-- x
|   |-- y
|   `-- z
|-- jet_int.map
|-- ro
|   |-- x
|   |-- y
|   `-- z
|-- ynr.txt

4 directories, 32 files
```

Figure 8.2: Directory tree for a sample entry in the earthquake scenario database.

8.3.2 Necessary Files

In order to create a new entry for the earthquake scenario database a user must provide a number of files of different categories:

1. Maps
2. Configuration files
3. Seismic data files

In the following subsections these files are described in detail. The above given tree structure for the Alsdorf earthquake scenario as part of the Cologne Basin scenario region serves as example for the explanations. Some of the filenames are at least partly obligatory once a directory name is chosen. In this example **cb** as scenario region directory name (abbreviated for Cologne Basin) and **a1** for the scenario itself (abbreviated for Alsdorf) is chosen.

8.3.3 Maps

Figure 8.2 shows a screen shot from the running database application which gives an impression of the usage of the application in practice. One of the main capabilities is the visualization of different ground motion parameters at a specific location which is chosen by the user via a map interface. For the creation of a new entry one or more maps for this interface have to be provided by the user in GIF format. The respective files have to be named alike the scenario region directory plus a numbering and the denotation “grid”. In this case the directory was called **cb**, so the files must be named:

cbgrid1.gif

cbgrid2.gif

cbgrid3.gif

and so forth. Maps itself can be chosen arbitrarily, nevertheless some hints for a useful choice may be given here.

- A topographical view of the area is always useful. Even if the scenario is a completely virtual one such as homogenous half space a provided topographical map is not only a visual gain but can also provide a length-scale.
- One of the maps should represent main characteristics of the model that was used in the simulation the scenario dataset is based on. In this example an isoline plot of the basin model is used. Other possibilities involve topography or a representation of the source model.
- As this scenario database is a web based application it is designed for usage of different people in different locations using different hardware. It is recommended to check the appearance of maps on more than one computer and screen in order to provide a widely usable dataset.

One additional picture (which must not but can be a map as well) is used for the starting page to represent the individual scenario regions within a browser window. Whereas this picture itself is completely arbitrary the filename is obligatory and has to be alike the directory name chosen for the scenario region. In this example the directory was named **cb**, so the file must be called:

cb.gif

8.3.4 Configuration files

All information that is displayed by the PHP-based earthquake scenario database is generated dynamically. To achieve this, the main module `Index.php` collects necessary information from a number of configuration files the user must provide. From the organization of the directory structure shown in figure 8.2 it can be understood that these files are linked to the individual regional model. Therefore the user must create these files when adding a regional model, or edit existing ones when a new scenario is added to an available regional model.

All configuration filenames start with the common syllable `.sim_` and have an ending which gives a hint on their content. Some of the `.sim` files contain only plain ASCII text, whereas others contain PHP code that is parsed by the preprocessor. These files must be edited carefully in order to keep the correct syntax. It is a recommendation, addressed especially to Windows users, to use only simple text editors when changing the configuration files in order to avoid side effects due to control characters. In the following paragraphs the necessary `.sim` files are described in detail.

.sim_name This file contains the name of the regional model in plain ASCII text. No special syntax is necessary. Nevertheless, as it will appear on the screen it is recommended to provide meaningful names. As mentioned above it is obligatory to use different regional models for different receiver geometries because the configuration files are linked to the regional model and not to a single scenario. This is also the location to give information about the method with which the simulations were carried out. Therefore it may be helpful to provide a bit more information at this point (e.g. not only “Cologne Basin”, but “Cologne Basin FD 1 km resolution”, “Yanhui basin with numerical Greens functions” or “LA Basin SpecFEM”, etc.).

.sim_scenarios This file is passed to the PHP parser, therefore correct syntax is crucial. It contains the names of scenarios available within the current regional model as they should appear on the web page and the directory names where the database application looks for the data related to the individual scenario. Below an example is shown for the Cologne Basin regional model.

```
<? // This is a php parsed file, so the syntax must be correct
for it to work correctly. Just add scenarios here. Use \'s
to escape any " 's
$${'al'} = "M4.9 Alsdorf 2002";
$${'ro'} = "M5.9 Roermond 1992";
```

```

$S{'ek'} = "M5.7 Euskirchen 1951";
$S{'du'} = "M6.1 Dueren 1756";
?>

```

.sim_coordstr This file contains a function which calculates the receiver coordinates within the model area and provides a formatted coordinate string for the plotting routines. This file is a piece of PHP code so the syntax must be correct, otherwise the PHP preprocessor produces an error. The following code excerpt shows the important lines of the file which are subject to changes.

```

<?
...
$dx=1;
$rot=0.0;
$faclon=71.4;
$faclat=111.1;
$alonbeg=6.0;
$alatbeg=50.00;
....
$a11=($n1-1)*$dx;
$a12=($n2-1)*$dx;
$fac11=$faclon*cos($rot*$pi/180.0);
$fac12=$faclat*sin($rot*$pi/180.0);
$fac21=$faclon*sin($rot*$pi/180.0);
$fac22=$faclat*cos($rot*$pi/180.0);
....
$coordstring = sprintf("Lat:  %.2f, Lon:  %.2f", $alat, $alon);
?>

```

The user must provide the following information which is stored in variables:

\$dx: The receiver spacing, note that in the current implementation only regular, equidistant receiver geometries are allowed.

\$rot: A rotation angle for the whole model area with respect to the origin.

\$faclon: Factor for converting distances into geographic longitudes.

\$faclat: Factor for converting distances into geographic latitudes.

\$alatbeg: The geographical latitude of the model origin.

\$alonbeg: The geographical longitude of the model origin.

In the following main part of the function coordinates for the individual position is dynamically calculated when acquired and delivered in a formatted string using the `sprintf` (string print formatted as its known from C) command. This line has to be changed when a user wishes a different format for the coordinates appearing on the screen.

.sim_params This plain ASCII file contains the information necessary for the application to calculate values from the data and visualize them in a reasonable way. It includes useful comments which make the file self-explanatory. Nevertheless the most important parameters should be briefly described.

```
axislab_x = "N/S"
axislab_y = "E/W"
axislab_z = "Vertical"
```

Containing the captions for all seismogram plots.

```
...
map_w = 555 # width of usable portion of map
map_h = 570 # height of usable portion of map
map_x = 50 # x translation value
map_y = 560 # y translation value
cell_w = 131 # width of matrix
cell_h = 131 # height of matrix
...
```

Most important are the variables `cell_w` and `cell_h` containing the number of receivers in x direction and y direction respectively. These values must be consistent with the provided dataset, otherwise all the plots become bizarre.

```
...
# these are for horizontal (x) scaling (histories)
begsec = 0 # time range start
endsec = 60 # time range end
hist_samps = 360 // another comment
si = 0.04
...
```

These variables provide information concerning sampling rate, start and end time of the traces etc. For example a static time offset could be provided herein.

```
# these are for vertical (y) scaling (histories)
val_min = -25 # min val in cm/sec
val_max = 25 # max val in cm/sec
hist_plot_h = 150 # how high to make each plot (min to max)
```

```
hist_plot_vgap = 25 # gap between each plot
...

```

These parameters are mainly of interest for changing window appearance.

8.3.5 Seismic data

This subsection explains the steps necessary to produce a dataset which can be uploaded into the scenario database.

8.3.5.1 Required Format

The scenario database works with binary data in order to keep the disk space small when storing many scenarios.

IMPORTANT: As the application is running on a central server all data files must be in the native binary machine format of that machine for uploading new scenarios.

As the scenario database is a server-side application there is no data actually passed from server to client. If data is downloaded through the provided interface it is converted first to ASCII and displayed as text, just like the figures are displayed. That implies that for downloading data the machine format has not to be concerned. As mentioned above the receiver geometry must be an equidistant, regular grid. Grid spacing and the number of rows and columns have to be consistent with the values provided in the related lines of the parameter files.

In the examples given here the sampling of seismograms is fixed to 360 time steps. That restriction results in seismogram plots of reasonable size for most common screen dimensions. As a consequence some consideration concerning frequency content of the provided datasets has to be made. As synthetic seismograms normally have a significantly higher sampling rate it is recommended to filter individual traces to periods which can be resolved well by 360 samples. Figure 8.3 illustrates the similarity of a resampled and the appropriately filtered trace from the example dataset. The visualization of such resampled traces as velocity seismograms does not result in difficulties. However, derived quantities like displacement time series are often problematic due to the integration of a very limited number of samples. It must be stated that the visualization tools of the WWW scenario database remain on a qualitative level.

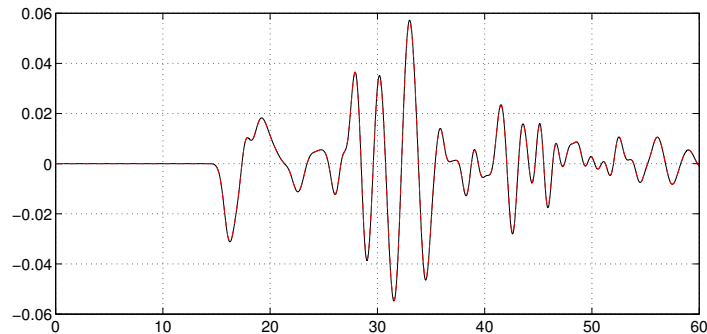


Figure 8.3: Seismogram for the WWW scenario database. Black: Filtered seismogram at original sample rate, red dashed: Resampled seismogram.

8.3.5.2 Preparing a dataset

Code level Of course output of adequate datasets requires implementation of appropriately designed output routines. However, the output of seismograms on equidistant receivers is a simple task at least for any method based on a rectangular grid. As an example may serve the subroutine `yac_seisgrid.f90` which is provided with the complete YAC simulation code with this work (see Appendix A). Some difficulties may arise in the presence of parallelism in the code. Output files from the different machines have to be collected and rearranged in the way the scenario database requires the data.

Post processing Seismic datasets adequate for the visualization with the WWW scenario database must all have a common file layout. This is not necessarily the same structure as the output of an arbitrary wave propagation code delivers. In the following the file layout used in the database is explained in a way that allows the potential user rearranging of datasets. There is only one file for each component of the seismogram (later named simply *x*, *y* and *z* in the database). Note on 2D simulations: The problem arises that these kind of simulations normally produce only two components of motion. The database application, however strictly expects three components, if one is missing an error is produced. A simple work-around is to use one component twice and note that in the file `.sim_params`. Of course the particular seismogram is then displayed twice. A similar approach can be made for rotational motions, important is the correct description in the `.sim_params` file. The component files contain all seismograms in the model area resampled to 360 time steps, and written one after another like figure 8.4 illustrates. The first trace is located in the bottom left corner of the model area. Other traces have to be written row by row.

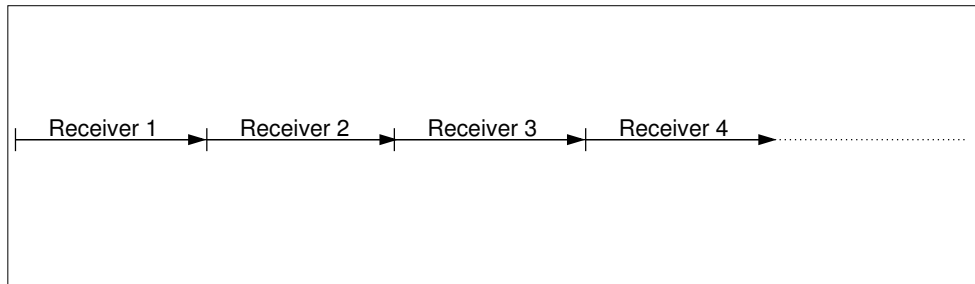


Figure 8.4: In the file format used by the scenario database complete traces are written one after another.

Note on file size Resampling of the raw data to a sampling rate which is optimized for the display of seismograms on a web page results in significantly smaller file sizes. The use of binary data adds to this effect. Values from the Cologne Basin example illustrate the reduction of storage requirements from ASCII raw data to the resampled binary format which is stored in the scenario database.

ASCII raw: 23 GB

Resampled binary: 81 MB

Only 0.35 percent of the original data volume has to be stored. It is noteworthy that an amount on the order of 100 MB can be uploaded in reasonable time via the Internet. The following example illustrates the processing procedure and demonstrate capabilities of the reduced dataset.

Example: Düren vertical component As an example the dataset of the simulated m_L 6.1 1756 Düren earthquake is chosen in order to demonstrate potential benefits of the earthquake scenario database. Figure 8.5 shows the complete set of seismograms as it is stored in the scenario database. Due to the scaling individual seismograms can not be recognized, but the peak amplitudes of the traces draw a kind of grey scale picture of the peak ground velocities over the whole model area. It is noteworthy that in this single figure about 20.000 seismograms are plotted. Figure 8.6 shows a closer view of the area marked as red dashed rectangle in figure 8.5. Gradual differences between the individual profiles become recognizable. In 8.7 a further close up depicts three neighboring seismogram sections chosen from the marked area in the previous figure. Individual seismograms become visible at this level of magnification. It should be noted that the visualization tools of the scenario database provide the ability to explore such datasets of three component seismograms with dynamically produced profiles in both vertical and horizontal direction. The position of these profiles is thereby chosen interactively using the mouse. For locations of interest time series of displacement, velocity and acceleration can be plotted. Finally, data for the seismograms can be downloaded in ASCII format. Using these functionalities requires only a web browser.

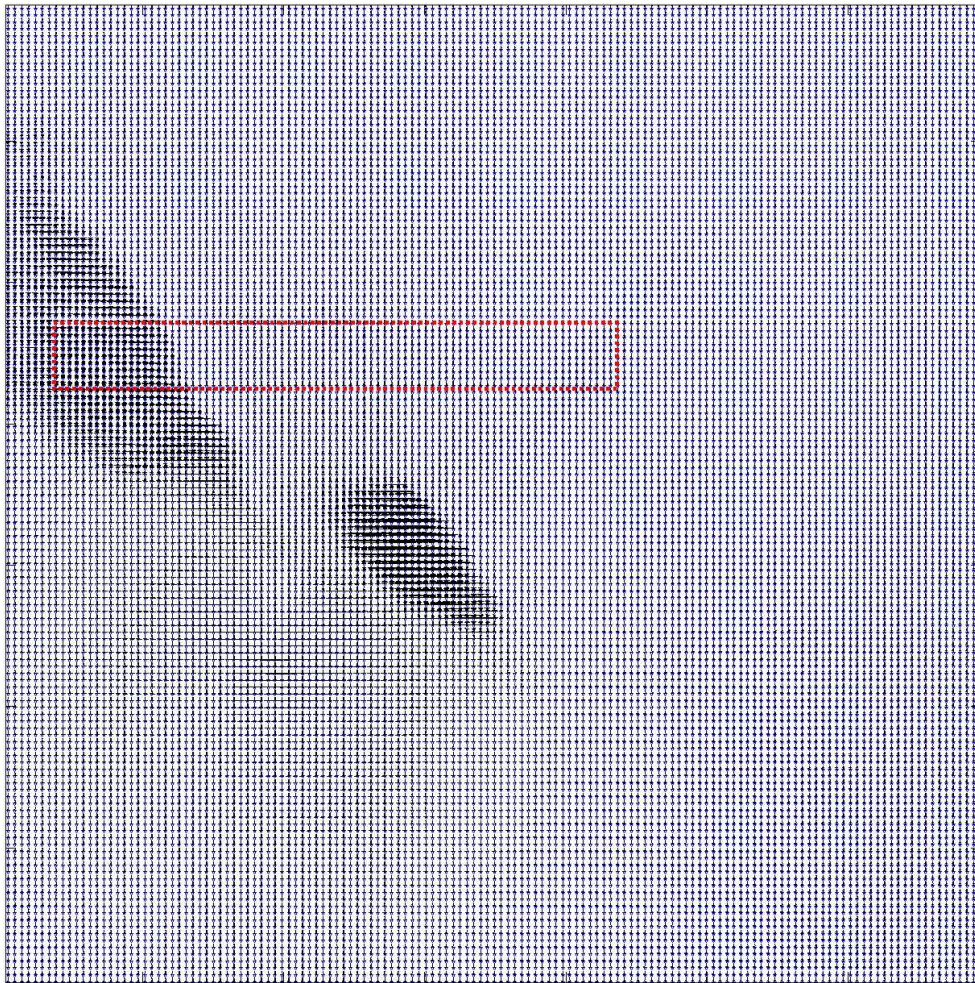


Figure 8.5: Complete dataset of synthetic seismograms for one component of ground motion as it is present in the earthquake scenario database. Red dashed box indicates the area shown in figure 8.6 in more detail. (Seismograms for this example are taken from the simulation of the M 6.1, 1756 Düren earthquake.

8.3.6 Upload Procedure

Once the data is processed and prepared in the correct format for the scenario database, the upload procedure can be done. The following steps are recommended for doing so:

1. Install a local version of the scenario database without data.
2. Download a set of .sim parameter files.
3. Edit these files according to the recommendations to fit the parameters of the new scenario.
4. Create the necessary directories according to the structure explained above.

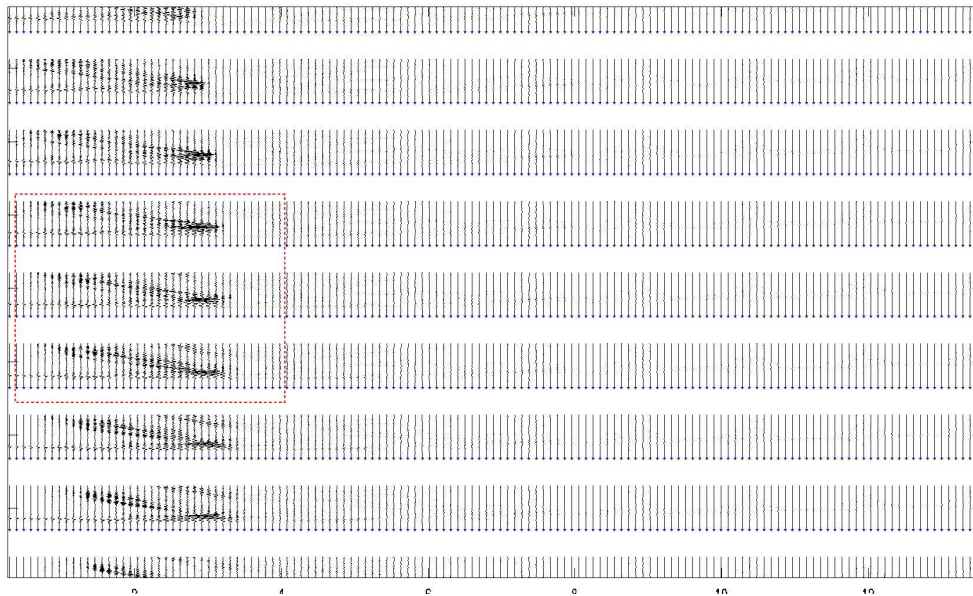


Figure 8.6: Excerpt from the dataset shown in figure 8.5. Red dashed box indicates the area shown in 8.7 in a closer view. Note the slight differences between individual profiles.

5. Test the database with the new scenario data locally.
6. Upload to the central database.

If anything is not working as it is on your local system this is likely due to some permission problem, in that case ask the system administrator.

8.4 Possible Applications

A detailed description of the individual visualization interfaces provided by the scenario data base application can be found in Rieger (2005). Nevertheless, example screen shots shown in figures 8.9 and 8.10 illustrate some of the provided possibilities to retrieve information graphically for a chosen earthquake scenario. In figure 8.9 the main interactive window is presented. A map showing the study area for the scenario is used as interface to chose positions of interest. Three component time series of ground displacement, velocity and acceleration can be retrieved interactively by clicking on the desired location within the map area. It becomes clear that a significant map associated with the earthquake scenario is preferable. In figure 8.10 an example for a seismogram section along a horizontally oriented profile is shown. Again the position in north-south direction can be chosen interactively using the mouse. The profile section is then generated dynamically and displayed. In the following subsections a few possible areas of application for the scenario database are outlined.

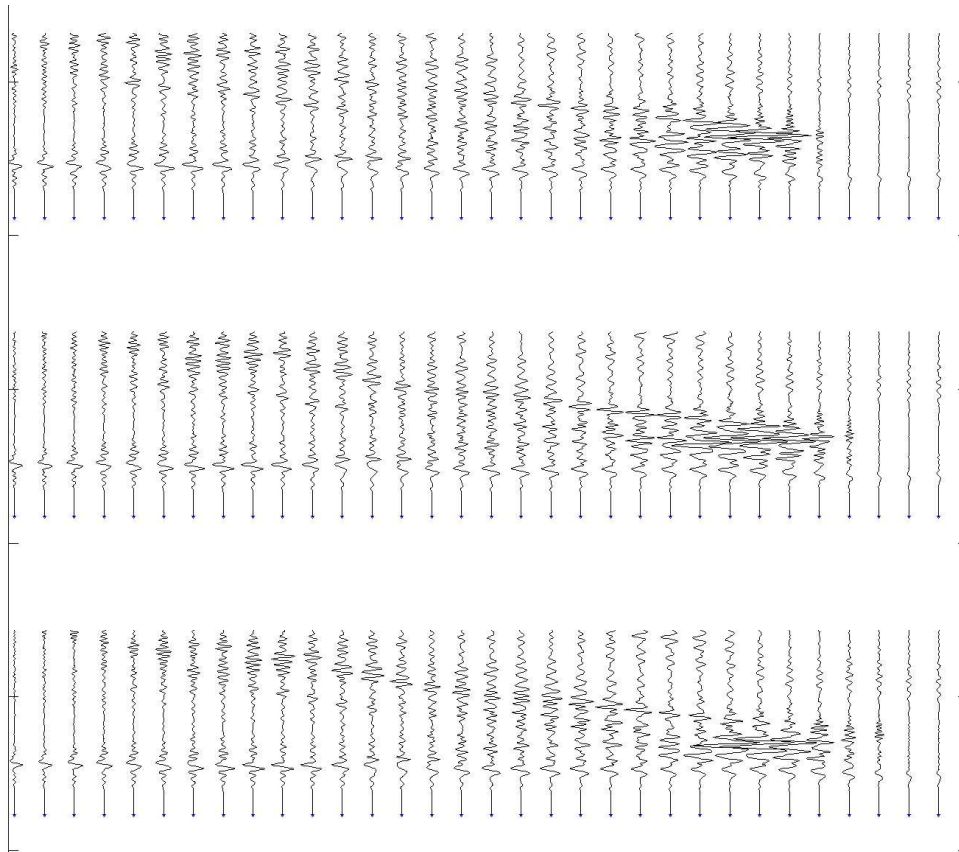


Figure 8.7: Excerpt from the dataset shown in previous figures 8.5 and 8.7. At this level of magnification details individual traces can be recognized.

8.4.1 Research

Labeling of the Scenario Database already imposes the purpose of the application as a collection of synthetic scenario data. Within the range of this work already a number of scenarios for the regional model of the Cologne basin have been uploaded:

- Düren, 1756
- Euskirchen, 1951
- Roermond, 1992
- Alsdorf, 2002

If the application is accepted among a larger number of scientists an interesting database for synthetics from different simulation techniques and locations could evolve. The main advantage consists in the common availability of these data through standardized visualization interfaces. The examples given above impose that a broad range of research and teaching applications could potentially benefit from this tool.

8.4.2 Educational Purposes

One possible future application of the scenario database interface would be the usage for teaching purposes, including courses, seminars or workshops. A local installation of the database with temporary character could be used for that purpose. Within hands on sessions with simple codes (or advanced codes using simple models), as it is the case most times, it is possible for the participant to create datasets which can be uploaded directly to the database and visualize the results taking advantage of the interfaces provided. For example subgroups of a course using slightly modified codes on the same model can quickly compare their results and see the impact of changes. The advantage is that no special software has to be provided for all participants and installed on individual notebooks which is often a time consuming issue. Instead every participant can simply use his preferred web browser in order to access the data base, upload data and visualize his own or other results. Figure 8.8 illustrates the concept of a workshop using the scenario database with a remote server and connecting via Internet to the application.

8.4.3 Data Sharing

Of course one of the goals of the Scenario Database is upload of synthetic data for a broad range of simulations (areas, methods, models etc.). The relatively small amount of data makes it possible for researchers to easily upload via the net. It also helps keeping the database in a reasonable size.

8.4.4 Benchmarking

Access to synthetic data from different groups in a standardized way might also ease the process of benchmarking results. Different local groups can use the database to

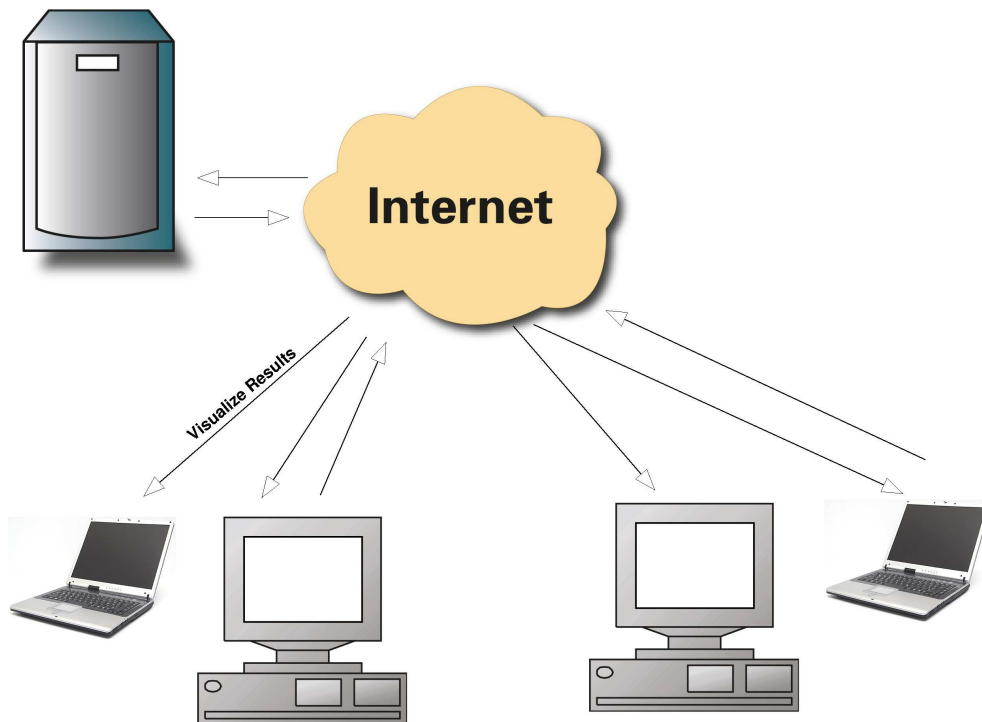


Figure 8.8: Concept of data flow for the WWW scenario database.

upload their individual solutions for a given benchmark model and make it available to other groups. Although the interfaces of the scenario database application do not provide the capability of performing a quantitative comparison of solutions, an often helpful qualitative check of the different solutions can be done quickly. This may help speeding up a benchmark process between remote groups.

8.5 Discussion

The earthquake scenario database provides a standardized way of storing and accessing synthetic ground motion data. Several tools for visualization of these datasets are implemented. A number of areas of application which could potentially benefit from this tool have been outlined in the section above. An interesting extension could be the implementation of a qualitative or quantitative comparison between different datasets. Nevertheless, the value of benefit for this application relies on the amount of uploaded data and the number of researchers using it.

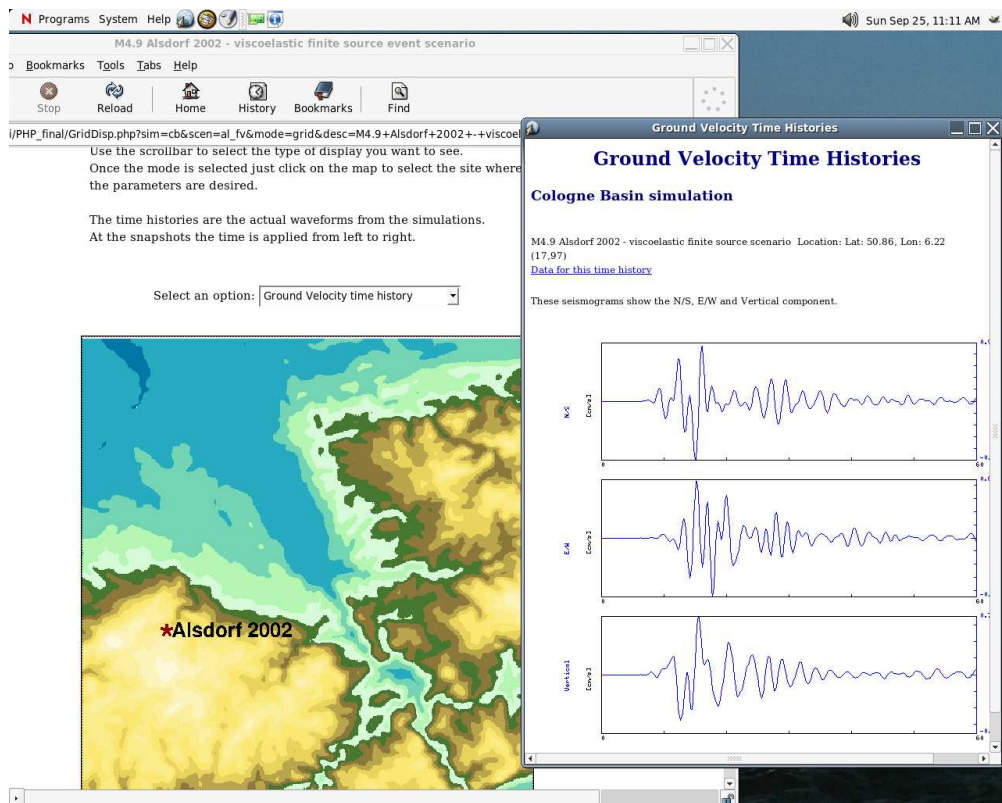


Figure 8.9: Screen shot from the earthquake scenario database - inspection of time series at interactively chosen location within study area.

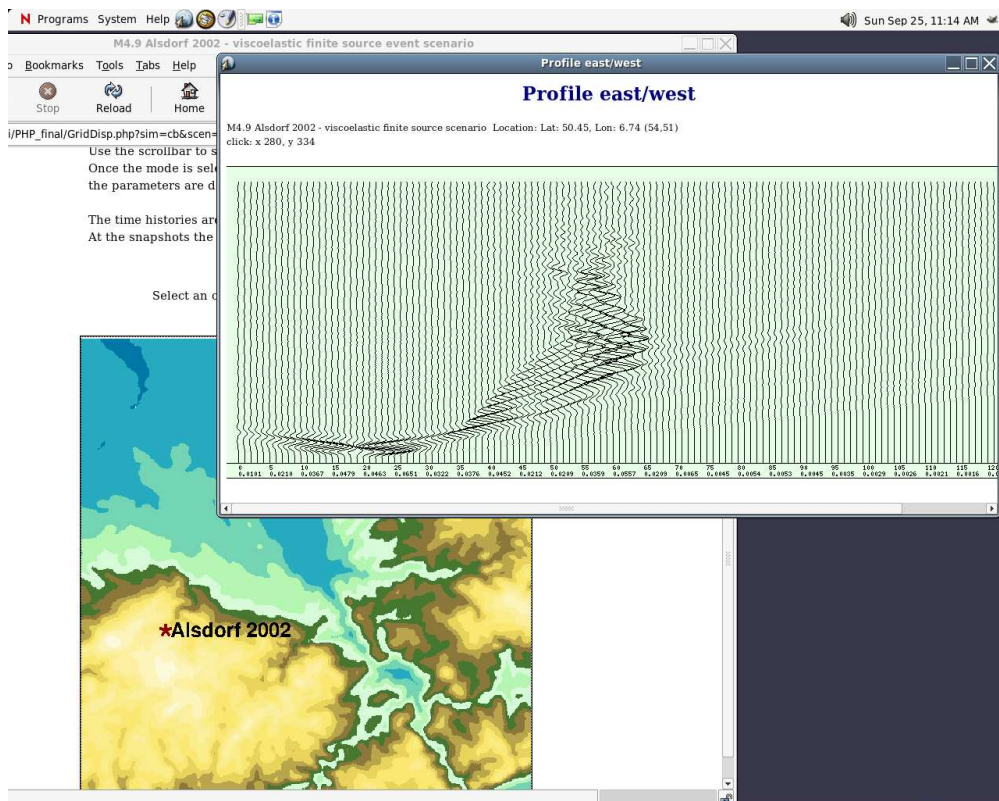


Figure 8.10: Screen shot from the earthquake scenario database - dynamically produced seismogram section.

Chapter 9

Conclusions

As stated in the introduction, evaluation of seismic hazard in regions of low recent seismicity is afflicted with difficulties and uncertainties due to the dearth of observed strong ground motion data in such areas. Among various techniques which can be employed in order to face this challenge numerical modeling of earthquake ground motions may play a major role as it is capable of providing realistic limits on earthquake ground motions and therefore eliminate the lack of observations. In this work the first three-dimensional simulations of earthquake scenarios and of the resulting seismic hazard in the Lower Rhine Embayment are presented. The occurrence of a magnitude 4.9 earthquake within the study area just after the installation of a seismic network provided an excellent dataset which allowed the first quantitative comparison of synthetic and observed strong ground motion data in this region. In the following the main results of the previous chapters are summarized and final remarks are presented.

9.1 Summary

In chapter 5 a comparing study of simulations for three earthquake scenarios in the Lower Rhine Embayment using a simple and one advanced model is presented. Model complexity is introduced in terms of viscoelasticity and the incorporation of a finite source. Resolution of the computational grid is increased by a factor of two in horizontal and by a factor of four in vertical direction, taking advantage of a variable grid size. The goal of the latter was achieving a smoother and more realistic representation of the sedimentary basin structure. Corresponding to the dearth of observational data for these three earthquakes investigations of ground motion were carried out in a qualitative way. Besides the analysis of virtual receiver profiles the main focus was set on the analysis of derived parameters mapped over the whole study region.

Whereas the rough contour and amplitude of areas with elevated ground motion level is comparable for both settings, numerous improvements due to increased model resolution and complexity on a detail level can be recognized. Some of these details could be tracked down to obvious shortcomings of the basic model representation and were consequently modeled more reliably using the advanced setup. Shaking duration mapping resulted in smoother distributions for the advanced simulations making these results easier to interpret and also more reliable. For the one station (TGA) and event

(Roermond) where unclipped data is available a direct comparison of synthetic and observed waveforms was carried out. Significant improvements in the reproduction of waveforms can be assigned to the usage of a advanced simulation setting.

In consequence of the magnitude 5.9 1992 Roermond earthquake and the consequently raised interest in seismic hazard assessment in the region of the Lower Rhine Embayment, a network of strong motion seismometers has been deployed in the basin area. The magnitude 4.9 2002 Alsdorf earthquake delivered a set of observations eligible for investigating the accuracy of numerical ground motion simulations in this region. A detailed study on this topic is presented in chapter 6. Four simulations were carried out, using an elastic simulation with point source approximation as a starting point. Complexity in terms of the source is introduced by a finite source representation and in terms of the media due to anelastic behavior. Effects caused by these complexities are analyzed independently as well as the combination of both. It came clear that synthetic and observed seismograms are not alike within a scope that allows the investigation of differential effects from the direct comparison of seismograms. However, with respect to its reliability in hazard assessment, the goal of these simulations can be defined as the reproduction of equivalent seismograms. Equivalence is considered in this chapter as a matching in a number of characteristics, such as peak amplitude, envelope and spectral content.

The main findings are: 1) Comparison of PGV on basin and bedrock sites at distances between 20 and 120 km have proven the importance of introducing both viscoelastic attenuation and finite source representation into the simulation setting in order to reproduce realistic attenuation of ground motion with epicdistance. 2) The finite source representation used in this study, namely a circular fault with homogeneous moment release, overrates the influence of the finite source when a radius is used that is derived from real data, where surely a heterogeneous source is involved. Using a smaller effective radius for the homogeneous sources or introducing artificial heterogeneities into the source plane for the simulations could solve this problem. 3) The spectral content of synthetic data matches the observation a lot better, when a finite source description is involved. 4) Significant effects of viscoelastic attenuation are observable. Overestimation of damping is recognizable in some parts of the basin and suggests a heterogeneous attenuation model.

In chapter 7 a first step towards a kind of brute force approach to the quantification of variability of simulation results related to uncertainties in input datasets is presented. Uncertainty is modeled by the stepwise variation of input parameters independently from each other within assumed error margins. It must be emphasized that the variation range used in this study is arbitrarily chosen in order to demonstrate the feasibility of the approach. For the application these error margins must be carefully defined and it will be a crucial point to find accurate and realistic values. As output value again peak ground velocity and the derived intensity was chosen as it is a quantity of central interest in hazard assessment and it is adequate in producing area-wide mappings. Additionally, seismograms are compared at numerous stations chosen in order to reveal the origins of peak amplitude variations. Resulting differential effects are ascertained to show significant heterogeneities. From the range of input parameters sedimentary basin depth, hypocenter depth and the strike angle as representation of the source mechanism were chosen to be modified and studied in their significance

to the simulation results. As main results can be seen: 1) A slight change in basin depth of 5 or 10 percent can result in locally 50 percent variation in peak ground velocity. This astonishing result can be understood from the inspection of seismograms in the associated regions. The largest differential effects depend on the appearance of resonant shaking at specific locations. Such effects are highly sensitive to changes in the basin geometry. Due to the complex basin structure and consequently complex wavefield the pattern of amplification and deamplification related to changes in basin depth becomes highly heterogeneous. 2) Change in hypocentral depth results also in significant variations of local peak amplitudes, the same being valid for a change in source mechanism modeled by modifications on strike angle. The overall pattern of variations in these cases is easier to understand than it was the case for varying basin depth. Nevertheless, there are clear indications for complex interactions of source parameters with the sedimentary structure. Consequently, the results have significant heterogeneities as well.

Due to limited computational resources and according to the nature of this study as pilot study for the quantification approach the error space determined by the parameter axes was explored only along the error axes themselves. The above discussed coupling effects of different parameter variations strongly suggest the investigation of the error space as a whole using Monte Carlo techniques. Future steps for this kind of investigations have been suggested. It becomes clear that this kind of investigation results in large computational effort. Parallel computation of tens to hundreds of simulations will be necessary in order to keep the overall time at a reasonable value.

In chapter 8 a webbased approach is presented for archiving and displaying simulation data. A description of the production and necessary processing of data for potential users of this tool is provided. By means of an example from the simulations presented in this work the use of several visualization interfaces provided with the earthquake scenario database is described. A few possible areas of application for the program are outlined.

9.2 Outlook

Comparison of synthetic seismograms from three-dimensional earthquake simulations with observed strong motion data have proven the capability of such simulations in achieving realistic ground motion estimates. However, these results have also revealed a number of short-comings of the velocity and attenuation model used in this study. The findings suggest the construction of a real three-dimensional velocity model for the sedimentary structures of the Lower Rhine Embayment like the SCEC model for the region of Southern California.

As it is the case for most finite difference simulations the velocity model used in this study is simplified in the uppermost part. Due to computational requirements the lowest velocity modeled is fixed to a value which is valid for a depth of approximately 350 m. This restriction implies that the effects of shallow structures on wave propagation, the so called site effects, are neglected. Whereas these effects can be considered small for the low frequency part of the wavefield, they must be taken into account for future simulations which may reach the frequency range of building resonance. Con-

sequently, computational requirements for such a simulation will increase rapidly as both the higher frequency and the lower velocities result in the necessity of denser grid spacing.

Surface topography is another issue which is neglected in the simulations presented in this work. The part of the study area located on sediments on which this study is focused is characterized by relatively small elevations. Therefore the assumption of a flat surface is considered a valid first order approximation. However, simulations with increased model complexity in terms of attenuation and source representation have resulted in a degree of similarity with observed waveforms where topography effects may play an important role. Accurate modeling of complex free surfaces can be suggested as a next step for further improvements in ground motion modeling for this area.

Similar considerations can be made for the effects of anisotropic wave propagation caused by intrinsic anisotropy of the media or anisotropy due to aligned cracks and interfaces within an intrinsically isotropic medium. Both mechanisms are not included in the simulations presented in this work, the first due to the assumption of isotropic media, the latter due to the lack of structures like cracks or interfaces within the sediments.

It is important to keep in mind that the incorporation of model complexities like the ones discussed above does not necessarily result in an improved modeling. In contrast, careful tuning of these additional degrees of freedom will be necessary in order to take advantage from their employment. This results in large numbers of simulations to be carried out. The increasing computational capabilities of the coming years will allow for that.

Bibliography

- Aagaard, B. T., Hall, J. F., and Heaton, T. H. (2001). Characterization of near-source ground motions with earthquake simulations. *Earthquake Spectra*, 17(2):177–207.
- Aagaard, B. T., Hall, J. F., and Heaton, T. H. (2004). Effects of fault dip and slip rake angles on near-source ground motions: Why rupture directivity was minimal in the 1999 Chi-Chi, Taiwan, earthquake. *Bull. Seism. Soc. Am.*, 94(1):155–170.
- Ahorner, L. (1975). Present-day stress field and seismotectonic block movements along major fault zones in Central Europe. *Tectonophysics*, 29:233–249.
- Ahorner, L. (1992). Das Erdbeben bei Roermond am 13. April 1992 und die daraus zu ziehenden Lehren für das Erdbebengefährdungspotential im Rheinland. *Mitt. Deutsch. Geoph. Ges.*, (1-2):51–57.
- Ahorner, L. (1994). Fault-plane solutions and source parameters of the 1992 Roermond, the Netherlands, mainshock and its stronger aftershocks from regional seismic data. *Geologie en Mijnbouw (Special Issue: The Roer Valley Graben, eds. van Eck, T. and Davenport, C. A.)*, 73:199–214.
- Ahorner, L., Baier, B., and Bonjer, K.-P. (1983). General pattern of the seismotectonic dislocation and the earthquake generating stress field in Central Europe between the Alps and the North Sea. In Fuchs, K., v. Gehlen, K., v. Mälzer, K., Murawski, H., and Semmel, A., editors, *Plateau Uplift, the Rhenish Shield - A Case History*, pages 187–197. Springer, Berlin, Heidelberg.
- Aki, K. and Richards, P. G. (1980). *Quantitative Seismology*. W.H. Freeman, San Francisco.
- Alexandre, P. (1994). Historical seismicity of the lower Rhine and Meuse valleys from 600 to 1525: A new critical review. *Geologie en Mijnbouw (Special Issue: The Roer Valley Graben, eds. van Eck, T. and Davenport, C. A.)*, 73:431–438.
- Anderson, J. G., Lee, Y., Zeng, Y., and Day, S. (1996). Control of strong motion by the upper 30 meters. *Bull. Seism. Soc. Am.*, 86:1749–1759.
- Aochi, H. and Fukuyama, E. (2002). Three-dimensional nonplanar simulation of the 1992 Landers earthquake. *J. Geophys. Res.*, 107.
- Aochi, H., Fukuyama, E., and Matsuúra, M. (2000). Spontaneous rupture propagation on a non-planar fault in 3D elastic medium. *Pure appl. geophys.*, 157:2003–2027.

- Aochi, H. and Madariaga, R. (2003). The 1999 Izmit, Turkey, earthquake: Non-planar fault structure, dynamic rupture process and strong ground motion. *Bull. Seism. Soc. Am.*, 93:1249–1266.
- Aoi, S. and Fujiwara, H. (1997). 3D seismic wave simulation using finite-difference method with discontinuous grid. *EOS*, 78:F424.
- Ashford, S. A., Sitar, N., Lysmer, J., and Deng, N. (1997). Topographic effects on the seismic response of steep slopes. *Bull. Seism. Soc. Am.*, 87:701–709.
- Atakan, K., Midzi, V., Toiran, B. M., Vanneste, K., Camelbeeck, T., and Meghraoui, M. (2000). Seismic hazard in regions of present day low seismic activity: uncertainties in the paleoseismic investigations along the Bree Fault Scarp (Roer Graben, Belgium). *Soil Dynamics and Earthquake Engineering*, 20:415–427.
- Bao, H., Bielak, J., Ghattas, O., Kallivokas, F., OHallaron, D. R., and Shewchuck, J. R. (1998). Large-scale simulation of elastic wave propagation in heterogeneous media on parallel computers. *Comp. Methods Appl. Mech. Eng.*, 152:85–102.
- Baumann, H. and Illies, J. H. (1983). Stress field and strain release in the Rhenish Massif. In Fuchs, K., v. Gehlen, K., v. Mälzer, K., Murawski, H., and Semmel, A., editors, *Plateau Uplift, the Rhenish Shield - A Case History*, pages 177–186. Springer, Berlin, Heidelberg.
- Ben-Zion, Y. (2001). Dynamic ruptures in recent models of earthquake faults. *J. Mech. Phys. Solids*, 49:2209–2244.
- Ben-Zion, Y. and Andrews, D. J. (1998). Properties and implications of dynamic rupture along a material interface. *Bull. Seism. Soc. Am.*, 88:1085–1094.
- Ben-Zion, Y. and Huang, Y. (2002). Dynamic rupture on an interface between a compliant fault zone layer and a stiffer surrounding solid. *J. Geophys. Res.*, 107(B2).
- Berenger, J. (1994). A perfectly matched layer for the absorption of electromagnetic waves. *J. Comp. Phys.*, 114:185–200.
- Berenger, J. (1996). Three-dimensional perfectly matched layer for the absorption of electromagnetic waves. *J. Comp. Phys.*, 127:363–379.
- Berz, G. (1994). Assessment of the losses caused by the 1992 Roermond earthquake, the Netherlands (extended abstract). *Geologie en Mijnbouw (Special Issue: The Roer Valley Graben, eds. van Eck, T. and Davenport, C. A.)*, 73:281.
- Bielak, J. and Ghattas, O. (1999). Earthquake ground motion and structural response in alluvial valleys. *J. Geotech. Geoenv. Eng.*, 125:413–423.
- Blanch, J. O., Robertsson, J. O. A., and Symes, W. W. (1995). Modeling of a constant Q: Methodology and algorithm for an efficient and optimally inexpensive viscoelastic technique. *Geophysics*, 60(1):176–184.
- Boatwright, J. A. (1980). A spectral theory for circular seismic sources: Simple estimates of source dimension, dynamic stress drop, and radiated energy. *Bull. Seism. Soc. Am.*, 70:1–27.

- Bommer, J. J., Abrahamson, N. A., Strasser, F. O., Pecker, A., Bard, P.-Y., Bungum, H., Cotton, F., Faeh, D., Sabetta, F., Scherbaum, F., and Studer, J. (2004). The challenge of defining upper bounds on earthquake ground motions. *Seism. Res. Lett.*, 75(1):82–95.
- Bouwkamp, J. (1994). The 1992 Roermond earthquake, the Netherlands: Earthquake engineering. *Geologie en Mijnbouw (Special Issue: The Roer Valley Graben, eds. van Eck, T. and Davenport, C. A.)*, 73:291–298.
- Braunmiller, J., Dahm, T., and Bonjer, K. P. (1994). Source mechanism of the 1992 Roermond, the Netherlands, earthquake from inversion of regional surface waves (extended abstract). *Geologie en Mijnbouw (Special Issue: The Roer Valley Graben, eds. van Eck, T. and Davenport, C. A.)*, 73:225–227.
- Brietzke, G. (2003). Numerical simulation of kinematic and dynamic ruptures in anisotropic media. Master's thesis, Inst. f. Allg. und Angew. Geophysik, LMU München.
- Budny, M. (1984). Seismische Bestimmung der bodendynamischen Kennwerte von oberflächennahen Schichten in Erdbebengebieten der Niederrheinischen Bucht und ihre ingenieurseismologische Anwendung.
- Camelbeeck, T., Alexandre, P., Vanneste, K., and Meghraoui, M. (2000). Longterm seismicity in regions of present day low seismic activity: the example of western Europe. *Soil Dynamics and Earthquake Engineering*, 20:405–415.
- Camelbeeck, T., Galadini, F., Meghraoui, M., and van den Berg, M. (2001). Evaluation of the potential for large earthquakes in regions of present day low seismic activity in Europe. *Geologie en Mijnbouw*, 80(3-4):67–58.
- Camelbeeck, T. and Meghraoui, M. (1998). Geological and geophysical evidence for large paleo-earthquakes with surface faulting in the Roer Graben (northwest Europe). *Geophysical Journal International*, 132:347–362.
- Camelbeeck, T., van Eck, T., Pelzing, R., Ahorner, L., Loohuis, J., Haak, H., Hoang-Trong, P., and Hollnack, D. (1994). The 1992 Roermond earthquake, the Netherlands, and its aftershocks. *Geologie en Mijnbouw (Special Issue: The Roer Valley Graben, eds. van Eck, T. and Davenport, C. A.)*, 73:181–197.
- Carcione, J. M., Kosloff, D., and Kosloff, R. (1988). Viscoacoustic wave propagation simulation in the Earth. *Geophysics*, 53:769–777.
- Cerjan, C., Kosloff, D., Kosloff, R., and Reshef, M. (1985). A non-reflecting boundary condition for discrete acoustic and elastic wave equations. *Geophysics*, 50:705–708.
- Chen, K., McAneney, J., Blong, R., Leigh, R., Hunter, L., and Magill, C. (2004). Defining area at risk and its effect in catastrophe loss estimation: a dasymetric mapping approach. *Applied Geography*, 24:97–117.
- Clayton, R. and Engquist, B. (1977). Absorbing boundary conditions for acoustic and elastic wave equations. *Bull. Seism. Soc. Am.*, 67(6):1529–1540.

- Cloetingh, S., Ziegler, P. A., Beekman, F., Andriessen, P. A. M., Matenco, L., Bada, G., Garcia-Castellanos, D., Hardebol, N., Dezes, P., and Sokoutis, D. (2005). Lithospheric memory, state of stress and rheology: neotectonic controls on Europe's intraplate continental topography. *Quaternary Science Reviews*, 24:241–304.
- Collino, F. and Tsogka, C. (2001). Application of the perfectly matched absorbing layer model to the linear elastodynamic problem in anisotropic heterogeneous media. *Geophysics*, 66(3):294–307.
- Corradini, M. L. (2003). Letter from chairman of the US Nuclear Waste Technical Review Board to the Director of the Office of Civil Radioactive Waste Management. available online at <http://www.nwtrb.gov/corr/mic010.pdf>.
- Cropp, W. and Lusk, E. (1996a). Installation guide for mpich, a portable implementation of MPI. Technical Report ANL-96/5, Argonne National Laboratory.
- Cropp, W. and Lusk, E. (1996b). User's guide for mpich, a portable implementation of MPI. Technical Report ANL-96/6, Argonne National Laboratory.
- Cruz-Atienza, V. M. and Virieux, J. (2004). Dynamic rupture simulation of non-planar faults with a finite-difference approach. *Geophysical Journal International*, 157:1–16.
- Dablain, M. A. (1986). The application of high-order differencing to the scalar wave equation. *Geophysics*, 51:127–139.
- Dahlen, F. and Tromp, J. (1998). *Theoretical Global Seismology*. Princeton University Press, Princeton, New Jersey.
- Davenport, C. A. (1994). Geotechnical consequences of ground motion: Hazard perspectives. *Geologie en Mijnbouw (Special Issue: The Roer Valley Graben, eds. van Eck, T. and Davenport, C. A.)*, 73:339–356.
- Day, S. M. and Minster, J. B. (1984). Numerical simulation of attenuated wavefields using a Padé approximation method. *Geophys. J. R. astr. Soc.*, 78:105–118.
- de Crook, T. (1994). Earthquake hazard for Roermond, the Netherlands. *Geologie en Mijnbouw (Special Issue: The Roer Valley Graben, eds. van Eck, T. and Davenport, C. A.)*, 73:425–429.
- Dezes, P., Schmid, S. M., and Ziegler, P. A. (2004). Evolution of the European Cenozoic Rift System: Interaction of the Alpine and Pyrenean orogens with their foreland lithosphere. *Tectonophysics*, 389:1–33.
- Dong, Z. and McMechan, G. A. (1995). 3-D viscoelastic anisotropic modeling of data from a multicomponent, multi-azimuth seismic experiment in northeast Texas. *Geophysics*, 60(4):1128–1138.
- Dost, B. and Sleeman, R. (1994). Exchange of digital seismological waveform data in Europe: Status as illustrated by data collection for the 1992 Roermond earthquake, the Netherlands. *Geologie en Mijnbouw (Special Issue: The Roer Valley Graben, eds. van Eck, T. and Davenport, C. A.)*, 73:253–263.

- Dreger, D. and Kaverina, A. (2000). Seismic remote sensing for the earthquake source process and near-source strong shaking: A case study of the October 16, 1999 Hector Mine earthquake. *Geophysical Research Letters*, 27(13):1941–1944.
- Dziewonski, A., Ekström, G., and Salganik, M. (1993). Centroid-moment tensor solutions for April-June 1992. *Phys. Earth Planet Int.*, 77:151–163.
- Ewald, M. (2001). Numerical simulation of site effects with application to the Cologne Basin. Master's thesis, Inst. f. Allg. und Angew. Geophysik, LMU München.
- Ewald, M., Igel, H., Hinzen, K.-G., and Scherbaum, F. (2005). Basin-related effects on ground motion for earthquake scenarios in the Lower Rhine Embayment. submitted to *Geophysical Journal International*.
- Fäh, D., Kind, F., and Giardini, D. (2003). Inversion of local S-wave velocity structures from average H/V ratios, and their use for the estimation of site-effects. *Journal of Seismology*, 7:449–467.
- Falk, J., Tessmer, E., and Gajewski, D. (1998). Efficient finite-difference modelling of seismic waves using locally adjustable timesteps. *Geophys. Prospect.*, 46:603–616.
- Faust, L. Y. (1950). Seismic velocity as a function of depth and geologic time. *Bull. Seism. Soc. Am.*, 40:192–206.
- Frankel, A. (1993). Three-dimensional simulations of ground motions in the San Bernardino Valley, California, for hypothetical earthquakes on the San Andreas fault. *Bull. Seism. Soc. Am.*, 83:1020–1041.
- Garatani, K., Nakamura, H., Okuda, H., and Yagawa, G. (2000). Large-scale parallel wave propagation analysis by GeoFEM. *Lect. Notes Comp. Sci.*, 1823:445–453.
- Gariel, J., Horrent, C., Jongmans, D., and Camelbeeck, T. (1994). Strong ground motion computations of the 1992 Roermond earthquake, the Netherlands, from linear methods using locally recorded aftershocks. *Geologie en Mijnbouw (Special Issue: The Roer Valley Graben, eds. van Eck, T. and Davenport, C. A.)*, 73:315–321.
- Geller, R. J. and Takeuchi, N. (1998). Optimally accurate time-domain second-order finite difference scheme for the elastic equation of motion: one-dimensional case. *Geophysical Journal International*, 135:48–62.
- Geluk, M., Duin, E., Dusaar, M., Rijkers, R., van den Berg, M., and van Rooijen, P. (1994). Stratigraphy and tectonics of the Roer Valley Graben. *Geologie en Mijnbouw (Special Issue: The Roer Valley Graben, eds. van Eck, T. and Davenport, C. A.)*, 73:129–141.
- Gibbs, J. F., Boore, D. M., Joyner, W. B., and Fumal, T. E. (1994). The attenuation of seismic shear waves in quaternary alluvium in Santa Clara Valley, California. *Bull. Seism. Soc. Am.*, 84(1):76–90.
- Gölke, M. and Coblenz, D. (1996). Origins of the European stress field. *Tectonophysics*, 266:11–24.

- Graves, R. W. (1993). Modeling three-dimensional site response effects in the Marina District Basin, San Francisco, California. *Bull. Seism. Soc. Am.*, 83(4):1042–1063.
- Graves, R. W. (1996). Simulating seismic wave propagation in 3D elastic media using staggered-grid finite-differences. *Bull. Seism. Soc. Am.*, 86(4):1091–1106.
- Graves, R. W. and Wald, D. J. (2004). Observed and simulated ground motion in the San Bernardino basin region for the Hector Mine, California, earthquake. *Bull. Seism. Soc. Am.*, 94(1):131–146.
- Grünthal, G. and Stromeier, D. (1992). The recent crustal stress field in Europe: trajectories and finite element modeling. *J. Geophys. Res.*, 97:11805–11820.
- Grünthal, G. and Stromeier, D. (1994). The recent crustal stress field in Central Europe sensu lato and its quantitative modelling. *Geologie en Mijnbouw (Special Issue: The Roer Valley Graben, eds. van Eck, T. and Davenport, C. A.)*, 73:173–180.
- Haak, H. (1994). Seismotectonics and seismic hazard in the Roer Valley Graben; with emphasis on the Roermond earthquake of April 13, 1992, workshop recommendations. *Geologie en Mijnbouw (Special Issue: The Roer Valley Graben, eds. van Eck, T. and Davenport, C. A.)*, 73:93–94.
- Harari, I., Slavutin, M., and Turkel, E. (2000). Analytical and numerical studies of a finite element PML for the Helmholtz equation. *J. Comp. Ac.*, 8:121–137.
- Hastings, F., Schneider, J., and Broschat, S. (1996). Application of the perfectly matched layer (PML) absorbing boundary condition to elastic wave propagation. *J. Acoust. Soc. Am.*, 100(5):3061–3069.
- Hayashi, K., Burns, D. R., and Toksöz, M. N. (2001). Discontinuous-grid finite-difference seismic modeling including surface topography. *Bull. Seism. Soc. Am.*, 91(6):1750–1764.
- Herrero, A. and Bernard, P. (1994). A kinematic self-similar rupture process for earthquakes. *Bull. Seism. Soc. Am.*, 84(4):1216–1228.
- Hinzen, K.-G. (2002). Source parameters for the alsdorf 2002 earthquake. available online at <http://www.seismo.uni-koeln.de/frames/main/station/aktuell/alsdorf/>.
- Hinzen, K.-G. (2003). Stress field in the Northern Rhine Area, Central Europe, from earthquake fault plane solutions. *Tectonophysics*, 377(325-356).
- Hinzen, K.-G. and Oemisch, M. (2001). Location and magnitude from seismic intensity data of recent and historic earthquakes in the northern Rhine Area, Central Europe. *Bull. Seism. Soc. Am.*, 91(1):40–56.
- Hinzen, K.-G., Scherbaum, F., and Weber, B. (2004). On the lateral resolution of H/V measurements to determine sediment thickness, a case study across a normal fault in the Lower Rhine Embayment, Germany. *Journal of Earthquake Engineering*, 8(6):909–926.

- Hoshiha, M., Rietbrock, A., Scherbaum, F., Nakahara, H., and Haberland, C. (2001). Scattering attenuation and intrinsic absorption using uniform and depth dependent model - application to full seismogram envelope recorded in Northern Chile. *Journal of Seismology*, 5:157–179.
- Ide, S. (2002). Estimation of radiated energy of finite-source earthquake models. *Bull. Seism. Soc. Am.*, 92(8):2994–3005.
- Igel, H., Mora, P., and Rioulet, B. (1995). Anisotropic wave propagation through finite-difference grids. *Geophysics*, 60(4):1203–1216.
- Jackson, J. and White, N. (1989). Normal faulting in the upper continental crust: observations from regions of active extension. *J. Struct. Geology*, 11:15–36.
- Jastram, C. and Behle, A. (1992). Acoustic modelling on a grid of vertically varying spacing. *Geophysical Prospecting*, 40:157–169.
- Jastram, C. and Tessmer, E. (1994). Elastic modelling on a grid with vertically varying spacing. *Geophysical Prospecting*, 42:357–370.
- Kang, T. and Baag, C. (2004). Finite-difference seismic simulation combining discontinuous grids with locally variable timesteps. *Bull. Seism. Soc. Am.*, 94(1):207–219.
- Kaverina, A. and Dreger, D. (2002). The combined inversion of seismic and geodetic data for the source process of the 16 October 1999 M_w 7.1 Hector Mine, California, earthquake. *Bull. Seism. Soc. Am.*, 92(4):1266–1280.
- Klett, M., Eichhorst, F., and Schäfer, A. (2002). Facies interpretation from well logs applied to the Tertiary Lower Rhine Basin fill. *Geologie en Mijnbouw*, 81:167–176.
- Kneib, G. and Kerner, C. (1993). Accurate and efficient seismic modelling in random media. *Geophysics*, 58:576–588.
- Komatitsch, D., Liu, Q., Tromp, J., Süss, P., Stidham, C., and Shaw, J. H. (2004). Simulations of ground motion in the Los Angeles Basin based upon the spectral-element method. *Bull. Seism. Soc. Am.*, 94(1):187–206.
- Komatitsch, D. and Tromp, J. (1999). Introduction to the spectral element method for three-dimensional seismic wave propagation. *Geophysical Journal International*, 139:806–822.
- Komatitsch, D. and Vilotte, J.-P. (1998). The spectral element method: An efficient tool to simulate the seismic response of 2D and 3D geological structures. *Bull. Seism. Soc. Am.*, 88(2):368–392.
- Krüger, O. S., Saenger, E. H., and Shapiro, S. A. (2005). Scattering and diffraction by a single crack: An accuracy analysis of the rotated staggered grid. *Geophysical Journal International*, 162(1):25.
- Levander, A. R. (1988). Fourth-order finite-difference P-SV seismograms. *Geophysics*, 53(11):1425–1436.

- Liu, Q. and Tao, J. (1997). The perfectly matched layer for acoustic waves in absorptive media. *J. Acoust. Soc. Am.*, 102(4):2072–2082.
- Luger, H., Meijers, P., and Brinkman, J. (1994). Loading of foundation piles during the 1992 Roermond earthquake, the Netherlands. *Geologie en Mijnbouw (Special Issue: The Roer Valley Graben, eds. van Eck, T. and Davenport, C. A.)*, 73:303–307.
- Madariaga, R. (1976). Dynamics of an expanding circular fault. *Bull. Seism. Soc. Am.*, 66:163–182.
- Mai, P. M. (2005). Kinematic source models in a nutshell, course notes. Institute of Geophysics, ETH Zürich.
- Marcinkovich, C. and Olsen, K. B. (2002). On the implementation of perfectly matched layers in a 3D fourth-order velocity-stress finite-difference scheme. *Bull. Seism. Soc. Am.*, 92.
- Meidow, H. (1994). Comparison of the macroseismic field of the 1992 Roermond earthquake, the Netherlands, with those of large historical earthquakes in the Lower Rhine Embayment and its vicinity. *Geologie en Mijnbouw (Special Issue: The Roer Valley Graben, eds. van Eck, T. and Davenport, C. A.)*, 73:283–289.
- Meidow, H. and Ahorner, L. (1994). Macroseismic effects in Germany of the 1992 Roermond earthquake and their interpretation. *Geologie en Mijnbouw (Special Issue: The Roer Valley Graben, eds. van Eck, T. and Davenport, C. A.)*, 73:271–279.
- Message Passing Interface Forum (1996). MPI: A message-passing interface standard. Computer Science Dept. Technical Report CS-94-230, University of Tennessee.
- MGuire, R. K. (1994). Using expert opinion for assessing seismic hazard in low-seismicity areas. *Geologie en Mijnbouw (Special Issue: The Roer Valley Graben, eds. van Eck, T. and Davenport, C. A.)*, 73:407–414.
- Michon, L. and van Balen, R. T. (2005). Characterization and quantification of active faulting in the Roer Valley Rift System based on high precision digital elevation models. *Quaternary Science Reviews*, 24:457–474.
- Michon, L., van Balen, R. T., Merle, O., and Pagnier, H. (2003). The Cenozoic evolution of the Roer Valley Rift System integrated at a European scale. *Tectonophysics*, 367:101–126.
- Miyatake, T. (1980a). Numerical simulations of earthquake source process by a three-dimensional crack model. Part I. Rupture process. *Journal Physical Earth*, 28:565–598.
- Miyatake, T. (1980b). Numerical simulations of earthquake source process by a three-dimensional crack model. Part II. Seismic waves and spectrum. *Journal Physical Earth*, 28:599–616.
- Moczo, P., Kristek, J., Vavrycuk, V., Archuleta, R. J., and Halada, L. (2002). 3D heterogeneous staggered-grid finite-difference modeling of seismic motion with volume harmonic and arithmetic averaging of elastic moduli and densities. *Bull. Seism. Soc. Am.*, 92(8):3042–3066.

- Müller, B., Wehrle, V., Zeyen, H., and Fuchs, K. (1997). Short-scale variations of tectonic regimes in the western European stress province north of the Alps and Pyrenees. *Tectonophysics*, 275:199–219.
- Müller, B., Zoback, M. L., Fuchs, K., Mastin, L., Gregersen, S., Pavoni, N., Stephansson, O., and Ljunggren, C. (1992). Regional patterns of tectonic stress in Europe. *J. Geophys. Res.*, 97:11783–11803.
- Murphy, J. R. and O'Brien, L. J. (1977). The correlation of peak ground acceleration amplitude with seismic intensity and other physical parameters. *Bull. Seism. Soc. Am.*, 67(3):877–915.
- Murphy, W. M. (1983). Effects of partial water saturation on attenuation in Massillon sandstone and Vycor porous glass. *J. Acoust. Soc. Am.*, 71:1458–1486.
- Ohrnberger, M., Scherbaum, F., Krüger, F., Pelzing, R., and Reamer, S. K. (2004). How good are shear wave velocity models in the Lower Rhine Embayment (NW-Germany) obtained from inversion of ambient vibrations? *Bolletino di Geofisica Teorica ed Applicata*, 45(3):215–232.
- Olsen, K. B. (2000). Site amplification in the Los Angeles Basin from three-dimensional modeling of ground motion. *Bull. Seism. Soc. Am.*, 90(6B):S77–S94.
- Olsen, K. B. (2001). Three-dimensional ground motion simulations for large earthquakes on the San Andreas fault with dynamic and observational constraints. *J. Comp. Acoust.*, 9(3):1203–1215.
- Olsen, K. B., Pechmann, J., and Schuster, G. (1995). Simulation of 3-D elastic wave propagation in the Salt Lake Basin. *Bull. Seism. Soc. Am.*, 85:1688–1710.
- Pappin, J., Coburn, A., and Pratt, C. (1994). Observations of damage ratios to buildings in the epicentral region of the 1992 Roermond earthquake, the Netherlands (extended abstract). *Geologie en Mijnbouw (Special Issue: The Roer Valley Graben, eds. van Eck, T. and Davenport, C. A.)*, 73:299–302.
- Parolai, S., Bormann, P., and Milkereit, C. (2002). New relationships between V_S , thickness of sediments, and resonance frequency calculated by the H/V ratio of seismic noise for the Cologne Area (Germany). *Bull. Seism. Soc. Am.*, 92(6):2521–2527.
- Parolai, S., Picozzi, M., Richwalski, S. M., and Milkereit, B. (2005). Joint inversion of phase velocity dispersion and H/V ratio curves from seismic noise recordings using a genetic algorithm, considering higher modes. *Geophysical Research Letters*, 32.
- Paulssen, H., B. D., and van Eck, T. (1992). The April 13, 1992 earthquake of Roermond (The Netherlands); first interpretation of the NARS seismograms. *Geol. Mijnbouw*, 71:91–98.
- Pelzing, R. (1994). Source parameters of the 1992 Roermond earthquake, the Netherlands, and some of its aftershocks recorded at the stations of the Geological Survey of Northrhine-Westphalia. *Geologie en Mijnbouw (Special Issue: The Roer Valley Graben, eds. van Eck, T. and Davenport, C. A.)*, 73:215–223.

- Petersen, H. A., Sanchez-Sesma, F., and Campillo, M. (1994). Three-dimensional scattering by two-dimensional topographies. *Bull. Seism. Soc. Am.*, 84:1169–1183.
- Peyrat, S., Olsen, K. B., and Madariaga, R. (2001). Dynamic modeling of the 1992 Landers earthquake. *J. Geophys. Res.*, 106:26467–26482.
- Pipkin, A. C. (1986). *Lectures on viscoelasticity theory*. Springer Verlag, New York, Inc.
- Pitarka, A. (1999). 3D elastic finite-difference modeling of seismic motion using staggered grids with nonuniform spacing. *Bull. Seism. Soc. Am.*, 89(1):54–68.
- Pitarka, A., Irikura, K., Iwata, T., and Kagawa, T. (1996). Basin structure effects in the Kobe area inferred from modeling of ground motions from two aftershocks of the January 17, 1995, Hyogo-ken Nanbu earthquake. *Journal Physical Earth*, 44:563–576.
- Pitarka, A., Irikura, K., Iwata, T., and Sekiguchi, H. (1998). Three-dimensional simulation of the near-fault ground motion for the 1995 Hyogo-ken Nanbu (Kobe), Japan earthquake. *Bull. Seism. Soc. Am.*, 88(2):428–440.
- Plenefisch, T. and Bonjer, K.-P. (1994). The stress tensor in the Rhine Graben area derived from earthquake focal mechanism (extended abstract). *Geologie en Mijnbouw (Special Issue: The Roer Valley Graben, eds. van Eck, T. and Davenport, C. A.)*, 73:169–172.
- Plenefisch, T. and Bonjer, K.-P. (1997). The stress field in the Rhine Graben area inferred from earthquake focal mechanisms and estimation of frictional parameters. *Tectonophysics*, 275:71–97.
- Reinecker, J., Heidbach, O., and Mueller, B. (2003). The 2003 release of the World Stress Map. available online at <http://www.world-stress-map.org>.
- Reynolds, A. C. (1978). Boundary conditions for the numerical solution of wave propagation problems. *Geophysics*, 43:1099–1110.
- Rial, J. A. (1996). An anomalous seismic response of the ground at the Tarzana Hill site during the Northridge 1994 southern California earthquake: A resonance sliding block?. *Bull. Seism. Soc. Am.*, 86:1714–1723.
- Rieger, S. (2005). Visualization of synthetic earthquake scenarios with a PHP-based interactive database. Master's thesis, Department of Earth and Environmental Sciences, LMU München.
- Robertsson, J. O. A., Blanch, J. O., and Symes, W. W. (1994). Viscoelastic finite-difference modeling. *Geophysics*, 59(9):1444–1456.
- Rosenhauer, W. and Ahorner, L. (1994). Seismic hazard assessment for the Lower Rhine Embayment before and after the 1992 Roermond earthquake. *Geologie en Mijnbouw (Special Issue: The Roer Valley Graben, eds. van Eck, T. and Davenport, C. A.)*, 73:415–424.

- Saenger, E. H. (2000). Wave propagation in fractured media: Theory and applications of the rotated staggered finite-difference grid.
- Saenger, E. H., Gold, N., and Shapiro, S. A. (2000). Modeling the propagation of elastic waves using a modified finite-difference grid. *Wave Motion*, 31(1):77–92.
- Saenger, E. H. and Shapiro, S. A. (2000). Effective velocities in fractured media: A numerical study using the rotated staggered grid. *J. Geophys. Res.*
- Saenger, E. H., Shapiro, S. A., and Keehm, Y. (2005). Seismic effects of viscous Biot-coupling: Finite difference simulations on micro-scale. *Geophysical Research Letters*, 32.
- Satoh, T., Kawase, H., Sato, T., and Pitarka, A. (2001). Three-dimensional finite-difference modeling of strong ground motions observed in the Sendai basin, Japan. *Bull. Seism. Soc. Am.*, 91:365–380.
- Scherbaum, F. (1994). Modelling the Roermond earthquake of 1992 April 13 by stochastic simulation of its high-frequency strong ground motion. *Geophysical Journal International*, 119:31–43.
- Scherbaum, F., Hinzen, K.-G., and Ohrnberger, M. (2003). Determination of shallow shear wave velocity profiles in the Cologne/Germany area using ambient vibrations. *Geophysical Journal International*, 152:597–612.
- Schreiber, U. and Rotsch, S. (1998). Cenozoic block rotation according to a conjugate shear system in central Europe - indications from paleomagnetic measurements. *Tectonophysics*, 299:111–142.
- Schumacher, M. E. (2002). Upper Rhine Graben: The role of preexisting structures during rift evolution. *Tectonics*, 21:6.1–6.17.
- Simone, A. and Hestholm, S. (1998). Instability in applying absorbing boundary conditions to high-order seismic modeling algorithms. *Geophysics*, 63:1017–1023.
- Singer, I. and Turkel, E. (2004). A perfectly matched layer for the Helmholtz equation in a semi-infinite strip. *J. Comp. Phys.*, 201:439–465.
- Sintubin, M., Sels, O., and Buffel, P. (2001). Late Tertiary fault activity in the southwestern boundary fault system of the Roer Valley Graben: evidence from the Bree area (NE Belgium). *Geologie en Mijnbouw*, 80(3-4):69–78.
- Sissingh, W. (2003). Tertiary paleogeographic and tectonostratigraphic evolution of the Rhenish triple junction. *Paleogeography, Paleoclimatology, Paleoecology*, 196:229–263.
- Sochacki, J., Kubichek, R., George, J., Fletcher, W., and Smithson, S. (1987). Absorbing boundary conditions and surface waves. *Geophysics*, 52:60–71.
- Stacey, F. D., Gladwin, M. T., McKavanagh, B., Linde, A. T., and Hastic, L. M. (1975). Anelastic damping of acoustic and seismic pulses. *Geophys. Surveys*, 2:133–151.

- Takeuchi, N. and Geller, R. J. (2000). Optimally accurate second-order time-domain finite difference scheme for computing synthetic seismograms in 2-D and 3-D media. *Phys. Earth planet. Int.*, 119:99–131.
- Takeuchi, N. and Geller, R. J. (2003). Accurate numerical methods for solving the elastic equation of motion for arbitrary source locations. *Geophysical Journal International*, 154:852–866.
- Tessmer, E. (2000). Seismic finite-difference modeling with spatially varying time steps. *Geophysics*, 65:1290–1293.
- Tsuboi, S., Komatitsch, D., Ji, C., and Tromp, J. (2004). Modeling of global seismic wave propagation on the Earth Simulator. *Journal of the Earth Simulator*, 1:57–66.
- Turkel, E. and Yefet, A. (1998). Absorbing PML boundary layers for wave-like equations. *Appl. Numer. Math.*, 27(4):553–557.
- van Balen, R. T., Houtgast, R. F., and Cloetingh, S. A. P. L. (2005). Neotectonics of The Netherlands: A review. *Quaternary Science Reviews*, 24:439–454.
- van den Berg, M. (1994). Neotectonics of the Roer Valley rift system. Style and rate of crustal deformation inferred from syn-tectonic sedimentation. *Geologie en Mijnbouw (Special Issue: The Roer Valley Graben, eds. van Eck, T. and Davenport, C. A.)*, 73:143–156.
- van den Berg, M., Groenewoud, W., Lorenz, G., Lubbers, P., Brus, D., and Kroonenberg, S. (1994). Patterns and velocities of recent crustal movements in the Dutch part of the Roer Valley rift system. *Geologie en Mijnbouw (Special Issue: The Roer Valley Graben, eds. van Eck, T. and Davenport, C. A.)*, 73:157–168.
- van Eck, T. and Davenport, C. (1994). Seismotectonics and seismic hazard in the Roer Valley Graben: An overview. *Geologie en Mijnbouw (Special Issue: The Roer Valley Graben, eds. van Eck, T. and Davenport, C. A.)*, 73:95–98.
- Virieux, J. (1984). SH-wave propagation in heterogeneous media: Velocity-stress finite-difference method. *Geophysics*, 49:1933–1942.
- von Seht, M. I. and Wohlenberg, J. (1999). Microtremor measurements used to map thickness of soft sediments. *Bull. Seism. Soc. Am.*, 89:250–259.
- Wald, D. J., Quitoriano, V., Heaton, T. H., and Kanamori, H. (1999). Relationships between peak ground acceleration, peak ground velocity and Modified Mercalli Intensity in California. *Earthquake Spectra*, 15(3):557–564.
- Wang, Y., Xu, J., and Schuster, G. (2001). Viscoelastic wave simulation in basins by a variable-grid finite-difference method. *Bull. Seism. Soc. Am.*, 91:1741–1749.
- White, R. E. (1992). The accuracy of estimating Q from seismic data. *Geophysics*, 57:1508–1511.
- Wilson, D. C. and Pavlis, G. L. (2000). Near-surface site effects in crystalline bedrock: A comprehensive analysis of spectral amplitudes determined from a dense, three-component seismic array. *Earth Interactions*, 4(2):1–31.

- Winkler, K. W. and Nur, A. (1982). Seismic attenuation: Effects of pore fluids and frictional sliding. *Geophysics*, 47:1–15.
- Worum, G., Michon, L., van Balen, R. T., van Wees, J.-D., Cloetingh, S., and Pagnier, H. (2005). Pre-Neogene controls on present-day fault activity in the West Netherlands Basin and Roer Valley Rift System (Southern Netherlands): role of variation in fault orientation in a uniform low-stress regime. *Quaternary Science Reviews*, 24:475–490.
- Worum, G., Wees, J. D. V., G-Bada, van Balen, R. T., Cloetingh, S. A. P. L., and Pagnier, H. (2004). Slip tendency analysis as a tool to constrain fault reactivation: a numerical approach applied to 3-D fault models in the Roer Valley Rift System (Southeast Netherlands). *J. Geophys. Res.*, 109.
- Xu, T. and McMechan, G. A. (1995). Composite memory variables for viscoelastic synthetic seismograms. *Geophysical Journal International*, 121:634–639.
- Xu, T. and McMechan, G. A. (1998). Efficient 3-D viscoelastic modeling with application to near-surface land seismic data. *Geophysics*, 63(2):601–612.
- Zener, M. (1948). *Elasticity and Anelasticity of Metals*. University of Chicago, Illinois.
- Zeng, Y. and Liu, Q. (2001). A staggered-grid finite-difference method with perfectly matched layers for poroelastic wave equations. *J. Acoust. Soc. Am.*, 109(6):2571–2580.
- Ziegler, P. A. (1994). Cenozoic rift system of western and central Europe: An overview. *Geologie en Mijnbouw (Special Issue: The Roer Valley Graben, eds. van Eck, T. and Davenport, C. A.)*, 73:99–127.
- Zijerveld, L., Stephenson, R., Cloetingh, S., Duin, E., and van den berg, M. W. (1992). Subsidence analysis and modelling of the Roer Valley Graben (SE Netherlands). *Tectonophysics*, 208:159–171.
- Zoback, M. (1992). First- and second-order patterns of stress in the lithosphere. *J. Geophys. Res.*, 97:11703–11728.
- Zoback, M., Zoback, M. D., Adams, J., Assumpcao, M., Bell, S., Bergman, E. A., Blümling, P., Bereton, N., Denham, D., Ding, J., Fuchs, K., Gay, N., Gregerson, S., Gupta, H. K., Gvishiani, A., Jacob, K., Klein, R., Knoll, P., Magee, M., Mercier, J. L., Müller, B. C., Paquin, C., Rajendran, J., Stephansson, O., Suarez, G., Suter, M., Udias, A., Xu, Z. H., and Zhizhin, M. (1989). Global patterns of tectonic stress. *Nature*, 341:291–298.

List of Figures

2.1	Standard Linear Solid.	10
3.1	Sketch of the Staggered-Grid mesh. The location of individual wave-field variables and model parameters is shown.	16
3.2	Sketch showing the mechanical analogies of the Standard Linear Solid (SLS).	18
3.3	Dependency of the effective quality factor q on relaxation times. See text for details.	20
3.4	Relaxation time pairs for stress and strain appropriate to model a fixed quality factor at fixed frequency.	21
3.5	Allowing an error margin on the modeled quality factor leads to a broader range of possible relaxation time pairs.	22
3.6	Resulting quality factors are averaged over the target frequency range to find the best fitting combination of relaxation times.	22
3.7	Representation of finite sources used for the verification of the method. a) Source plane with color-coded fraction of seismic moment applied to the individual point sources distributed across the circular fault. b) Color-coded rupture time for the individual point sources.	25
3.8	Three-dimensional view of the fault planes used for the finite source verification. The active area of each plane is demarked in solid color.	27
3.9	Snapshots of surface wave field from finite source verification. For the rotated fault (right column) the derived equivalent components of horizontal ground motions are shown to make a visual comparison feasible (see text).	28
3.10	Receiver distribution for the verification of the finite source implementation. Orientations of the reference and rotated fault are plotted in red.	29
3.11	Seismograms from finite source verification at the innermost receiver ring (distance = 7 km). Black traces: Fault plane aligned with grid (reference case), red dashed traces: Fault plane rotated by 27 degrees with respect to the computational grid.	29
3.12	Seismograms from finite source verification at 2nd receiver ring (distance = 12 km). See figure 3.11 for details.	30
3.13	Seismograms from finite source verification at 4th receiver ring (distance = 22 km). See figure 3.11 for details.	30

3.14	One dimensional representation of a non-uniform finite difference grid stencil as it is used in this work.	33
3.15	Example for a finite difference grid with nonuniform spacing in vertical direction.	34
3.16	Receiver setup for the verification of the nonuniform grid approach. Depth of the triangular shaped low velocity structure is demarked in colors.	36
3.17	Crosssections of the model representations using a homogeneous grid spacing (a) and a vertically varying spacing (b). Actual grid lines are plotted in light gray. The different discretization of the homogeneous part of the model is obvious. Hypocenter location is demarked by the yellow cross.	37
3.18	Comparison of three component seismograms recorded along receiver profile 1 (see 3.16). Black traces demark synthetics achieved with a uniform grid, red dashed traces are modeled using a nonuniform grid.	38
3.19	Comparison of three component seismograms recorded along receiver profile 2 (see 3.16). Black traces demark synthetics achieved with a uniform grid, red dashed traces are modeled using a nonuniform grid.	39
3.20	Evolution of the standard staggered grid scheme (a) to the alternatively oriented differential operators of the rotated staggered grid scheme (d). See text for details.	41
3.21	Wave propagation in porous media simulated by the rotated staggered grid approach. Snapshots of resulting P-wave field at 4, 5 and 6 micro seconds. Cavities in the left column are filled with air and with oil in the right column.	47
3.22	Wave propagation in porous media simulated by the rotated staggered grid approach. Snapshots of resulting P-wave field at 7, 8 and 9 micro seconds. Cavities in the left column are filled with air and with oil in the right column.	48
3.23	Wave propagation in presence of topography modeled with the rotated staggered grid approach. Snapshots of North-South horizontal component at 0.6, 1.2 and 1.8 seconds.	49
3.24	Wave propagation in presence of topography modeled with the rotated staggered grid approach. Snapshots of North-South horizontal component at 2.4, 3.0 and 3.6 seconds.	50
3.25	Wavefield emanating from kinematic rupture on curved fault. Snapshots of North-South horizontal component. Left column: assumed rupture speed below shear wave velocity, right column: assumed rupture speed above shear wave velocity.	51
3.26	Wavefield emanating from kinematic rupture on curved fault. Snapshots of North-South horizontal component. Left column: assumed rupture speed below shear wave velocity, right column: assumed rupture speed above shear wave velocity.	52
3.27	Examples for 4 and 9 nodes demonstrating the reduced amount of necessary communication when parallelization is applied in two directions.	57

3.28	Layout of two-dimensional parallelization, margins shared by 2 nodes are demarked light blue, corners shared by 4 nodes are demarked dark blue.	58
3.29	Message passing communication scheme at domain corners, where grid points are shared by 4 nodes.	59
4.1	Tectonic elements of the European Cenozoic Rift System (modified after van Balen et al. (2005)).	62
4.2	Structural framework of the Lower Rhine Embayment (van Balen et al. (2005)).	65
4.3	Cenozoic subsidence history of individual tectonic blocks within the Lower Rhine Embayment (Michon et al. (2003)).	66
4.4	Directions of clastic and marine sediment transport in the Lower Rhine Embayment during early Miocene (Sissingh (2003)).	67
4.5	Seismic line and profile of structural interpretation across the Veldhoven fault (marked a in subfigure). The Mesozoic age of main tectonic fault systems is clearly expressed in the stratigraphy (Michon et al. (2003)).	68
4.6	Seismic line and structural profile across the Peel Boundary fault (marked b in map embodied in figure 4.5 (Michon et al. (2003)).	69
4.7	Neogene evolution of the European stress field (Michon et al. (2003)).	70
4.8	Maximum horizontal stress directions in Northwestern Europe, based on various parameters as listed in legend. A NW-SE orientation of stress in the region of the Lower Rhine Embayment can be recognized (Reinecker et al. (2003)).	71
4.9	Directions of principal stresses in the region of the Lower Rhine Embayment from various studies (Hinzen (2003)).	73
4.10	Epicentral locations for strong historical earthquakes (diamonds) and events during the 20th century (circles) in the Lower Rhine Embayment (Camelbeeck et al. (2000)).	74
4.11	Location of the Feldbiss fault system with respect to the urban areas of Born and Sittard (Michon and van Balen (2005)).	75
4.12	The town of Uden is located between the main and secondary fault of the Peel Boundary fault system (Michon and van Balen (2005)). . . .	76
5.1	Grid representation for the new simulations. Vertical spacing increases from 50 m at the top of the model where low velocities are present, to 120 m at the bottom. For clarity reasons only every 5th grid line in horizontal direction is shown.	81
5.2	S-wave velocity vs. depth relation used for the sedimentary basin structure in this work (Parolai et al. (2002)).	85

5.3	Shear wave velocity profiles for two model representations along the receiver line A - A' (see figure 5.4). Setup I: Homogeneous sediments embedded by homogeneous bedrock model, setup II: Sedimentary structure with velocity gradient embedded by layered bedrock model.	86
5.4	Detailed map of the study area. Dimensions and directions are given by UTM coordinates based on sector 32 U. Red stars indicate epicenters of the simulated earthquakes. Grayscale shading depicts regional topography whereas urban areas are colored in dark gray. The sedimentary basin depth is indicated by dashed isolines in 100 m intervals. The basin reaches a maximum depth of about 1900 m. Seismic network stations are marked as stars and by their station codes. A synthetic profile A-A' with 30 receivers is shown as black dots.	89
5.5	Snapshots of the East-West component ground velocity wavefield at the surface. Background contour plot indicates the depth of the sedimentary basin. Results from simulations using setup I.	92
5.6	Snapshots of the East-West component ground velocity wavefield at the surface. Background contour plot indicates the depth of the sedimentary basin. Results from simulations using setup II.	93
5.7	Comparison of commonly used seismic intensity scales. The MSK and Modified Mercalli scales are most commonly used for European earthquakes (after Murphy and O'Brien (1977)).	95
5.8	Modified Mercalli intensities for the magnitude 6.1 1756 Düren earthquake derived from simulation results using setup I (a) and setup II (b). Background contour plot indicates the depth of the sedimentary basin. Black star denotes epicentral location. Dimensions and directions are given by UTM coordinates based on sector 32 U.	96
5.9	Modified Mercalli intensities for the magnitude 5.7 1951 Euskirchen earthquake derived from simulation results using setup I (a) and setup II (b). Background contour plot indicates the depth of the sedimentary basin. Black star denotes epicentral location. Dimensions and directions are given by UTM coordinates based on sector 32 U.	98
5.10	Modified Mercalli intensities for the magnitude 5.9 1992 Roermond earthquake derived from simulation results using setup I (a) and setup II (b). Background contour plot indicates the depth of the sedimentary basin. Black star denotes epicentral location. Dimensions and directions are given by UTM coordinates based on sector 32 U.	100
5.11	Shaking duration is defined in this study as the interval between first and last exceedance of a certain threshold value (4 cm/s).	102
5.12	Shaking duration for the magnitude 6.1 1756 Düren earthquake scenario from simulation results achieved with setup I (a) and setup II (b). Background contour plot indicates the depth of the sedimentary basin. Black star denotes epicentral location. Dimensions and directions are given by UTM coordinates based on sector 32 U.	103

5.13	Shaking duration for the magnitude 5.7 1951 Euskirchen earthquake scenario from simulation results achieved with setup I (a) and setup II (b). Background contour plot indicates the depth of the sedimentary basin. Black star denotes epicentral location. Dimensions and directions are given by UTM coordinates based on sector 32 U.	104
5.14	Shaking duration for the magnitude 5.9 1992 Roermond earthquake scenario from simulation results achieved with setup I (a) and setup II (b). Background contour plot indicates the depth of the sedimentary basin. Black star denotes epicentral location. Dimensions and directions are given by UTM coordinates based on sector 32 U.	106
5.15	Seismogram section of the east-west velocity component along the profile A-A' (5.4). Synthetics for the three earthquake scenarios are produced using setup I.	108
5.16	Seismogram section of the east-west velocity component along the profile A-A' (5.4). Synthetics for the three earthquake scenarios are produced using setup II.	109
5.17	Seismogram section of the north-south velocity component along the profile A-A' (5.4). Synthetics for the three earthquake scenarios are produced using setup I.	111
5.18	Seismogram section of the north-south velocity component along the profile A-A' (5.4). Synthetics for the three earthquake scenarios are produced using setup II.	112
5.19	Seismogram section of the vertical velocity component along the profile A-A' (5.4). Synthetics for the three earthquake scenarios are produced using setup I.	114
5.20	Seismogram section of the vertical velocity component along the profile A-A' (5.4). Synthetics for the three earthquake scenarios are produced using setup II.	115
5.21	Comparison of east-west component seismograms at station TGA for the 1992 Roermond earthquake. Synthetics achieved with setup I (left) and setup II (right) are plotted in red along with observed ground motion (black).	116
5.22	Comparison of north-south component seismograms at station TGA for the 1992 Roermond earthquake. Synthetics achieved with setup I (left) and setup II (right) are plotted in red along with observed ground motion (black).	116
5.23	Comparison of vertical component seismograms at station TGA for the 1992 Roermond earthquake. Synthetics achieved with setup I (left) and setup II (right) are plotted in red along with observed ground motion (black).	117

- 5.24 Evolution of combined intensities achieved with setup I throughout the sequence of the simulated three scenarios (a - c) and comparison with the current seismic hazard map for the study area (d). The black lines with numbers indicate the probabilistic earthquake intensity isolines with an occurrence rate of 0.001 per year (after Rosenhauer and Ahorner (1994)). Dimensions and directions are given by UTM coordinates based on sector 32 U. 119
- 5.25 Evolution of combined intensities achieved with setup II throughout the sequence of the simulated three scenarios (a - c) and comparison with the current seismic hazard map for the study area (d). The black lines with numbers indicate the probabilistic earthquake intensity isolines with an occurrence rate of 0.001 per year (after Rosenhauer and Ahorner (1994)). Dimensions and directions are given by UTM coordinates based on sector 32 U. 120
- 6.1 Location of the 2002 Alsdorf earthquake (M_L 4.9) in its geographic context. Dimensions and directions are given by UTM coordinates based on sector 32 U. Grayscale shading depicts regional topography. The sedimentary basin depth is indicated by dashed isolines in 100 m intervals. The basin reaches a maximum depth of about 1900 m. Seismic network stations are marked as stars and by their station codes. A synthetic profile A-A' with 30 receivers is shown as black dots. Urban areas within the Lower Rhine Embayment are colored dark-gray. . . . 127
- 6.2 Fault plane solution for the M_L 4.9 2002 Alsdorf earthquake (after Hinzen (2002)). Black and red dots indicate stations observing positive and negative amplitudes of the first arrivals, respectively. 128
- 6.3 Slight damage onto buildings (broken chimneys and damaged roofs) could be observed in the epicentral region of the M_L 4.9 2002 Alsdorf earthquake (after Hinzen (2002)). 128
- 6.4 Map of observed seismic intensities for the M_L 4.9 2002 Alsdorf earthquake (after Hinzen (2002)). 129
- 6.5 Isoline plot of basin depth showing the distribution of seismic stations of the recently employed subnet. Stations are demarked as red crosses attached with their abbreviated names. 130
- 6.6 Profiles of synthetic three component seismograms. Black trace: Point source elastic simulation, red trace: Finite source elastic simulation. Embedded blow-ups clarify the effects on the waveforms. 134
- 6.7 Profiles of synthetic three component seismograms. Black trace: Point source elastic simulation, red trace: Point source viscoelastic simulation. Embedded blow-ups clarify the effects on the waveforms. 136
- 6.8 Profiles of synthetic three component seismograms. Black trace: Finite source elastic simulation, red trace: Finite source viscoelastic simulation. Embedded blow-ups clarify the effects on the waveforms. . . . 137

6.9	Logarithmic plot of observed (black) and synthetic (red) peak ground velocities vs. epidistance. Synthetics are achieved using a finite source model and including viscoelastic attenuation in the simulations. Horizontal East-West and North-South component are demarked as circles and triangles, respectively. Crosses indicate vertical ground motion.	138
6.10	Ratio of synthetic to observed peak ground velocity at Bensberg seismic network stations. Values are derived from East-West component seismograms filtered at 1 Hz. Red: Elastic simulation with point source, blue: Viscoelastic simulation with point source, green: Elastic simulation with finite source, black: Viscoelastic simulation with finite source.	140
6.11	Same as figure 6.10 for the North-South component.	140
6.12	Same as 6.10 for the vertical component.	141
6.13	Frequency dependence of the ratio of synthetic to observed peak ground velocity for the East-West component averaged over all stations.	143
6.14	Frequency dependence of the ratio of synthetic to observed peak ground velocity for the North-South component averaged over all stations.	143
6.15	Frequency dependence of the ratio of synthetic to observed peak ground velocity for the vertical component averaged over all stations.	144
6.16	Seismogram comparison at station BNS. Synthetics (red traces) from four simulation types (as indicated) are compared with observed data (black). Amplitudes are given in cm/s.	147
6.17	Comparison of point source (blue traces) and finite source (red traces) synthetics, both achieved with an elastic model, with data (black) at station BNS. Amplitudes are given in cm/s.	148
6.18	Comparison of elastic (blue traces) and viscoelastic (red traces) synthetics, both achieved with finite source simulations with data (black) at station BNS. Amplitudes are given in cm/s.	148
6.19	Seismogram comparison at station PES. Synthetics (red) from four simulation types (as indicated) are compared with observed data. Amplitudes are given in cm/s.	150
6.20	Comparison of point source (blue traces) and finite source (red traces) synthetics, both achieved with an elastic model, with data (black) at station PES. Amplitudes are given in cm/s.	151
6.21	Comparison of elastic (blue traces) and viscoelastic (red traces) synthetics, both achieved with finite source simulations with data (black) at station PES. Amplitudes are given in cm/s.	151
6.22	Seismogram comparison at station MIL. Synthetics (red) from four simulation types (as indicated) are compared with observed data. Amplitudes are given in cm/s.	153
6.23	Comparison of point source (blue traces) and finite source (red traces) synthetics, both achieved with an elastic model, with data (black) at station MIL. Amplitudes are given in cm/s.	154

- 6.24 Comparison of elastic (blue traces) and viscoelastic (red traces) synthetics, both achieved with finite source simulations with data (black) at station MIL. Amplitudes are given in cm/s. 154
- 6.25 Seismogram comparison at station GMA. Synthetics (red) from four simulation types (as indicated) are compared with observed data. Amplitudes are given in cm/s. 156
- 6.26 Comparison of point source (blue traces) and finite source (red traces) synthetics, both achieved with an elastic model, with data (black) at station GMA. Amplitudes are given in cm/s. 157
- 6.27 Comparison of elastic (blue traces) and viscoelastic (red traces) synthetics, both achieved with finite source simulations with data (black) at station GMA. Amplitudes are given in cm/s. 157
- 6.28 Normalized envelopes of East-West component seismograms at station BNS (Bensberg). Traces are low pass filtered with a cut-off period ranging from 0.8 seconds to 3.6 seconds. Observed data is plotted in black against synthetics (red) achieved with different simulation settings as indicated. 159
- 6.29 Normalized envelopes of East-West component seismograms at station GMA (Gut Margaretenhöhe). traces are low pass filtered with a cut-off period ranging from 0.8 seconds to 3.6 seconds. Observed data is plotted in black against synthetics (red) achieved with different simulation settings as indicated. 161
- 6.30 Normalized envelopes of East-West component seismograms at station MIL (Millendorf). Traces are low pass filtered with a cut-off period ranging from 0.8 seconds to 3.6 seconds. Observed data is plotted in black against synthetics (red) achieved with different simulation settings as indicated. 162
- 6.31 Normalized envelopes of East-West component seismograms at station PES (Pesch). Traces are low pass filtered with a cut-off period ranging from 0.8 seconds to 3.6 seconds. Observed data is plotted in black against synthetics (red) achieved with different simulation settings as indicated. 163
- 6.32 Envelopes of synthetic (red) and observed (black) seismograms low pass filtered with 0.8 s cut-off period at station PES. Synthetics result from simulations with point source and elastic model (PE), point source and viscoelastic model (PV) finite source and elastic model (FE), finite source and viscoelastic model (FV). Introduction of complexities into the simulation setting results in an improved agreement of envelopes. 164
- 6.33 Normalized amplitude spectra of East-West component seismograms at station BNS. Traces are low pass filtered with cut-off periods from 0.8 to 3.6 s. Synthetics with setups as indicated are plotted red, observed data is plotted black. 167

6.34	Normalized amplitude spectra of East-West component seismograms at station GMA. Traces are low pass filtered with cut-off periods from 0.8 to 3.6 s. Synthetics with setups as indicated are plotted red, observed data is plotted black.	169
6.35	Normalized amplitude spectra of East-West component seismograms at station FUN. Traces are low pass filtered in a period range from 0.8 seconds to 3.6 seconds. Synthetics with setups as indicated are plotted red, observed data is plotted black.	170
6.36	Normalized amplitude spectra of East-West component seismograms at station MIL. Traces are low pass filtered in a period range from 0.8 seconds to 3.6 seconds. Synthetics with setups as indicated are plotted red, observed data is plotted black.	171
6.37	Normalized amplitude spectra of East-West component seismograms at station PES. Traces are low pass filtered in a period range from 0.8 seconds to 3.6 seconds. Synthetics with setups as indicated are plotted red, observed data is plotted black.	173
6.38	Spectrograms of observed and synthetic seismograms at station PES (Pesche). From bottom to top: Point source elastic, point source viscoelastic, finite-source elastic, finite-source viscoelastic, observation. Increasing similarity with enhanced simulation complexity can be recognized.	175
7.1	Three axes (basin depth, source depth and source mechanism) defining the three dimensional error space investigated in this study.	184
7.2	Variation in basin depth by +/- 10 percent. The blue line in a) indicates the location of a depth-profile which is shown in b).	185
7.3	Uncertainty in hypocenter location for the 2002 Alsdorf earthquake modeled by a variation of +/- 5 percent on source depth.	186
7.4	Variation in strike orientation is used to identify the effects of uncertainties in source mechanism parameters.	187
7.5	Comparison of observed seismic intensities (grayscale map) to simulated intensity distribution of the reference model.	189
7.6	Distribution of virtual receivers used in this study to detect variabilities depending on changes in input datasets.	190
7.7	Seismic intensities from simulations with varying basin depth (left column). The relative difference between the individual models is shown in the middle, whereas the right column shows differences in resulting seismic intensity.	191
7.8	Distribution of virtual receivers used in this study. The four stations from which seismogram comparisons are presented in this section are demarked with large red numbers.	192
7.9	East-West component seismograms at station 33 (see 7.8 for location) achieved using models with basin depth variations from -10 % to +10 % as indicated (a). Maximum amplitudes for individual phases and the resulting peak ground velocity of the traces are plotted in (b).	193

7.10	East-West component seismograms at station 67 (see 7.8 for location) achieved using models with basin depth variations from -10 % to +10 % as indicated (a). Maximum amplitudes for individual phases and the resulting peak ground velocity of the traces are plotted in (b).	194
7.11	East-West component seismograms at station 81 (see 7.8 for location) achieved using models with basin depth variations from -10 % to +10 % as indicated (a). Maximum amplitudes for individual phases and the resulting peak ground velocity of the traces are plotted in (b).	195
7.12	East-West component seismograms at station 131 (see 7.8 for location) achieved using models with basin depth variations from -10 % to +10 % as indicated (a). Maximum amplitudes for individual phases and the resulting peak ground velocity of the traces are plotted in (b).	195
7.13	Seismic intensities from simulations with varying source depth (left column). The relative difference between the individual models is shown in the middle, whereas the right column shows differences in resulting seismic intensity.	197
7.14	Distribution of virtual receivers used in this study. The four stations from which seismogram comparison is presented in this section are demarked with large red numbers.	198
7.15	East-West component seismograms at station 73 (see 7.14 for location) achieved using models with variations in source depth of -5 % and +5 % from the reference value as indicated (a). Maximum amplitudes for individual phases and the resulting peak ground velocity of the traces are plotted in (b).	199
7.16	East-West component seismograms at station 43 (see 7.14 for location) achieved using models with variations in source depth of -5 % and +5 % from the reference value as indicated (a). Maximum amplitudes for individual phases and the resulting peak ground velocity of the traces are plotted in (b).	200
7.17	East-West component seismograms at station 101 (see 7.14 for location) achieved using models with variations in source depth of -5 % and +5 % from the reference value as indicated (a). Maximum amplitudes for individual phases and the resulting peak ground velocity of the traces are plotted in (b).	201
7.18	East-West component seismograms at station 105 (see 7.14 for location) achieved using models with variations in source depth of -5 % and +5 % from the reference value as indicated (a). Maximum amplitudes for individual phases and the resulting peak ground velocity of the traces are plotted in (b).	201
7.19	Seismic intensities from simulations with varying strike orientation (left column). The relative difference between the individual models is shown in the middle, whereas the right column shows differences in resulting seismic intensity.	203

7.20	Distribution of virtual receivers used in this study. The five stations from which seismogram comparison is presented in this section are demarked with large red numbers.	204
7.21	East-West component seismograms at station 35 (see 7.14 for location) achieved using models with variations in strike orientation of -10° to $+10^\circ$ from the reference value as indicated (a). Maximum amplitudes for individual phases and the resulting peak ground velocity of the traces are plotted in (b).	205
7.22	East-West component seismograms at station 38 (see 7.14 for location) achieved using models with variations in strike orientation of -10° to $+10^\circ$ from the reference value as indicated (a). Maximum amplitudes for individual phases and the resulting peak ground velocity of the traces are plotted in (b).	205
7.23	East-West component seismograms at station 152 (see 7.14 for location) achieved using models with variations in strike orientation of -10° to $+10^\circ$ from the reference value as indicated (a). Maximum amplitudes for individual phases and the resulting peak ground velocity of the traces are plotted in (b).	206
7.24	East-West component seismograms at station 143 (see 7.14 for location) achieved using models with variations in strike orientation of -10° to $+10^\circ$ from the reference value as indicated (a). Maximum amplitudes for individual phases and the resulting peak ground velocity of the traces are plotted in (b).	207
7.25	East-West component seismograms at station 106 (see 7.14 for location) achieved using models with variations in strike orientation of -10° to $+10^\circ$ from the reference value as indicated (a). Maximum amplitudes for individual phases and the resulting peak ground velocity of the traces are plotted in (b).	207
7.26	Assumed Gaussian probability relation for individual model variations.	209
7.27	Possible output format displaying combined results from multiple simulations with variable input datasets.	210
7.28	Principle of combination of uncertainties. Squares indicate positions within the error space where variability is known, circles combinations with unknown result.	212
8.1	Screen shot from scenario earthquake database entry page.	215
8.2	Directory tree for a sample entry in the earthquake scenario database.	217
8.3	Seismogram for the WWW scenario database. Black: Filtered seismogram at original sample rate, red dashed: Resampled seismogram. . .	223
8.4	In the file format used by the scenario database complete traces are written one after another.	224

8.5	Complete dataset of synthetic seismograms for one component of ground motion as it is present in the earthquake scenario database. Red dashed box indicates the area shown in figure 8.6 in more detail. (Seismograms for this example are taken from the simulation of the M 6.1, 1756 Düren earthquake.	225
8.6	Excerpt from the dataset shown in figure 8.5. Red dashed box indicates the area shown in 8.7 in a closer view. Note the slight differences between individual profiles.	226
8.7	Excerpt from the dataset shown in previous figures 8.5 and 8.7. At this level of magnification details individual traces can be recognized. . . .	227
8.8	Concept of data flow for the WWW scenario database.	229
8.9	Screen shot from the earthquake scenario database - inspection of time series at interactively chosen location within study area.	230
8.10	Screen shot from the earthquake scenario database - dynamically produced seismogram section.	231
A.1	Program YAC - flowchart part 1	266
A.2	Program YAC - flowchart part 2	267
B.1	Program using the rotated staggered grid approach - flowchart.	278

List of Tables

3.1	Parameters for verification setup.	26
3.2	Verification of nonuniform grid implementation - parameters.	35
3.3	Simulation parameters for the simulation of porous media using the rotated staggered grid.	44
3.4	Parameters for the simulations of a complex topography using the rotated staggered grid.	45
3.5	Parameters for the simulation of a kinematic rupture on a non-planar fault using the rotated staggered grid approach.	46
5.1	Comparison of computational parameters for the different simulation setups.	83
5.2	Comparison of model parameters used in the different simulation setups.	83
5.3	Source parameters for the three scenarios.	90
6.1	Computational parameters for the simulations of the 2002 Alsdorf earthquake.	124
6.2	Media parameters for elastic and viscoelastic models.	125
6.3	Source parameters for the M_L 4.9 2002 Alsdorf earthquake as used in this study.	126
6.4	Stations of the Bensberg seismic network with their individual site conditions and epicdistance to the Alsdorf, 2002 earthquake.	131
7.1	Computational parameters for the simulations in this chapter.	181
7.2	Source parameters for the 2002 Alsdorf earthquake (M_L 4.9).	182

Appendix A

YAC - Code Description

A.1 Overview

The program YAC (which simply stands for Yet Another Code) is a finite difference wave propagation code working with staggered grids. The code is designed for parallelization in two horizontal directions by message passing. It includes viscoelasticity implemented by Standard Linear Solids and simple finite source models (circular cracks with homogeneous slip rate). Material contrasts within the media can be smoothed by an averaging of material contrasts. This behavior is determined by a switch in the input parameters. The program is restricted to isotropic media. Absorbing boundaries are implemented using the PML approach. The code is written in Fortran90 using MPI library calls for the inter node communication. The flowchart shown in figures A.1 and A.2 illustrates the design of the main program.

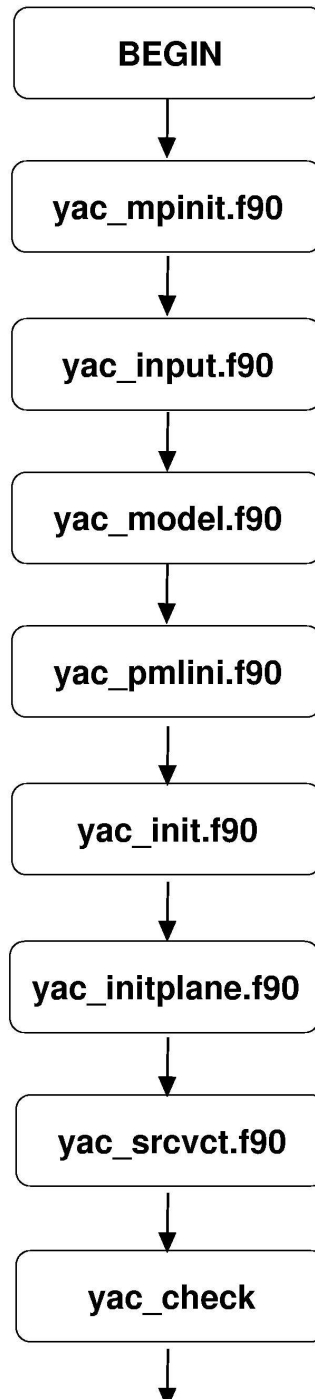


Figure A.1: Program YAC - flowchart part 1

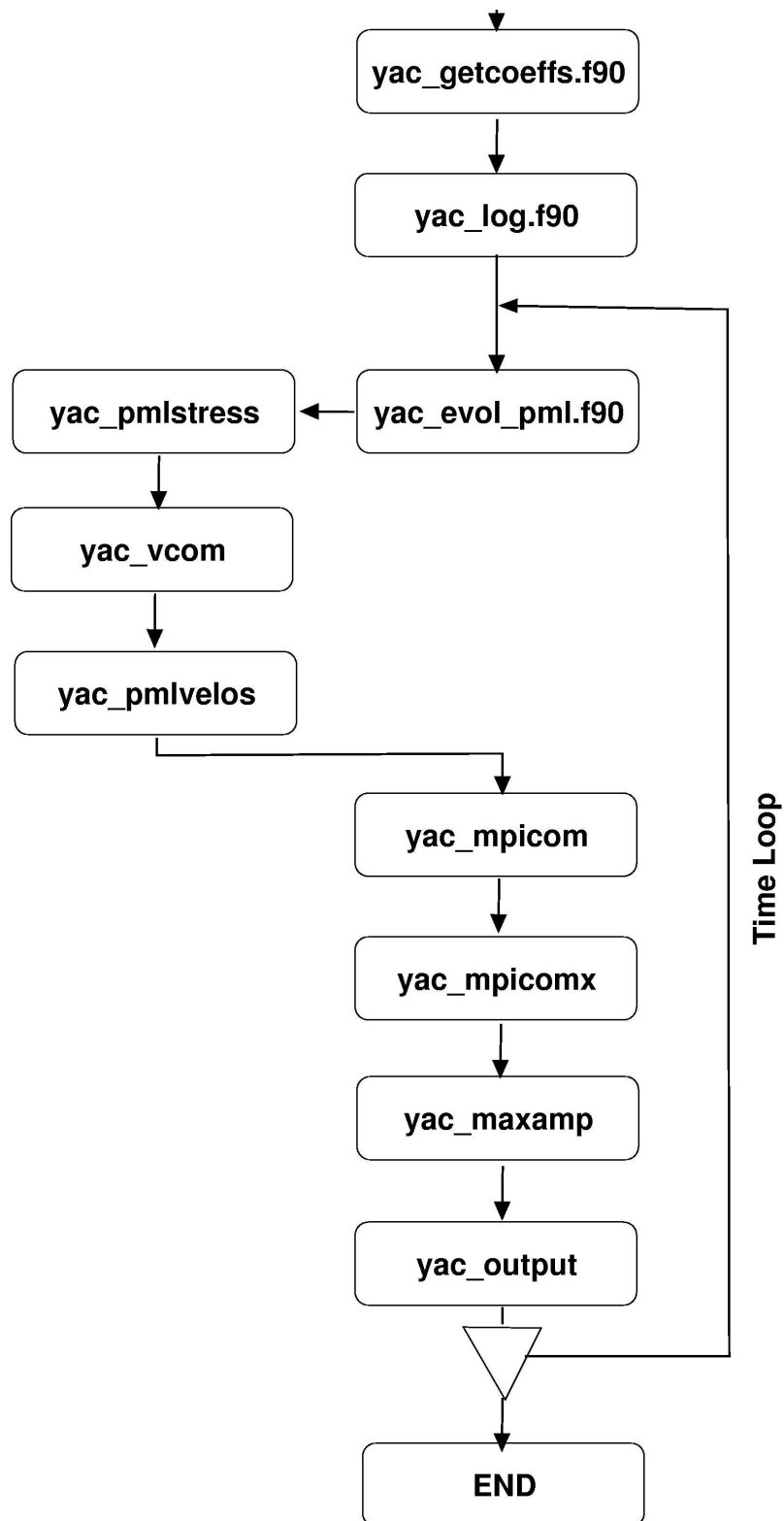


Figure A.2: Program YAC - flowchart part 2

A.2 Code Files

A.2.1 Parameter Files

params.h This include file entails the definition of constants necessary to be initialized and known by the program at compilation time. As many crucial things are defined herein the complete listing is shown in the following and described in detail.

```

! global specifications
implicit none
integer nx,ny,nz,maxnt,maxnr,maxdom,np,np_x,np_y,tshift
integer gridsamp,sgx,sgy
real pi
!for 1 node
parameter(nx=224,ny=224,nz=72)
!for 2 nodes
!parameter(nx=114,ny=224,nz=72)
!for 4 nodes
!parameter(nx=114,ny=114,nz=72)
!parameter(nx=52,ny=52,nz=80)
parameter(maxnt=1400)
parameter(maxnr=10)
parameter(maxdom=10)
!parameter(izfree=5)
parameter(pi=3.1415926535898)
!for 1 node
parameter(np=1)
parameter(np_x=1)
parameter(np_y=1)
!for 2 nodes
!parameter(np=2)
!parameter(np_x=2)
!parameter(np_y=1)
!for 4 nodes
!parameter(np=4)
!parameter(np_x=2)
!parameter(np_y=2)
parameter(tshift=500)
parameter(gridsamp=50)
parameter(sgx=5)
parameter(sgy=5)

```

The YAC code is parallelized with respect to the two horizontal directions X and Y. Parameter `np` denotes the number of overall nodes used for the simulation, whereas `np_x` and `np_y` indicate the number of nodes in X and Y direction respectively. As a necessary consequence the condition $np = np_x * np_y$ must be fulfilled. The grid dimensions for individual nodes are set by the parameters `nx`, `ny` and `nz`. For communication purposes a 4 points wide margin is shared among neighboring nodes. Thus the resulting overall grid dimensions can be calculated as $\hat{nx} = np_x * (nx - 4) + 4$ and $\hat{ny} = np_y * (ny - 4) + 4$. The additional 4 points being associated with the last node in each row or column not having a neighbor. These dimensions must be matched by the provided velocity model.

The parameter `maxnt` denotes the maximum number of timesteps that can be calculated. This value has to be known at compilation time in order to define storage space for the seismograms. As the time increment is calculated at run time of the program accordingly to the stability criterion the actual number of time steps is not fixed at compile time. An estimation has to be done beforehand in order to ensure $maxnt > nt$.

A similar consideration accounts for `maxnr` which indicates the maximum number of receivers involved. Receiver locations are handed to the program through a receiver file as described below. It is crucial that the number of receivers fits into the maximum number which is defined here.

The parameter `tshift` defines the maximum temporal shift of the source time function when a finite source model is considered. Again, the consideration is that the actual time delay for an arbitrary point within the finite source plane is calculated at run time, whereas the maximum has to be known at compilation time.

common.h In this include file all global variables necessary to be known by all subroutines are defined, except for the specific arrays and variables which are related to the PML boundaries.

simpl.h Variables defining the PML domain which is added to the physical model space in order to suppress artificial reflections are defined in this include file.

A.2.2 Subroutines

yac_main.f90 As the name imposes this is the main program of the code. It entails only calls to various subroutines which are described in the following and a number of timing routine suggestions related to specific environments such as the Hitachi SR8000 and a PC cluster. All of them are commented and should be adopted to the individual environment. As timing routines necessarily contain system calls here are the pitfalls when the code is ported.

yac_check.f90 Actually no real checking is carried out in this routine, it mainly writes the setup to standard output.

yac_evolution.f90 Most of the work is done within this subroutine. It entails the evolution of the propagating wavefield in time and space. Subroutines for updating stress fields (**yac_pmlstress.f90**) and velocity fields (**yac_pml_velocities.f90**) are called from within, as well as the necessary communication of velocities between nodes (**yac_vcom.f90**).

yac_init.f90 In this subroutine most of the general initialization is done, for example the source location is set and the source time function is built up. Furthermore the locations of receivers are set properly and in parallel case the routine checks which receivers are associated with individual nodes.

yac_input.f90 From a file called parcal parameters for the actual simulation run are read. The structure of that file is shown and described below.

yac_log.f90 The same output as in **yac_check.f90** written to a log file.

yac_maxamp.f90 Peak amplitudes of the wave field at surface for all components as well as the vector quantity are stored for the later output of PGV maps. Values of recorded shaking duration are also updated in this routine.

yac_model.f90 In this subroutine the velocity model is being built up. There are numerous predefined models such as a homogeneous case, a layered model and the possibility to define a three-dimensional model by providing a depth-to basin map and a table containing bedrock velocities. The number of layers for the bedrock model is currently fixed to 8. The file containing this table is also hard coded into bk_mod.dat, the idea being that this part of the model is not subject to frequent changes. Within this definition also the velocity gradient within the sedimentary layer is defined. Relaxation times for the modeling of viscoelastic attenuation are also defined within this subroutine.

yac_mpicom.f90 Internode communication using message passing is performed in this subroutine. Stress values necessary at the boundaries are updated from neighboring nodes in Y-direction of the computational grid. A detailed description of the 2D parallelization design is given in chapter 3.

yac_mpicomx.f90 Internode communication using message passing is performed in this subroutine. Stress values necessary at the boundaries are updated from neighboring nodes in X-direction of the computational grid. A detailed description of the 2D parallelization design is given in chapter 3.

yac_mpinit.f90 Initializes variables necessary to perform message passing internode communication. The global communicator is initialized and the neighbor nodes of each node are defined. A consistency check is performed and the addresses are written to standard output.

yac_outmap.f90 Area wide maps of PGV and shaking duration that were stored in **yac_maxamp.f90** are written to file.

yac_output.f90 Contains the main output routines for snapshots and seismograms. Ground motion values are interpolated to the given receiver locations and being stored. A parameter (iflush) in the input file parcal defines how often these values are written to disk.

yac_pmlini.f90 Arrays necessary for the absorbing PML boundary condition are initialized. Coefficients determining the absorption behavior are defined to a standard value from literature.

yac_pml_stress.f90 In this subroutine the stress fields are updated using PML boundaries. The greatest part of this file consists in the formulation of derivatives within the PML margins and their attenuation.

yac_pml_velocity.f90 Analog to **yac_pml_stress.f90** the velocity fields are updated and the PML calculations are performed.

yac_srcvct.f90 The moment tensor point source is initialized from the given values of strike, dip and rake defined in the input file parcal.

yac_vcom.f90 Velocities at the boundaries have to be updated before the stress fields are updated. This is done in this routine in Y-direction of the computational grid.

yac_vcomx.f90 Same as **yac_vcom.f90** but for the X-direction of the grid.

A.3 Input Files

parcal In this file all specifications necessary at run time are being provided. In the following a listing of an example file is shown along with additional explanations.

seisfile =Data/cal !filename of simulation run

This filename provides both the path to an output directory (which must be existing and writable), as well as the name base (in this case cal) onto which the code adds the numerous endings for individual output content. For example seismograms of the X-component would be written to **./Data/cal_x** in this case.

recfile =Receivers/rec_cross.dat

Analog to the output file the directory and file indicated here must be existent and readable. The design of the receiver file is described in the paragraph below.

sedfile =layer1.dat

The depth to bedrock values for a sedimentary basin model (or alike models) is provided within the specified file. The file is accessed only when model_type 3 is chosen (see below). Nevertheless some filename has to be provided in any case.

tmax =40. !length of simulation in s

Duration of the simulated wave propagation is indicated. Attention has to be given to the number of resulting time steps.

nop =4 !length of operator (2,4,or 8)

Length of differential operator, only 4 is allowed with the current version.

xmax =160000. !side length x (m)

ymax =160000. !side length y (m)

zmax =60000. !side length z (m)

The model dimensions are denoted in meters. Together with the grid dimensions defined in **params.h** from these values the grid spacing is derived. As the time step is depending on the grid spacing according to the stability criterion a change in this parameter can have numerous influences.

model_type =1 !1=homog. isotr.

Available model_types are explained in the description of **yac_model.f90**.

vs0 =5900. !vs for homo model PREM at 80km depth

vp0 =8000. !vp for homo model PREM at 80km depth

rho0 =2800. !rho for homo model PREM at 80km depth

Some homogeneous standard model.

Source—————

modx0 =0. !model origin x

mody0 =0. !model origin y

Origin of the model space. These parameters are useful when a realistic model is concerned. These static offsets then allows the usage of real coordinates for source and receiver.

xxs =82000.0 !x-coord center of point source

yys =82000.0 !y-coord center of point source

zzs =34400. !z-coord center of point source

Source coordinates in meters.

source_type =10 !1-fx,2-fy,3-fz,4-expl,5-planeP

Definition of the source type. 10 denotes moment tensor point source, 12 stands for a finite source.

momentum =

8.4e15

strike =90. !Strike

dip =90. !Dip

rake =0. !Rake

Source parameters, the momentum has to be given in Nm, the strike, dip and rake angles in degree.

sxangle =20. !plane wave angle (deg) with x axis

syangle =0. !plane wave angle (deg) with y axis

srcper(s) =2.0 !dominat period (s) of source

Period of Gaussian source time function. If this parameter is set to zero a delta pulse is applied.

alphaxy =30. !Half width of source gauss (m)

A Gaussian function for smoothing the point source over a finite volume can be defined here.

MISC_____

isamp =1 !seismograms: use every 'isamp' sample

Sampling rate for output seismograms given in timesteps.

tsnap =1. !snapshot after 'tsnap' seconds

Time interval between snapshots provided in seconds.

iflush =500 !seis output interval

Time interval in timesteps after which seismograms are actually written to hard disk. Depending on machine architecture this is an important tuning parameter.

icheck =1 !max/min values out

Some simple information like the actual maximum values for field variables is written to standard output with an interval defined by this parameter.

nabs =50

Unused parameter for the definition of absorbing boundaries. The width of the PML boundary is defined in **simpml.h**.

thresdur =0.04

This parameter describes the threshold value from which shaking duration is derived.

In the following a few switches have to be set.

1

The free surface condition is applied with simple mirroring of stresses (0) or with a more advanced approach (1).

0

currently unused

1

Model parameters are spatially interpolated if set to 1 to achieve smoother model representation, if set to 0 no interpolation is performed.

1.0

A basin model can be stretched in depth by the value provided here.

src_rad =1000.

Radius of the circular finite source.

src_shape =1

Optional switch for the usage of predefined source shapes (circular, elliptic, rectangular etc.). Currently only circular sources are implemented.

fmidy =75000.

fmidz =10000.

Also unused at the moment. These variables can be used for independent definition of source plane and hypocenter. In the current version the hypocenter is located in the middle of the circular fault.

Most of the parameters provided are explained already within the file. However, a few explanations should be given.

A.3.1 Receiver Location

Locations of virtual receivers where time series of ground motion are recorded have to be defined in the receiver file given in `parcal`. This file has the following simple layout. The first line indicates the number of receivers to come, the following lines denote their location in x and y direction in meters. The model origin given in `parcal` by the variables `modx` and `mody` is subtracted from that positions to simplify the usage of geographic coordinates like UTM. It is likely that receiver locations defined herein do not coincide with grid points of the computational model. Seismogram samples are therefore interpolated from the nearest grid points.

A.3.2 Velocity Model Definition

One of the most important parts of the input dataset for a wave propagation code is the definition of the velocity model. As mentioned above this is done in the subroutine `yac_model.f90`.

Standard Models There are a number of standard models available such as homogeneous and layered models (corresponding to `model_type` 1 and 4). These kind of models are defined on grid basis and can be easily varied by editing the source code.

Sedimentary Basin Definition Main target of the code is modeling wave propagation in presence of sedimentary basins. A relatively convenient way in defining a such a basin is implemented as `model_type` 3. A two-dimensional basin depth map matching the overall dimensions of the grid surface is handed to the program. Depth values within this file must have negative sign. The program projects this depth values onto the grid, using either homogeneous velocities within the basin (defined in `yac_model.f90`) or depth dependent velocities (also defined in this subroutine). Seismic velocities for the circumjacent bedrock are provided via a file called `bk_mod.dat` consisting of a simple table with bedrock parameters.

3D model Definition Another possibility of defining a velocity model handing the program a complete 3D model representation as it is provided for example by the SCEC model. This feature is currently implemented only for the usage with one node. As it is in experimental status the filename to be provided is hard coded as `pmod2.dat`. Taking advantage of the parallel output functionality it would be easy to extent this into a parallel version.

A.4 Output Files

Several types of output values are produced and written to hard disk by the code. Files are named after the name base provided in the input file `parcal`. In this example `./Data` as output directory and the name base `cal` is assumed.

For the usage in a parallel environment each filename is extended by the number of the individual computation node, starting with zero. In the current implementation two digits are used for this extension so the maximum number of nodes is restricted to 100.

Seismograms Three component seismograms at the locations provided in the receiver file are written in the files **cal_x**, **cal_y** and **cal_z**. All of them start with a single line giving the number of receivers, then the samples are written.

Snapshots Up to nine snapshot files are created and collect particle motions at specified times.

cal_Xxs, **cal_Xys** and **cal_Xzs** contain snapshots of three components of particle velocity within a plane dissecting the model space in center along the Y axis. (That means that the X coordinate is constant and therefrom originates the filename).

cal_Yxs, **cal_Yys** and **cal_Yzs** contain snapshots of three components of particle velocity within a plane dissecting the model space in center along the X axis.

cal_Zxs, **cal_Zys** and **cal_Zzs** contain snapshots of three components of particle velocity at the surface.

Shakemaps **cal_shm_x**, **cal_shm_y** and **cal_shm_z** contain peak ground velocity values for the x, y and z component of ground motion at the surface. **cal_shm_v** contains the vectorial maxima of surface velocity.

Cumulative Energy Additionally, the cumulative energy is recorded over the model surface. This quantity is given by the product of instantaneous ground velocity multiplied by local density integrated over the simulation time. The different components are contained in **cal_ekin_x**, **cal_ekin_y** and **cal_ekin_z**.

Shaking duration The procedure of deriving an estimate on the duration of strong ground motion is described in chapter 5. Durations for the different components are contained in **cal_durx**, **cal_dury** and **cal_durz**.

Time series on a grid For the usage in tools like the WWW-based earthquake scenario database a dataset of seismograms on a regular grid of receiver locations is necessary. These are recorded with a spacing defined in **params.h** and written to the files **cal_sg_x**, **cal_sg_y** and **cal_sg_z**.

Model and setup checks Numerous files are created providing a logging of important parameters of computational and model parameters. The file **surfvel.dat** contains the velocities at the surface. In a number of files with common name **cal_splane** coordinates of the effective source plane are stored. The file **fd3log** holds a complete parameter setup.

A.5 Tested Environments

The code has been tested on the Hitachi SR8000 and on PCs running under LINUX with various compilers, such as PGI F95 or different versions of the Intel Fortran Compiler. As the code is written in parallel form an installation of the MPI standard must be available. The code works with the MPICH implementation. It has also run on multiprocessor shared memory architectures. However, due to a high memory access rate the performance is not very good.

A.6 Matlab Tool for Relaxation Times

Appropriate relaxation times for the standard linear solid formulation of viscoelastic attenuation used in the code can be derived using the Matlab script `qtsolver2.m`. The tool can be found on the CD-ROM in a subdirectory of the YAC code directory. The physical concept behind the script and sample output can be found in section 3.3. In the following the code is briefly described in order to enable adjustments to the individual demands by the user.

From the matlab prompt the script reads a target quality factor and a related range of variation. Afterwards a loop over a hard coded range of frequencies is performed. For each frequency combinations of relaxation times within a also hard coded range are evaluated in terms of effective quality factors. The resulting matrices are stapled for all frequencies. Finally, a color-coded plot of the matrix of stapled quality factors is generated from which the optimal combination of relaxation times can be estimated.

Appendix B

Rotated Staggered Grid - Code Description

As discussed in chapter 3 a finite difference approach on a alternatively oriented staggered grid is capable of circumventing some problems of the standard formulation. A simple implementation of this method is provided with this work and described in the following.

B.1 Overview

The code is designed in the manner of a training code (as defined by the SPICE code library), appropriately the structure of the program is kept simple. From the flowchart shown in figure B.1 it can be understood how the program is organized and where changes have to be applied in order to adopt the program to specific problems. Input and output are also kept in a very basic style and serve only as examples. As can be seen in the flowchart first parameters are read from a file called **parameters.txt**. This file is also kept in a basic style without any comments. The content is described in the section below. The next program step is the initialization of global variables. Wavefield arrays are set to zero, a velocity model is initialized and a test function for the rotated differential operators is passed before wave propagation is modeled in the evolution. A basic output routine is called from within the evolution. The individual program parts are described in the following to an extent that should enable the potential user to understand, use and modify the code according to his requirements.

B.2 Code Files

B.2.1 Parameter Files

globals.h This file contains all global variables necessary for modeling wave propagation. The listing below shows the individual entries with descriptions.

```
integer nx,ny,nz  
integer sx,sy,sz
```

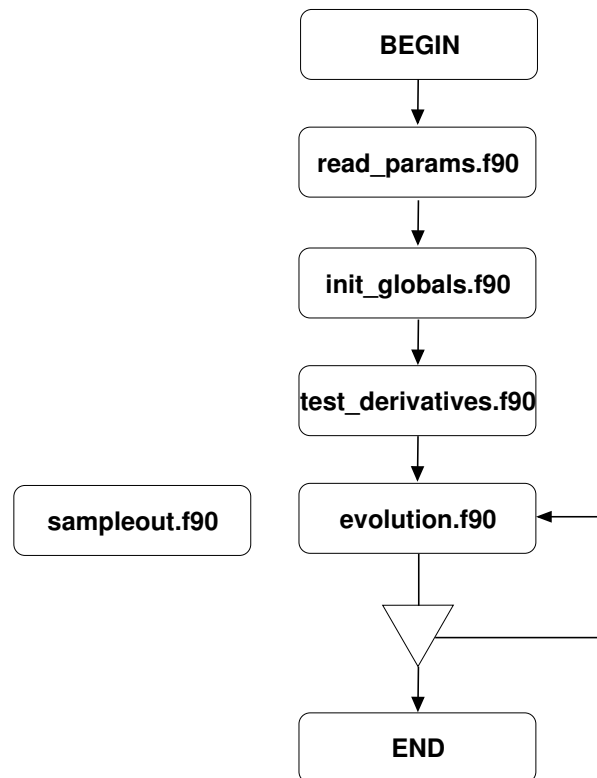


Figure B.1: Program using the rotated staggered grid approach - flowchart.

```
integer it,nt,nop
integer maxnt
parameter (nx=300)
parameter (ny=300)
parameter (nz=61)
```

The model size is defined.

```
parameter (maxnt=2000)
```

Maximum number of time steps for the simulation. This has to be known at compilation time also the actual number of time steps is defined through an input file. The number defined in the file **parameters.txt** must be less or equal to the here defined maximum.

```
integer grid,surf,izfree
```

The important variable is **grid** which represents a switch between standard grid orientation and rotated staggered grid. It is set by the input file **parameters.txt**.

```
real, dimension(nx,ny,nz) :: v11,v12,v13
real, dimension(nx,ny,nz) :: v21,v22,v23
real, dimension(nx,ny,nz) :: s11,s12,s13,s14,s15,s16
real, dimension(nx,ny,nz) :: s21,s22,s23,s24,s25,s26
```

Field variables for stress and velocities of the modeled wavefield as well as their derivatives.

```
real, dimension(nx,ny,nz) :: d1v11,d2v11,d3v11,d4v11,
d1v12,d2v12,d3v12,d4v12,
d1v13,d2v13,d3v13,d4v13
real, dimension(nx,ny,nz) :: d1s11,d2s11,d3s11,d4s11,
d1s12,d2s12,d3s12,d4s12,
d1s13,d2s13,d3s13,d4s13
real, dimension(nx,ny,nz) :: d1s14,d2s14,d3s14,d4s14,
d1s15,d2s15,d3s15,d4s15,
d1s16,d2s16,d3s16,d4s16
```

These variables contain the partial derivatives obtained by the rotated differential operators. In the rotated grid formulation four partial derivatives along the space diagonals are used in different combinations in order to produce the orthogonal derivatives of stresses and velocities.

```
real, dimension(nx,ny,nz) :: exx,eyy,ezz,exy,exz,eyz
real, dimension(nx,ny,nz) :: rho,lamda,mu,gauss,vps,vss
```

Model variables, defining density and velocities.

```
real, dimension(nx,maxnt) :: seisx,seisy,seisz
```

Variables used for seismogram output.

```
real dx,dy,dz,dt
```

Grid spacing and time increment.

```
real dl, aa
```

dl is the effective grid spacing in the rotated direction (along the space diagonals), whereas aa is used to define a smoothing Gaussian around the point source.

```
real vp0, vs0, rho0
```

Values for the definition of a homogeneous model.

```
real, dimension(1000)::src
```

Source time function.

```
integer, dimension(nx,ny)::topo
```

A topography model to be loaded into the code and described by a vacuum formulation.

B.2.2 Subroutines

diffops.f90 This subroutine contains the differential operators along the rotated directions working on stresses. The listing below shows the formulation of these operators. It can be easily understood that the difference to a standard formulation is only the different grid length which is associated with the space diagonal and the direction of the operator exposed by the indices within the finite difference scheme.

```
...
g1=0.0416666666
g2=-1.125
g3=-g2
g4=-g1
...
elseif (swop.EQ.4) then
do z=3, nz-2
do y=3, ny-2
do x=3, nx-2
out(x,y,z)=1/dl*(g1*in(x-1,y-1,z-1)+g2*in(x,y,z)+
+g3*in(x+1,y+1,z+1)+g4*in(x+2,y+2,z+2))
enddo
enddo
enddo
endif
```

diffopv.f90 Analog to **diffops.f90** this one contains the differential operators for velocities.

evolution.f90 Within this subroutine the temporal evolution of the propagating wavefield is modeled. Depending on the grid type chosen in **parameters.txt** subroutines **divops.f90** and **divopv.f90** or **pder.f90** are called in order to carry out the necessary partial derivation of the wavefield variables. The remaining code is a standard finite-difference scheme including a simple point source formulation. A simple output routine **sampleout.f90** is called from within.

initglobals.f90 Both field variables and model are initialized in this subroutine. There are a number of predefined models available, such as homogeneous, layered model, homogeneous model including a topography with air above it.

main.f90 The main program of the rotated staggered grid training code. It contains only subroutine calls and is shown as flowchart above.

old_pder.f90 The standard formulation of differential operators.

readparams.f90 This subroutine reads input parameters defining the simulation setting from a file called **parameters.txt** which is listed above.

sampleout.f90 A very simple output routine which opens a number of files for seismograms and snapshots when it is called the first time and then writes data to the hard disk.

testdev.f90 This is a testing routine for the new differential operators. A Gaussian function is defined and differentiated by standard finite difference operators as well as new rotated operators and absolute values for both are written into file

B.3 Input files

parameters.txt The initialization of both physical and computational parameters is carried out using this one file. It contains simply a several numbers which are explained in the following using the one provided with the code as an example.

```

50 Grid spacing [m]
3000 P-wave velocity for homogeneous model [m/s]
1800 S-wave velocity for homogeneous model [m/s]
2100 Density for homogeneous model [m/s]
500 Number of time steps
0.2 Time increment [s]
111 Source location X coordinate [grid points]
81 Source location Y coordinate [grid points]
50 Source location Z coordinate [grid points]
2 Operator length
1 Grid type switch 1: rotated grid 0: standard grid
2 Surface switch 1:free surface at top of domain, 2: surface
  topography is read from file

```

model_file If the appropriate model type is chosen a topography file can be provided which is then discretized into the computational grid. Grid points below this surface are set to the values defined by **parameters.txt** as it is the case for the homogeneous model. For grid points above a air-like set of parameters is defined.

For simplification the provided model must already contain the topography in grid points (i.e. integer values fitting properly into the model space).

B.4 Output Files

files created by testderivates.f90 As mentioned above a subroutine called testderivates is part of the code which allows to check results produced by the rotated differential operators against analytical solutions as well as results produced by the standard finite difference staggered grid operators.

For this aim a three-dimensional Gaussian is initialized within the model space and derivatives are calculated using standard and rotated operators. An analytical solution evaluated at the same positions as given by the individual simulation run is written to file as well. The files are:

files produced by sampleout.f90 The subroutine **sampleout.f90** produces two kinds of output files:

- 1) Snapshots of velocity and stresses
- 2) Seismograms along a specified grid line

Appendix C

Supplementary CD-ROM

The CD-ROM contains three directories:

- Thesis
Contains a soft version of this document in PDF format.
- Codes
Contains the YAC and Rotated Staggered Grid code.
- Database
Contains the PHP code of the earthquake scenario database along with data from the simulations presented in this work.

Danksagung

Viele Personen haben auf vielfältige Weise zum Gelingen dieser Dissertation beigetragen. Ich möchte mir nicht anmaßen, die individuellen Hilfestellungen zu kommentieren oder zu bewerten. Mein herzlicher Dank gilt den Folgenden:

Prof. Heiner Igel, Prof. Frank Scherbaum, Dr. Klaus-Günther Hinzen, Prof. Hans-Peter Bunge, Dr. Anselm Smolka, Dr. Gerhard Berz, Dr. Joachim Wassermann, Steffi Rieger, Kim Bak Olsen, Gilbert Brietzke, Toni Kraft, Markus Tremml, Jens Oeser, Wiwit Suryanto, Haijang Wang, Bernhard Schubert, Alex Hornung, Peter Danecek, Teresa Reinwald, Gunnar Jahnke, Martin Käser, Max Strasser, Melanie Lochmann, Maren Luesse, sowie meiner gesamten Familie.

Die der Arbeit zugrunde liegenden numerischen Berechnungen wurden auf dem Bundeshöchstleistungsrechner des Leibniz Rechen Zentrums, München durchgeführt.

Die Durchführung dieser Arbeit wurde finanziert durch ein Stipendium der Münchener Rück, sowie die Forschungsprojekte KONWIHR und BaCaTec.

Für musikalische Begleitung sorgten:

Social Distortion, Nile, The Duskfall, Nightrage, Arch Enemy & Nevermore.

Curriculum vitae

Persönliche Daten

Name Michael Andreas Ewald
Anschrift Waldstr. 11
85635 Höhenkirchen
Tel. 08102 - 74 83 28
email: ewi@geophysik.uni-muenchen.de
Geburtsdatum 6.4.1971
Geburtsort München
Familienstand ledig

Schulbildung

1977 - 1981 Volksschule Höhenkirchen
1981 - 1990 Gymnasium Ottobrunn
Abitur im Juni 1990

Wehrdienst

1990 - 1991 3. PzArtBtl 565 Bayernkaserne München

Berufsausbildung

1991 - 1993 Ausbildung zum Ingenieursassistenten Fachrichtung Datentechnik
an der Berufsfachschule der Siemens AG

Studium

1995 Beginn des Studiums der Geophysik (Diplom)
an der Ludwig Maximilians Universität München
1997 Vordiplom
2000-2001 Diplomarbeit zum Thema
"Numerical Simulation of Site Effects in the Cologne Basin"
30.01.2002 Abschluß: Diplom-Geophysiker
2001-2005 Doktorarbeit zum Thema
"Numerical Simulations of Earthquake Scenarios
in the Lower Rhine Embayment Area"